Novel Synthetic Magnetic Materials Optimised for RF and Microwave Applications

SWINDELLS, CHARLES,RICHARD

Novel Synthetic Magnetic Materials Optimised for RF and Microwave Applications

Charles Swindells

A Thesis presented for the degree of Doctor of Philosophy

Centre for Material Physics

Department of Physics

Durham University

December 2020

Abstract

Understanding and controlling the dynamic magnetisation behaviour of magnetic systems is fundamental to current and future technological applications. This thesis examines the underlying physics and explores the potential of magnetic thin-film systems for high frequency applications. Particular focus was directed towards exploiting interfacial phenomena, to enhance the frequency bandwidth response, and lithographic patterning to control the resonant frequency.

The design, development and functional capabilities of a purpose built integrated system to probe the dynamic response of magnetic thin-film systems as a function of applied magnetic field, excitation frequency (up to 15 GHz) and sample orientation is detailed. Sample motion, with respect to the measurement transmission line, was achieved with 5μm vertical motion precision and an angular step precision of 1.8°.

Physical mechanisms and parameters involved in damping were investigated on multilayers combining ferromagnetic (Co, CoFeB) and heavy metal layers (Pt, Ru) to quantify interfacial spin-transport. Enhanced interfacial transparency, leading to higher damping, is observed for more closely matched FM/HM crystal structures. Including a thickness-dependent spin-diffusion length gives a bulk value of $\lambda_s = 9.4 \pm 0.7$ nm for Pt. The propagation of spin current into Pt was shown to be suppressed beyond a nominal SiO_2 insulating barrier of 2 nm corresponding to the formation of a continuous SiO_2 layers, from x-ray reflectivity analysis.

The role of the induced moment in Pt with respect to interfacial damping was explored using synchrotron radiation. The nature of the induced moment was first explored by investigating the alignment of the Pt moment across the transition-metal-rare-earth ferrimagnetic magnetisation compensation transition. It was shown that the moment aligns with the transition-metal regardless of the dominant sublattice. The induced moment was correlated with the magnetic damping in CoFe/Pt and NiFe/Pt systems with Au and Cu spacer layers. The relation between an induced moment and enhanced damping highlights the role of $d - d$ hybridisation.

Photolithography was used to pattern materials to enhance the effective magnetic field. An almost linear relation was observed between the aspect ratio and the induced anisotropy field, and hence the resonant frequency. This relation was used to produce tessellated patterns with varying aspect ratio, that demonstrated an isotropic, broadband and field-free dynamic magnetisation response.

Declaration

Unless explicitly stated otherwise, the work in this thesis is solely that of the author. No part of this thesis has been submitted elsewhere for examination for any other degree at any University.

Design and production of the integrated ferromagnetic resonance systems presented in chapter 7 was undertaken with the support of the Electronic Engineering Service technical support team, in particular specific designs and production of the housing, microcontroller boards, and power regulation were undertaken by Andrew Hunter. Initial code to control the motors, and designs of the motor stands were produced by Katarina Henning, a RISE student, supervised by the author.

The synchrotron measurements used in chapter 9 involved the work of several persons. Data acquisition was undertaken by the author, along with Professor Del Atkinson, Professor Thomas Hase and Dr. Yongseong Choi. Some of the ferrimagnetic samples used in the first half of chapter 9 were grown by Dr. Oto-obong Inyang in Durham University, with MPMS-SQUID magnetometery undertaken by Ben Nicholson at the Materials Characterisation Lab, ISIS Neutron and Muon Source. Thickness gradient wedges used in the second half of chapter 9 were grown and partially characterised using VNA-FMR by Dr. Hubert Głowiński at the Institute for Molecular Physics, Poznan, Poland. All subsequent analysis of all samples was undertaken by the author.

This work has been supported by the Engineering and Physical Sciences Research Council. The content in this thesis has been reviewed and agreed for public release by BAE Systems. Published data used in this thesis can be found at `https://doi.org/10.15128/r27m01bk728`, `https://doi:10.15128/r2cf95jb46b` and `http://doi.org/10.15128/r2765371377`.

Acknowledgements

There are a great number of people without whom this thesis would not have been possible. Firstly, I would like to thank Professor Del Atkinson for his support, guidance and friendship over the past few years. I am grateful for his insight into Physical phenomena and general life advice, as well as parking tips and skills with a Raspberry Pi. I would also like to thank Dr Aidan Hindmarch for motivation, all the helpful discussions and his incredible experimental expertise. I am grateful to Prof Andrew Gallant for his support on the project and general engineering advice.

Thanks also go to Dr Ian Sturland and Alex Duncan from the project sponsors for their input. The x-ray resonant magnetic reflectivity measurements would not have been possible without the support, assistance and humour from Dr Yongseong Choi at Argonne National Lab, and Dr Tom Hase at the University of Warwick. I am grateful to Dr Piotr Kuświck and Dr Hubert Głowiński for their support and generosity while hosting me at the Institute for Molecular Physics in Poznan.

Much of this work would not have been achievable without the support of Stephen Lishman and the Mechanical Workshop team and Andrew Hunter in the Electronic Workshop, all of whom I am grateful to. I would also like to thank the two RISE summer students I hosted, Gesa-Roxanne Siemann and Katarina Henning who both contributed to the project.

I am grateful to have worked alongside many intelligent and entertaining people in Ph142 over the years, including Dr Sinan Azzawi, Dr Liam Stubbington, Dr Oto-obong Inyang, Dr Joe Troughton, Alejandro Galan-Gonzalez, João Luis and Kalel Alsaeed, and in particular the support and friendship of Ben Nicholson and Ariam Mora-Hernandez who began this journey at the same time.

Finally, I wish to thank my friends and family, in particular Charlotte for keeping me mostly sane.

List Of Publications

Portions of this Thesis have been published in peer-reviewed journals. The first half of chapter 8 is partially summarised in:

Spin transport across the interface in ferromagnetic/nonmagnetic systems
C. Swindells, A. Hindmarch, A. Gallant and D. Atkinson
Physical Review B, **99**, 064406 (2019)

The second half of chapter 8 is partially summarised in:

Spin current transparency of insulating layers in multilayered ferromagnetic systems
C. Swindells, A. Hindmarch, A. Gallant and D. Atkinson
Applied Physics Letters, **116**, 042403 (2020)

The first half of chapter 9 is partially summarised in:

Proximity-induced magnetism in Pt layered with rare-earth–transition-metal ferrimagnetic alloys
C. Swindells, B. Nicholson, O. Inyang, Y. Choi, T. Hase and D. Atkinson
Physical Review Research, **2**, 033280 (2020)

Additional co-authored publications by the candidate, with results not directly included within this Thesis:

The role of low Gd concentrations on magnetisation behaviour in rare earth:transition metal alloy films
O. Inyang, A. Rafiq, **C. Swindells**, S. Ali, and D. Atkinson
Scientific Reports, **10**, 9767 (2020)

Conferences Presentations

Work contained within this Thesis has been presented at the following conferences:

Magnetism and Magnetic Materials (MMM),
Las Vegas 2019 (Talk)
Spin transport and conflicting values of spin diffusion length in FM/HM systems.

Joint European Magnetic Symposium (JEMS),
Uppsala 2019 (Poster)
Resolving conflict in reported values of spin diffusion length for spin transport in FM/HM systems

IOP Magnetism,
Leeds 2019 (Talk)
Resolving conflict in reported values of spin diffusion length for spin transport in FM/HM systems

International Colloquium on Magnetic Films and Surfaces (ICMFS),
Santa Cruz 2018 (Poster)
Influence of interfacial structure and heavy metal thickness on precessional damping and spin-mixing conductance

IOP Magnetism,
Manchester 2018 (Poster)
Influence of interfacial structure and heavy metal thickness on precessional damping and spin-mixing conductance

Contents

Chapter 1

Introduction and Outline

1.1 Background

Magnetic materials and interactions underpin a wide range of current and potential technological applications. One important phenomena of interest is the relationship between electromagnetic radiation (EM) and magnetic moments, which can induce a precession of the moment. For EM radiation with frequencies typically in the microwave (GHz) regime, this precession evolves into resonant behaviour, leading to maximal absorption of the wave. In traditional microwave electronic systems, this increase in loss can impose limits on the frequency of operation, however, for applications in which the increase in loss is desirable, such as microwave absorbers, it is necessary to understand how to tune material parameters to exploit this magnetic phenomena.

Existing microwave absorbers based on magnetic materials typically involve small particles of magnetic material dispersed in a polymer matrix. With advances in thin-film and lithographic processing it is possible to fabricate large areas of uniform thin-film magnetic structures, whose properties could be more finely tuned compared to polymer based materials, due to the degree of control over the large parameter space available with thin-films. However, an open question remains regarding the capabilities of magnetic thin-film systems to produce an isotropic and external magnetic field-free response, based on resonant behaviour.

Magnetic interactions in thin-film systems already underpin a wide range of interesting physical phenomena, forming the basis of the field of spintronics, that has evolved since the discovery of giant magnetoresistance [1, 2] which led to significant advances in magnetic memory devices. In particular, interfacial effects between ferromagnetic and non-magnetic materials in multilayered materials, notably the torque from a spin current passing across the interface [3], have been exploited to produce new generations of magnetic memory [4].

A further interfacial effect of interest is the additional energy loss channel available when a precessing ferromagnetic layer is in contact with a heavy metal layer such as Pt, which leads to an increase in magnetic damping. This process is often referred to *spin-pumping*, and is attributed to a transfer of spin angular momentum across the interface from the precessing ferromagnetic layer into the non-magnetic layer. Frequently, any increase in damping is an undesirable effect, for example in magnonic applications, systems are developed to reduce the damping as much as possible in order to maintain the coherence of the spin current [5, 6]. However, any increase in damping results in a broadening of the resonance and hence a more broadband frequency response, which is favourable for absorbing materials.

Before interfacial increases in damping can be fully exploited in technological applications, the underlying physics and physical parameters must first be well understood. The magnitude of the enhancement in damping is dependent on the interface between the ferromagnetic and non-magnetic material, and therefore the nature of the interface itself must be explored. However, conflicting measurements in the literature result in variations over an order of magnitude for key parameters such as the lengthscale of coherent spin current transfer, known as the *spin diffusion length*, and therefore the thickness of material required for significant damping enhancement is uncertain [7–9]. Additionally, the effects introduction of a spacer layer of insulating material between the magnetic and non-magnetic material has also produced conflicting results, with reports of a damping enhancement [10], suppression [11], or even spin-current tunnelling through the layer [12]. It is clear a detailed characterisation of interfacial structure with respect to dynamic behaviour is required to fully investigate interfacial dynamic magnetisation behaviour.

It is not only the nature of the interface which remains to be understood. The correlation between material parameters of the non-magnetic material with regards to interfacial phenomena, such as damping enhancement or spin related torques, remain the subject of debate. Electronic hybridisation at the interface between a ferromagnetic material and some heavy metal non-magnetic materials, such as Pt, has been shown to induce a moment in the non-magnetic material when paired with transition metal ferromagnets [13], the details of which are closely associated with the interface [14], and is termed *proximity induced magnetism* (PIM). However, the presence, magnitude and nature of this induced moment remain the subject of debate in ferrimagnetic oxide materials [15, 16], in which two magnetic sublattices compete to produce the net moment, suggesting it is perhaps not simply a static moment in the FM layer which is required to induce a moment through hybridisation. Additionally, the consequences of this induced moment on the interfacial phenomena remain the subject of debate. This is evident both in models of inter-

facial enhancement, in which the induced moment either has no role, or is related through inclusions of orbital hybridisation, and in experimental investigations, in which the induced moment is either directly correlated with the interfacial damping enhancement [17], or is reported to be irrelevant to interfacial phenomena [18].

The damping parameter, modulated through interfacial effects which enhance the frequency bandwidth, is only one variable of interest that determines the high frequency response of magnetic thin-film systems. The frequency of ferromagnetic resonance is directly related to the effective magnetic field of a magnetic material. This effective magnetic field is a summation of both external and internal anisotropic fields. Thus to alter the resonance frequency, the magnitude of the effective magnetic field must be modified. In typical ferromagnetic resonance measurements, this is achieved by either increasing or decreasing an external magnetic field, however, for device applications it is not feasible to rely on an external magnetic field to achieve a desired resonance frequency, and therefore the internal anisotropy field must be enhanced or suppressed.

Previous studies investigating methods to enhance the anisotropy field of thin-film magnetic systems have either exploited interfacial effects, such as exchange bias, in multilayered systems [19] or lithographic patterning to enforce a magnetic anisotropy in the thin-films. This has been shown to induce an anisotropy capable of achieving resonances up to 10 GHz by altering the aspect ratio of striped patterns [20]. Though lithographic methods are generally more industrially compatible, the resultant anisotropy primarily enhances the resonant response only along the long axis of the pattern. Hence the interaction between the RF energy and the material system is not isotropic, with field-free resonance observed only in one orientation.

Though the large parameter space of magnetic thin-film systems allows for a high degree of control of the high frequency response, a series of open questions remain regarding both the underlying physical phenomena, and the variables which can be tuned in magnetic multilayered thin-film systems to produce a significant broadband, field-free high frequency response.

1.2 Aim of Thesis

The aim of this thesis is to produce and analyse magnetic multilayered structures in a parametrised way to better understand and control the physical phenomena related to synthetic magnetic materials which are required to produce an isotropic, broadband and field-free ferromagnetic resonant response.

Prior to investigations into exploiting material parameters to tune high frequency

responses, a bespoke, flexible, integrated measurement system was developed to characterise ferromagnetic resonant behaviour as a function of magnetic field, excitation frequency and angular sample orientation. The focus is then directed to two key parameters that determine the dynamic magnetisation behaviour: the magnetic damping and the effective magnetic field.

By fully characterising the dependence of both FM and NM thickness parameter spaces on the dynamic magnetisation response of thin-film systems and building upon existing models in the literature, outstanding discrepancies in the field between key physical parameters are addressed. Structural analysis of magnetic thin-film samples, using x-ray reflectivity, highlights the role of interfacial structuring with regards to interfacial spin transport. Element specific measurements using synchrotron radiation, along with dynamic magnetisation measurements were brought together to further investigate the nature of the induced moment in Pt layered with ferrimagnetic materials, and allow correlation between the static induced moment, the dynamic response and the interfacial structuring. These measurements address the material parameters and physics which lead to an enhancement in the magnetic damping, and thus the frequency bandwidth response.

Thin-film systems were then patterned into ordered arrays of shaped structures using lithographic procedures, to investigate both the magnitude of the induced magnetic field, needed for field-free resonance, and the resonant response as a function of angle with respect to the RF excitation frequency. Novel tessellated structures with varying aspect ratio stripe patterns were produced and analysed using the bespoke integrated system, demonstrating the capabilities of thin-film systems to produce an isotropic and field-free response.

1.3 Thesis Outline

This thesis begins by detailing the underpinning physics of thin film magnetism which is used as a basis throughout the remainder of the work. Chapter 2 opens with a brief discussion regarding the origins of magnetic moments, and the material classifications arising from their ordering in solid systems. Following this, a short description is given of the energy contributions in magnetic materials, as well as introducing the concept of effective magnetic fields. An overview of band theory and magnetism in rare-earth transition-metal alloys is then given, with a brief introduction to spin-dependent electron conduction and resistivity concluding the chapter.

Chapter 3 builds on the static magnetic theory from chapter 2, and describes dynamic magnetisation processes, which is a central theme of this thesis. Focus is

directed to physical models that describe the angular dependence of ferromagnetic resonance and to descriptions of magnetic damping phenomena. The chapter concludes with a description of the physics surrounding behaviour at interfaces between precessing ferromagnetic metals with non-magnetic materials.

In chapter 4, a brief survey of radio-frequency (RF) loss processes and existing RF materials present in the literature is first given. This is followed by the description of a simple model, based on wave impedances, which can be used to model the dynamic RF response of a multilayered structure. This model was further developed here through the inclusion of an enhancement in damping arising from interfacial phenomena outlined in chapter 3.

Prior to the discussion of any experimental results, the techniques used to both fabricate and characterise the samples investigated are first outlined. Chapter 5 introduces the methods of sample growth and lithographic patterning, and includes a brief discussion of the structures formed following growth processes that is helpful in later discussions. The chapter concludes by outlining the principles and data fitting procedure of x-ray reflectivity, a non-destructive technique that provides structural information regarding multilayered structures, and is used extensively throughout later chapters. Chapter 6 details the quasi-static magnetic characterisation techniques used within this thesis, and builds upon the structural techniques introduced in the previous chapter to begin with a description of x-ray magnetic reflectivity, which allows for a probe of element specific magnetic moments. The two other techniques (MOKE and SQUID) outlined in this chapter describe methods to acquire magnetic hysteresis loops of thin film samples used in this work.

Chapter 7 opens with a brief introduction into frequency domain techniques used to measure the RF response of magnetic thin film systems. Following this, the design and development of a system, used throughout this work, for measuring dynamic magnetisation behaviour is presented. Initial design iterations based on a vector network analyser are first detailed, before the development of an integrated system capable of performing broadband and angular dynamic measurements is discussed. Descriptions of the system components and control code are given, along with testing and comparisons with other research systems to highlight the capabilities of the integrated system.

In chapter 8, the results of two published investigations which cover methods to both enhance and suppress additional magnetic damping from interfacial effects are presented. The first half describes spin transport across the interface between ferromagnetic (FM) and heavy metal (HM) interfaces, with Co and CoFeB investigated as FM materials, and Pt and Ru as HMs. Particular focus is given to combining models of spin transport with models of resistivity, in order to better understand

key interfacial parameters which remain the subject of debate. The second half focuses on spin transport with an insulating spacer layer in CoFeB/SiO_2/Pt systems, in order to correlate interfacial structure with the reduction in interfacial damping enhancement.

While chapter 8 explores interfacial damping phenomena, the role of the induced moment, which is often present in heavy metal layers, in relation to the damping enhancement forms the basis of chapter 9. The nature of the induced moment is first investigated by considering the induced moment in rare-earth transition-metal ferrimagnetic systems, and whether the induced moment follows the net moment or aligns to one of the individual sub-lattices. The physics governing induced magnetism is then applied and correlated with the damping measurements across metallic spacer layers in the second half. Samples in this section feature thickness gradient wedges consisting of Cu, Pt, Pd and Au with CoFe and NiFe ferromagnetic materials, grown in collaboration with the Institute of Molecular Physics in Poznan, Poland.

Chapters 8 and 9 focus on understanding and exploiting interfacial effects to control the magnetic damping in order to tune the RF response. Chapter 10 introduces a separate method to manipulate the dynamic behaviour, in which photolithography is used to induce a shape anisotropy to enhance the the effective magnetic field, in order to produce a material capable of resonance without an external magnetic field present. The first half investigates the dependence of the magnitude of the induced field on the aspect ratio of patterned striped arrays. This relation is then applied in the second half to produce tessellated structures capable of an isotropic field-free response.

Overall conclusions are given in chapter 11, providing a summary of findings from each results chapter. A discussion of possible further work building on the results presented here is also given. At the beginning of each chapter, a brief introduction outlines the topics covered in each section within the chapter, and for each chapter where new results are present, a short summary is given which emphasises the findings detailed within the chapter.

1.4 Unit Systems in Magnetism

Both SI and CGS unit systems are used interchangeably within the field of thin-film magnetism. In this thesis, the CGS system is predominantly used, particularly when reporting quantities. However for completeness, equations are often given in both systems. The table below highlights the difference in units used.

Variable	Symbol	SI	CGS
Induction	B	Tesla	Gauss
Field	H	A/m	Oersteds
Magnetisation	M	A/m	Emu/cm^3
Relation		$B = \mu_0(H + M)$	$B = H + 4\pi M$

With conversion factors:

$$1 \text{ Oersted} = (1000/4\pi) \text{ A/m}$$

$$1 \text{ Gauss} = 10^{-4} \text{ Tesla}$$

$$1 \text{ Emu/cm}^3 = 1000 \text{ A/m}$$

Chapter 2

Magnetism in Thin Films

2.1 Introduction

This chapter introduces the physical origins of magnetism as well as discussing the underlying phenomena which give rise to the static magnetic properties of thin film systems. Firstly, the concept of the magnetic moment and how the arrangement of many of these moments allows for the classification of materials. Following this a discussion of the Stoner Criterion, a requirement for ferromagnetism, is given, which introduces the concept of induced magnetism in a non-magnetic material at the interface with a magnetic material.

Next, the energy contributions that arise in magnetic systems are introduced, as well as the resulting material classifications arising from these interactions. Finally a brief description of electron transport in these materials is given, with the consequences for the resulting dynamic behaviour discussed in the following chapter.

2.2 Magnetic Moments

Observable macroscopic magnetic behaviour arises as a result of the collective properties of individual atomic magnetic moments. Short range interactions between the moments can lead to long range ordering, which gives rise to the measurable quantities of the thin film systems in this thesis. This section details the origin of these magnetic moments and how they interact with one another to fill atomic energy levels.

2.2.1 Origins of Electronic Magnetic Moments

Two kinds of fundamental angular momentum are associated with electrons; *spin* and *orbital* angular momentum. The spin angular momentum, m_s is an intrinsic property of an electron, and as the electron is a fermion, is quantised as $\pm\frac{1}{2}\hbar$ where $\hbar$ is the reduced Plank's constant. This quantisation is also commonly referred to as either spin-up ($\uparrow$) or spin-down ($\downarrow$). In a system with multiple electrons the spin angular momentum is the sum of each of the momenta, i.e. $S = \Sigma m_s$ [21].

The second component is the orbital angular momentum, m_l. Classically, this is considered as a magnetic moment arising from the orbital motion of a charged particle (the electron) about the atomic nucleus. However, this angular momentum is not restricted to atomic systems, free electrons can also carry orbital momentum along the direction of propagation, known as a vortex beam [22–24]. Similarly to the spin angular momentum, for multiple electron systems the net orbital angular momentum is given by $L = \Sigma m_l$.

The total angular momentum vector, $\vec{J}$, is given by the sum of these two contributions, $\vec{J} = \vec{L} + \vec{S}$, and the total atomic moment vector [25]

$$\vec{\mu}_{\text{tot}} = -\gamma\vec{J} = -\frac{g\mu_{\text{B}}}{\hbar}\vec{J}, \tag{2.1}$$

where μ_{B} is the Bohr magneton, and γ the gyromagnetic ratio. The Landé g-factor, g, is given by,

$$g = 1 + \frac{J(J+1) + S(S+1) - L(L+1)}{2J(J+1)}, \tag{2.2}$$

with J, L and S the magnitudes of $\vec{J}$, $\vec{L}$ and $\vec{S}$. Atoms with full electron shells have no net spin or orbital angular momentum, and therefore contribute no net magnetic moment. The rules governing the filling of shells based these quantised momenta are discussed below.

2.2.2 The Spin-Orbit Interaction

The spin and orbital angular momenta do not exist in isolation, the coupling between them, known as the *spin-orbit interaction* (SOI) or *spin-orbit coupling* (SOC), must also be taken into account. This phenomenon underpins many of the observed magnetic properties discussed in this thesis, such as magnetic anisotropies, spin-dependent scattering and magnetic damping, which are discussed in later sections and chapters.

Semi-classically, the SOI can be considered as an interaction between an electron and the stationary positive nucleus that it is orbiting. From the reference frame of the electron, the positive nucleus orbits the electron forming a closed current loop that produces an associated magnetic field, which can interact and couple to the moment created by the electron spin. For a single electron, the Hamiltonian associated with the SOI is,

$$\hat{H}_{\mathrm{SOI}} = \frac{Ze^2}{2m_{\mathrm{e}}^2 c^2 r^3}\, \vec{L} \cdot \vec{S}, \tag{2.3}$$

with m_{e} and e the electron's mass and charge, c the speed of light, r the electron orbital radius and Z the atomic number. The expectation value of $\langle r^{-3} \rangle$, is proportional to Z^3, hence the core electron SOI scales as Z^4 [26].

For more complex systems, the Hamiltonian can be modelled as $\lambda \vec{L} \cdot \vec{S}$, with λ proportional to the strength of the SOI. For lighter elements, $Z < 30$, this can be treated as a perturbation after computing the total angular momentum, which is known as $L-S$ coupling [21]. As the SOI scales with the fourth power of the atomic number, for heavier elements this interaction becomes significant, and is applied to each electron when calculating J, instead of being treated as a perturbation, this is termed $J-J$ coupling [21]. Due to the SOI, the energy of a system depends on the total angular momentum. The SOI splits the energy levels of a system in a similar manner to the Zeeman effect, resulting in electronic *fine structuring*.

2.2.3 Hund's Rules

By taking into account the spin and orbital angular momenta, as well as the interaction between them, the net magnetic moment can be determined by considering how electrons fill the ground state of the key orbitals. Hund's rules [27] provide a set of principles that govern how electrons fill energy levels to minimise the system energy while obeying the Pauli exclusion principle:

1. Maximise the spin angular momentum, S, to reduce the Coulombic repulsion energy by ensuring all orbital angular momentum states are first occupied

2. Maximise the orbital angular momentum, L, to reduce the Coulombic repulsion energy by first filling states with the same orbital direction

3. Consider a perturbation due to the SOI to find J. If a partially filled shell is less than half full, $J = |L - S|$, else, $J = |L + S|$.

Co, for example, has 27 electrons, where the first 18 follow the electron configuration of Ar, the next 2 fill the lower energy $4s$ state and the remaining 7 electrons fill $3d$ states. Using Hund's rules, the first 5 electrons in the $3d$ orbitals fill unoccupied m_l states (-2,-1,0,1,2) as spin-up to maximise S. The remaining 2 electrons occupy spin-down states with $m_l = 2, 1$ to maximise L. Summing these contributions results in $S = 3/2$ and $L = 3$. Finally, as the energy level is over half full, $J = L + S = 9/2$. The magnetic moment is therefore,

$$\mu = g\mu_{\mathrm{B}}\sqrt{J(J+1)} = 6.6\,\mu_{\mathrm{B}} \tag{2.4}$$

with g and μ_{B} as defined previously. These rules are valid for isolated atomic systems; for light metals additional energy contributions, such as the crystal field, can dominate over the SOI.

2.2.4 Quenching of the Orbital Moment

In partially filled $3d$ transition metals, the crystalline environment can influence the orbital angular momentum due to the electric field from neighbouring atoms' electron orbitals. This *crystal field* causes the average expectation value of the orbital angular momentum to fall to zero, though the magnitude is left unchanged, in a process known as *orbital quenching* [25]. Classically, this can be understood as the orbital contribution precessing around the crystal field such that the average is zero, though the vector of each orbital moment still has magnitude.

In lighter systems, the crystal field is larger than the contribution from the SOI, hence the moment can be corrected to [26]

$$\mu = 2\mu_{\mathrm{B}}\sqrt{S(S+1)} \tag{2.5}$$

and the g-factor [28],

$$g = 2\left(1 \pm \frac{\vec{\mu}_L}{\vec{\mu}_S}\right) \tag{2.6}$$

with μ_L and μ_S the orbital and spin magnetic moments. Deviations from $g = 2$ indicate an orbital contribution, which can arise along specific crystallographic axes [29] or due to symmetry breaking at interfaces [28]. A value of $g > 2$ implies the spin and orbital moments lie parallel, while $g < 2$ implies they lie antiparallel.

For magnetic moments in heavier systems, such as $5d$ transition metals, orbital quenching becomes more difficult to model due to the larger SOI, which becomes comparable to the crystal field.

2.3 Magnetic Materials

The interaction of many atomic magnetic moments in a system produces an overall net moment which is responsible for the magnetic response of the system. The interaction between these moments is mediated by an *exchange energy*, J_{ex}. Later sections will provide further detail regarding the energy contributions to a magnetic material (2.4) and how a system with many atoms can be treated (2.5). However by considering first how individual atomic moments align in a system, and respond to external magnetic fields and temperatures, materials can be classified into different magnetic categories.

This section briefly details some of the measurable parameters that depend upon the net moment of a system, before describing the main classifications of magnetic materials used in this thesis.

2.3.1 Magnetic Material Parameters

For a system of identical atoms, the magnetisation is given by $M = n_{\mathrm{a}}\mu_{\mathrm{a}}$, with n_{a} the number of dipole moments per unit volume. The response of a system to an external field, H is

$$\vec{M} = \chi_{\mathrm{M}}\vec{H}, \tag{2.7}$$

where χ_{M} is the magnetic susceptibility, that quantifies the magnetisation per unit field. Another closely related parameter of interest is the *magnetic permeability*,

$$\vec{B} = \mu\vec{H} = \mu_{\mathrm{r}}\mu_0\vec{H}, \tag{2.8}$$

where $\vec{B}$ is the flux density in a system, μ_0 the permeability of free space and μ_r the *relative magnetic permeability*. In a material, $\vec{B} = \mu_0\left(\vec{H} + \vec{M}\right)$ in SI, where $\mu_0 = 4\pi \times 10^{-7}$ H/m, and $\vec{B} = \vec{H} + 4\pi\vec{M}$ in CGS, where the $\mu_0 = 1$. Through this relation, the relative permeability can be expressed as,

$$\mu_r = \chi_{\mathrm{M}} + 1 \ \text{(SI)}\,, \ \mu_r = 4\pi\chi_{\mathrm{M}} + 1 \ \text{(CGS)}\,. \tag{2.9}$$

The relative permeability can also be expressed as a function of frequency, and has both real and imaginary components, as discussed in later chapters.

2.3.2 Diamagnetism

All material systems show weak diamagnetic properties, whereupon with the application of an external magnetic field, a magnetic moment develops to oppose the direction of the field, and increases linearly with the field. Figure 2.1 shows the magnetisation response as a function of field and temperature. Classically, this can be interpreted as the external field acting upon the orbital motion of the electrons, where a current is induced, which due to Lenz's law, opposes the external field. This can occur even for completely filled shells where $L = 0$ [25]. This results in a negative susceptibility which is independent of temperature, and typically is much smaller than the other effects described. In this work the diamagnetic response of a Si substrate creates a large background which much be subtracted in static M-H measurements of samples, as discussed in later chapters.

2.3.3 Paramagnetism

Atoms with unpaired electrons have a non-zero magnetic moment. In paramagnetic materials, these moments are effectively independent and are randomly orientated with no net magnetisation in zero field. However, in the presence of an external magnetic field there is some net magnetisation, overcoming the thermal motion of the moments, as shown along in the field and temperature profiles in figure 2.2. This results in a positive magnetic susceptibility, which for an ionic paramagnet has an inverse temperature dependence given by Curie's law $\chi_{\mathrm{M}} = C/T$ [30], with C a material specific quantity. Curie paramagnetism is not the sole theory of paramagnetism, temperature independent Pauli paramagnetism is discussed later in this chapter.

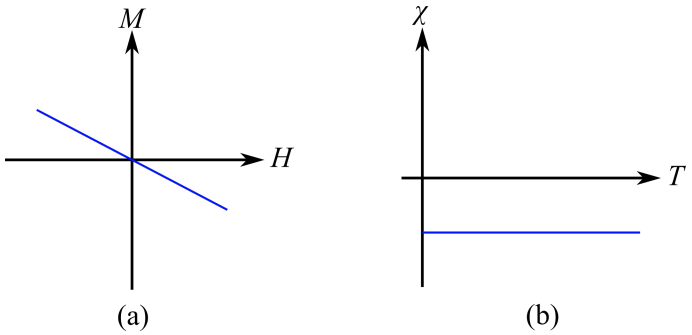

Figure 2.1: Illustrations of: (a) The magnetisation of a diamagnetic material as a function of applied magnetic field. (b) The diamagnetic susceptibility as a function of temperature.

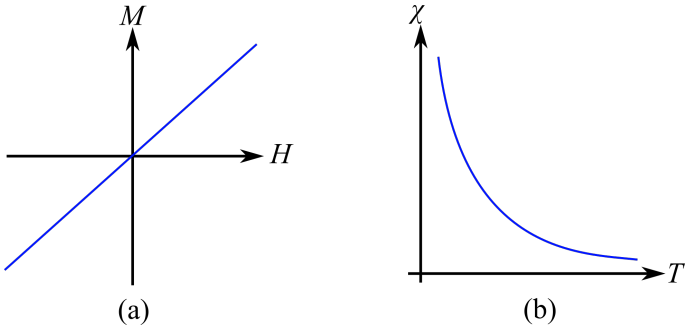

Figure 2.2: Illustrations of: (a) The magnetisation of a paramagnetic material as a function of a small applied field. (b) The paramagnetic susceptibility as a function of temperature.

2.3.4 Ferromagnetism

Ferromagnetism refers to a class of materials where, unlike paramagnetism, there is a net magnetic moment even in the absence of an applied magnetic field, as illustrated in figure 2.3. An additional short range coupling, known as the *exchange interaction*, between the magnetic moments favours parallel alignment between neighbouring magnetic moments which leads to long range ordering of the atomic magnetic moments. At higher temperatures, the thermal energy is enough to overcome this interaction, and the material behaves as a paramagnet. The temperature at which this occurs is known as the *Curie temperature*, T_{C}, which can be modelled with the Curie-Weiss law [31],

$$\chi_{\mathrm{M}} = \frac{C}{T - T_{\mathrm{C}}} \tag{2.10}$$

with C a material specific Curie constant.

The exchange interactions lead to local ordering, but over a larger scale the magnetisation directions may not be uniform due to other effects. The application of a

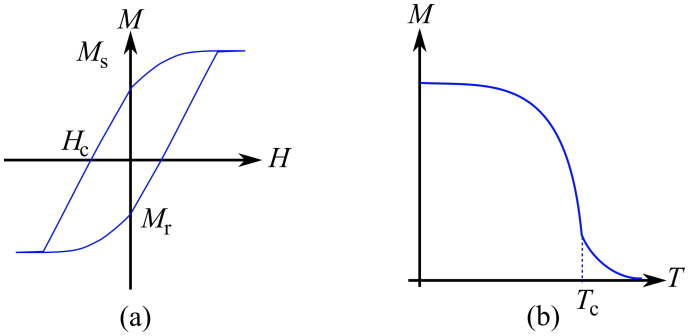

Figure 2.3: Illustrations of: (a) The magnetisation of a ferromagnetic material as a function of applied magnetic field, resulting in a hysteresis loop. (b) The saturation magnetisation of a ferromagnetic material as a function of temperature. Above T_{c}, the material becomes paramagnetic.

large external magnetic field aligns the magnetic moments with the field, resulting in a state known as *magnetisation saturation*, M_s. Removing the field results in a state known as magnetic remanence or remanent magnetisation, M_r, where a net moment still remains. Reversing the field will reverse the sign of the magnetisation, passing through zero magnetisation at a magnetic field known as the *coercive field*, or *coercivity*, H_c. Completing a cycle of magnetic field will produce a magnetic hysteresis loop. In the absence of an external magnetic field, or below the field required for saturation, magnetic moments in a material will typically form local areas where the moments are aligned, known as *magnetic domains*, which are separated by magnetic *domain walls*, in order to reduce the total energy of a system by reducing the stray field, and the magnetostatic energy.

2.3.5 Antiferromagnetism

While the exchange is positive for ferromagnetic materials, giving parallel spin alignment, a negative exchange energy produces a system where neighbouring magnetic moments have an antiparallel arrangement of local moments, forming an *antiferromagnetic* material. Figure 2.4 shows a schematic of this behaviour. An external field will cant the antiparallel moments away from each other, leading to a small positive magnetic susceptibility. Similarly to ferromagnets, a sufficiently high temperature will provide enough thermal energy to overcome the exchange interaction. The ordering temperature at which this happens in antiferromagnetic materials is called the Néel temperature, T_N.

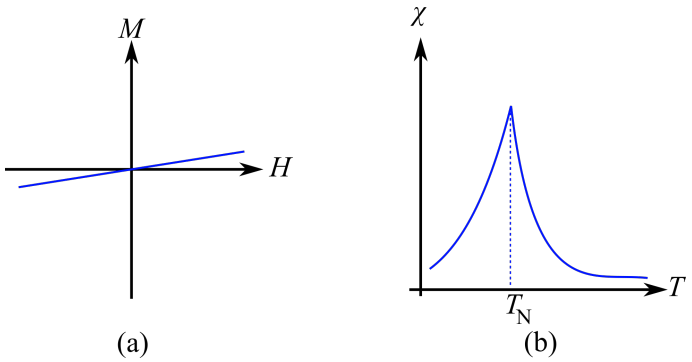

Figure 2.4: Illustrations of: (a) The magnetisation of an antiferromagnetic material as a function of applied field. (b) The susceptibility of an antiferromagnetic material as a function of temperature. Above T_N, the material becomes paramagnetic.

2.3.6 Ferrimagnetism

Ferrimagnetic materials behave in a similar manner to ferromagnetic materials, in that they have a spontaneous magnetic moment below a critical temperature, which aligns with an external magnetic field, producing a positive magnetic susceptibility, and the magnetisation can be subdivided into magnetic domains. However, in a similar manner to antiferromagnets, they are composed of antiparallel alignments of magnetic moments, but ferrimagnets differ in that the magnetisation of one of the opposing sub-lattices is smaller than the other, leading to a net magnetic moment.

Due to the alternating moments, ferrimagnetic materials may not be composed of identical atomic or ionic species. Typical ferrimagnetic systems are either oxide based, such as magnetite (Fe_3O_4) or yttrium iron garnet, commonly known as YIG ($Y_3Fe_5O_{12}$), or rare-earth transition metal alloys (RE-TM), such as CoGd. The details of the sub-lattice exchange depend on the system. For YIG, the two sub-lattices are composed of Fe^{3+} and Fe^{2+} ions, which couple via an intermediate oxygen atom. RE-TM alloys are composed of sub-lattices which have different responses to temperature changes, i.e. different Curie temperatures. For example, in Gd based RE-TM alloys, Gd has a larger moment at low temperatures, but a lower Curie temperature than 3*d* transition metals such as Co, hence there will be a temperature at which the magnitude of the moments of the two sub-lattices are equal and opposite and cancel, resulting in no net magnetisation. This is known as the *magnetisation compensation point*. Figure 2.5 illustrates the typical response to field and temperature changes for such an alloy. The temperature of this compensation is dependent upon which materials form the alloy, as well as the composition, i.e. Co_xGd_{1-x} [32]. A second compensation temperature also occurs at which the angular momentum of the two alloys is matched, known as the *angular momentum compensation*, which

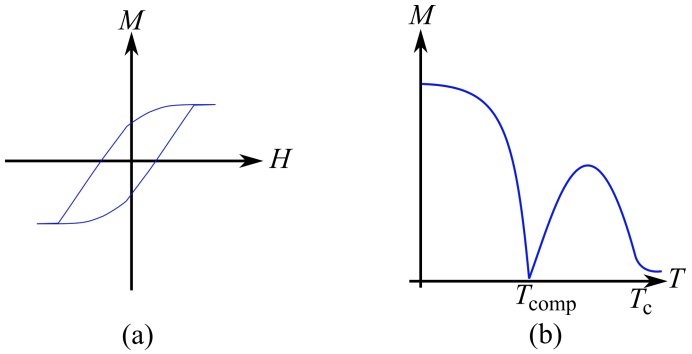

Figure 2.5: Illustrations of: (a) The magnetisation of a ferrimagnetic material as a function of applied field, resulting in a hysteresis loop. (b) The magnetisation of a RE-TM ferrimagnetic material as a function of temperature. At T_{comp} the net magnetisation is zero as the two sub lattices cancel. Above T_c, the material becomes paramagnetic.

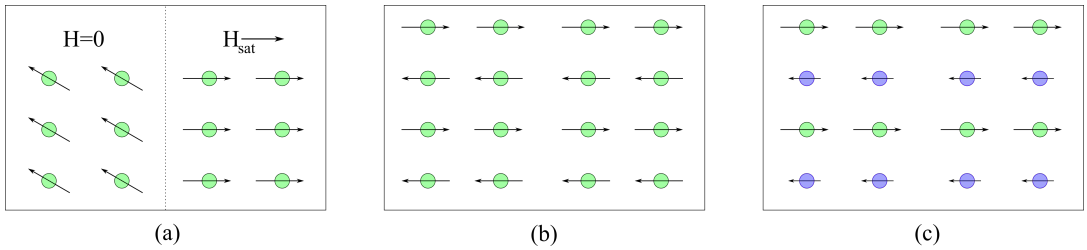

Figure 2.6: Illustrations of the arrangements of magnetic moments in: (a) a ferromagnetic material (b) an antiferromagnetic material (c) a ferrimagnetic material consisting of two sub-lattices of different sized moments.

again depends on alloy composition [33]. A further discussion of the interactions resulting in ferrimagnetic order and useful applications is included in later results chapters.

An illustration summarising the arrangements of magnetic moments in ferromagnetic, antiferromagnetic and ferrimagnetic materials is shown in figure 2.6.

2.4 Energy Contributions and Effective Fields

This section details the underlying energy contributions which leads to magnetic ordering and anisotropy. While other energetic contributions, such as perpendicular anisotropy, exchange bias and magnetostriction, exist, the focus here is on energy contributions relevant to this thesis. The concept of *effective magnetic fields* is also introduced, which has implications for the dynamic response of magnetic materials and is a key aspect of this thesis.

2.4.1 Exchange Interaction

Exchange interactions describe the localised interactions between magnetic moments that leads to macroscopic long range ordering observed in ferro and ferri magnetic systems. If this interaction is strong enough to overcome thermal fluctuations, magnetic ordering occurs. Exchange interactions can be broadly classified into two categories; *direct*, in which there is direct overlap of electron orbitals responsible for magnetic moments, and *indirect*, in which the interaction between two magnetic moments is mediated by the overlap of intermediate orbitals, such as in RE-TM alloys, or with an intermediate species, such as in YIG [25]. This can be the overlap of the p orbitals of an oxygen atom in *superexchange*, with conduction electrons in the *Ruderman–Kittel–Kasuya–Yosida* (RKKY) interaction [34–36], or $4f$-$3d$ exchange mediated by $5d$ states in the Campbell model [37], as elaborated on in later sections. While other types of exchange exist, they are beyond the scope of this thesis.

Heisenberg Exchange

Heisenberg exchange [38] is the most common description of direct exchange and leads to either parallel or antiparallel alignment of magnetic moments in the absence of a magnetic field. This interaction is short range and is usually treated as an interaction between neighbouring spins, the energy density contributions, ε_{ex} arising as a result of this direct exchange can be expressed as a summation of interactions between neighbouring spins,

$$\varepsilon_{\text{ex}} = -2J_{\text{ex}} \sum_{ij} \hat{S}_i \cdot \hat{S}_j \tag{2.11}$$

where J_{ex} is a parameter known as the exchange constant, which quantifies the strength of the interaction, and $\hat{S}_{i,j}$ the spin states at neighbouring sites. For negative values of J_{ex}, an antiparallel alignment is favoured, while a positive value leads to parallel alignment.

The Bethe-Slater curve [39, 40] provides a method of predicting the sign of the exchange constant depending on the ratio of the interatomic spacing between two atoms, a, to the d orbital radius, r, as shown in figure 2.7. Heisenberg exchange arises as a result of Coulombic repulsion between two electrons, which have to obey Pauli exclusion, i.e. they may not share the same quantum numbers. The two electrons can therefore form either a spin singlet state, with antiparallel spins, or a spin triplet state, with parallel spins.

Three regimes depend on the overlap of the electron orbitals. For systems with minimal overlap, the triplet state is typically preferred as it has lower energy as the Coulomb interaction is minimised. This corresponds to a positive value of J_{ex}

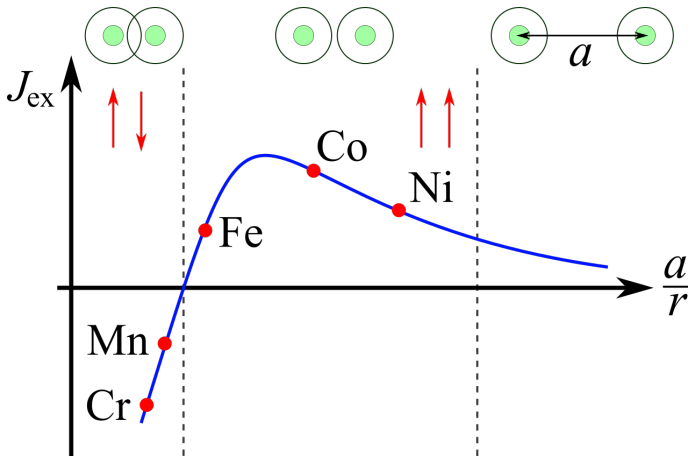

Figure 2.7: Schematic plot of the Bethe-Slater curve, illustrating the dependence of the sign and magnitude of the exchange constant on the ratio of the interatomic spacing, a to the d orbital radius, r, leading to three regimes of exchange.

and to ferromagnetic ordering. For $4f$ RE ferromagnets, such as Gd, there is no direct overlap between f states, and hence J_{ex}, is much smaller, leading to lower Curie temperatures. As the spacing between the two atoms is reduced, the overlap of wavefunctions and repulsion strength increases, hence the minimum energy state corresponds to the singlet state where the spins align antiparallel. This corresponds to negative values of J_{ex} and antiferromagnetic ordering. The final case is where the separation is much larger than the d orbital radius, here both the overlap and repulsive forces are minimised, so exchange is negligible, and the material is paramagnetic in nature. It should be noted that the Bethe-Slater relation provides a simplified view of magnetic exchange and does not explain more complicated magnetic behaviour [41].

Superexchange

Superexchange is a form of indirect exchange prevalent in oxide compounds, in which the interaction between two different cation d spin states is mediated by overlap with an adjacent p state. This type of interaction is dependent upon the vacant states of the species involved. The coupling of two species with partially filled orbitals between one with a filled orbital, such as O will lead to antiferromagnetic order, whereas the inverse will lead to ferromagnetic ordering. This form of exchange is responsible for the ferrimagnetic ordering in YIG [42], in which two differently charged Fe ions with different sized magnetic moments are coupled across O.

Ruderman–Kittel–Kasuya–Yosida Exchange

Ruderman–Kittel–Kasuya–Yosida exchange is another form of indirect exchange [34–36], in which a magnetic moment can couple to an electron gas, which can in turn couple to another localised moment, indirectly coupling the two separate moments. A defining feature of RKKY exchange is the oscillatory nature of the coupling, depending on the separation of the two magnetic moments, which can lead to ferromagnetic and antiferromagnetic coupling depending on the separation. The exchange constant can be described by [25],

$$J_{\mathrm{ex}} = J_0 \cos\left(\vec{k}_{\mathrm{F}} \cdot \vec{r}\right) \tag{2.12}$$

where r is the separation between the two moments, and $\vec{k}_{\mathrm{F}}$ the Fermi wave-vector of the free conduction electrons. An illustration of this behaviour is shown in figure 2.8. This coupling is used in magnetoresistive data storage device structures [43]. RKKY coupling also explains the interaction of magnetic moments in $4f$ metals such as Gd, where the overlap is small between $4f$ states [44], and coupling is mediated by $5d$

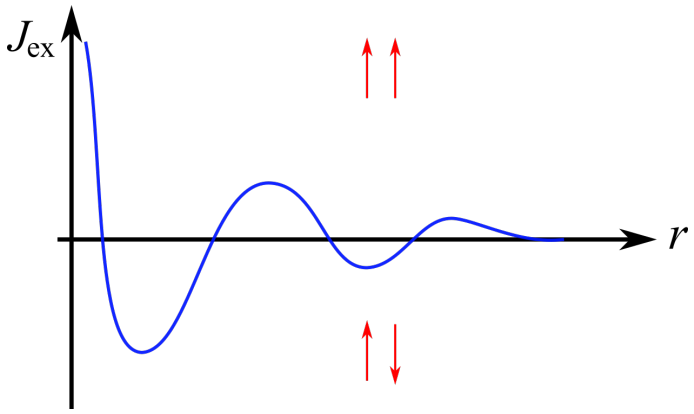

Figure 2.8: Illustration of the oscillatory behaviour of the exchange constant, J_{ex}, in the RKKY interaction as a function of separation of magnetic moments, r.

states. It should also be mentioned that this is not the sole mechanism proposed for RE magnetic ordering, as direct coupling through hybridisation of $4f$ and $5d$ states has also been theorised [37, 45], this will be discussed in later sections.

2.4.2 Zeeman Energy

A key energy contribution in magnetic systems arises from the interaction of magnetic moments with an external field. This interaction is known as the *Zeeman* interaction, and favours alignments of magnetic moments parallel to an external magnetic field. The energy density contribution is described through,

$$\varepsilon_Z = -\mu_0 \vec{M} \cdot \vec{H}_{ext} \tag{2.13}$$

with $\vec{H}_{ext}$ the external magnetic field.

2.4.3 Magnetocrystalline Anisotropy

As a result of the SOI, the spin of moments of the atoms in a material are coupled to the crystal lattice of the material. For crystalline materials, this results in energetically favourable axes along which the magnetisation of a material lies, resulting in magnetic *hard* and *easy* axes, which relate to the crystallographic axes. This behaviour is known as *magnetocrystalline anisotropy*, two examples of which are discussed here, with a further discussion of crystal growth, and unit cells in later chapters.

Cubic Anisotropy

Cubic magnetocrystalline anisotropy occurs in materials with a defined cubic crystal structure below the Curie temperature. The energy density contribution can be expressed as [30],

$$\varepsilon_{\mathrm{C}} = K_1 \left(\cos^2\alpha\, \cos^2\beta + \cos^2\alpha\, \cos^2\gamma + \cos^2\gamma\, \cos^2\alpha\right) \tag{2.14}$$

$$+ K_2 \left(\cos^2\alpha\, \cos^2\beta\, \cos^2\gamma\right), \tag{2.15}$$

where K_1 and K_2 are the 1st and 2nd order material dependent anisotropy constants and α, β and γ the angles between the magnetisation vector and the crystal axes. For body centred cubic (BCC) crystals, such as Fe, the easy axes are along the cube edges, and hard axes along the cube diagonals. For face centred cubic (FCC) materials, such as Ni, the reverse is the case.

Uniaxial Anisotropy

In systems with uniaxial symmetry, there is only one easy axis. The energy density contribution is,

$$\varepsilon_{\mathrm{u}} = K_{\mathrm{u}}\, \sin^2\alpha, \tag{2.16}$$

where K_{u} is the uniaxial anisotropy constant, and α the angle between the easy axis and the magnetisation. Hexagonally close packed (HCP) materials such as bulk Co, have magnetocrystalline uniaxial anisotropy, with the magnetic easy axis along the crystallographic c-axis. Uniaxial anisotropy can also be induced in materials through various methods such as strain or deposition in a magnetic field [46].

2.4.4 Shape Anisotropy

The shape of a finite magnetic material can also determine the magnetostatic energy of a sample. In a uniformly magnetised material, free poles at the edges of the sample result in an internal magnetic field that is opposite to the magnetisation that creates the free poles. This results in a *self-demagnetising* field and a magnetostatic energy, which is dependent on the geometry of the sample and the magnetisation [30]. The energy density associated with this shape anisotropy is,

$$\varepsilon_{\mathrm{D}} = -\frac{\mu_0}{2}\vec{M} \cdot \vec{H}_{\mathrm{D}}, \tag{2.17}$$

where H_{D} is the demagnetising field, given by $\mathbf{N}\vec{M}$, where $\mathbf{N}$ is the demagnetising tensor,

$$\mathbf{N} = \begin{pmatrix} N_x & 0 & 0 \\ 0 & N_y & 0 \\ 0 & 0 & N_z \end{pmatrix} \tag{2.18}$$

where N_x, N_y and N_z are the demagnetising factors, such that $N_x + N_y + N_z = 1$ in SI and $N_x + N_y + N_z = 4\pi$ in CGS. For an un-patterned thin film, with the z-axis perpendicular to the film plane, $N_x = N_y \approx 0$ and $N_z \approx 1$, hence,

$$\varepsilon_{\mathrm{D}} = -\frac{\mu_0 M_{\mathrm{s}}^2}{2} \cos^2 \alpha_z \tag{2.19}$$

where α_z is the angle between the magnetisation and the film plane.

For patterned shapes, such as an ellipsoid, the energy density contribution is given by,

$$\varepsilon_{\mathrm{D}} = \frac{\mu_0 M_{\mathrm{s}}^2}{2} \left(N_x \cos^2 \alpha_x + N_y \cos^2 \alpha_y + N_z \cos^2 \alpha_z \right), \tag{2.20}$$

where α_i denotes the angle between the magnetisation and the $i = x, y, z$-axis. For patterned elongated rectangular shapes, the self-demagnetising field will induce a uniaxial anisotropy, which is used to model such systems in later chapters.

2.4.5 Effective Magnetic Fields

The total magnetic energy density of a magnetic system, ε_{T}, can be expressed by the sum of these components,

$$\varepsilon_{\mathrm{T}} = \varepsilon_{\mathrm{ex}} + \varepsilon_{\mathrm{Z}} + \varepsilon_{\mathrm{C}} + \varepsilon_{\mathrm{u}} + \varepsilon_{\mathrm{D}} \tag{2.21}$$

with all energy terms as defined earlier. The effective magnetic field acting on a moment is a result of the combination of all of these energy contributions, with the Zeeman term dominating at high external fields. The effective magnetic field is given by the derivative of the total energy with respect to the magnetisation [47],

$$\vec{H}_{\mathrm{eff}} = -\frac{1}{\mu_0} \nabla_{\vec{M}} \varepsilon_{\mathrm{T}}. \tag{2.22}$$

This effective field has a profound effect upon the dynamic response of a system, particularly as a result of the presence of anisotropies, which can produce a dynamic magnetisation response in the absence of a significant external magnetic field, i.e. no Zeeman contribution, when interacting with incident RF energy.

2.5 Band Theory

Previous sections dealt with individual magnetic moments, and the interactions between them. However, for solid metallic materials, the outer electrons are no longer localised, leading to the overlap of many orbitals of an electron gas. This section details how electronic structure becomes complicated in large systems and can be modelled as energy levels or bands. This is then applied to explain the interactions in $3d$ and $4f$ magnetic metals, as well as induced magnetism in normally non-magnetic metals.

2.5.1 Energy Bands

In a system with significant overlap of the electronic wavefunctions of neighbouring atoms, the Pauli exclusion splits the energy levels of the system as electrons cannot occupy the same quantum states. This results in many closely spaced energy levels, such that the system no longer has discrete levels, but there exists a continuum of available states, known as *energy bands* [25]. The density of energy levels within a band depends on the energy of the system.

Within each shell, the electrons may be either spin-up or spin-down, with completely filled energy bands providing no contribution to the magnetic moment of a system as there are no unpaired electrons. Electrons fill the lowest energy levels first, up to the Fermi energy, E_{F}, the highest occupied states. Applications of band structure to magnetic systems were first proposed by Stoner and Slater [48, 49], where for transition metals, the outermost electrons occupy the $4s$ and $3d$ shells, which overlap in energy. The $4s$ band is closer to the nucleus and lower in energy than the $3d$ band and is filled first. The $3d$ band has two sub-bands, corresponding to spin-up and spin-down states, with the electron density in the spin-up and spin-down bands given by [25],

$$n_{\uparrow} = \int_0^{E_{\mathrm{F}}} g_{\uparrow}(E)\, dE, \quad n_{\downarrow} = \int_0^{E_{\mathrm{F}}} g_{\downarrow}(E)\, dE, \tag{2.23}$$

where $g_{\uparrow}(E)$ and $g_{\uparrow}(E)$ are the density of states for the spin-up and spin-down bands.

Figure 2.9 shows a simplified schematic of the band structure of both a ferromagnetic, and a non-ferromagnetic metal. For a completely filled d band, as is the case with Zn, the d band lies below the Fermi level and hence there is no magnetic moment. In a partially filled d band, if the density of states of the spin-up and spin-down sub bands are equal, then there is also no magnetic moment, as there is no spin-imbalance. However, the exchange interaction can lift the degeneracy of the two half-bands, as parallel alignment is favoured. This leads to an imbalance in

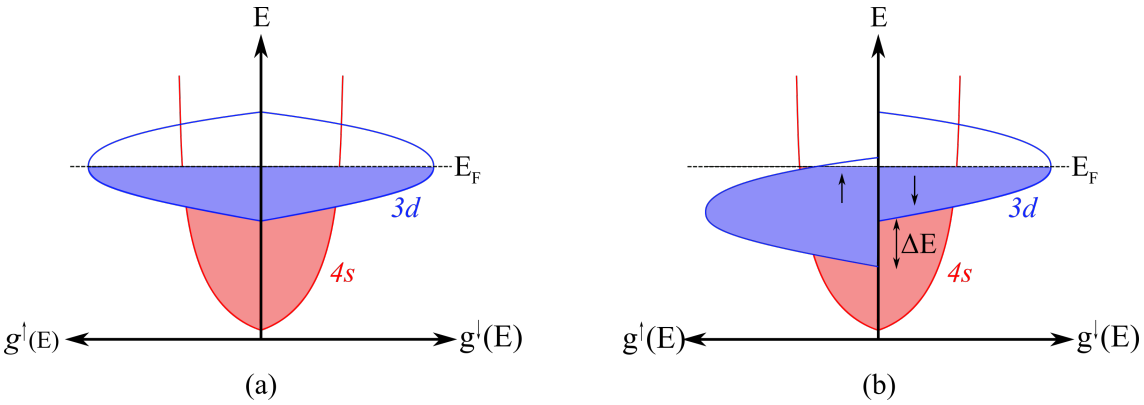

Figure 2.9: Illustration of the electronic band structure for (a) a non-magnetic transition metal and (b) a ferromagnetic transition metal with band splitting in the $3d$ states.

the density of states, as one spin state is preferentially filled before the other [21], producing a net magnetic moment. The magnetisation due to this imbalance is,

$$M = \frac{n_\uparrow - n_\downarrow}{\mu_\mathrm{B}} \tag{2.24}$$

where the strength of the magnetisation depends on the size of the exchange splitting in the d band.

Itinerant Magnetism and Local Moments

For delocalised systems, where magnetic interactions are mediated by conduction band electrons in an electron gas, the moments are no longer tied to one atomic site. Weak ferromagnetic materials such as Ni_3Al are not well described in terms of real-space localised moments which follow a Curie-Weiss law based on Heisenberg exchange [50]. Instead they are described by itinerant magnetism, in which the long range ordering of delocalised moments are modelled as spin density fluctuations, localised in reciprocal space [51]. Calculations of magnetic parameters, such as the magnetisation, of materials based on this model are much more difficult than those based on the local moment theory, as band structure calculations utilising density functional theory must be undertaken [21].

It is therefore useful to understand which materials the local model fails to describe accurately. A simple relation, known as the Rhodes-Wohlfarth relation [52], compares the predicted moment, q_c, from the local moment model determined from the Curie constant, with the saturation moment per unit atom, q_s. If $q_\mathrm{c}/q_\mathrm{s} = 1$, i.e. they are equal, then material parameters determined from local moment theory are reasonably accurate. If the ratio is greater than 1, then the system is more delocalised and must be treated with fluctuations in the spin density. Plotting this

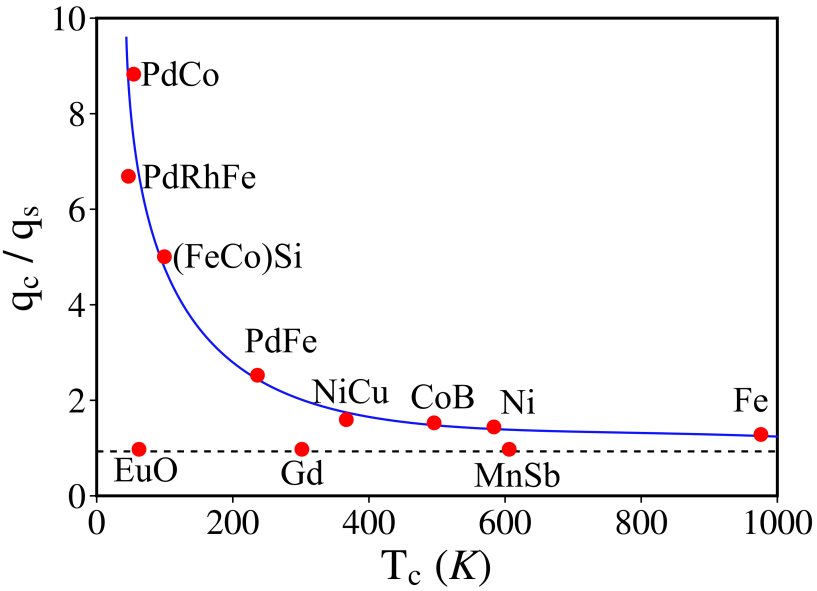

Figure 2.10: Illustrative plot of the Rhodes-Wohlfarth ratio, q_c/q_s for various materials, adapted from [50].

ratio as a function of Curie temperature, shows a roughly inverse relationship, known as the Rhodes-Wohlfarth plot [51], as shown in figure 2.10.

In $4f$ ferromagnets, such as Gd, the $4f$ shell responsible for magnetism is tightly localised to an atomic site, hence the system is well described by the local moment theory. Similarly for $3d$ transition metal ferromagnets, the ratio is also close to 1, and direct Heisenberg exchange is applicable. However for more dilute ferromagnetic alloys this no longer holds, and the system must be treated as itinerant with a delocalised spin density.

2.5.2 Magnetism in Rare Earths and Transition Metals

For alloys based on rare-earth transition metals (RE-TM), the interactions between energy bands can lead to various forms of magnetic ordering. In RE metals, such as Gd, the magnetic moment arises from the localised $4f$ electrons, however unlike the $3d$ band in transition metals, overlap between $4f$ orbitals is unlikely, hence interactions between between magnetic moments must be mediated through another mechanism [53]. Two models have been proposed which mediate this interaction [54–56]. The first is based on the RKKY interaction [34], in which the conduction electrons (mostly the $6s$ band, but also some $5d$) are polarised, and form an indirect

exchange [51], which can be modelled as [57],

$$\hat{H} = -\sum_{i,j} J_{\mathrm{RR}} \left(g-1\right)^2 \vec{J} \cdot \vec{J} \tag{2.25}$$

with g the Landé g-factor, and J_{RR} is the $4f-4f$ exchange parameter.

The second model for $4f-4f$ exchange was proposed by Campbell [37]. In this model the less de-localised $5d$ states can couple with one another and with the $4f$ states, producing a ferromagnetic interaction between the localised $4f$ moments [56]. This model acts on a much shorter range, and treats the $6s$ and $5d$ bands separately.

For RE-TM alloys the interactions become more complicated, as the $3d-4f$ interactions, which determine the magnetic ordering, must be considered. While the coupling strength has been observed to vary as $(g-1)\vec{J}$ throughout the RE series, which would imply RKKY coupling, including the role of the $5d$ state provides an explanation as to why both ferro- and ferrimagnetic order are observed in Gd based ferrimagnets [58, 59]. In the Campbell model, interactions between the $3d$ states in the TM and $4f$ states in the RE are mediated through the $5d$ state, which can couple to either state. The exchange splitting of the $5d$ state, which is almost empty prior to hybridisation [58], is much smaller than that of the $3d$ state, which is almost full, and the polarisation arises from coupling to the $4f$ state [53]. When the $3d$ and $5d$ states hybridise, the $5d$ band becomes slightly occupied, with a larger occupation in the minority spin state compared to the $3d$ state [58], hence the coupling of *spin* momentum between the two states is always antiferromagnetic in nature [55].

For light RE materials, $Z < 60$, the *total* moment between $4f$ and $3d$ is parallel and ferromagnetic in nature, whereas for heavier RE materials it is antiparallel and antiferromagnetic [51]. In all cases, the $5d$ and $3d$ electron spin-momentum states are polarised antiparallel, and the $5d$ and $4f$ parallel using the mechanisms described. The direction of the total moment of the RE in a RE-TM system is then dependent upon the direction of the orbital contribution. In light REs, $\vec{J} = \left|\vec{L} - \vec{S}\right|$, hence the total moment is antiparallel to the $4f$ and $5d$ spin-momentum states, and parallel to the total moment of the TM, and for heavy REs, $J = \left|\vec{L} + \vec{S}\right|$ so the total moment is parallel to the $4f$ and $5d$ spin-momentum states, and antiparallel to the total moment of the TM [55].

In heavy RE-TM systems, this results in two regimes as a function of temperature, due to the differing Curie temperatures of the two sub-lattices. At low temperatures, RE materials with a lower Curie temperature will align with an external field, and the TM will align antiparallel opposite to the field. At higher temperatures, the opposite is true, and the TM moment will be larger, hence it will align with an external field, and the RE will align antiparallel.

2.5.3 Stoner Criterion and Induced Magnetism

The *Stoner criterion* provides a basis for when ferromagnetic ordering is energetically favourable. Mathematically, this is given by,

$$I \cdot g\left(E_{\mathrm{F}}\right) > 1 \tag{2.26}$$

with $g\left(E_{\mathrm{F}}\right)$ the density of states at the Fermi level, and I the exchange integral, which is related to the magnitude of the exchange energy. Hence, the density of states is critical in determining whether ferromagnetic ordering will occur.

While most paramagnetic materials have no long range magnetic ordering, some may be come magnetised in a process known as *proximity induced magnetism* (PIM). This can occur through a variety of processes, such as doping or alloying with a ferromagnet [60], or at the interface between certain paramagnetic metals, such as Pt and Pd [17], and a ferromagnetic material. The induced magnetism with ferrimagnets is more complicated. Layering Pt with oxide ferrimagnets, such as YIG, induces a moment that is an order of magnitude smaller compared to Fe [15], whereas for RE-TM ferrimagnets, it is unclear what role the competing sub-lattices have. This will be addressed in later results chapters.

For paramagnetic materials, this enhancement can be treated in a similar manner to exchange in ferromagnets [25], as an extension to Pauli paramagnetism. Here, a magnetic field lifts the degeneracy of the spin-up and spin-down bands due to the Zeeman interaction. This results in a magnetisation similar to equation 2.24, and can be further expressed as,

$$M = 2\mu_{\mathrm{B}}^2\, n\left(E_{\mathrm{F}}\right) \mu_0 H, \tag{2.27}$$

with the temperature independent paramagnetic Pauli susceptibility $\chi_{\mathrm{P}} = M/H$. Between neighbouring moments the 'exchange', can be treated as an additional field-like term, given as $H_{\mathrm{ex}} = J_{i,j}M$, with exchange constant, $J_{i,j}$ proportional to the exchange integral, I. For a paramagnetic material the enhanced magnetic susceptibility is given by,

$$\chi = \frac{\chi_{\mathrm{P}}}{1 - J_{i,j} \cdot \chi_{\mathrm{P}}}. \tag{2.28}$$

This equation diverges as $J_{i,j}\chi_{\mathrm{P}}$ tends to 1. Materials with $J_{i,j}\chi_{\mathrm{P}} > 1$, are ferromagnetic, as they have met the Stoner criterion, as $J_{i,j} \propto I$ and $\chi_{\mathrm{P}} \propto n\left(E_{\mathrm{F}}\right)$. Materials below this criteria, but with a large density of states at the Fermi level, such as Pd and Pt, have a large enhanced magnetic susceptibility, with $J_{i,j}\chi_{\mathrm{P}}$ approaching unity, are close to the threshold for ferromagnetism, and will take on ferromagnetic properties when in contact with a ferromagnetic material, as this allows $d-d$ hy-

bridisation of the orbitals. The role and nature of PIM with Pt in ferrimagnets and other systems is discussed in later results chapters.

2.6 Electron Transport

The transport of electronic charge in metallic materials is driven by electrons in the conduction band. However, for magnetic materials, additional considerations have to be applied due to the difference in the density of states for different spin bands. This section details a brief description of transport through materials, and the scattering processes when considering magnetic ordering, that are used in the discussion of dynamic processes in later chapters.

2.6.1 Spin-dependent Conduction

Electron conductivity in metals can be approached first with a simplistic Drude free electron model, where the electrons that contribute to conduction lie at or above the Fermi energy. Electrical properties are therefore determined by the shape and density of states of bands at the Fermi level. In this model for bulk-like systems, the resistivity is determined by scattering processes from the crystal lattice or lattice vibrations, known as phonons, and the lengthscales between these scattering events. An expression for the resistivity in this model is [30],

$$\rho = \frac{1}{\sigma} = \frac{m^*}{ne^2\tau}, \tag{2.29}$$

with e the electron charge, n the concentration per unit volume of free carriers and m^* the effective charge carrier mass, inversely proportional to the band curvature. The relaxation time between scattering events, τ, is given by,

$$\tau = l_\mathrm{e}/\nu_\mathrm{F}, \tag{2.30}$$

with ν_F the Fermi velocity, and l_e the mean free path of the conduction electrons between scattering processes.

The resistivity is dependent on the density of states. For magnetic metals, there is an exchange splitting at the Fermi level, leading to different populations of spin-up and spin-down states, which can be quantified by defining the degree of *spin-polarisation* of charge carriers,

$$P = \frac{g_\uparrow(E_\mathrm{F}) - g_\downarrow(E_\mathrm{F})}{g_\uparrow(E_\mathrm{F}) + g_\downarrow(E_\mathrm{F})} \tag{2.31}$$

with $g_{\uparrow}(E_{\mathrm{F}})$ and $g_{\downarrow}(E_{\mathrm{F}})$ the density of states for the spin-up and spin-down sub-bands respectively. For transition metals, there is an overlap of the s and d bands at the Fermi level, which allows s-band electrons to scatter into d states, a process known as $s-d$ scattering. The large density of unoccupied states for the d-band given by the large curvature means that this process has a high probability of occurring. A manifestation of this effect is seen in the decrease in resistivity as a ferromagnetic material is cooled below the Curie temperature. Here, ferromagnetic exchange increases the splitting of the d-band, reducing the total number of available d states to scatter into at the Fermi level, and hence the resistivity is also lowered.

An approach to describing this behaviour was developed by Mott [61], in which the current in a ferromagnet can be described as operating in two separate channels; one for spin-up and one for spin-down. Each channel has a corresponding resistivity, and different scattering. Ignoring spin-flipping processes, the total resistivity is given by,

$$\rho = \frac{\rho_{\uparrow}\,\rho_{\downarrow}}{\rho_{\uparrow}+\rho_{\downarrow}}, \tag{2.32}$$

with the arrows denoting the resistivity of the spin channels. For large values of exchange splitting, such that the spin-up band is shifted below the Fermi level, there will only be unoccupied spin-down states to scatter into, hence in this example $\rho_{\downarrow}$ will be the dominant contribution.

At higher temperatures, spin wave excitations, known as magnons, allow mixing between spin-up and spin-down states through *spin-flip scattering* [62]. The resistivity can be adapted to include this through,

$$\rho = \frac{\rho_{\uparrow}\,\rho_{\downarrow}+\rho_{\uparrow\downarrow}\,(\rho_{\uparrow}+\rho_{\downarrow})}{\rho_{\uparrow}+\rho_{\downarrow}+4\rho_{\uparrow\downarrow}}, \tag{2.33}$$

where $\rho_{\uparrow\downarrow}$ is an extra resistivity term that characterises the spin-flip process. All resistivities used have their own lengthscales in a similar manner to equation 2.29. Higher temperatures lead to increased magnon excitations generating more spin-flip events, and hence a higher resistivity. The spin-flip lengthscales, which will be discussed further in the following chapter, are also relevant for non-magnetic materials, in which the spin-flip length is dependent upon the strength of the SOI, which results in shorter lengthscales for materials such as Pt.

It should be noted that this resistivity model results in isotropic conductivity. Further models which include the effect of the SOI can explain observed anisotropic magnetoresistance, but are not included in this thesis. Currents passing through a magnetic material are scattered at different rates for the spin-up and spin-down bands [26], which produces a spin-polarised charge current, and associated pure

spin-current, which will be detailed in the next chapter, where the transfer of spin angular momentum across material interfaces is discussed.

2.6.2 Models of Resistivity in the Thin Film Limit

The above relations apply to bulk like systems, where resistivities are assumed to be thickness independent, with the form

$$\rho = \frac{RA}{L}, \tag{2.34}$$

where R is the resistance of the material, A the cross-sectional area and L the length of the region measured. However, with nanoscale thin films additional scattering at the surfaces and interfaces can lead to increases in the resistivity. A description of the enhanced scattering associated with thin films where an interface has a much larger role was developed by Fuchs and Sondheimer [63, 64] based on Boltzmann transport equations under three assumptions. The first is that the probability of scattering is independent of initial direction, secondly, that the number of scattering events is independent of scattered direction, and finally that the mean free path is constant. The resistivity is split into two regimes, for the case where the thickness is less than the mean free path, $t < l_{\mathrm{e}}$,

$$\rho = \rho_0 \frac{4}{3} \frac{1-p}{1+p} \frac{l_{\mathrm{e}}}{t \ln\left(\frac{l_{\mathrm{e}}}{t}\right)}, \tag{2.35}$$

and for the opposite case, $t > l_{\mathrm{e}}$,

$$\rho = \rho_0 \left(1 + \frac{3}{8} \frac{l_{\mathrm{e}}}{t} (1-p)\right), \tag{2.36}$$

where ρ_0 is the bulk resistivity and p is a parameter determining the fraction of elastically scattered electrons. For $p = 0$ the scattering is diffuse, and for $p = 1$ the scattering is specular.

Another source of enhanced scattering, particularly for polycrystalline films, is from grain boundaries. A formalism based on grain size was developed by Mayadas and Shatzkes [65], where additional scattering occurs at grain boundary edges as a current passes through a material. For a single crystal, the resistivity is identical to that obtained from the Fuchs-Sondheimer model, whereas for a polycrystalline material, the additional resistivity is dependent on parameters such as the grain size and grain spacing, the reflection coefficient at grain boundaries, as well as the mean free path within a grain. It also assumes grain boundaries are perpendicular to current propagation [66]. The total resistivity using this model has no analytic

solution, however numerical solutions can be used to compare with experiment.

In real materials, both of these enhancements to the scattering can occur [67]. However in the low thickness regime, neither formalism fully describes the measured spin-mixing resistivity [68]. An alternative phenomenological model for the spin-mixing resistivity has been shown to fit experimental data [69],

$$\rho_{\uparrow\downarrow}(t) = \rho^{\mathrm{b}}_{\uparrow\downarrow} + \rho^{0}_{\uparrow\downarrow} \exp(-t/t_0) \tag{2.37}$$

with bulk spin-mixing resistivity $\rho^{\mathrm{b}}_{\uparrow\downarrow}$, $\rho^{0}_{\uparrow\downarrow}$ a hypothetical zero-thickness resistivity, and t_0 a characteristic lengthscale. This relation will be used in subsequent chapters when investigating spin transfer across an interface, as a result of dynamic magnetic processes.

Chapter 3

Dynamic Magnetisation Behaviour: Bulk and Interfaces

3.1 Introduction

This chapter builds upon the physical concepts of magnetism detailed in the previous chapter to present a description of the dynamic magnetisation behaviour in magnetic thin film systems. The focus here, and in this thesis, is on the response of synthetic magnetic materials at microwave frequencies. In this region of the electromagnetic spectrum, magnetic materials typically exhibit resonant behaviour. The phenomenological and mathematical description of damped precessional motion of a magnetic moment about an effective field is presented, as well as the influence of magnetic anisotropy on the resonant behaviour, which creates an angular response. A brief discussion of magnetic damping then follows, with both intrinsic and extrinsic mechanisms of energy loss in precessing magnetic systems.

Theories underpinning the dynamic behaviour of layered systems of ferromagnetic and non-magnetic materials are then presented, with a particular focus given to the enhancement of magnetic damping via the propagation of spin across an interface, and the competing models which describe this process.

3.2 Ferromagnetic Resonance

Ferromagnetic resonance (FMR) was first observed by Arkad'yev in 1911, with the observation of selective absorption of centimetre radiowaves by nickel iron wires [70]. Dorfman proposed in 1923 that this absorption arises due to Zeeman splitting of the energy levels, leading to transitions between two energy levels [70]. Landau and Lifshitz modelled this behaviour as a precessing magnetisation in 1935 [71], with Kittel showing application of these equations to describe resonating ferromagnetic systems [72–74]. Gilbert then adapted these equations by introducing a new damping term in 1955 [75], characterised by a parameter that is now named after him.

Semiclassically, magnetic moments in ferromagnetic materials will orientate themselves about the direction of an effective magnetic field, governed by the interactions introduced in the previous chapter. The orientation process is not instantaneous, and moments will precess around the effective magnetic field direction. For the thin films and magnetic anisotropies detailed in this thesis, this precession occurs over a nanosecond timescale, corresponding to microwave frequencies in the gigahertz range. Damping of this precessional motion causes the amplitude of the precession to decrease and the moments to align with the field, with the magnetic energy being ultimately transferred to the crystal lattice as heat. Constant stimulation with an external RF magnetic field creates a torque on the magnetic moment that drives the system into resonance, absorbing some of the RF energy in the process.

The treatment of resonating ferromagnetic systems in terms of a torque caused by an external RF field differs from the treatment of electron paramagnetic resonance (EPR) in which a Hamiltonian describes the splitting of energy levels due to SOC and the Zeeman effect [76]. Additional energy contributions in ferromagnets, such as exchange, which leads to net moments, and large anisotropy values result in FMR being better described by this model of precessing magnetisation.

This section introduces the dynamic equations used to describe resonant behaviour as well as their angular dependence. A brief description then follows of the processes which contribute to magnetic damping that leads to the transfer of energy to the crystal lattice.

3.2.1 Landau-Lifshitz-Gilbert Equation

Dynamic magnetisation is most commonly described with the framework proposed by Landau and Lifshitz [71], in which the precessional motion of the magnetisation about an effective magnetic field is described by

$$\frac{d\vec{M}}{dt} = -\gamma \left(\vec{M} \times \vec{H}_{\text{eff}} \right) \tag{3.1}$$

with γ the gyromagnetic ratio and $\vec{H}_{\text{eff}}$ the effective magnetic field as introduced in the previous chapter. Figure 3.1a illustrates this motion. With energy loss, a precessing moment will eventually reach an equilibrium condition in which it aligns with the effective field, dissipating energy as it does so, as shown in figure 3.1b. The Landau-Lifshitz (LL) equation including their damping term is,

$$\frac{d\vec{M}}{dt} = -\gamma\left(\vec{M}\times\vec{H}_{\text{eff}}\right) - \frac{\lambda}{M_{\text{s}}^2}\vec{M}\times\left(\vec{M}\times\vec{H}_{\text{eff}}\right) \tag{3.2}$$

where λ is a damping frequency, the inverse of the relaxation time, τ_{m}. For heavily damped systems, this equation results in fast relaxation. Gilbert modified the LL equation, introducing a dimensionless damping parameter, resulting in what is now called the Landau-Lifshitz-Gilbert (LLG) equation [75],

$$\frac{d\vec{M}}{dt} = -\gamma\left(\vec{M}\times\vec{H}_{\text{eff}}\right) + \frac{\alpha}{M_{\text{s}}}\left(\vec{M}\times\frac{d\vec{M}}{dt}\right) \tag{3.3}$$

where α is the dimensionless Gilbert damping parameter. Large values of damping result in faster relaxation of the magnetisation towards the effective magnetic field direction. The processes governing damping are discussed in more detail in section 3.2.3, however for all mechanisms the result is the same; energy is ultimately dissipated to the material lattice.

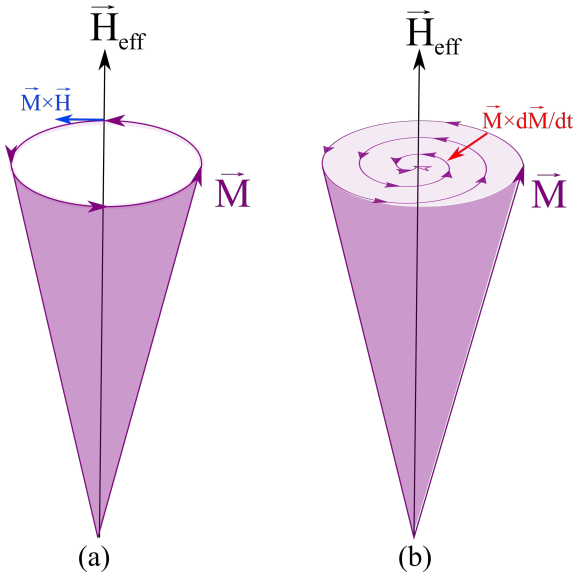

Figure 3.1: Illustration of (a) the precession of a magnetic moment about an effective magnetic field (b) damping acting perpendicular to the direction of precessional motion, causing the magnetisation to align with the magnetic field.

Resonance Condition

The LLG equation describes the relaxation of a magnetic moment towards an effective magnetic field, however general analytic solutions are made difficult by the two time derivatives. By solving the equation with the inclusion of a microwave excitation perpendicular to the effective field which produces a torque on the magnetisation, and with several assumptions, such as a fixed angle of external magnetic field, a general formula for the resonant frequency, now known as the *Kittel equation*, of a magnetic system can be obtained [74].

A solution to the LLG equation for a thin-film system, as shown in figure 3.2, with a uniaxial anisotropy field, H_{u}, and external field, $\vec{H}_{\mathrm{ext}}$, aligned along the $\hat{x}$ direction, and a microwave magnetic field, $\vec{h}$ applied perpendicularly along the $\hat{y}$ direction, can be found by considering the energy contributions discussed in the previous chapter. Here these terms include the dipolar interaction between the magnetisation and both the external field and the microwave field, the surface anisotropy term, and the uniaxial anisotropy term. The effective field can be then found through $\vec{H}_{\mathrm{eff}} = -\frac{1}{\mu_0}\nabla_{\vec{M}}\varepsilon_{\mathrm{T}}$. For this example system, it can be simplified to [47]

$$\vec{H}_{\mathrm{eff}} = (H_{\mathrm{ext}} + H_{\mathrm{u}})\,\hat{x} \;+\; h\,\hat{y} \;-\; M_{\mathrm{eff}}\frac{M_z}{M_{\mathrm{s}}}\hat{z}, \tag{3.4}$$

where H_{u}, the uniaxial magnetic field arising from anisotropy, is given by,

$$H_{\mathrm{u}} = \frac{2K_{\mathrm{u}}}{\mu_0 M_{\mathrm{s}}} \tag{3.5}$$

with K_{u} an in-plane uniaxial anisotropy constant. The effective magnetisation, M_{eff},

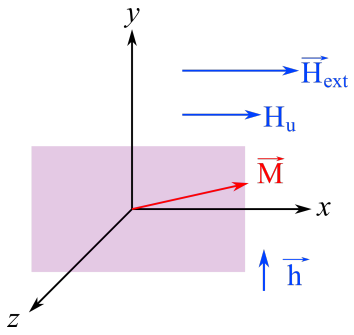

Figure 3.2: Schematic illustration of the setup for solving the LLG equation for a thin film with uniaxial anisotropy.

is [77]

$$M_{\text{eff}} = M_{\text{s}} + \frac{2K_{\text{s}}}{\mu_0 M_{\text{s}} d} \text{ (SI)}, \tag{3.6}$$

$$4\pi_{\text{eff}} M = 4\pi M_{\text{s}} + \frac{2K_{\text{s}}}{M_{\text{s}} d} \text{ (CGS)} \tag{3.7}$$

with surface anisotropy constant, K_{s}, and the thickness of the ferromagnetic material, d. Substituting this expression, along with a complex time-dependent microwave field and magnetisation (i.e. $\exp(i\omega t)$), into equation 3.3 yields the Kittel equation, for ferromagnetic resonance [47, 74],

$$f = \frac{\gamma\mu_0}{2\pi}\sqrt{(H_{\text{ext}} + H_{\text{u}})(H_{\text{ext}} + H_{\text{u}} + M_{\text{eff}})} \text{ (SI)}, \tag{3.8}$$

$$f = \frac{\gamma}{2\pi}\sqrt{(H_{\text{ext}} + H_{\text{u}})(H_{\text{ext}} + H_{\text{u}} + 4\pi M_{\text{eff}})} \text{ (CGS)} \tag{3.9}$$

with all terms as defined previously. The resulting plots of this expression are known as *Kittel curves*. This relation provides a description of where a resonance frequency occurs, as a function of magnetic field for a set of material parameters, that includes the saturation magnetisation and the anisotropy, which in turn can be altered using techniques mentioned in the previous chapter, such as nano and microscale patterning. Figure 3.3 shows the effect of changing either the magnetisation or the anisotropy on the Kittel curve. With the inclusion of magnetic anisotropy, resonant dynamic behaviour is achieved without the presence of an external magnetic field.

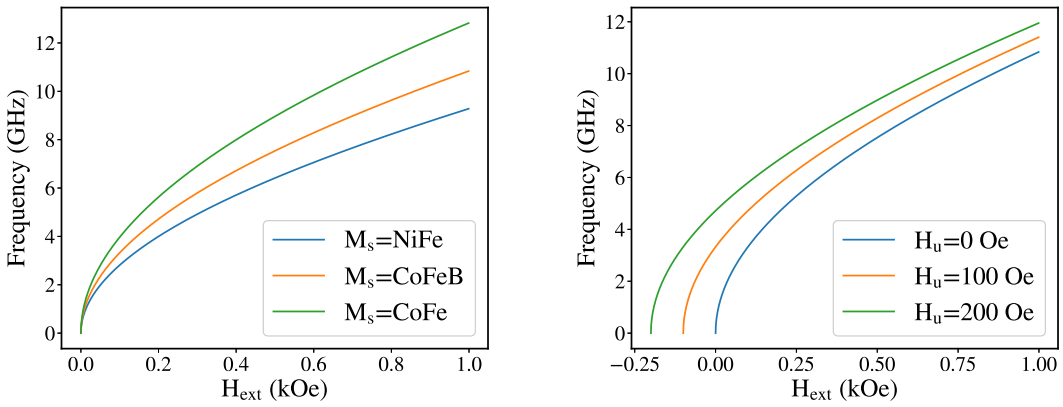

(a) (b)

Figure 3.3: Evaluations of the Kittel equation for: (a) Three different ferromagnetic materials, showing the effect of changing the saturation magnetisation, 10 kG (NiFe), 14 kG (CoFeB) and 20kG (CoFe) (b) Three different values of in-plane anisotropy for the same magnetisation value. Note the absence of a resonance at zero field in the case of no additional anisotropy.

The resonant response of a magnetic material is not a delta function at a single frequency, but rather a Lorentzian lineshape, the linewidth of which is dependent upon the damping. For the frequency domain and the full width half maximum (FHWM) linewidth, this is derived as [47],

$$\Delta f = \frac{\gamma\mu_0}{2\pi}\alpha\left(2H_{\text{ext}} + 2H_{\text{u}} + M_{\text{eff}}\right) \text{ (SI)}, \tag{3.10}$$

$$\Delta f = \frac{\gamma}{2\pi}\alpha\left(2H_{\text{ext}} + 2H_{\text{u}} + 4\pi M_{\text{eff}}\right) \text{ (CGS)} \tag{3.11}$$

and for the FWHM in the field domain as [47, 78],

$$\Delta H = \frac{4\pi\alpha}{\gamma} f \tag{3.12}$$

For realistic thin films, other scattering processes can increase the linewidth of a material, as discussed in a later section. In the LLG formalism used here, this usually adds as an extra term to the field linewidth [79],

$$\Delta H = \frac{4\pi\alpha}{\gamma} f + \Delta H_0, \tag{3.13}$$

with ΔH_0 representing these additional damping processes. In FMR experiments, as discussed in later chapters, typically either the frequency or the external magnetic field is fixed, and the other parameter varied, producing either of these linewidths, though it is possible to convert between field and frequency domains [80].

Dynamic Permeability

At resonance, the magnetic permeability of a material also shows rapid variations compared to in the static regime. From the LLG equation, the relative complex dynamic permeability has been derived as [78, 81]

$$\mu\left(f\right) = 1 + \frac{M^2}{MH - \left(\frac{f}{\gamma/2\pi}\right)^2 + i\alpha M\left(\frac{f}{\gamma/2\pi}\right)}, \tag{3.14}$$

where this expression is in CGS units with H in Oe, M in G and f in MHz. This relation is used in the next chapter to simulate the response of a thin film system to incident RF energy, in which the impedance (dependent upon the permeability) determines the reflectivity of a material.

Bloch–Bloembergen Equation

While the LLG equation is widely used to model dynamic behaviour of magnetic moments, it is not without several assumptions which do not necessarily hold, particularly with itinerant systems [76]. The dynamic behaviour of the spins are treated as a uniform precession, with a $k = 0$ mode, which is not the case at high temperatures, where additional excited modes can enhance the scattering times and therefore the damping of a system [82]. At finite temperatures, the LLG equation can be modified to include an additional thermal noise term to account for temperature effects [83], with the magnetisation vector treated with a fixed magnitude, which is unchanged with temperature.

An alternate form of dynamic relation is the Bloch–Bloembergen (BB) equation [84, 85], in which there are two separate relaxations; a longitudinal relaxation of the main mode straight to the lattice (spin-lattice), and a transverse relaxation in which the main mode divides into separate spin wave modes with $k \neq 0$ (spin-spin) [86], which then relax to the lattice. For an external magnetic field along a z axis, this is given mathematically by,

$$\frac{dM_z}{dt} = -\gamma \left(M_z \times H_z\right) - \frac{M_z - M_\mathrm{s}}{T_1}, \tag{3.15}$$

$$\frac{dM_{x,y}}{dt} = -\gamma \left(M_{x,y} \times H_{x,y}\right) - \frac{M_{x,y}}{T_2} \tag{3.16}$$

with T_1 the longitudinal relaxation time and T_2 the transverse relaxation time. The BB model describes the dynamic behaviour of a collection of spins well, but does not for individual moments [77], hence the LLG equations must be used in this case.

It is also worth noting that there are models which combine the two frameworks, known as the Landau-Lifshitz-Bloch (LLB) equations, in which individual spins are treated interacting with an environment, producing LLG-like results at low temperatures, and BB-like results at higher temperatures [82, 87]. In this framework, two separate damping constants for the longitudinal and transverse directions are used. For this thesis however, focus was directed towards the LLG equation, as the Gilbert damping term was of principle interest for characterising synthetic materials.

3.2.2 Angular Dependence of Dynamic Magnetisation Behaviour

Though it provides a useful description of the frequency of ferromagnetic resonance for a thin film system, the derivation of Kittel's equation applies to a single angle of M-H alignment only. For measurements undertaken in a resonant microwave cavity,

where only one frequency is available, samples are often rotated in the field, and the angular dependence of the resonant behaviour is measured. Similarly, for materials with additional anisotropy, such as patterned materials, it is useful to characterise the dynamic response as a function of angle, where the additional degrees of freedom provide a more robust method to extract parameters.

One such approach was provided by Smit and Suhl in 1955 [88, 89] for the resonance condition in terms of the total free energy density, ε_{tot}, with respect to the polar, θ_{M}, and azimuthal, ϕ_{M}, angles of the magnetisation. Figure 3.4 shows a schematic illustration of the orientation, with the crystal axes aligned along the x, y, z axes.

With an external applied magnetic field, the magnetisation vector will move until the magnetic energy density is minimised, and the system is in equilibrium. This condition can be expressed as,

$$\frac{\partial \varepsilon_{\text{tot}}}{\partial \theta_{\text{M}}} = 0\,, \quad \frac{\partial \varepsilon_{\text{tot}}}{\partial \phi_{\text{M}}} = 0. \tag{3.17}$$

The Smit-Suhl equation for ferromagnetic resonance is then derived to be [47, 88, 89],

$$\left(\frac{\omega_{\text{res}}}{\gamma}\right)^2 = \frac{1}{M_{\text{s}} \sin^2 \theta_{\text{M}}} \left[\frac{\partial^2 \varepsilon_{\text{tot}}}{\partial \theta_{\text{M}}^2} \frac{\partial^2 \varepsilon_{\text{tot}}}{\partial \phi_{\text{M}}^2} - \left(\frac{\partial^2 \varepsilon_{\text{tot}}}{\partial \theta_{\text{M}} \phi_{\text{M}}} \right)^2 \right], \tag{3.18}$$

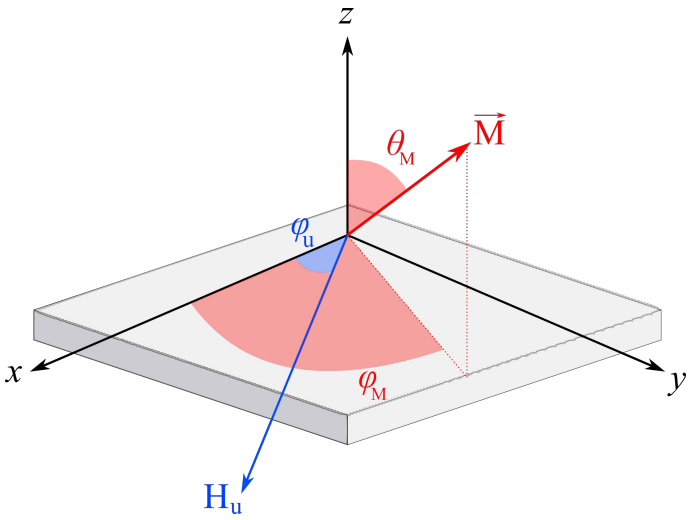

Figure 3.4: Schematic illustration of the coordinates in the Smit-Suhl approach, with x, y, z corresponding to the cubic easy axes, and uniaxial anisotropy axis H_{u}. Direction and angles of the external magnetic field are not depicted for clarity.

with the frequency linewidth,

$$\Delta\omega = \frac{\alpha\gamma}{M_\mathrm{s}}\left[\frac{\partial^2\varepsilon_\mathrm{tot}}{\partial\theta_\mathrm{M}^2} + \frac{1}{\sin^2\theta_\mathrm{M}}\frac{\partial^2\varepsilon_\mathrm{tot}}{\partial\phi_\mathrm{M}^2}\right] \tag{3.19}$$

and the field linewidth [90],

$$\Delta H = \frac{1}{\partial\omega_\mathrm{res}/\partial H_\mathrm{ext}}\frac{\alpha\gamma}{M_\mathrm{s}}\left[\frac{\partial^2\varepsilon_\mathrm{tot}}{\partial\theta_\mathrm{M}^2} + \frac{1}{\sin^2\theta_\mathrm{M}}\frac{\partial^2\varepsilon_\mathrm{tot}}{\partial\phi_\mathrm{M}^2}\right] \tag{3.20}$$

with all equations evaluated at the equilibrium condition, i.e. $\theta_\mathrm{M} = \theta_\mathrm{M}^\mathrm{equi}$, $\phi_\mathrm{M} = \phi_\mathrm{M}^\mathrm{equi}$. For a thin film, evaluating all the contributions to the energy leads to a large and complex equation for the dynamic response of the system. However, by restricting the geometry when undertaking angular measurements and through several assumptions, the Smit-Suhl equations are simplified.

For the case of an in-plane external magnetic field ($\theta_\mathrm{H} = \frac{\pi}{2}$) applied to a sample with in-plane uniaxial anisotropy only, i.e. $\phi_\mathrm{u} = 0$ and $\theta_\mathrm{M} = \frac{\pi}{2}$, the equilibrium condition is given as [47],

$$H_\mathrm{u}\sin\phi_\mathrm{M} \;=\; 2H_\mathrm{ext}\sin\left(\phi_\mathrm{H} - \phi_\mathrm{M}\right) \tag{3.21}$$

with the uniaxial anisotropy field, H_u and angle of the external field, ϕ_H. The resonance condition is then,

$$\begin{aligned}\left(\frac{\omega_\mathrm{res}}{\gamma}\right)^2 &= \left[H_\mathrm{ext}\cos\left(\phi_\mathrm{H} - \phi_\mathrm{M}\right) + H_\mathrm{u}\cos 2\phi_\mathrm{M}\right] \\ &\times \left[H_\mathrm{ext}\cos\left(\phi_\mathrm{H} - \phi_\mathrm{M}\right) + 4\pi M_\mathrm{eff} + H_\mathrm{u}\cos^2\phi_\mathrm{M}\right]\end{aligned} \tag{3.22}$$

with the frequency linewidth,

$$\Delta\omega = \alpha\gamma\left[2H_\mathrm{ext}\cos\left(\phi_\mathrm{H} - \phi_\mathrm{M}\right) + 4\pi M_\mathrm{eff} + H_\mathrm{u}\left(3\cos^2\phi_\mathrm{M} - 1\right)\right] \tag{3.23}$$

and the field linewidth,

$$\Delta H \;=\; \frac{2\alpha\omega_\mathrm{res}}{\gamma}\frac{1}{\cos\left(\phi_\mathrm{H} - \phi_\mathrm{M}\right)}. \tag{3.24}$$

Setting $\phi_\mathrm{H} = 0$, yields $\phi_\mathrm{M} = 0$ from the equilibrium condition and results in equations 3.22, 3.23 and 3.24 following the same standard form from the LLG equation as discussed in the previous section. In the angular measurements used in this thesis, samples were rotated with respect to the applied magnetic field, which is equivalent to rotating the field angle, ϕ_H. For fitting it is necessary to evaluate the equilibrium

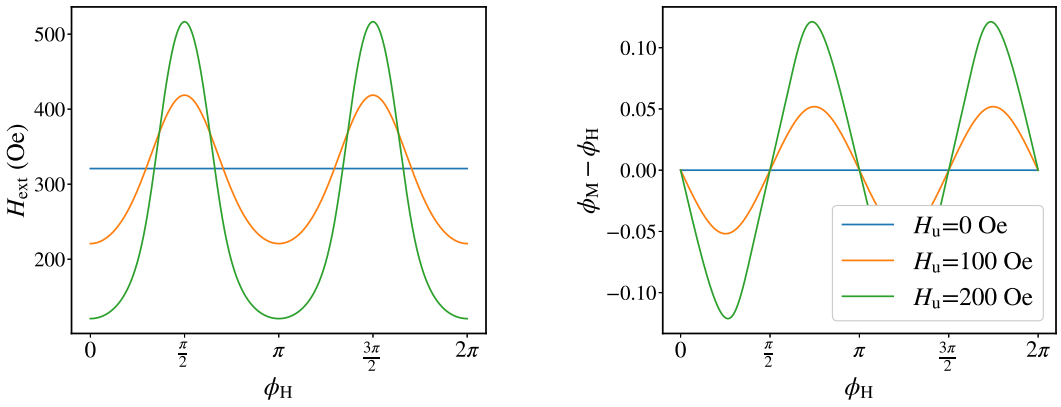

(a) (b)

Figure 3.5: (a) Simulations of the angular dependence curve of the external magnetic field required for resonance at 6 GHz for three uniaxial anisotropy values. (b) The dependence of the angle of magnetisation with respect to the field angle against the angle of the external field, for the three anisotropy values, determined using the equilibrium condition in equation 3.21.

condition 3.21 to determine ϕ_M at each field angle, before applying equation 3.22 to fit the data. Figure 3.5 shows a simulation of the angular behaviour of the external magnetic field required to undergo resonance at 6 GHz for three different uniaxial anisotropy values set at $\phi_H = \theta_H = 0$. For the case where the external and uniaxial anisotropy fields are aligned, a smaller external magnetic field is required to excite FMR than where the external field is orientated at $\frac{\pi}{2}$ to the uniaxial anisotropy easy axis. With no anisotropy, the resonant field is independent of the applied field angle. The larger the anisotropy value, the larger the phase lag between the angle of the external magnetic field, and the angle of the magnetisation, as shown in figure 3.5b.

3.2.3 Intrinsic and Extrinsic Magnetic Damping

Magnetic damping processes refer to the transfer of energy from a resonantly precessing spin system to the material lattice. For many spintronic devices it is favourable to have a small damping constant, which corresponds to faster switching of the magnetisation [91, 92], similarly in magnon-based devices, where a small damping constant leads to long lifetimes of coherent spin waves [6]. However for absorbing materials, a large damping constant enhances the imaginary component of the permeability and increases the loss of RF energy within a material, as well as the frequency bandwidth over which it acts, and is therefore favourable.

The main resonant mode in FMR, which arises from the uniform collective behaviour of the precessing moments, can be described as a spin-wave, or magnon,

with $k = 0$. Damping processes transfer energy from this excited state to the lattice. These processes can be broadly split into two categories; *intrinsic damping*, defined by the Gilbert damping constant, in which the fundamental mode decays directly to the lattice, and *extrinsic damping*, in which the main mode scatters into non-uniform modes, which then decay to the lattice via similar damping [77].

Intrinsic Mechanisms

In the model developed by Heinrich *et al.* [93], intrinsic Gilbert damping occurs as a result of scattering processes between electrons and uniform magnons. In these interactions, a magnon is annihilated and the electron is promoted to an excited state in the same energy band, (*intraband*), or a higher energy level band (*interband*), resulting in the formation of an electron-hole pair. The relaxation of this state, (electon-hole recombination), via scattering with phonons or lattice defects transfers the energy to the lattice, which can be characterised with a relaxation time, τ_{m} [94].

The SOI provides one of the energy contributions which affect the Fermi surface of a material. In systems with dynamic magnetisation, this SOI results in periodic time variations of the Fermi surface, referred to as the *breathing Fermi surface* [95]. This altering of the Fermi surface changes the equilibrium density of states of a system, producing levels which electrons can be promoted into for a short period. The contribution to the damping occurring as a result of these intraband transitions from electron-magnon interactions, is linearly proportional to τ_{m} and hence is referred to as a conductivity-like contribution, which increases with decreasing temperature [96]. This contribution is also anisotropic for crystalline materials [94].

For interband, or *bubbling Fermi surface* contributions, the initial and excited states have the same wave vector (i.e. similar to direct semiconductor transitions). The scale of this contribution is therefore dependent upon the number of states available to transition into [96]. From the uncertainty principle, the spread of energy levels of a system is inversely proportional to the relaxation time, with a smaller τ_{m} increasing the life time broadening of energy levels of a system. The number of available states to scatter into is therefore inversely proportional to τ_{m}. This inverse relation means that this term is known as a resistivity-like contribution, which increases with temperature, and is also anisotropic at low temperature [94, 97].

In a real system both of these processes occur, and both contribute to the anisotropic Gilbert damping term, represented as a tensor. However, for transition metals at room temperature the interband resistivity-like contribution dominates, and at these temperatures the thermal energy is higher than the spin-orbit contribution which favours certain crystallographic axes [94], hence the Gilbert damping is well approximated as a scalar for the work in this thesis.

Extrinsic and Other Mechanisms

Extrinsic damping refers to a second set of mechanisms in which the uniform mode is dissipated into modes with $k \neq 0$, which then in turn dissipate energy to the lattice. As this process is indirect and involves the generation of secondary magnons, it is referred to as 'slow' compared with intrinsic contributions. However, it still provides an enhancement to the overall damping of a system, particularly when there are increased scattering centres, such as impurities, defects [98], or dopants [99] in a material.

The most common form of scattering of the uniform precessional magnon into non-uniform modes is known as *two-magnon scattering*. The BB equation described previously (equation 3.15) provides a theoretical description for this process, where two relaxation pathways occur; longitudinal spin-lattice, characterised with relaxation time T_1, and transverse spin-spin, characterised with a relaxation time T_2. It is this second relaxation which quantifies the two-magnon contribution [76]. The spin-wave dispersion is both frequency dependent and anisotropic, and can be modelled as a contribution to the FMR linewidth through [100]

$$\Delta H_{\mathrm{2Magnon}} = \Gamma \arcsin \sqrt{\frac{\left(\omega^2 + \omega_0^2/4\right)^{1/2} - \omega_0/2}{\left(\omega^2 + \omega_0^2/4\right)^{1/2} + \omega_0/2}}, \tag{3.25}$$

with Γ characterising the strength of the scattering process and $\omega_0 = \gamma H_{\mathrm{p}}$, where $H_{\mathrm{p}} = (2K - 4\pi M_{\mathrm{s}})$ is the effective perpendicular magnetic field. The two-magnon contribution is removed if the magnetisation is perpendicular to the film plane, as the spin-wave vector is within the film plane only. Two-magnon scattering contributions modelled in this form produce a large contribution to the linewidth at lower frequencies.

This formulation, however, does not always hold, for example in the case of periodic defects of Cr introduced through patterning, the frequency relation arises due to the dependence of the resonance condition on the external field, with maximum scattering occurring when the wavevector matches the periodicity of the defects [98]. Within the LLG framework, this contribution is most commonly included as a frequency independent contribution to the linewidth, ΔH_0 [79].

Broadening of the resonance linewidth can also arise due to a variation of parameters, such as local fields, composition, thickness etc on a large scale in a sample [101]. These contributions, however, are much smaller than the other contributions and can usually be neglected [100]. Higher order scattering mechanisms, such as three- [102, 103] or four-magnon [104, 105], also exist, but are less common and not addressed in this thesis.

3.3 Dynamic Magnetisation Behaviour and Interfaces

The previous section detailed models and descriptions of the dynamic response of a ferromagnetic material, a large area of research however, is directed to the physics occurring between layers of ferromagnetic and non-magnetic materials, where the resultant interfacial behaviour is fundamental to spintronic device functionality and applications. Of primary interest in this thesis is the phenomena known as *spin pumping*, in which spin angular momentum may be transferred across such an interface, providing an additional method to control the damping of a system.

This section details the mechanism and some of the theories behind the enhancement of damping due to a ferromagnetic and non-magnetic interface, as well as the relaxation mechanisms within the non-magnetic materials. A brief description then follows of other key interfacial effects not used in this thesis, but relate to the same underlying physics.

3.3.1 Interfacial Enhancement of Damping

The increase in the measured damping of a ferromagnetic system when in contact with a non-(ferro)magnetic material has been known in the literature for many years [106, 107]. This enhancement is an interfacial effect, the magnitude of which is dependent upon the NM, and is proportional to the NM thickness [108], inversely proportional to the FM thicknesses [109], and dependent upon the structure of the interface itself [108, 110, 111].

Various models exist to describe the increase of Gilbert damping at interfaces, with the most common the spin-pumping model proposed by Tserkovnyak *et al.* [112, 113], in which spin angular momentum is transferred across an interface, and then relaxes inside the NM material. Other models focus on the $s-d$ and $d-d$ exchange across interfaces [114], which produces similar results as the spin-pumping model for free electrons, and the tight-binding model including SOC developed by Barati *et al.* [115].

Spin Relaxation in Non-Magnetic Metals

Before discussing theories of interfacial enhancement of damping further, it is necessary to introduce the spin relaxation processes which transfer energy to the lattice and the lengthscales which they occur within non-magnetic materials. Unlike ferromagnetic materials, which have spin splitting in the d band at the Fermi energy, in bulk non-ferromagnetic metals, the Fermi level is symmetric with respect to the

spin states and hence there is no preference to which spin state electrons scatter into; the net scattering is spin independent. When a spin-polarised current passes through such a metal, scattering events reduce the overall polarisation until there are an equal number of spin-up and spin-down states.

Two mechanisms are usually responsible for spin-relaxation processes in metals, both of which are dependent upon the spin-relaxation time, τ_{sf}, and the electron momentum scattering time, τ_{e}. In the Elliot-Yafet (EY) scattering process [116, 117], at each momentum scattering event an associated spin-flip may occur, the probability of which is dependent upon the strength of the SOI, which allows the mixing of spin states. The spin-flip scattering relaxation time is therefore proportional to the rate of momentum scattering, i.e. $\tau_{\mathrm{sf}} \propto \tau_{\mathrm{e}}$ [118].

The second mechanism is D'yakonov-Perel (DP) spin relaxation [119], and is prevalent in systems with broken inversion symmetry, such as interfaces or semiconductors, where there is a large directional SOI. Spins precess about this effective SO field, and de-phase as they do so [120]. The spin-flip relaxation time here is inversely proportional to the momentum scattering, $\tau_{\mathrm{sf}} \propto 1/\tau_{\mathrm{e}}$. Both of these mechanisms can occur within a material, for a common spintronic non-ferromagnetic metal such as Pt, however, the DP contribution is suppressed at room temperatures and the EY contribution is dominant [120, 121].

The lengthscale over which the polarisation of a spin-current decreases by a factor $1/e$ is known as the *spin-diffusion* or *spin-flip* length, λ_{sf}, related to the momentum scattering through [120],

$$\lambda_{\mathrm{sf}} = \sqrt{\frac{\nu_{\mathrm{F}} l_{\mathrm{e}} \tau_{\mathrm{sf}}}{3}} \tag{3.26}$$

with Fermi velocity, ν_{F}, and electron mean free path, $l_{\mathrm{e}} = \nu_{\mathrm{F}}\tau_{\mathrm{e}}$ [113]. One outstanding issue in the literature is the value of the spin diffusion length for Pt. This length is one of the parameters which quantifies the enhancement of the magnetic damping of a system, and therefore must be well-defined in order to confidently produce synthetic structures which perform over a range of frequencies. As will be discussed and addressed in later results chapters, the reported values of this length varies over an order of magnitude for Pt depending on the method used to measure it, and the assumptions upon which it is derived [7].

Spin-Pumping Model

One of the most common approaches to provide a physical description of the enhancement of the magnetic damping at interfaces is the spin-pumping model developed by Tserkovnyak *et al.* based on scattering theory [112, 113, 122–125]. In this model, a precessing magnetisation in a FM layer creates an unbalanced electrochem-

ical potential, μ_c at the interface between a FM and NM layer, which leads to the accumulation of one spin state at the interface, $\mu_s^{\uparrow}$ or $\mu_s^{\downarrow}$. It is this spin accumulation which drives an associated spin current, J_s across the interface, analogous to a conventional battery, for this reason the transfer of spin angular momentum in this way has been termed a spin battery [122]. The pure spin current is able to transfer across an interface due to $s-d$ interactions between the FM and NM layers [125]. Figure 3.6 illustrates this process, in which the injected spin current decays over a characteristic lengthscale due to the mechanisms previously described.

The magnitude of the spin current transferred across an interface is therefore dependent on both the NM material parameters, and the physical properties of the interface itself. The transmission of spin current across an interface can be characterised in terms of a *spin-mixing conductance*, $G^{\uparrow\downarrow}$, (units of inverse Ohms), or more commonly the mixing conductance per unit area, $g^{\uparrow\downarrow}$, which itself can be expressed as [123],

$$g^{\uparrow\downarrow} = g_r^{\uparrow\downarrow} + i g_i^{\uparrow\downarrow} \tag{3.27}$$

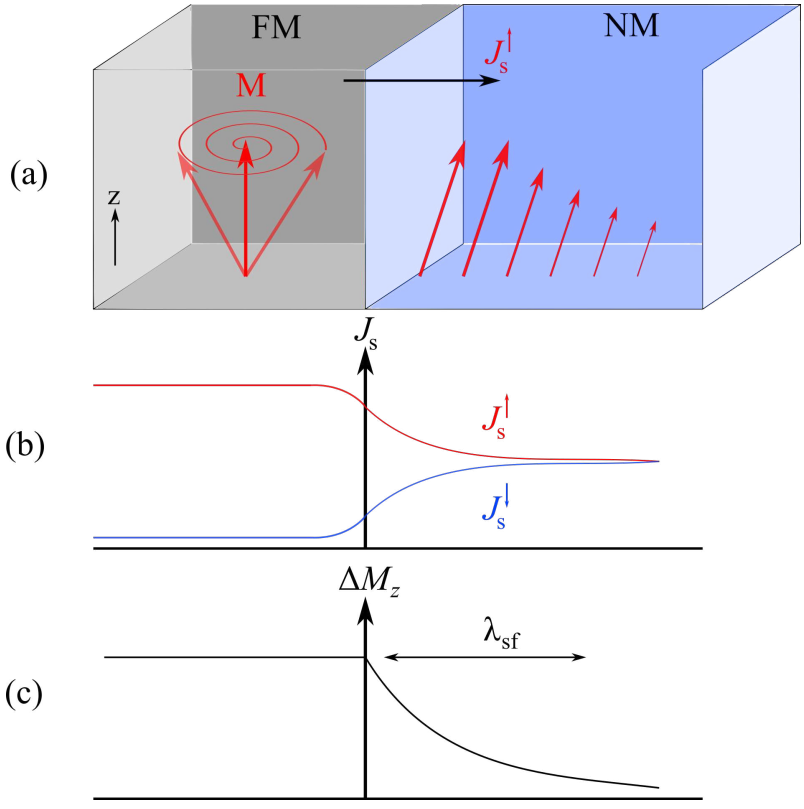

Figure 3.6: Schematic illustration of: (a) The injection of a spin current across an interface into a NM layer due to precessing magnetisation in a FM layer. (b) The decay of the spin polarisation inside the NM layer, characterised as a decay in the spin current for one spin state. (c) The decay of the spin current characterised as a decay in the magnitude of the z-component of the magnetisation.

where $g_r^{\uparrow\downarrow}$ represents the transmitted part of the spin current aligned with the transverse component of the spin accumulation, and $g_i^{\uparrow\downarrow}$ the dephasing of the spins due to the precession about the direction of the FM magnetisation as they transfer across an interface [126]. For the metallic interfaces under consideration in this thesis, it is commonly assumed that $g_r^{\uparrow\downarrow} \gg g_i^{\uparrow\downarrow}$ [113], and therefore,

$$g^{\uparrow\downarrow} \approx g_r^{\uparrow\downarrow} \approx g_N^{\mathrm{SH}} \tag{3.28}$$

where g_N^{SH} is the Sharvin conductance, which quantifies the number of transport channels across an interface between two materials [123]. The spin current pumped into the NM is then,

$$J_s^{\mathrm{p}} = \frac{\hbar}{4\pi} g^{\uparrow\downarrow}\, \hat{m} \times \frac{d\hat{m}}{dt} \tag{3.29}$$

with $\hat{m}$ the magnetic moment [127]. A current in a NM layer can also flow into a FM layer, this process can exert a torque on the magnetic moments in the FM layer, and induce dynamic behaviour, as discussed in the next section. Here, a component of the pumped spins can also flow back into the FM layer [113], given by

$$J_s^{\mathrm{b}} = -\frac{\hbar}{4\pi} g^{\uparrow\downarrow}\, \hat{m} \times \hat{\mu_s} \times \hat{m}, \tag{3.30}$$

with the net spin current flow,

$$J_s^{\mathrm{t}} = J_s^{\mathrm{p}} - J_s^{\mathrm{b}}. \tag{3.31}$$

The dynamics of the ferromagnetic moments can then be modelled with a modified LLG equation with an additional term, $\frac{\gamma}{M_s} J_s^{\mathrm{t}}$ [113], and the spin accumulation, μ_s, found through solving a 1D spin diffusion equation,

$$i\omega\mu_s = D\frac{\partial^2 \mu_s}{\partial x^2} - \frac{\mu_s}{\tau_{sf}} \tag{3.32}$$

where τ_{sf} is the spin-flip relaxation time and D the diffusion coefficient ($D = \nu_F^2 \tau_e/3$), with τ_e the momentum relaxation time. This injected spin current relaxes within the NM layer, and therefore enhances the intrinsic magnetic damping, by providing an additional pathway for the uniform mode to decay to the lattice.

The enhancement of damping due to interfacial effects, such as spin-pumping, is usually modelled as an addition to the bulk-like Gilbert damping, i.e. $\alpha = \alpha_0 + \alpha_s$, with $\alpha_s = \Delta\alpha$ the surface term. As a function of the properties of the NM layer this

increase can be expressed as [113],

$$\frac{\alpha_{\mathrm{s}}}{\alpha_{\mathrm{s}}^{\infty}} = \frac{1}{1 + [\sqrt{\epsilon}\tanh\left(L/\lambda_{\mathrm{sf}}\right)]^{-1}} \tag{3.33}$$

with L the thickness of the NM material and ϵ representing the ratio of the momentum scattering time (or length) to the spin-flip scattering time (or length) in the EY formalism discussed earlier. The value of ϵ is dependent upon the strength of SOI in the NM material, and hence simplistically varies as Z^4, with larger values producing higher damping, and shorter spin-diffusion lengths. This is one of the reasons why Pt has a much shorter spin-diffusion length compared to Cu [7]. $\alpha_{\mathrm{s}}^{\infty}$ represents the enhancement of damping in the case $L > \lambda_{\mathrm{sf}}$, and is given by

$$\alpha_{\mathrm{s}}^{\infty} = \frac{g\,\mathrm{g}^{\uparrow\downarrow}}{4\pi M}, \tag{3.34}$$

with g the g-factor defined previously. The damping can also be expressed in terms of the ferromagnetic thickness [128],

$$\alpha_{\mathrm{s}} = \frac{\gamma\hbar}{4\pi M_{\mathrm{s}} t}\mathrm{g}_{\mathrm{eff}}^{\uparrow\downarrow}, \tag{3.35}$$

with t the thickness of the ferromagnet, and $\mathrm{g}_{\mathrm{eff}}^{\uparrow\downarrow}$ the effective spin-mixing conductance per unit area for a given thickness of a NM layer.

In the spin-pumping formalism, the key material parameters are ϵ, λ_{sf}, and $\mathrm{g}^{\uparrow\downarrow}$. Materials such as Pt, are referred to as good *spin-sinks*, as due to the large SOC producing a short spin-diffusion length, the spin currents quickly dissipate inside the NM material. Better matching of material structure at the interface can also increase the number of conductance channels and reduce the reflection amplitude, thereby increasing $\mathrm{g}^{\uparrow\downarrow}$ and hence the overall damping [108, 110].

As discussed in the previous chapter, for a NM close to the Stoner criterion, e.g. Pt and Pd, at the interface with a FM, they may become magnetically polarised in a region confined to the interface. In the spin-pumping theory described here, the enhanced spin susceptibility in these proximity polarised NM materials plays no role in the transmission of spin current across an interface, as the computed Sharvin conductance is mostly unchanged, even for ultrathin films [123]. Additionally, the non-equilibrium spin accumulation, μ_{s}, which drives the spin current, is also unaffected by the Stoner enhancement through equilibrium polarisation, even though the proximity spin density is affected. Nevertheless, the influence of proximity polarisation on the damping is a topic of active discussion in the literature, with reports claiming proximity induced magnetisation has a profound effect [17] or no effect at

all [18] on interfacial spin-transport phenomena. This discrepancy is discussed in further detail in the results chapters.

Barati-Umerski Model of Enhanced Damping

An alternative description of the enhancement of Gilbert damping with interfaces between FM and NM materials based on first principles calculations has been proposed by Barati, Cinal, Edwards and Umerski [115], based on the model by Kambersk̀y [95]. In this atomic layer-by-layer model, a tight-binding scheme with localised orbitals was used to determine a Hamiltonian that considers the spin-orbit interactions between the orbitals of first and second nearest neighbours. Damping is then calculated through a perturbation using this Hamiltonian to determine the relaxation arising from inter and intraband transitions as described previously. Crucially, the calculated damping is dependent upon an electron scattering rate, the density of states, and the spin-orbit coupling strength.

For purely FM materials, this model predicts that the largest contribution to the damping occurs at the interfacial region, i.e. the first and last layers. In the case of FM/NM bilayers, the damping contribution is again largest at the interface for all NM metals, with the rate at which the damping contributions for each layer falls to zero dependent upon the electron scattering rate. For NM metals with a full d band, such as Cu or Ag, the interfacial enhancement arises due to modification to the structure of the top FM layer due to orbital overlap, which is typically small and hence results in a small contribution, whereas for materials such as Pd and Pt, where the d band crosses the Fermi energy giving a large density of states which provides opportunity for hybridisation, the damping contribution is much greater [115]. Large damping from NM metal interfaces in this model therefore requires large SOC and a large density of states.

Similar to the spin-pumping model, the dependence of the damping on the ferromagnetic thickness follows the same form (equation 3.35). Both the electron scattering rate used here, and the spin-diffusion length from spin-pumping theory are also both dependent on the SOC strength of the NM metal. However, there is no immediate relation between the density of states of the conducting electrons, used here to determine the size of the enhanced damping, with the spin-mixing conductance in the previous spin-pumping model, in which the mixing conductance is determined by how well states match across the interface. As well as this, unlike the previous model, the effect of proximity induced polarisation here may also directly relate to the damping, as both depend on the hybridisation of states at the interface.

3.3.2 Spin Hall Effect and Torques

The enhancement of magnetic damping via the transmission of spin current across an interface is just one of several interfacial phenomena which underpin potential spintronic applications. A brief discussion is given here of a closely related process; the *spin Hall effect* (SHE). Previously, it was discussed that the backflow of spin current in a NM layer can alter the dynamic behaviour of the FM layer. This can be included in dynamic equations of motion as an effective magnetic field [129],

$$J_{\mathrm{ex}}\mu_{\mathrm{s}} = a\mu_{\mathrm{s}} \times M + b\mu_{\mathrm{s}}, \tag{3.36}$$

where J_{ex} is the exchange coupling, and a and b are material dependent parameters, relating to parameters such as the spin-mixing conductance. An altered LLG equation is given as [125],

$$\frac{d\vec{M}}{dt} = -\gamma\vec{M} \times \left(\vec{H}_{\mathrm{eff}} + J_{\mathrm{ex}}\mu_{\mathrm{s}}\right) + \frac{\alpha}{M_{\mathrm{s}}}\left(\vec{M} \times \frac{d\vec{M}}{dt}\right). \tag{3.37}$$

Two additional torques arise, a *field-like* term due to $bM \times \mu_{\mathrm{s}}$, and a *damping-like* term due to $aM \times \mu_{\mathrm{s}} \times M$. Both of these torques can act with, or against the magnetic damping, and allow an additional method to manipulate magnetisation dynamics [130].

It is not only the backflow of spin current pumped across an interface which can exert a torque. In 1971 D'yakonov and Perel reported the possibility of the spins in a charge current orientating to form a perpendicular spin current [131]. This was developed further by Hirsch in 1999 [132], and termed the spin Hall effect, where due to the SOI, the accumulation of opposite spin at the edge of a sample occurs when a charge current passes through a material, such as a heavy metal [133] or semiconductor [134]. This can be thought of as spin current flowing perpendicularly to the charge current, with opposite spin flowing in opposite directions. Spin pumping can produce an *inverse spin Hall effect* (ISHE), where the pumped pure spin current relaxes producing a corresponding charge current [135, 136].

The SHE occurs as a result of intrinsic and extrinsic mechanisms. Intrinsic mechanism are related to the band structure of a material, whereas extrinsic mechanisms rely on scattering due to material impurities. Extrinsic process are subdivided into skew-scattering, in which different spin states are scattered in opposite directions due to the magnetic field generated through the SOI, and side-jump scattering, in which different spin states are scattered oppositely due to the electric field gradient upon approaching an impurity [130]. Further details are not required in this thesis.

The SHE created due to a charge current passing through a NM layer in contact

with a FM layer creates a corresponding spin current, which can cross the interface and exert a torque on the magnetisation as described earlier. This allows electrical current control of magnetisation dynamics, with both magnetisation switching [137] and resonance [138] induced through this effect. An important parameter which parameterises the efficiency of this charge-to-spin process, is the spin Hall angle, θ_{SH},

$$\theta_{\mathrm{SH}} = \frac{J_{\mathrm{s}}}{J_{\mathrm{e}}} \tag{3.38}$$

with spin current, J_{s} and charge current J_{e}. The spin Hall angle has an inverse relation to the spin diffusion length, and like the spin diffusion length, there exists a wide range of values in the literature for the spin Hall angle of Pt [92]. This discrepancy in reported values of key interfacial parameters forms a portion of the results presented in Chapter 8.

Chapter 4

The Physics of Materials for RF Applications

4.1 Introduction

This chapter provides first a brief introduction into current materials for RF applications, specifically microwave absorbers. The common methods for enhancing RF loss are outlined, followed by a short summary of existing composite and synthetic materials, of which magnetic thin films form a part.

Following this, a model for simulating the response of magnetic thin film systems, based on impedances, is described. Particular focus is given to the controllable thin film parameters, such as the saturation magnetisation and the effective magnetic field, which determine the high frequency response. By considering the interfacial phenomena introduced in the previous chapter, this model has been further extended to account for the enhancement of magnetic damping due to spin pumping of a resonating ferromagnetic layer in contact with a heavy metal layer.

4.2 RF Material Systems

Before discussing materials and their responses at high frequency, it is necessary to introduce the parameters which determine such behaviour. The reflectance and absorbance of an incident high frequency electromagnetic wave are governed by how both the electric and magnetic fields behave in a material. An important parameter that quantifies this is the wave impedance, given by [139],

$$Z = \sqrt{\frac{\mu_{\mathrm{r}}\mu_0}{\varepsilon_{\mathrm{r}}\varepsilon_0}} = Z_0\sqrt{\frac{\mu_{\mathrm{r}}}{\varepsilon_{\mathrm{r}}}}, \tag{4.1}$$

with ε_0 and μ_0 the permittivity and permeability of free space, and Z_0 the impedance of free space. The relative permittivity, ε_{r}, and relative permeability, μ_{r}, are complex and can be written as,

$$\varepsilon_{\mathrm{r}} = \varepsilon'_{\mathrm{r}} - i\varepsilon''_{\mathrm{r}}, \qquad \mu_{\mathrm{r}} = \mu'_{\mathrm{r}} - i\mu''_{\mathrm{r}}. \tag{4.2}$$

The reflection at an interface between a material and vacuum is given by [139],

$$R = \left|\frac{1-Z}{1+Z}\right|, \tag{4.3}$$

where perfect transmission occurs when $Z = 1$, i.e. $\varepsilon_{\mathrm{r}} = \mu_{\mathrm{r}}$ [140], and partial reflectance when $Z \neq 1$. The reflectance of a wave in free space, or along a transmission line, as discussed in chapter 7, is usually described in terms of the logarithmic gain, $20\log_{10}(R)$, in decibels (dB). For a layer of material, reflectance can also occur at the second interface, particularly if the interface is with a *perfect electrical conductor* (PEC), which has 100% reflectance. In this instance, the total reflectance is then dependent upon the loss inside the material itself.

This section details methods to enhance the RF loss, either due to the dielectric or magnetic properties of the material, as well as discussing some synthetic materials, such as magnetic particles embedded within a dielectric, or the patterning of a material system on the microscale, either to produce metamaterials or to enhance the effective magnetic field of a ferromagnetic material. Although numerous reviews exist of absorbing materials [141–144], the purpose here is to highlight the tunability of magnetic thin film systems.

4.2.1 RF Absorption

Quarter Wavelength Structures

The simplest and earliest forms of absorbing materials is the Salisbury screen, which consists of a lossless dielectric as either a thickness of $\lambda/4$ on top of a PEC, or a thin sheet placed $\lambda/4$ away from a PEC, where λ is the wavelength of the incident EM radiation [145]. Part of the wave is reflected on the surface of the dielectric, and the remainder at the interface with the PEC. Destructive interference between the two reflected waves results in no net reflectance at one specific frequency. An alternative design is the Jaumann absorber, which consists of multiple lossy dielectric materials separated by $\lambda/4$ [145, 146] on top of a PEC. This has the advantage of a wider bandwidth, depending upon the number of spacings used, however the resultant structure is thick, even at microwave frequencies, for instance at 5 GHz, $\lambda/4 = 1.5$ cm. Both of these absorber designs are used to manage the electric field component of the EM wave, which is maximal at $\lambda/4$ away from the PEC, hence a lossy sheet placed here will have maximal effect [147]. The magnetic component of the EM wave however, is maximal at the surface of the PEC [148, 149], therefore magnetic absorbers can provide similar absorbative responses, for a fraction of the thickness.

Dielectric Loss

An EM wave incident upon a polarisable dielectric material can induce oscillations of the local electric dipoles [141]. This can occur with polar polymer [143] or organic bonds, such as graphene [150, 151] or in ferroelectric materials, such as TiO_3 [144, 152]. With a sufficiently high frequency, above the relaxation time, the dipoles do not have enough time to respond to the external electric field, resulting in a hysteretic response, analogous to the magnetic hysteresis detailed in previous chapters. The losses associated with the oscillation of these electric dipoles leads to the transfer of energy as heat to the surrounding material.

Magnetic Loss

As detailed in the previous chapter, at microwave frequencies, ferromagnetic materials will undergo resonant behaviour, absorbing incident RF radiation and converting it to heat in the material. The frequency and bandwidth of this resonance depends upon several material properties, to be outlined in the section 4.3. This is not the only loss mechanism in this frequency regime, similarly to dielectric loss, a time-varying magnetic field can induce eddy-currents in a metal which oppose the change

in flux [147]. Ferromagnetic resonance, however, can be tuned to a particular frequency or bandwidth, especially in thin film systems. Later results chapters detail investigations into methods to control these parameters.

RF absorbing systems based on magnetic loss suffer from the fact that magnetic materials are most commonly metals, and therefore have a high reflectance. In order to circumvent this, magnetic materials are often used as nanoscale layers, particles combined with dielectric materials, or as ferrite oxide complexes.

Frequency Selective Surfaces

Frequency selective surfaces (FSS) are a form of metamaterial, based on a periodic arrangement of patterned structures, which are able to absorb incident EM radiation. The spacing between, and shape of, the constituent metallic structures determines the capacitance and inductance of the material, and therefore the frequency of operation [142]. Incident RF energy drives the system into resonance, comparable to a RLC circuit, and is absorbed [145]. One common form of FSS are split ring resonators, a 'C-shaped' FSS where the gap determines the capacitance and frequency response [153]. Due to the sizes of the patterns, the incoming EM wavelength can be much larger than the structure itself and hence the response can be characterised with an effective capacitance and inductance. FSS only require a thin layer (depending on the skin depth and substrate permittivity) of metal, graphene [154], or water [155], making them lightweight [156], and can be made to be optically transparent while still absorbing in the microwave region [157]. Similarly to the quarter wavelength aborbers, FSS are designed to operate at a specific frequency, though a broader response can be achieved by changing the spacing between individual patterns by tapering the thickness to produce a pyramidal structure [158].

4.2.2 Synthetic Materials

Modern synthetic materials combine several of these loss mechanisms to further enhance the absorbance, and/or to increase the bandwidth over which they act. By combining dielectric and magnetic components, it is possible to tune the complex permittivity and permeability to better match to the impedance of free space. This is often achieved using pyramidal structures to produce an effective medium that does not have a sudden change of impedance due to an abrupt interface [159]. To minimise reflectance in multilayered structures, a better matched absorber has a gradual change of impedance from a free-space matched surface to subsequent layers with increasing loss [143]. The thin film deposition techniques, used in this thesis, have the ability to create multilayered structures with varying materials.

Magnetic-Dielectric Composites

One common method to produce lossy composite materials is to use a composite of rubber and a magnetic material, such as a ferrite powder [160, 161], or carbonyl iron, to form a magnetic polymer composite. The frequency response is then determined by the volume of magnetic material, and thickness of the composite material [162]. Another important parameter is the shape of the magnetic particles. By mechanically grinding spherical particles into flakes, before adding to a polymer complex, the permeability can be increased by altering the demagnetising factor and reducing eddy current losses, with the enhancement dependent upon initial particle size [163]. This increase in permeability allows for the same absorption, with thinner layers [164] and, by tuning the aspect ratio, an increase in absorption can be observed up to 18 GHz [165]. Oxidisation of ferrite flakes can better impedance match through the matching of the dielectric and magnetic properties by producing a FeOOH shell around the ferrite [166]. Treating carbonyl iron particles with hydrogen reduces the carbon and nitrogen content, producing regions of pure polycrystalline iron, which can significantly enhance the absorption properties [167].

To further increase the permeability by reducing eddy current losses, an alternative to flake-based composites are core-shell nanoparticles. The frequency response of these particles is determined by the constituent materials, and the shape of the particle itself. Carbon-coated ferrite [168] and nickel [169] particles were observed to have an increased loss at 6 GHz, while increasing the number of layers in an onion-like structure of ferrite/tin-oxide yolk-shell microspheres, was shown to lead to a large decrease in reflectance [170]. Compared to solid particles, the dielectric loss in hollow graphene oxide-ferrite bowl-shaped structures was significantly enhanced over a broad range from 2 to 18 GHz [171]. A carbon-ferrite nano-ring, behaving as a nano-antenna, was also shown to have enhanced absorption over a similar range [172]. Embedding ferrite particles in disordered graphene [173] or carbon nanotubes [174] has also been shown to reduce the specular reflection.

An additional method to impedance match by tuning the relative permittivity and permeability of a composite material is to incorporate ferroelectric materials with ferromagnetic materials. Ferroelectric materials, such as titanate compounds ($ZrTiO_3$, $BaTiO_3$, $CaCu_3Ti_4O_{12}$), have a net polarised electric moment, analogous to the magnetic moment in ferromagnets, and hence have a colossal static dielectric constant [175], which remains much larger than for other materials into the GHz region [176, 177]. Coated particles of $BaTiO_3$ with carbonyl iron, and NiCo alloys displayed enhanced loss due to better matching up to 16 GHz [178], with a similar behaviour observed for ferrites with $BaTiO_3$ [179] and $CaCu_3Ti_4O_{12}$ [152] embedded in a polymer based epoxy.

Magnetic Frequency Selective Surfaces

Magnetic materials can also be paired with frequency selective surfaces to provide additional loss mechanisms. Creating a patterned copper metamaterial on top of carbonyl iron was shown to increase the bandwidth and the absorption of the material [180, 181], while the bandwidth of a FSS was shown to increase by a third with the addition of a 200 nm FeCoB thin film, with a minimal increase in the overall thickness and weight [182]. A FSS structure based on carbonyl iron with a tapered pyramidal structure was also reported showing high reflection loss up to 40 GHz [159]

Effective Magnetic Fields

Synthetic absorbing materials based on flakes of magnetic material display high loss at a range of frequencies. However, this is not without disadvantages, with most composite materials referenced here requiring several millimetres of thickness to achieve high absorption, while the mechanical and chemical processes that produce flakes of magnetic material do not necessarily produce materials with a precise degree of control over important material parameters, such as the complex permittivity and permeability.

Magnetic thin film systems intrinsically have a high degree of control over material parameters, through layer material choice, and high accuracy over the thickness and size of individual layers, which determine the high frequency response, due to available growth and structural characterisation techniques, as detailed in the next chapter.

A common method to control the resonant frequency of a magnetic thin film, is through creating an effective magnetic field, as outlined in the previous chapter and the next section. An effective magnetic field can be generated through exchange bias, where an antiferromagnet pins the direction of the ferromagnetic moment. As this is an an interfacial effect, the magnitude of the field generated has a 1/t relation to the thickness, t, of the ferromagnetic layer. By combining multiple thicknesses of ferromagnetic material, varying effective magnetic fields can be produced. This was shown in a multilayer of ferromagnetic (NiFe,CoFe) and antiferromagnetic (IrMn,FeMn) layers to produce a broadband frequency response [19].

Introducing a shape anisotropy through patterning results in an effective magnetic field which depends upon the aspect ratio and the saturation magnetisation of the material. Arrays of stripes of permalloy ($Ni_{80}Fe_{20}$) [20, 183, 184], FeCoN [185], FeCoBSi [186], and modulated NiFe-FeCoB [187] all show a high degree of control of the resonant frequency dependent upon the aspect ratio of the stripes, with the

increase in effective magnetic field raising the resonant frequency from 1 GHz up to 10 GHz with microscale patterning [20]. These patterned stripe arrays have a strong angular dependence [188], and display a resonant behaviour as long as a component of the effective magnetic field is perpendicular to the magnetic field vector of the incident EM wave. Hence, varying the angle of EM incidence with respect to the material plane will produce a resonant response. Rotating the material in-plane however, will produce a sinusoidal behaviour, where no resonant behaviour will be observed when the effective magnetic field and the magnetic vector of the EM wave are parallel. In order to overcome this, shapes of different orientation must be used, this is addressed in chapter 10.

In this thesis, the focus is on utilising the high degree of control of thin film systems to study the underlying physics which produces the materials resonant behaviour, in order to better understand how to manipulate parameters of interest that determine how suitable a material is for RF applications. It is therefore of interest to model such systems, to observe the effects of varying material parameters.

4.3 Modelling Dynamic Behaviour

Various methods exist to model magnetic structures, ranging from first principles calculations using density functional theory, to micromagnetics in which the LLG equation is solved for a lattice of spins with given material parameters. In this thesis, of primary interest is the reflectance and transmission of RF energy incident upon a magnetic material. This section details a model presented by Wallace [81], based on wave transmission theory, in which the reflectance of a sample is determined by the wave impedance, with the permeability derived from the LLG equation. By varying material parameters, the change in reflectance can be simulated in either the frequency or field domains. This model has been extended in this work to account for spin pumping effects as detailed in the previous chapter.

4.3.1 Impedance of Layered Structures

The measured reflectance of RF electromagnetic waves from a material is determined by two factors; the change of impedance at an interface, and the loss within the material itself. For a single material on top of a PEC, with an impedance of zero (perfect reflectance), the wave impedance is given by [139],

$$Z^{\mathrm{W}} = \sqrt{\frac{\mu_{\mathrm{r}}}{\varepsilon_{\mathrm{r}}}} \tanh\left(\frac{2\pi t f}{c}\sqrt{\mu_{\mathrm{r}}\varepsilon_{\mathrm{r}}}\right), \tag{4.4}$$

with ε_r and μ_r the relative permittivity and permeability, f the frequency, c the speed of light and t the thickness of the material. For a multilayered structure, comprised of N layers, the wave impedance for the ith layer from transmission line theory is [139],

$$Z_i^{\mathrm{W}} = Z_i^{\mathrm{Ch}} \frac{Z_{i-1}^{\mathrm{W}} + Z_i^{\mathrm{Ch}} \tanh(arg_i)}{Z_i^{\mathrm{Ch}} + Z_{i-1}^{\mathrm{W}} \tanh(arg_i)}, \tag{4.5}$$

where i denotes the layer index, and the bottom PEC layer has impedance $Z_{i=0} = 0$. The characteristic impedance of each layer Z_i^{Ch} is,

$$Z_i^{\mathrm{Ch}} = \sqrt{\frac{\mu_i}{\varepsilon_i}}, \tag{4.6}$$

and,

$$arg_i = \frac{2\pi t_i f}{c} \sqrt{\mu_i \varepsilon_i}, \tag{4.7}$$

with all terms as defined. The reflectance from the top layer, $i = N$, can be calculated with,

$$R = \left| \frac{1 - Z_N^{\mathrm{W}}}{1 + Z_N^{\mathrm{W}}} \right|, \tag{4.8}$$

with the measured reflectance in terms of a gain given by $S_{11} = 20 \log_{10}(R)$, where S_{11} is a parameter denoting the reflectance measured at the source of the RF. A further discussion of S-parameters is given in chapter 7. A simplified equation 4.5 can be written as,

$$x_i = a \frac{x_{i-1} + ab}{a + x_{i-1} b} \tag{4.9}$$

with $x_{i=0} = 0$ as above. This expression tends to a (Z^{Ch}) at a rate determined by b, ($\tanh(arg)$), i.e. the expression converges faster for thicker films, or those with a larger $\sqrt{\mu\epsilon}$. Reflectance is therefore minimised when $Z^{\mathrm{Ch}} = 1$, which occurs when $\mu_r = \varepsilon_r$, which is why dielectric-magnetic composites, particularly those with large permittivities, such as titanates, when combined with large permeability materials display enhanced RF properties, as detailed in the previous section.

In the model developed by Wallace, the permeability of a magnetic layer, derived from the LLG equation, is given as [81],

$$\mu_r = 1 + \frac{M^2}{MH - \left(\frac{2\pi f}{\gamma}\right)^2 + i\alpha M \left(\frac{2\pi f}{\gamma}\right)}, \tag{4.10}$$

with M the saturation magnetisation, H the effective magnetic field, γ the gyromagnetic ratio, and α the Gilbert damping parameter, all of which were described in the previous chapter. For a non-magnetic layer $\mu_r = 1$. Figure 4.1a shows the

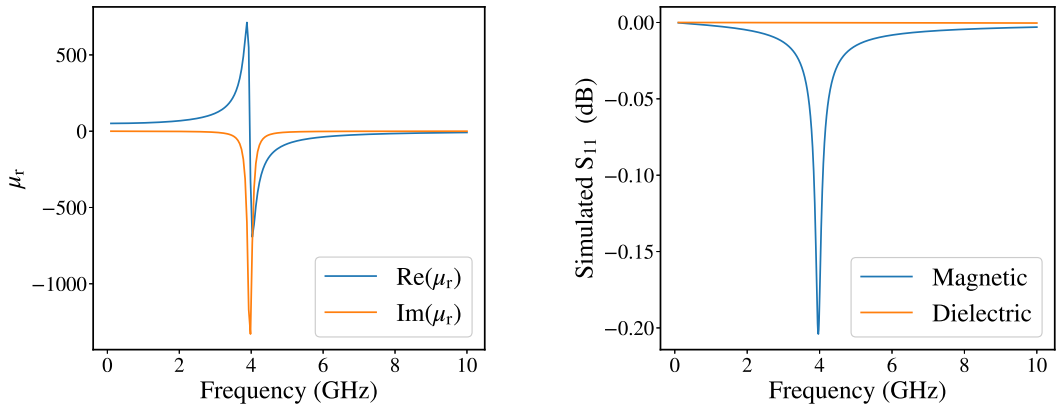

(a) (b)

Figure 4.1: (a) Evaluation of the frequency dependence of the permeability, using equation 4.10, for a typical NiFe alloy, with $H = 200$ Oe, $\alpha = 0.005$, and $4\pi M = 10$ kG. (b) The reflectance of the alloy, using equation 4.8, as a function of frequency, with the separated magnetic and dielectric components. On this graph 0 dB represents perfect reflectance.

rapid variation of both the real and imaginary parts of the relative permeability at resonance for a typical magnetic thin film.

For an insulating non-magnetic material, such as SiO_2, the permittivity can be assumed to be constant within the frequency range used in this thesis [189, 190] when compared to the changes in magnetic permeability at resonance. The relative permittivity can therefore be expressed as,

$$\varepsilon_r = \varepsilon_r' \left(1 + i \tan \delta\right), \tag{4.11}$$

where $\tan \delta = \frac{\varepsilon_r''}{\varepsilon_r'}$ is the loss tangent, the ratio of the loss of the electric part of the EM radiation compared to the lossless component. Metals, however, have free charge carriers and can react to oppose a varying electric field up to the plasma frequency, which is typically $\approx 10^{15}$ Hz for transition metals. The frequency dependence of the metallic permittivity can be expressed as,

$$\varepsilon_r(\omega) = 1 + \frac{i\sigma(\omega)}{\varepsilon_0 \omega}, \tag{4.12}$$

with ε_0 the permittivity of free space, and the frequency dependent conductivity,

$$\sigma(\omega) = \frac{\sigma_0}{1 - i\omega\tau}, \tag{4.13}$$

where σ_0 is the DC conductivity. The relaxation time, τ can also be expressed in

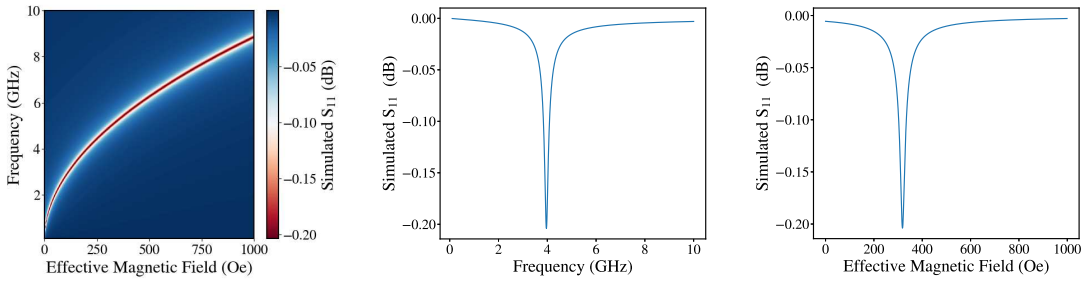

Figure 4.2: Simulated heatmap of the reflectance of a 100 nm NiFe alloy as a function of both applied magnetic field and frequency with $\alpha = 0.005$, and $4\pi M = 10$ kG, with field and frequency cuts. The maximum absorption (red line) occurs due to ferromagnetic resonance.

terms of the plasma frequency,

$$\tau = \frac{\sigma_0}{\varepsilon_0 \omega_p^2}. \tag{4.14}$$

For metals, the variation of the relative permittivity at the frequencies of interest in this thesis using these relations, is much smaller than the permeability changes due to ferromagnetic resonance, as shown in figure 4.1b, and hence can be ignored.

4.3.2 Varying Material Parameters

The model described here allows for changes to the reflectance profile, by varying the material parameters in the simulations in terms of either incident RF frequency or effective magnetic field. Typical ferromagnetic resonance experiments, as discussed in chapter 7, measure the absorption of RF energy as a function of either applied magnetic field, or RF frequency, in order to excite ferromagnetic resonance (FMR), and determine parameters of interest.

Using the equations described, the variation of the resonance in terms of frequency and magnetic field for a typical magnetic alloy used for RF applications, $Ni_{80}Fe_{20}$, can be seen in figure 4.2. Maximum absorption is achieved when the resonance condition is met, which is a function of both the magnetic field and the frequency, producing the typical square root relation in the Kittel equation. For a fixed magnetic field or frequency, the width of the region of maximum absorption increases as a function of the alternate parameter, as detailed in the previous chapter, where the magnetic field linewidth ΔH was shown to be a function of frequency.

The effect of varying the magnetic damping on the simulated reflectance, while keeping other parameters, such as thickness, fixed, can be seen as a function of frequency in figure 4.3a, and magnetic field in figure 4.3b. Increasing the Gilbert damping significantly reduces the peak RF loss, however, as highlighted in the in-

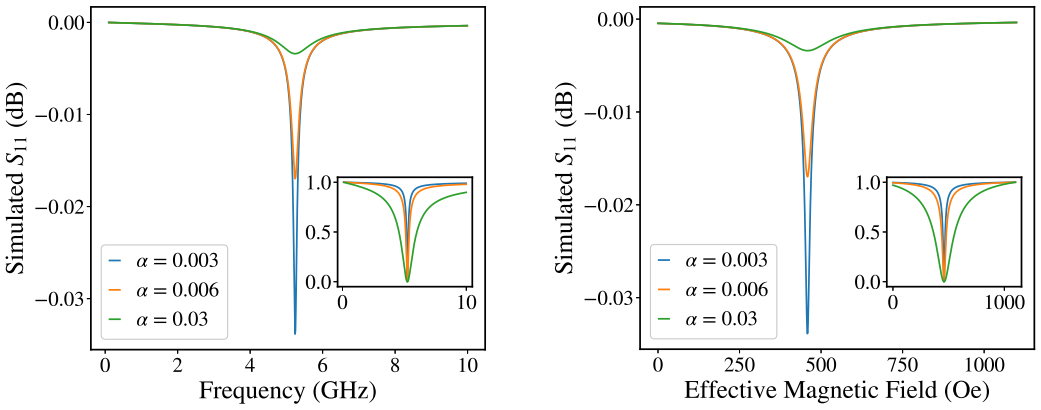

(a) (b)

Figure 4.3: (a) Simulated reflectance spectra as a function of frequency and (b) magnetic field, for a material with different Gilbert damping constants. Inset are the normalised reflectance to highlight the increase in linewidth.

set, this is accompanied by a large increase of the absorption bandwidth in both the frequency and magnetic field domains. In real thin films, the Gilbert damping is a material dependent parameter, which is difficult to reduce, but can be enhanced through various techniques, such as doping a ferromagnetic alloy with another transition metal [99]. The material parameters of interest, however, are interlinked, for example, altering the damping in this way through doping will also reduce the saturation magnetisation.

The variation of the reflectance as a function of frequency for a single layer of magnetic material is shown in figure 4.4 for three different, and realistic, saturation magnetisation values. As expected from the Kittel formula, increasing the saturation magnetisation increases the resonant frequency, for a fixed effective magnetic field. The bandwidth and maximum loss are also shown to increase, as the imaginary part of the complex permeability also depends on the saturation magnetisation, as detailed in equation 4.10.

The reflectance profiles of a synthetic material system composed of these layers stacked in a trilayer structure are shown in figure 4.5. The individual responses of each layer blend together to give a more broadband response at low magnetic field values, and separate into more distinct resonance peaks at higher magnetic fields. The damping is constant for all three layers, however, although an increase in damping would reduce the maximum absorption for a given thickness, it would merge the resonances and prevent the response from separating into such distinct absorption peaks. The physics governing the increase in damping in multilayered structures is a subject of later results chapters.

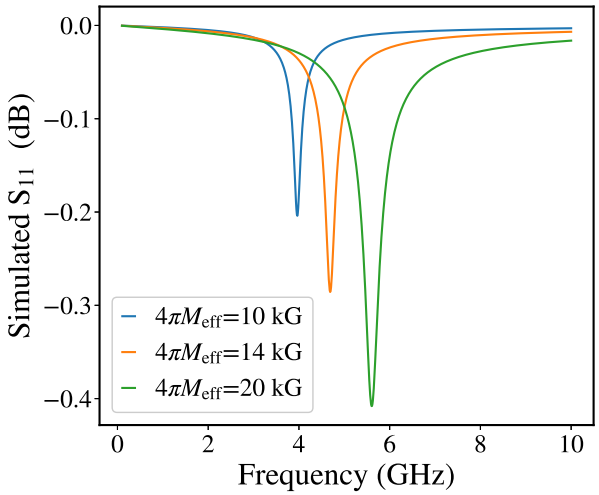

Figure 4.4: Simulated reflectance for a single 100 nm layer of magnetic material as a function of frequency, for three saturation magnetisation values, 10kG ($Ni_{80}Fe_{20}$), 14kG ($Co_{40}Fe_{40}B_{20}$) and 20kG ($Co_{50}Fe_{50}$), with $H = 200$ Oe.

Increasing the damping in a multilayered structure consisting of several saturation magnetisation values is not the only method to produce a broadband response solely from a magnetic thin film system. An alternative way is to produce many

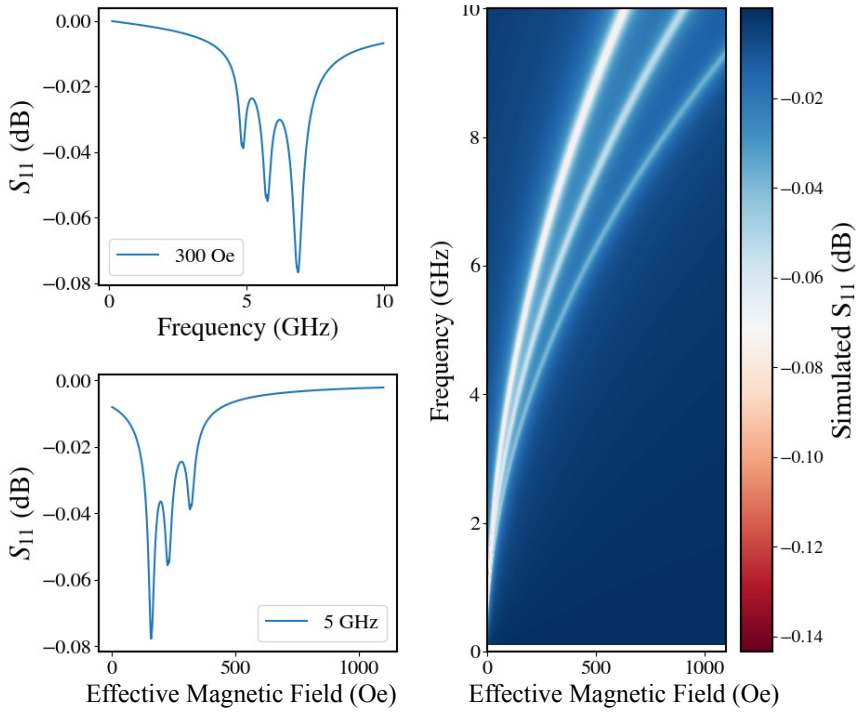

Figure 4.5: Simulated reflectance profiles for a magnetic trilayer structure, where each layer has a different saturation magnetisation, with the values the same as figure 4.4.

effective magnetic fields. Figures 4.6a and 4.6b show the reflectance profile for a multilayered system with 5 and 25 different effective magnetic fields respectively between 50 and 500 Oe. It can be seen clearly that increasing the number of effective magnetic field resonant components produces a more broader band absorption response. The creation of an isotropic broadband response using effective magnetic fields induced through microscale patterning, would therefore require patterned structures with both a range of angles and varying aspect ratios. The results of this are detailed further in chapter 10.

4.3.3 Inclusion of Interfaces into the Wallace Model

While the model proposed by Wallace provides a useful tool to model the reflectance of layered structures as a function of either magnetic field or frequency, it does not account for important interfacial effects as discussed in the previous chapter. One particular phenomena of interest in this thesis is the enhancement of damping due to an interface between a ferromagnetic and non-magnetic material. Spin pumping significantly enhances the damping under certain conditions, as shown in figure 4.7.

Spin pumping can be accounted for in a multilayer simulation, by inserting metallic non-magnetic layers (Pt) with a set of parameters (e.g. spin diffusion lengths), such that the simulation, when calculating the impedance for ferromagnetic layers, checks for adjacent layers which allow spin pumping. These layers do not contribute to the magnetic response. Where applicable, the given damping for the ferromagnetic layer is then enhanced using the equations introduced and is described in

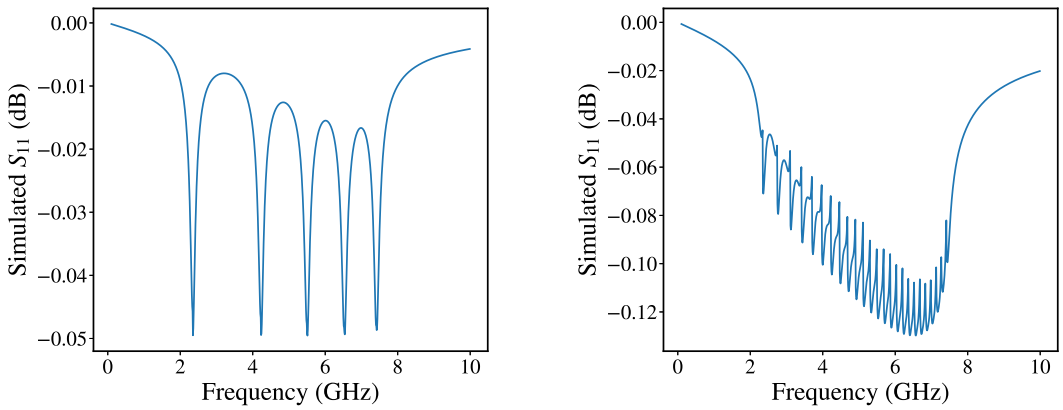

(a) (b)

Figure 4.6: Simulated reflectance profiles as a function of frequency for a system with (a) 5 and (b) 25 layers each with a different effective magnetic field between 50 and 500 Oe, with each layer 10 nm of $Co_{40}Fe_{40}B_{20}$ ($M_s = 14$ kG, $\alpha = 0.003$).

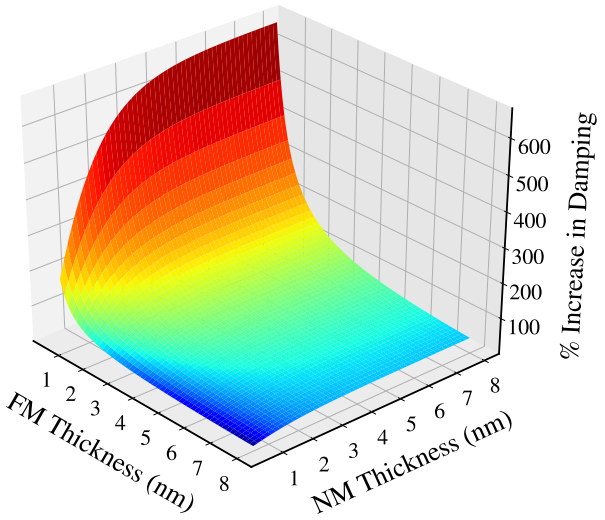

Figure 4.7: Calculated percentage increase in damping due to interfacial effects between a ferromagnetic and non-magnetic layer, with parameters from [109, 110].

chapter 3,

$$\Delta\alpha = \frac{\gamma\hbar}{4\pi M_s t} g_{\text{eff}}^{\uparrow\downarrow}, \tag{4.15}$$

where

$$g_{\text{eff}}^{\uparrow\downarrow} = \frac{g_{\infty}^{\uparrow\downarrow}\sqrt{\epsilon}}{\sqrt{\epsilon} + \coth\left(\frac{L}{\lambda_{\text{sf}}}\right)}, \tag{4.16}$$

with ferromagnetic thickness, t, non-magnetic thickness, L, and all terms as defined previously. The permeability and impedance of the layer, and subsequently the reflectance, are therefore altered.

As this enhancement is associated with interfacial contact to a non-magnetic layer, this enhancement becomes more pronounced for ultrathin ferromagnetic films. Figures 4.8a and 4.8b show the effect of turning spin pumping 'off' and 'on', in a multilayer stack, consisting of FM/HM sublayers, where the total thickness is constant. For the case with no spin pumping, there is no difference between one large layer compared to multiple individual ones. When spin pumping is allowed, the linewidth increases as the ferromagnetic thickness is reduced, as can be seen clearer in the inset.

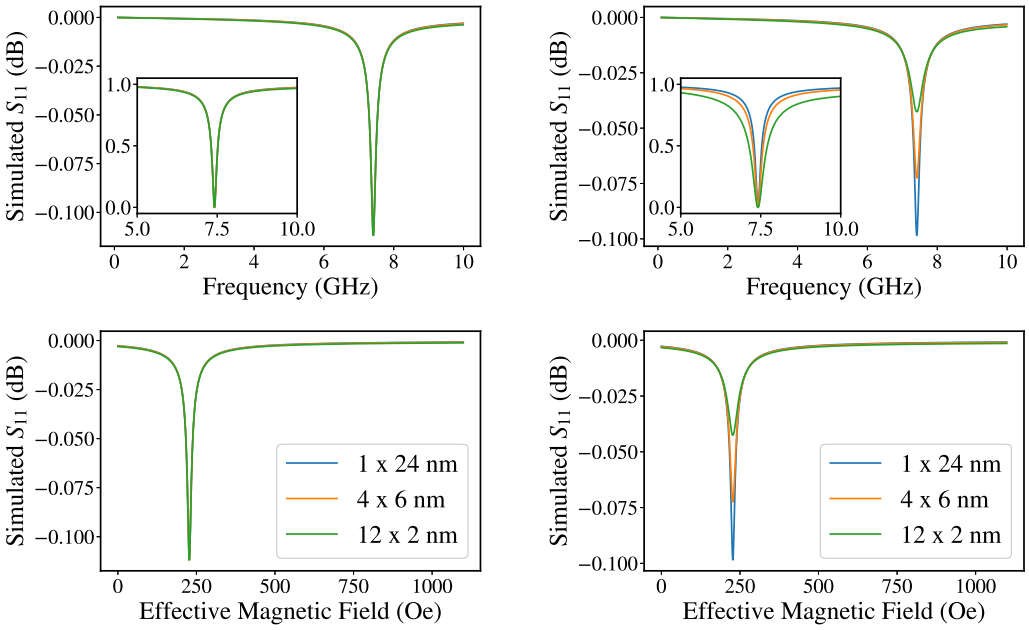

(a) (b)

Figure 4.8: Simulated reflectance profiles as a function of both field and frequency for (a) a multilayer system without interfacial damping enhancement and (b) with interfacial damping. Insets show the normalised spectra in the frequency domain, highlighting the increase in bandwidth.

4.4 Summary

In conclusion, this chapter detailed the underlying physics and mathematical descriptions which determine the reflectance of magnetic layered materials. A short review of existing magnetic materials for RF applications was then presented, highlighting the broad range of systems investigated in the literature. A model based on impedances developed by Wallace was used to explore a variety of frequency responses resulting from the control of thin-film properties. This model was further developed to account for the enhancement of damping due to spin pumping.

The simulations here provide insight into which parameters contribute to controlling the dynamic response, as well as the interplay between them. This insight forms the basis of the later results chapters, which examine methods to manipulate magnetic damping and the effective magnetic fields, to control and enhance isotropic absorption.

Chapter 5

Growth, Patterning and Structural Analysis

5.1 Introduction

This chapter presents the experimental techniques and procedures used to fabricate, pattern and structurally characterise the thin film magnetic systems developed and studied in this work. All samples used within this thesis were grown using magnetron sputtering in a high vacuum deposition chamber. The various film growth modes as well as the details of this deposition technique are discussed first. A brief description then follows of the lithographic procedures, specifically photolithography, used to pattern thin film systems within a cleanroom environment. Finally, X-ray Reflectivity (XRR), a non destructive technique using grazing incidence x-rays is introduced. This technique allows for the determination of structural information regarding layers and interfaces within a multilayered thin film structure by fitting the data to a model system, the fitting procedure is also discussed.

5.2 Thin Film Deposition

This section covers the thin film deposition process, from wafer preparation, through the details of the controlled process by which nanoscale layers are deposited, to the thin-film growth modes and the material crystal structures that are formed on the substrate.

5.2.1 Sample Preparation

All samples studied in this thesis were grown on single crystal silicon wafers with approximately 100 nm of thermally grown SiO_2 on the surface. For samples grown in Durham, the substrates were first cut to roughly 12 × 12 mm using a diamond tipped scribe, in order to be compatible with the measurement techniques detailed in later chapters. However, the compositional wedge samples grown at the Institute for Molecular Physics, Polish Academy of Sciences (IFMPAN) in Poznań were deposited on substrates that were approximately 10 × 20 mm, in order to produce a film thickness wedge over a larger length scale. While the SiO_2 layer on the substrate provides a surface with nanoscale roughness, the wafers required cleaning once cut to remove any organic materials and silicon debris. This was particularly important where lithographic patterning is concerned, as the feature sizes are often comparable to debris material on the surface. In Durham, substrates were cleaned by first agitating in acetone with an ultrasonic bath for two minutes, before repeating the process with isopropanol to remove any residual acetone. Finally, samples were dried with a N_2 gas gun before being transferred to a storage box, for deposition or further processing for lithographic patterning.

5.2.2 Magnetron Sputtering

Sputtering refers to a vapour phase deposition process by which material is removed from a target by bombardment with charged ions from a plasma. The atoms ejected from the target traverse through a vacuum before condensing onto surfaces including substrates located nearby. This process has widespread use in a variety of industries, from semiconductor fabrication to window coatings, due to the capacity for large scale areas to be coated, the ability to create high quality multi-layered film structures and the ability to deposit alloys through simultaneous sputtering from multiple targets, a process referred to as co-sputtering. The rate of deposition is dependent upon multiple factors, such as the working gas pressure, the power supplied to the target and both the angle and distance of the target with respect to the substrate.

An outline of this process can be seen in figure 5.1. For all sputtering used in this thesis, argon was used as the working gas. Ar is a common process gas as it is large enough to transfer sufficient momentum to eject atoms from the target, and small enough that it only transfers this to a single atom [191]. Another advantage of Ar is that it is inert, and thus does not react with the target material, though a process, known as reactive sputtering, can be useful in industry and academia to produce oxide films with O_2 as the working gas.

A negative electrical bias is applied to the target. This produces a localised strong electric field which ionises the working gas, resulting in a characteristically purple plasma of Ar^+ ions. These positive ions accelerate towards the negatively charged target resulting in the transfer of momentum to the target. Secondary electrons produced in this process also aid the stability of the plasma by ionising additional Ar atoms. While early sputter deposition processes were based on this mechanism, they suffered from the need for high working gas pressures to maintain a stable plasma [192], as a low pressure reduces the number of secondary electrons reducing the production of Ar ions, and hence the stability of the plasma. A high working pressure in turn results in low deposition rates as the ejected atoms from the target scatter due to multiple collisions with the sputtering gas. In order to overcome this, an improved technique known as magnetron sputtering was developed [193].

Magnetron sputtering utilises a magnetic field from two rings of permanent magnets arranged with opposite polarity to constrain the secondary electrons. A schematic of this setup is also shown in figure 5.1. The resultant permanent magnetic field is mostly parallel to the target and perpendicular to the electric field, this

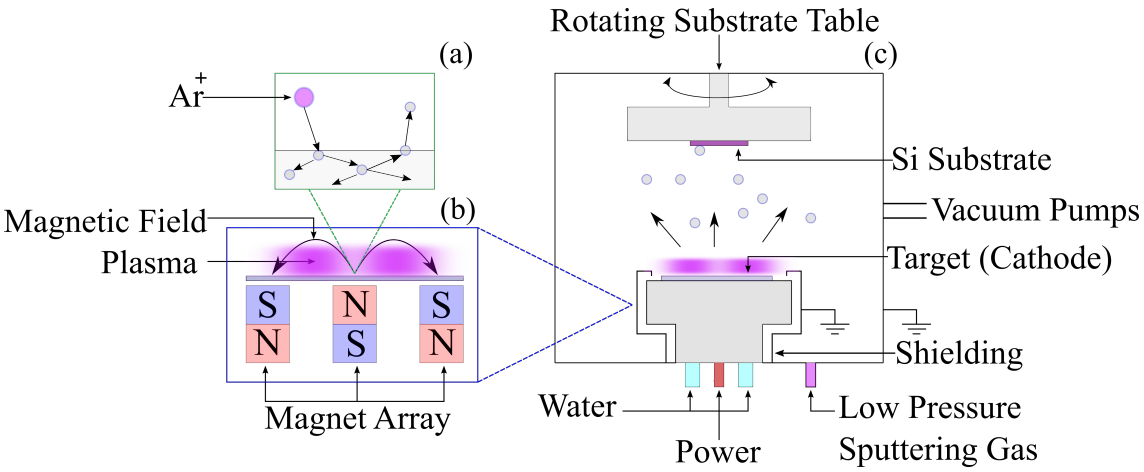

Figure 5.1: A schematic of the typical setup used for magnetron sputtering. (a): The transfer of momentum from an Ar^+ ion to a target material, resulting in target atoms being ejected. (b): The magnetic field arrangement used to confine the Ar plasma that defines magnetron sputtering. (c): Whole vacuum system arrangement for magnetron sputtering with target and rotating substrate table shown.

confines the secondary electrons in an epicyclic path due to the Lorentz force, leading to an enhanced rate of sputtering in this region and the formation of a characteristic *racetrack* due to the increased erosion of the target in this area. The confinement of the plasma close to the target, by the magnetic field, and the close proximity of an earthed shield around the target allows for the use of a lower working gas pressure.

While the process described above works perfectly well with a DC bias of the order of 400 V applied to the target for electrically conductive materials, it is unsuitable for insulating materials as the target would quickly build up positive charge from the Ar^+ ions, preventing further sputtering interactions from occurring. In this instance an alternating current source at RF frequencies is typically used. This alternates the voltage polarity of the target at a typical frequency of 13.56 MHz, which is sufficient to prevent Ar ions from sputtering the substrate during the period when the polarity is reversed, and allows the charge built up to dissipate. Using either DC or RF power sources heats the target material up, therefore cooling water to the target is a requirement.

The deposition system used for all samples fabricated in Durham was a Mantis QPrep500, a picture of which is shown in figure 5.2. The system features load lock and main chambers, separated by a gate valve, allowing for the loading of samples without the need to vent the main chamber, allowing a stable base pressure of 10^{-8} Torr in the main chamber. Samples are transferred between the two chambers through the use of a vacuum transfer arm. Both chambers are connected to individual rotary pumps, which pump the chambers from atmosphere down to 10 Torr, after which double turbo pumps on the main chamber, and a single turbo pump on the loadlock pump the chambers down to base pressure. A gas analyser allows for the detection of a suitable vacuum, and detects the presence of oxygen or other residual gases. The load lock chamber features a sample carousel, from which up to 5 sample plates can be mounted.

Figure 5.2 also shows an image of one of the targets ignited, from which the characteristic racetrack can be seen as a brighter ring. The system has five targets, each with its own shutter, which is closed when not in use to prevent cross contamination of targets. A quartz crystal microbalance (QCM) allows for monitoring of the deposition rate, this was calibrated using x-ray reflectivity. The substrate shutter allows the plasma to be ignited, the target surface to be sputter cleaned, and the desired deposition rate to be achieved by varying the gas pressure (typically 1 mTorr), or more commonly the power to the target, before beginning to deposit material onto the substrate. This is particularly useful with a new metallic target, where there is likely to be an oxide layer on the target surface. The sample substrates are rotated at 20 rpm during deposition to improve the uniformity of deposition coverage and

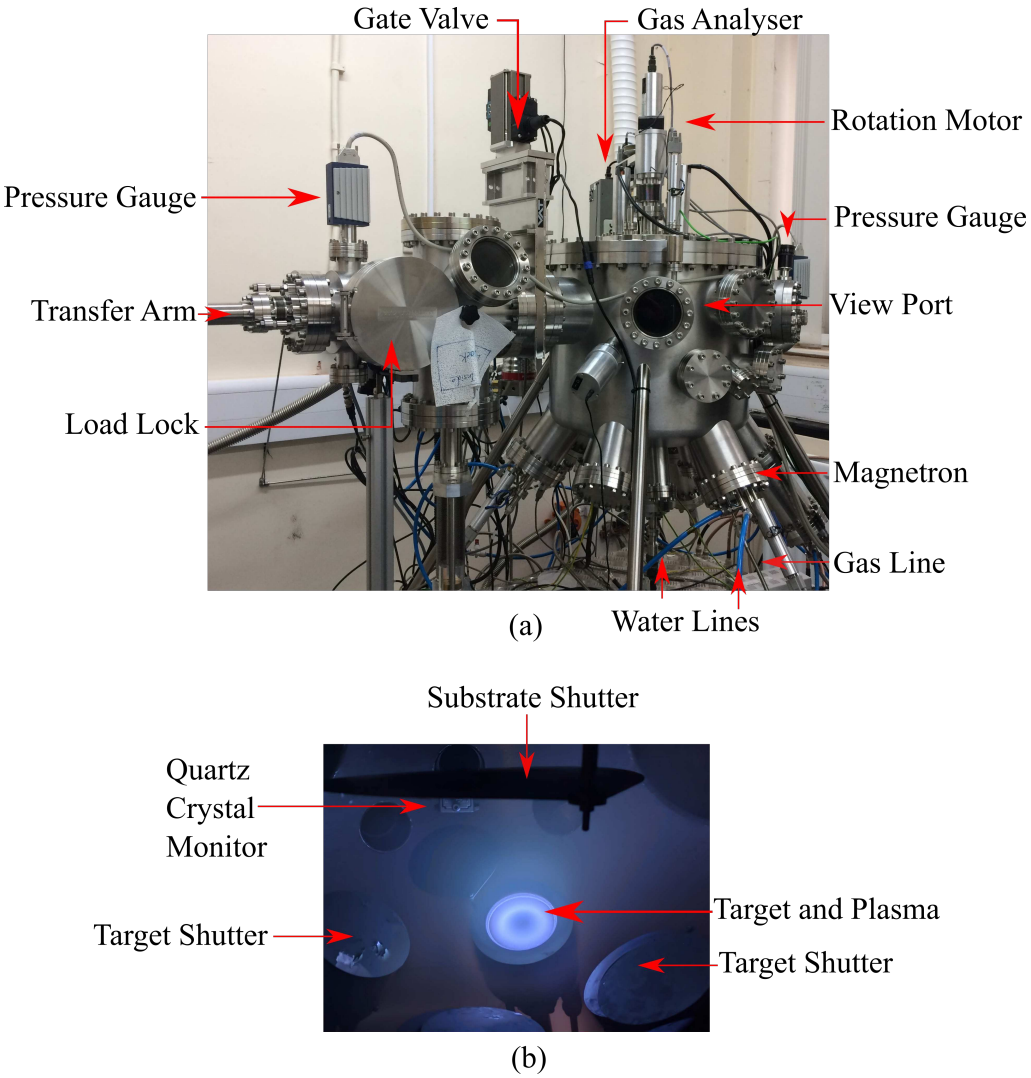

Figure 5.2: (a): The Mantis QPrep500 sputter system used to grow most of the samples in this work. (b): Image of sputter target with plasma ignited inside the main sputter chamber and with source shutter open. The bright ring visible is the magnetron racetrack.

to lessen any potential induced anisotropies from the static magnetic fields of the magnetrons, or due to oblique incidence flux of the target atoms.

The five magnetron sources are powered with either a RF power supply or one of two DC supplies, all of which are interlocked to the water supply, transfer arm, and system pressure. Both DC, or one DC and one RF supply can be active at the same time, allowing for deposition from multiple targets in order to create alloyed materials. This technique was used to fabricate the rare earth - transition metal ferrimagnets studied in subsequent chapters. The deposition rate for each individual target, calculated using the QCM, provides an estimate of the alloy composition which was verified ex-situ using energy dispersive x-ray spectroscopy.

The film thickness wedges grown at the IFMPAN were achieved by gradually

opening a shutter inside the deposition chamber to create a thicker material on one side of the substrate. For all materials grown in Durham, the DC current was in the region of 75 to 100 mA and the RF power 50 - 75 W, giving deposition rates between 0.1 and 0.2 Å/s. These low deposition rates allow for controlled growth of nanoscale layers, the mechanisms of which are detailed below.

5.2.3 Thin Film Growth Modes

The formation of nanoscale thin films is governed by the surface energies of the substrate and the target materials adsorbing onto the surface, and of the target atom-atom binding energies. Figure 5.3 illustrates the three main growth modes that occur. If the atom-substrate energy dominates over the atom-atom, epitaxial layer by layer growth, known as Frank-van der Merwe growth [194], occurs. The other extreme is where atom-atom bonding dominates, in which case the thin film minimises the free energy by the formation of islands, which is termed Volmer-Weber growth [195]. Finally, Stranski-Krastanov [196] growth refers to the process which starts off as monoloayer growth, but favours island formation above a threshold thickness due to strain [57]. The growth of these layers, if done epitaxially and at higher temperatures, leads to the formation of large grains with the same repeating sub unit, and crystalline structure.

5.2.4 The Structure of Materials

A crystalline structure is formed when a sub-unit known as a *unit cell* repeats to form a lattice structure [30, 197]. Although there are fourteen Bravais lattice structures [198], the three main metallic unit cells relevant to this thesis are the body-centred cubic (BCC), face-centred cubic (FCC) and hexagonally close packed

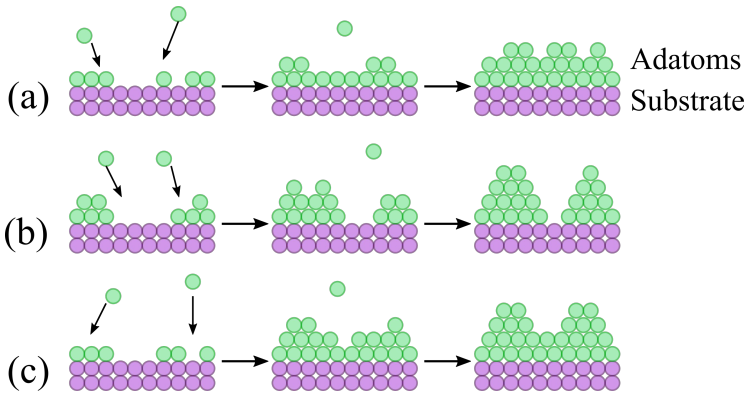

Figure 5.3: Illustration of the 3 main growth modes associated with thin film deposition: (a) Frank-van der Merwe, (b) Volmer-Weber and (c) Stranski-Krastanov.

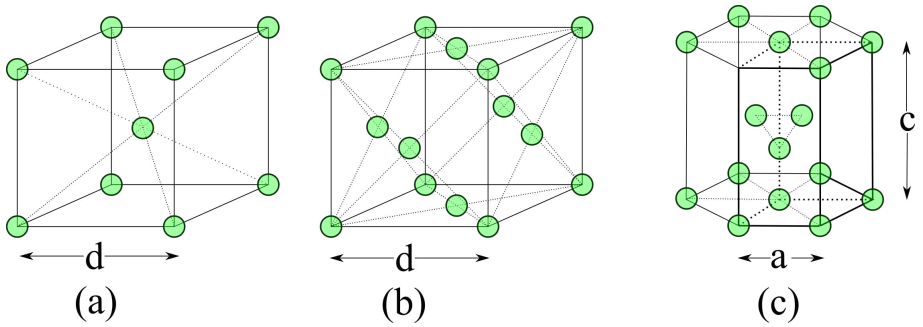

Figure 5.4: Unit cells of common metallic crystal structures [30]: (a) body-centred cubic (BCC), e.g. Fe, (b) face-centred cubic (FCC), e.g. Ni and (c) hexagonally closed packed (HCP), e.g. bulk Co [199].

(HCP). Figure 5.4 illustrates the unit cells of each of these systems. For BCC and FCC structures, each lattice point is separated by a lattice parameter, d, whereas for HCP, the separation occurs by a distance a in one direction and c in another.

The main difference in structure between FCC and HCP is related to the stacking of each monolayer on top of each other. Figure 5.5 illustrates this different stacking. For a bilayer of spheres there exists both tetragonal and octahedral voids. If the third monolayer lies in the tetrahedral void, the third and first layers align, forming an AB AB repeating layer structure. This forms an HCP structure. If the third layer lies in the octahedral void, then an ABC ABC repeating structure is formed, characteristic of FCC.

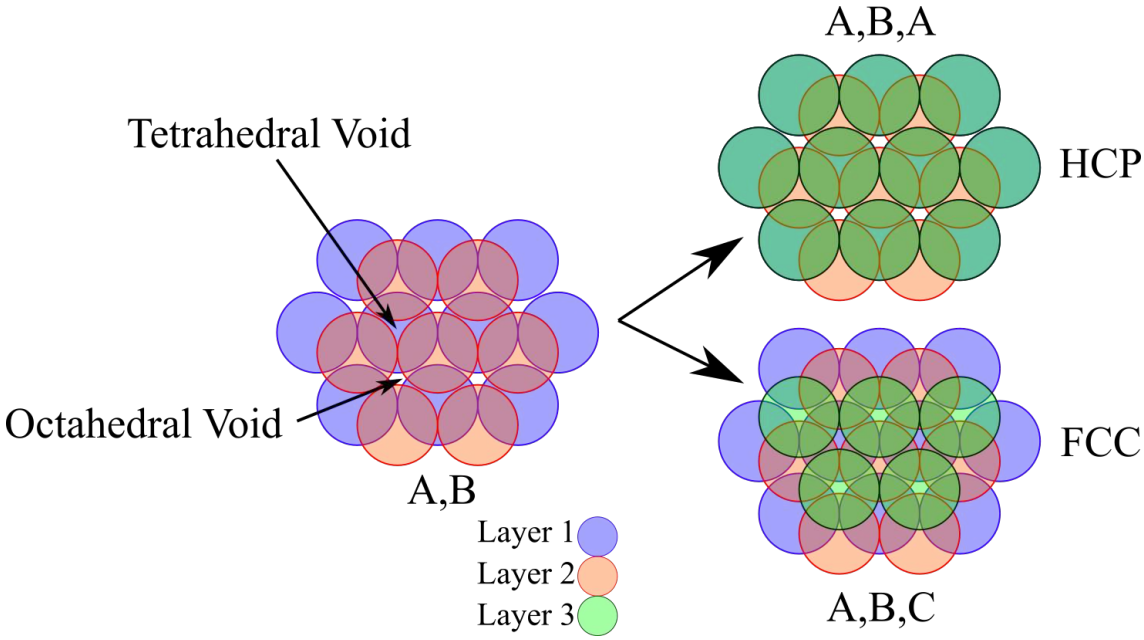

Figure 5.5: Growth modes with close packed spheres. The addition of a layer on top of a tetrahedral void leads to ABA stacking typical of HCP, while the addition of a layer onto an octahedral void leads to ABC stacking typical of FCC structures.

5.3 Patterning Microscale Structures

This section details the processes used to pattern thin film materials in order to introduce the in-plane shape anisotropy. Lithographic methods can be broadly summarised into two categories: *Bottom-up*, in which short range interactions between constituent elements lead to large scale self-assembly, and *top-down*, in which patterns are etched directly into large scale structures. While other techniques exist in both academia and industry for large scale patterning, such as nano imprint lithography, the focus here is on positive tone photolithography, a *top-down* process, used here due to the ease of designing and producing masks and the simple processes required for pattern transfer.

5.3.1 Photolithography

Optical lithographic methods rely on the interaction between UV light and an organic polymer sensitive to UV wavelengths, known as a photoresist. They can also be split into two categories; *positive tone photolithography*, where the polymer bonds break upon UV exposure reducing the polymer chain length and increasing the solubility of the polymer, and *negative tone photolithography*, where the polymers are cross linked by UV exposure, and become resistant to solvent. For positive tone photolithography, the exposed areas of the polymer become the location of the final features in a process known as *deposition and lift-off*, whereas for negative tone photolithography material structures form in areas of unexposed resist. The feature size achievable using these methods, following the optimisation of the procedure, is limited by both the wavelength of the UV light, and the resolution of the mask. Although methods do exist to increase the resolution by utilising destructive interference of the UV light though the use of a phase shift plate [200, 201].

The basic procedure for positive tone photolithography used in this thesis is shown in figure 5.6. A photo-resist [202] is first coated onto a substrate using a spin coater, giving a uniform resist thickness on the order of a few micrometers, before baking for a set time to remove solvents. A mask aligner, here an EVG 620, was used to align the mask with the substrate. Details of the mask are discussed below. While various modes are available, typically the mask is either in *hard contact*, in which a force is applied to push the substrate and mask together, or *soft contact*, in which there is direct contact, but without the high force, leading to longer lifetimes of the mask, at the potential expense of the resolution of features.

Following UV exposure in the mask aligner, for positive tone lithography, the samples were then developed in solution [203] for a set time to dissolve the exposed areas of photoresist. Too short an exposure time will leave partially exposed resist

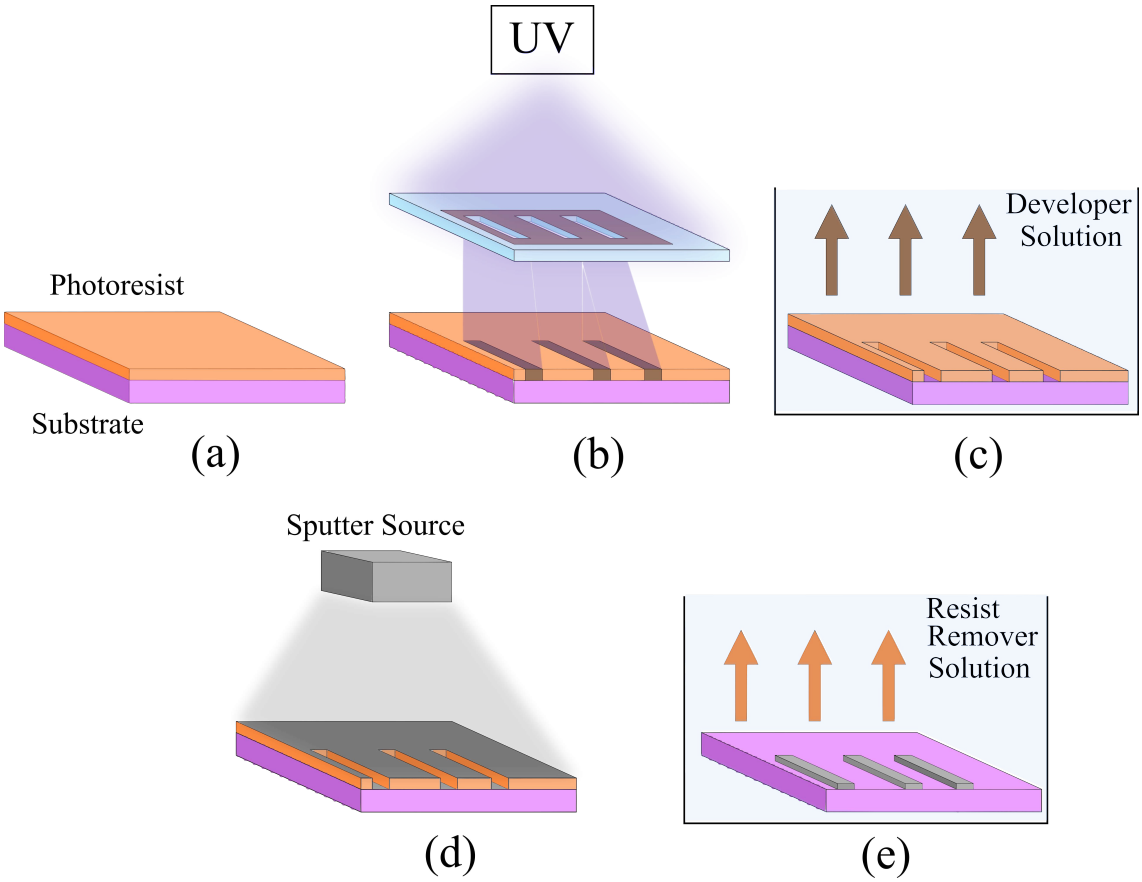

Figure 5.6: Schematic of the positive tone photolithography process used in this thesis: (a) Spin coat and Bake, (b) Expose, (c) Develop, (d) Deposition and (e) Lift-off.

within the exposed features, and too long an exposure time can lead to larger feature sizes. Magnetron sputtering was then used to deposit thin films over the whole sample surface. Finally, the samples were placed in an organic solvent to remove the remaining thin-film coated photoresist, leaving target material only in the exposed areas where the deposited thin film was in direct contact with the substrate.

5.3.2 Details of the Lithographic Procedure

The procedure used for the production of the majority of patterned samples used in this work is as follows:

- Spin coat S1813 photoresist onto cleaned substrate at 3700 rpm for 30 s to produce a 1.5 μm film
- Bake the sample using a hot plate 100 °C for 90 s to drive off resist solvent
- Expose sample to UV through mask using soft contact at 80 W/cm^2, with an EVG 620 mask aligner

- Develop exposed resist for 30 s in a diluted solution of AZ351B developer with water in ratio 4:1 water to AZ351B
- Wash sample in de-ionised water for 30 s, twice
- Deposit target thin-film material using magnetron sputtering
- Lift-off remaining photoresist using acetone
- Remove acetone with a isopropanol wash, followed with a de-ionised water rinse
- Blow dry sample with dry N_2 gas

Most masks used in this thesis were designed using CAD software before commercial production onto an acetate sheet. For the case where a mask was to be used multiple times, the pattern was transferred onto a glass slide to provide a more robust metallic mask. This was achieved using the same procedure as above, except an initial deposit of Cr occurs prior to the first step and instead of a second deposition, a chrome etch was used to remove the exposed areas where there was no photoresist to protect the Cr layer.

5.4 Energy Dispersive X-ray Spectroscopy

This section briefly details a technique, known as energy dispersive x-ray spectroscopy (EDX), that is used to determine the composition of alloy materials. In this thesis, it was primarily used to verify the composition of ferrimagnetic alloys grown using co-sputtering, and to investigate the fluorescence of atomic species with circularly polarised synchrotron radiation. The interaction of x-rays with matter can be broadly split into two processes: *absorption/emission* and *scattering*, the latter of which will be covered in subsequent sections within this chapter, while the following chapter will provide a further discussion of polarised x-rays and their behaviour in the absorption process.

In this process, a beam of x-rays from a synchrotron or an electron beam from a scanning electron microscope is focussed onto a sample, ejecting core electrons from the sample. For EDX described here, this is undertaken with an electron beam, while fluorescence due to the interaction of synchrotron x-rays with a sample is discussed in the next chapter. This ejection occurs above a threshold energy, known as the *absorption edge* with a decreasing barrier for levels with a higher principle quantum number. Above this barrier, there is a sharp increase in absorption coefficient. Following the ejection of the electron, the system relaxes through an electron from a

higher orbital falling into the lower orbital, emitting an x-ray. The energy of which is given by the difference in energies of the orbitals, and is therefore characteristic of the atomic species involved.

The absorption edges also feature steps in the absorption due to spin-orbit splitting. For the K (n=1) shell there is a single step, with three for the L (n=2) shell and five for the M (n=3) shell. The de-excitation transition is governed by quantum selection rules between the electronic orbitals, as illustrated in figure 5.7 [204]:

- Change of principle quantum number, $\Delta n \geqslant 1$
- Change of orbital angular quantum number by one, $\Delta l = \pm 1$
- Change of total angular quantum number by zero or one, $\Delta j = 0, \pm 1$

The energy change between orbitals is different for each element, thus an emission spectrum provides a fingerprint of the constituent elements within a sample. The emitted x-ray is measured either by its energy (*energy dispersive*) or wavelength (*wave dispersive*). By comparing the intensity of spectra peaks, with the use of database of intensities, it is possible to determine the composition of a sample. Figure 5.8 shows an example spectra obtained. In this work EDX measurement and analysis was done using a Hitachi SU-70 SEM system. Samples are first loaded into the SEM through a load lock to preserve vacuum, before being transferred into the

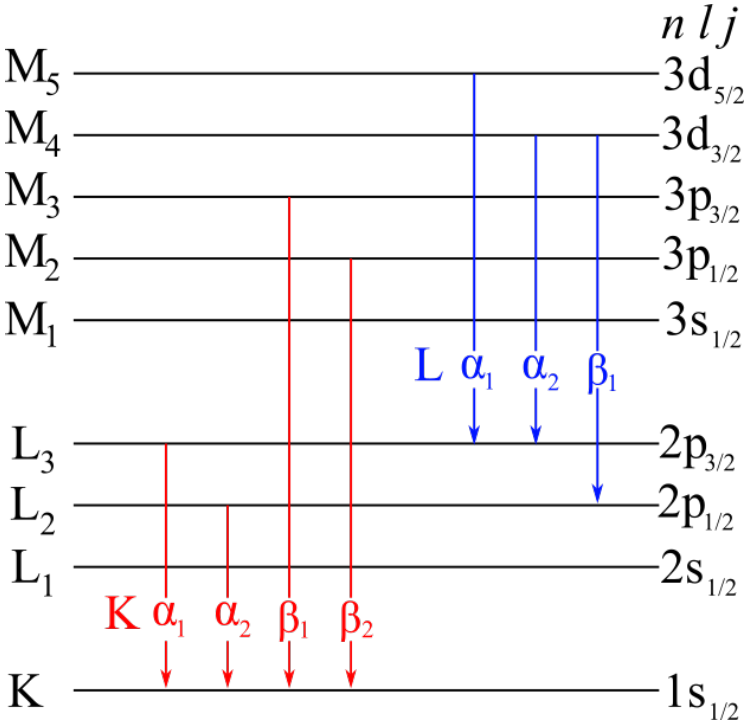

Figure 5.7: Illustration of the main allowed fluorescence transitions following the ionisation of the K or L shells.

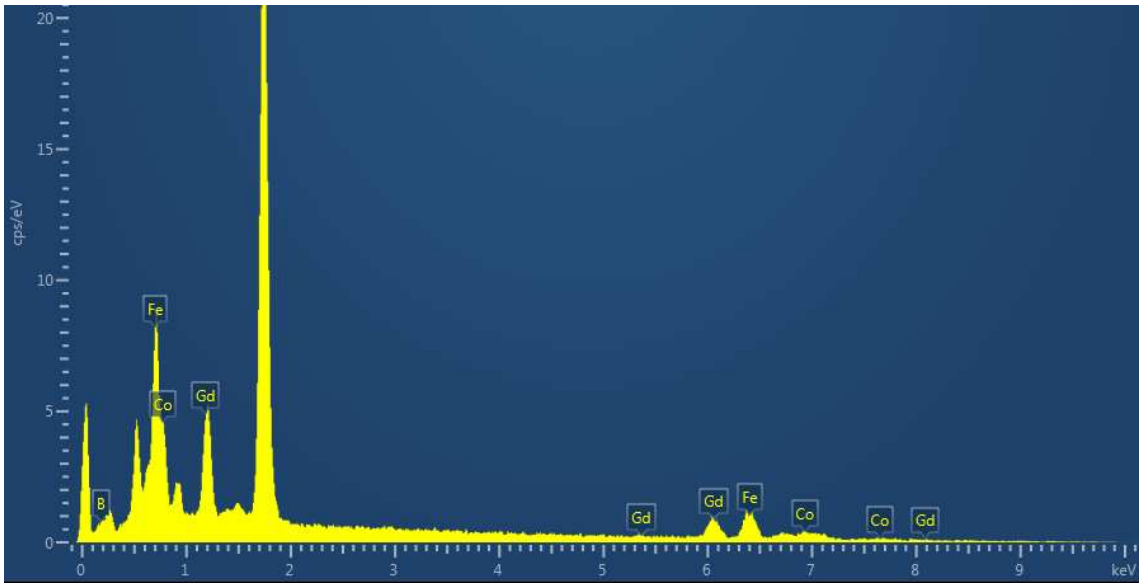

Figure 5.8: An example spectrum obtained from an SEM-EDX measurement on a thin film of CoFeGd, peaks correspond to emitted x-rays. The largest peak observed is Si, from the substrate of the sample.

main chamber of the SEM. Electrons are then accelerated to the sample at 20 kV, where they excite the transitions previously described, and a detector located nearby records the energy of the emitted x-rays. This analysis is normally done in almost realtime using commercial software, with the main limitation being the overlap of some characteristic x-ray energies for different elements. Scans are undertaken at least four areas on each sample to confirm uniformity, with an average taken for the final composition.

5.5 X-ray Reflectivity

Classically, incident electromagnetic radiation is scattered elastically from an atom due to the interaction of the electric field of the incoming wave and the atomic electron cloud. This interaction drives oscillations of the electrons, which then re-radiate the wave at the same energy. This elastic process is known as *Thompson* scattering. Illuminating an area with a large number of atoms leads to many spherical wavefronts re-emitted which can interfere with one another. In a multi-layered structure the resulting interference pattern is determined by the thickness and the refractive indices (related to the electron density) of each layer, as well as the difference between them at interfaces. This section briefly details the physics of a well established technique that exploits this phenomenon, known as grazing incidence X-ray Reflectivity (XRR). A more complete description of the interaction of x-rays with spintronic systems can be found elsewhere [127]. The parameters which

can be determined using this method are detailed and a short description of the method used to fit the data is also presented, as it is a key tool to derive structural information regarding the multi-layered films studied here.

5.5.1 Reflection and Scattering

Information obtained from scattering depends on the magnitude of the wave vector, Q. In small angle XRR, Q is given by the difference in incoming and reflected wave vectors, $k_i - k_r$, which is typically small, meaning the lengthscales probed in real space are larger than lattice spacings. Hence the information gathered is dependent on variations of the electron density, rather than the atomic lattice itself. For specular reflectivity, the angle of incidence, ω_i, is equal to the angle of reflection, ω_r, and hence the wave vector Q is normal to the surface, so the information gathered is sensitive to variations along the direction of the surface normal.

Two additional approximations are used in XRR: the *kinematic* approximation, in which multiple scattering events are ignored, resulting in scattering events from two electrons being separated by a given distance and phase, rather than a convolution, and the *Fraunhofer far field* approximation, in which the detector is at a distance much larger than the area of interaction on the sample and hence reflected waves can be considered parallel. A simplified picture of the interaction of grazing-incidence x-rays with the surface of a material is shown in figure 5.9, with the incident beam, transmitted and reflected beams illustrated. The refractive index of the material can be defined as,

$$n = \frac{c}{v} = 1 - \delta - i\beta \tag{5.1}$$

with c and v the speed of light in vacuum and in the medium respectively, and δ and

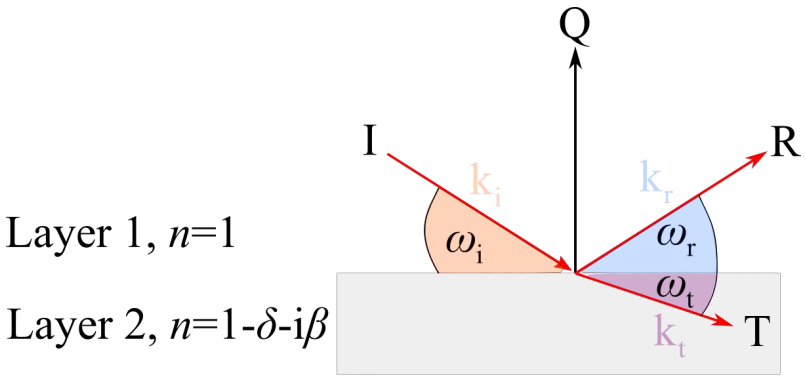

Figure 5.9: Schematic of the interaction of an incoming x-ray, with wave vector k_i at angle ω_i, which is reflected and transmitted at an interface between two layers of differing refractive indices, n.

β the dispersion and the absorption coefficients, both of which are dependent upon the electron density and x-ray energy, and which are typically small, meaning that n is of the order of unity. A further discussion of δ and β with regards to resonant reflectivity is presented in the following chapter.

Reflection from interfaces can be described using Snell's law, assuming $n = 1$ for the wave in the incoming medium,

$$\cos(\omega_\mathrm{i}) = n\cos(\omega_\mathrm{r}). \tag{5.2}$$

Total external reflection occurs when $\omega_\mathrm{r} = 0$, the critical angle is thus defined as,

$$\cos(\omega_\mathrm{c}) = n \approx 1 - \frac{\omega_\mathrm{c}^2}{2}, \tag{5.3}$$

$$\Rightarrow \omega_\mathrm{c} = \sqrt{2\delta}, \tag{5.4}$$

meaning the critical angle itself depends on properties such as the electron density and wavelength of the incoming x-ray. Below the critical angle, the incident wave enters the material as a decaying evanescent wave with a depth of a few nanometres. Above the critical angle, x-rays enter the material as a travelling wave and the reflected intensity drops as the inverse fourth power of the angle of incidence.

5.5.2 Specular Reflectivity from Thin Films

For a single layer of material the reflection and transmission of an x-ray are given by the Fresnel equations, for reflection, r, and transmissions, t,

$$\begin{aligned} r &= \frac{n_0\omega_\mathrm{i} - n_1\omega_\mathrm{t}}{n_0\omega_\mathrm{i} + n_1\omega_\mathrm{t}}, \\ t &= \frac{2n_0\omega_\mathrm{i}}{n_0\omega_\mathrm{i} + n_1\omega_\mathrm{t}}, \end{aligned} \tag{5.5}$$

with all terms as defined previously.

For a thin film consisting of multiple layers with differing electron densities, the combination of reflections and transmission at each interface must be considered. The total measurable reflected and transmitted intensities are given by $R = |r|^2$ and $T = |t|^2$.

For a simple bilayer structure, assuming perfect interfaces, the reflectance is given by the initial reflectance and subsequent reflections from the transmitted waves, as illustrated in figure 5.10a,

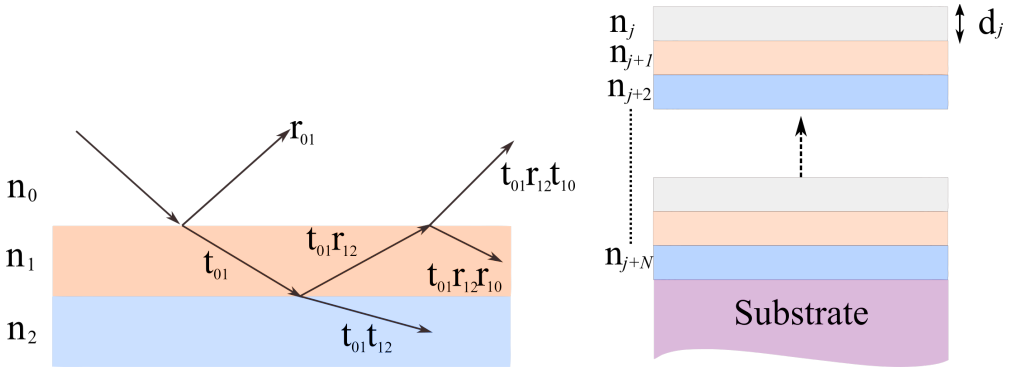

Figure 5.10: (a) Schematic illustration of reflected and transmitted x-rays in a material consisting of multiple layers. (b) Schematic of the interface notation used in the Paratt recursive formalism.

$$\begin{aligned} r_{\text{total}} &= r_{01} + t_{01}r_{12}t_{10}p^2 + t_{01}r_{12}r_{10}r_{12}t_{10}p^4 + ... \\ &= r_{01} + t_{01}r_{12}t_{10}p^2 \sum_{m=0}^{\infty} \left(r_{10}r_{12}p^2\right)^m, \end{aligned} \tag{5.6}$$

with phase factors, p, due to the path difference between reflected beams, such that $p^2 = \exp(iqd)$ with d the thickness of the layer, and $q = 2k_i \sin(\omega_i)$. This can be further simplified using the Als-Nielsen method [205] to give,

$$r_{\text{total}} = \frac{r_{01} + r_{12}p^2}{1 + r_{01}r_{12}p^2}. \tag{5.7}$$

Additional layers can be treated using Paratt's recursive formalism [206], in which each additional layer, j has a corresponding refractive index, n_j and thickness d_j. Figure 5.10b illustrates this layout. The reflectivity is then found recursively for any interface, given the interfaces underneath using,

$$r_j = \frac{r_{j,j+1} + r_j p_j^2}{1 + r_{j+1}r_{j,j+1}p_j^2}, \tag{5.8}$$

where the transmitted intensity at the substrate is zero, and p_j^2 is the phase difference from reflected beams. Due to the difference in phase from reflected beams, both constructive and destructive interference occur, creating a series of interference fringes as a function of incident angle. For a given film thickness, constructive interference follows Bragg's law,

$$2d \sin(\omega_{\text{i}}) = m\lambda, \tag{5.9}$$

with m an integer giving the fringe number and λ the wavelength.

These fringes, known as Kiessig fringes [207], vary as a function of incident angle given by

$$\Delta\omega_{\mathrm{i}} = \lambda/2d. \tag{5.10}$$

Examples of these fringes can be seen in figure 5.11a for a single layer of Co, that shows an increase in film thickness decreases the fringe spacing. For more complicated structures, multiple periods of Kiessig fringes may occur. Figure 5.11b shows simulations where a change in density for a single Co layer shifts the critical edge (inset) due to a change in the electron density and therefore a change of the r_j parameter.

5.5.3 Scattering and Interfaces

Thus far, the interfaces between layers have been assumed to be perfectly flat. In reality, due to film growth mechanics and conditions this is rarely the case and there exists a region between two layers where the electron density changes from one to the other. This may be due to topographical roughness, chemical intermixing, or some combination of the two. As described previously, in specular reflectivity the scattering vector, Q, is normal to the sample surface, and hence only information regarding the out-of-plane interface is obtained.

The two contributions to the interface width are illustrated in figure 5.12. One of the problems with standard specular scans is that both mechanisms contribute to a change in the electron density between any two layers and with a specular scan they are indistinguishable. However, the interface width can be defined as

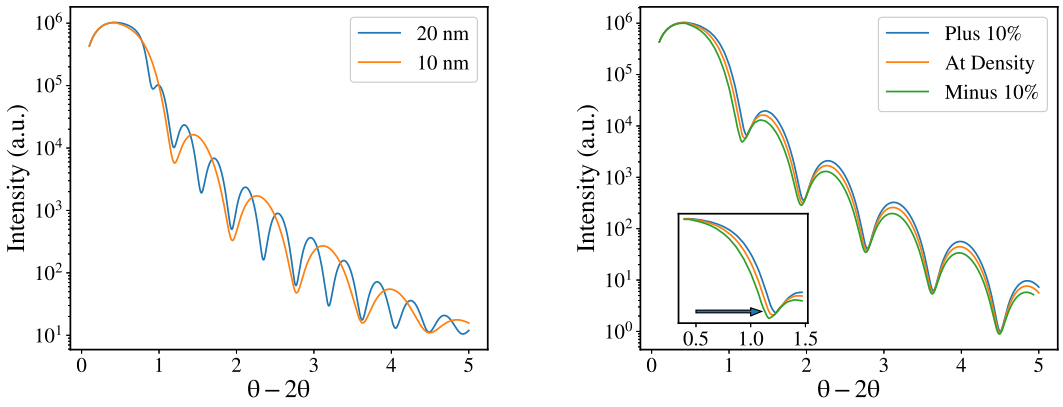

(a) (b)

Figure 5.11: Simulated XRR Spectra of Co thin films with (a) differing layer thickness and (b) differing electron density.

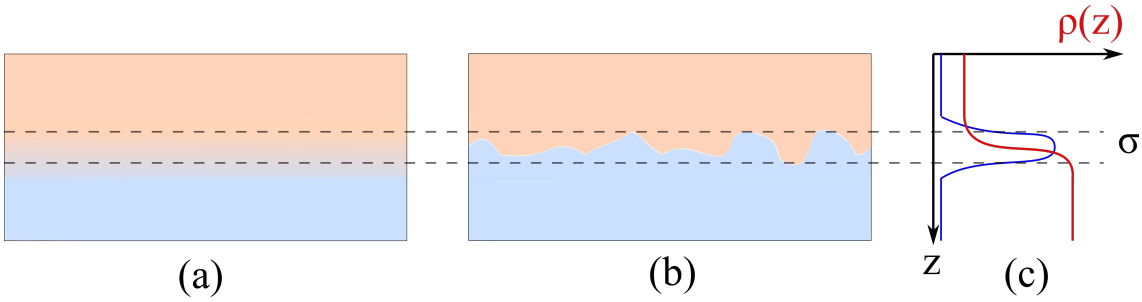

Figure 5.12: Schematic illustrations of the contributions to the interface width: (a) intermixing and (b) topographical roughness. (c) Specular reflectivity scans cannot distinguish between these two contributions, and produce the same interface width over the same length scale. The distribution may be represented by an error function (red), the derivative of which is a Gaussian distribution (blue).

$$\sigma = \sqrt{\sigma_{\text{top}}^2 + \sigma_{\text{int}}^2}, \tag{5.11}$$

and is usually represented in analytical models as an error function, as shown in figure 5.12. This contribution can be included into the Fresnel equations by,

$$r = r_{\text{s}} \int_0^\infty \frac{d}{dz}\left(\text{erf}\left(\frac{z}{\sqrt{2}\sigma}\right)\right)\exp(iQz)dz, \tag{5.12}$$

where r_{s} is the reflectivity of the smooth interface, and erf the error function. The additional parameter represented as an error function is the Debye-Waller factor [127], which can be simplified to

$$\frac{d}{dz}\left(\text{erf}\left(\frac{z}{\sqrt{2}\sigma}\right)\right) = \frac{1}{\sqrt{2\pi\sigma^2}}\exp\left(-\frac{z^2}{2\sigma^2}\right), \tag{5.13}$$

which becomes a Fourier transform in equation 5.12. This results in another Gaussian,

$$\exp\left(-\frac{Q^2\sigma^2}{2}\right), \tag{5.14}$$

which is the simplified Debye-Waller factor. The reflectivity is therefore,

$$r = r_{\text{s}}\exp\left(-\frac{Q^2\sigma^2}{2}\right), \tag{5.15}$$

with the total measurable reflected intensity given by,

$$R = |r|^2 = R_{\text{s}}\left|\exp\left(-\frac{Q^2\sigma^2}{2}\right)\right|^2 = R_{\text{s}}\exp\left(-Q^2\sigma^2\right). \tag{5.16}$$

A simulation of the effect of increasing the top interface width of a Co layer is shown in figure 5.13a, with the main effect being the reduction in amplitude of the Kiessig

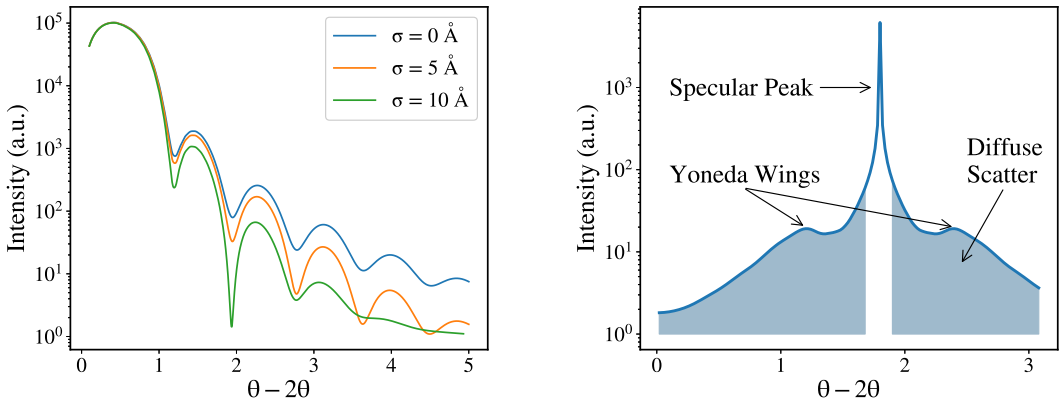

(a) (b)

Figure 5.13: Simulations of x-ray reflectivity, with (a) the effect of increasing the interface width of a single Co layer with vacuum, and (b) a simulated rocking curve showing the specular peak and diffuse scatter.

fringes at higher angles.

In order to differentiate between topography and intermixing at an interface, diffuse scans away from the specular condition must also be performed, as either the x or y density variations are then included in the scan due to the inclusion of in-plane scattering components. Typically, these scans are performed by fixing the 2θ angle and *rocking* the incident beam angle, ω_i or θ. In diffuse scatter features known as Yoneda wings [208] can occur, where the intensity is enhanced due to surface fields. The increase in diffuse scatter at the first wing corresponds to the specularly scattered beam travelling parallel to the sample surface. By reciprocity (reversal of wavevectors), the second wing occurs when the scattered beam entering the detector is parallel to the sample surface. Other parameters needed to simulate the shape are the Hurst parameter, a measure of the interfacial order, and the height correlation length. The inclusion of diffuse measurements both significantly increases the computational intensity needed to fit data, and can increase the number of solutions which give the same fit. This is discussed in the next section.

Nevertheless, the standard interface width, σ obtained from a specular measurement can be a useful measure of the extent of the interface and allows an assessment of the formation of a complete layer. It is proposed that a complete layer can only form when the thickness exceeds the interface width. Below this thickness, the layer is intermixed, discontinuous, or some combination of the two. Figure 5.14a shows the effect increasing interface width has on the reflectivity simulated for Co/Pt bilayers. The corresponding scattering length density profiles that are dependent upon the material's electron density, are shown in figure 5.14b, where an increasing σ gives a

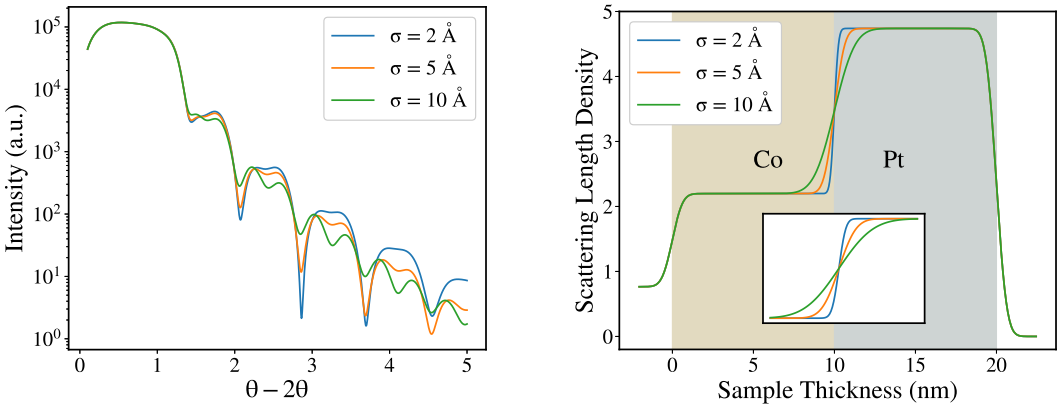

(a) (b)

Figure 5.14: (a) Simulations of x-ray reflectivity showing the effect of increasing the interface width for a Co/Pt bilayer. (b) The scattering length density profiles obtained from these simulations.

wider error function (inset), that represents a larger interface width. It is clear to see from the figure that both the Co and Pt have formed complete layers as indicated by the lack of change in the scattering length density within the Co and Pt regions.

5.5.4 Experimental Technique and Data Fitting Procedure

Method

All laboratory based XRR was undertaken using a Bede D1 reflectometer with a Cu-K_α source, a schematic of which can be seen in figure 5.15. From the right, a 16 mA beam of electrons is accelerated to a water cooled Cu target at 40 kV, resulting in an x-ray spectrum composed of Bremsstrahlung radiation along with Cu-K_α and Cu-K_β emission peaks. The primary source slits remove most of the Bremsstrahlung, and the channel-cut Si crystal removes the Cu-K_β using Bragg reflections and rotating the crystal to select the single Cu-K_α wavelength. The secondary slits are closed to 1 mm or 1.5 mm to set the beam width.

Samples were mounted on a rotating sample stage, with the beam incident varied through a range of angles, θ, and the detector was scanned in the specular condition at 2θ. Coupled $\theta-2\theta$ specular scans were performed and the intensity of the specular reflection at the detector was measured. Typical count times were 6 s per point, and a θ step size of 0.01°. A second scan with θ offset by 0.1° from the specular condition was undertaken to measure the forward diffuse reflectivity. This was subtracted from the measured specular data to obtain the true specular measurement.

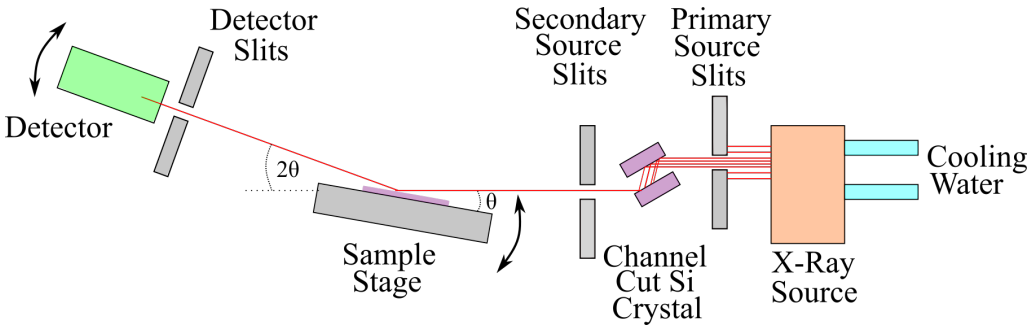

Figure 5.15: Schematic illustration of the setup in the Bede D1 x-ray reflectometer, in specular reflectivity mode.

Data Analysis and Parameter Fitting

Data fitting was undertaken using the genetic-algorithm-based open source GenX software [209]. The software varies the density, interface width and thickness of each layer with a given scattering factor to produce a scattering length density profile and corresponding simulation of $\theta - 2\theta$ scans to statistically compare with the data. However, in XRR, the intensity is recorded at the detector with information lost regarding the phase. This loss of information results in several possible structures giving the same reflectivity profile, i.e. there may be multiple minima when fitting the data by varying parameters with a cost function such as chi squared. It is therefore important to ensure the simulation is based on a model with physically realistic constraints.

GenX uses a model system of separate layers defined by the user, with the density, roughness and thickness as free parameters. Due to film growth mechanics, it is often necessary to sub-divide a layer of one material due to significant changes to the density between the interfacial region and the bulk. Figure 5.16a illustrates one of these scenarios, with the corresponding SLD shown in figure 5.16b. Here, raw data for a CoFeB (10 nm) / SiO_2 (5 nm) /Pt (10 nm) trilayer is shown along with the best fitting simulations based on one or two Pt layers. Both visually, and by quantifying the goodness of fit with a parameter such as chi squared, it is evident that the two layer Pt model gives the better fit. In this instance, similar treatment of the CoFeB and SiO_2 layers did not yield a better fitting model. In GenX, it is often necessary to split layers up when trying to model an interface profile which is not best represented by one error function between two electron densities. While it is possible to simulate the data with a large number of layers, the limitation of the number of measured data points provides a constraint on the number of free parameters that can reasonably be used.

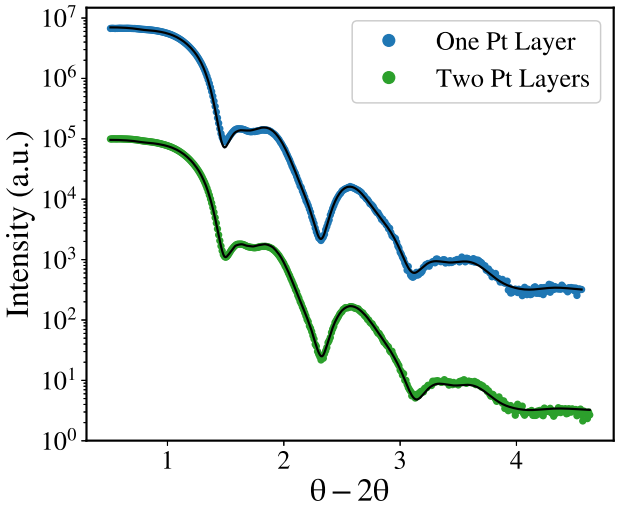

(a)

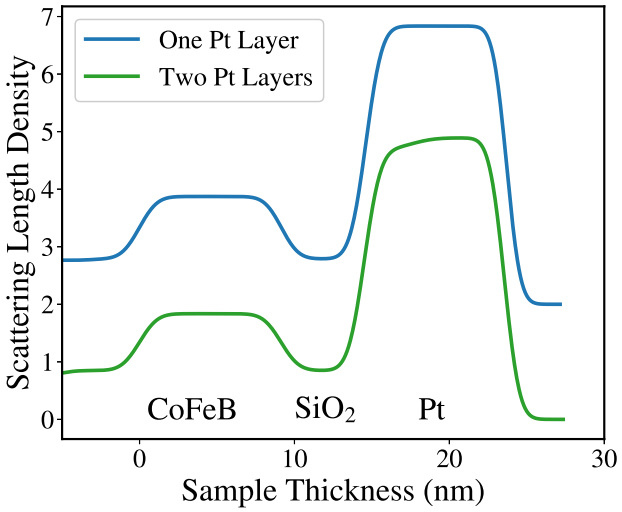

(b)

Figure 5.16: (a) XRR data and best fitting simulations for a CoFeB/SiO_2/Pt trilayer, with one and two Pt layers. (b) The scattering length density profiles for both fits. The datasets have been offset for clarity of presentation.

Chapter 6

Quasi-static Magnetic Investigative Techniques

6.1 Introduction

This chapter details the experimental methods used to probe the static magnetic properties of the thin film systems investigated in this thesis. Resonant x-ray magnetic reflectivity (XRMR) builds upon the reflectivity method introduced in the previous chapter, with the addition of providing a probe of the magnetism of a specific element. The theory and experimental setup for the magneto-optic Kerr effect (MOKE) is then introduced, before a brief description of a superconducting quantum interference device (SQUID) magnetometer used to measure the bulk magnetism of a sample. All three techniques can be used to produce magnetic hysteresis loops, each of which probe a different aspect of magnetism, (element specificity, surface and bulk sensitivity respectively), which can provide complementary information regarding the same sample.

6.2 X-Ray Resonant Magnetic Reflectivity

As detailed in the previous chapter, x-ray reflectivity can provide information regarding the thickness, density and interfacial profiles of thin film multilayered systems. By tuning the energy of circularly polarised x-rays to the energy of electronic transitions, the x-ray response of the material allows for the magnetic profile of a specific element to be acquired. This technique, x-ray resonant magnetic reflectivity (XRMR), was first observed in 1987 on the K edge of a Fe foil [210], and has become increasingly widespread with developments in synchrotron technology.

This section builds on the theory of interactions between x-rays and matter introduced in the previous chapter to describe EDX and XRR, to discuss the magnetic circular dichroic effect as well as a brief discussion of synchrotron radiation.

6.2.1 Magnetic Circular Dichroism

Magnetic circular dichroism refers to the change in absorption cross section of circularly polarised light incident upon a sample that depends upon the magnetisation state of the sample [211]. While section 6.3 later describes the interaction of polarised light with the valence states of a system, here the focus is on the core levels. The treatment of XRMR can be considered from a semiclassical perspective, with alterations to the refractive indices, allowing for the adaptation of the formulas used to describe standard XRR, or from a quantum mechanical picture involving electronic energy levels.

Semi-classical Treatment and Scattering Factors

The refractive index, as discussed previously, can be described by $n = 1-\delta+i\beta$, with δ and β the dispersive and absorptive components respectively. This index is dependent upon the frequency and polarisation of the incident waves, and hence these factors can be further expressed as a superposition of the response of all possible incident energies [211], embodied in the dispersive and absorptive components,

$$\delta(\omega) = \frac{r_0 \rho_a \lambda^2}{2\pi} f_1(\omega), \tag{6.1}$$

and

$$\beta(\omega) = \frac{r_0 \rho_a \lambda^2}{2\pi} f_2(\omega), \tag{6.2}$$

where r_0 is the classical electron radius, ω the angular frequency, λ the x-ray wavelength and ρ_a the atomic number density, such that $Z\rho_a = \rho_e$, the electron density. The atomic scattering parameters, $f_1(\omega)$ and $f_2(\omega)$, are the Henke-Gullikson scat-

tering factors [212], defined as $f_1(\omega) = Z + F'(\omega)$ and $f_2(\omega) = F''(\omega)$. For standard specular reflectivity, far from resonance, $f_1(\omega) \approx Z$, as $F'(\omega)$ (and $F''(\omega)$) have only a weak energy dependence and are small [205] away from resonance. $F'(\omega)$ can be determined through polarisation *rotation* measurements, comparing the difference in polarisations between incident and reflected waves, whereas $F''(\omega)$ can be determined through polarisation dependent *absorption* measurements [211].

In addition to these resonant scattering parameters, for magnetically sensitive transitions, the magnetic scattering lengths and structure factors must also be considered. The complete expression for the scattering length is given by [209],

$$f(\omega) = (\hat{\epsilon}_s \cdot \hat{\epsilon}_i)F^0(\omega) - i(\hat{\epsilon}_s \times \hat{\epsilon}_i) \cdot \hat{m}F^1(\omega), \tag{6.3}$$

where $\hat{\epsilon_s}$ and $\hat{\epsilon_i}$ denote the polarisation of the incident and scattered waves, and $F^0(\omega)$ the charge scattering length, equal to $f_1(\omega) + f_2(\omega)$ as before. $F^1(\omega)$ is the analogous magnetic scattering length, dependent upon m' and m'', the magnetic equivalents of f_1 and f_2. The modified refractive index is therefore,

$$n^{\pm} = 1 - \delta^{\pm}(f_1(\omega), \mp m') + i\beta^{\pm}(f_2(\omega), \mp m''), \tag{6.4}$$

where $\pm$ denotes a reversal of either the polarisation helicity of the incident beam, or a reversal of the sample magnetisation. This formalism allows for a change in the measured XRR intensity, due to either of these reversal processes, to be accounted for in Parratt's recursive algorithm, as detailed previously.

However, as before with structural scattering factors, XRMR probes intensity changes from a sample upon which incident light is both absorbed and re-emitted, and resonantly scattered. Therefore this technique measures both real (m') and imaginary (m'') components, alongside the corresponding structural scattering factors. By reversing either the magnetisation or the incident polarisation helicity, the structural scattering contributions can be removed, leaving only the magnetic contribution. An example of this measurement is detailed at the end of this section. The real and imaginary scattering length densities (mSLD) are given by the product of the real and imaginary scattering factors, m' and m'', with the magnetic density (the product of the moment per site and the atomic density). This mSLD provides an element specific, depth dependent magnetisation profile of the resonant species through the sample.

Quantum Mechanical Description and the Two Step Electronic Model

X-ray magnetic circular dichroism (XMCD) can also be understood from the picture of electronic energy levels. The focus here is given to transitions from the L edge, as these transitions correspond to the states responsible for magnetism. Figure 6.1 shows a typical energy scan over the L_2 and L_3 absorption edges. The two peaks arise due to spin-orbit splitting of the p level that lifts the degeneracy, resulting in a $p_{3/2}$ state corresponding to $l+s$, and a $p_{1/2}$ state corresponding to $l-s$. The two step model, proposed by Kapusta [213], provides a description of the XMCD process in terms of electronic transitions. In the first step, an incident photon is absorbed and excites an electron from a core level p state to the Fermi level. For circularly polarised x-rays this follows the transition rules [127],

$$\Delta j = 0, \pm 1,\ \Delta s = 0,\ \Delta l = \pm 1,\ \Delta m = \pm 1, \tag{6.5}$$

where the $\Delta m = \pm 1$ corresponds to transitions involving a helicity of incident light usually denoted as left circularly polarised (LCP) or right circularly polarised (RCP). The convention of LCP and RCP differs depending on whether the source or the observer is defining the helicity [214, 215]. It is therefore useful to also use σ notation, where σ^+ corresponds to a photon driving a $\Delta m = +1$ transition, and is *parallel* to the wavevector k, and vice versa for σ^-. These circularly polarised photons preferentially excite electrons with spin angular momentum collinear to

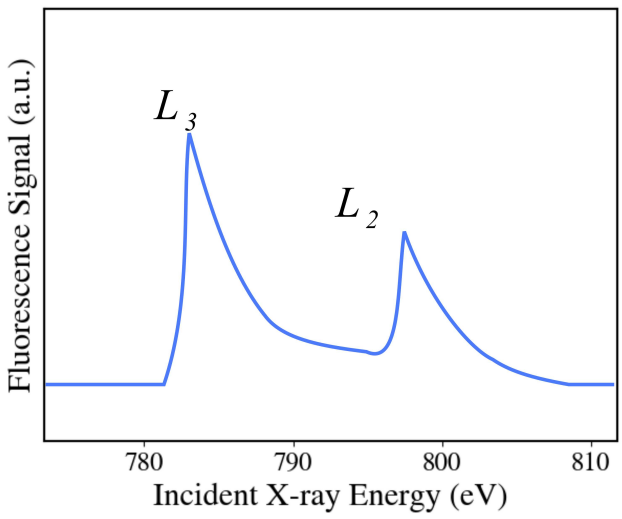

Figure 6.1: Illustration of the two absorption edges from a $p-d$ transition for Co, arising from splitting of the p band. The L_3 peak corresponds to a transition from the $p_{3/2}$ band to d states, and the L_2 peak corresponding to transitions from the $p_{1/2}$ state.

their own from the $p_{3/2}$ state, while the opposite is true for the $p_{1/2}$ state, due to opposite spin orbit coupling, i.e. $j = l - s$. An illustration of this process is shown in figure 6.2.

In the second step, due to an asymmetry in the density of spin states at the Fermi level, the spin-split d state acts as a filter. As the Pauli exclusion principle only allows transitions to vacant states, the absorption of one helicity will be suppressed from one of the p spin states and enhanced at the other, with the opposite effect for the other helicity. For example, in figure 6.2, there exists more spin-down states at the Fermi level, and hence σ^- transitions will be enhanced and σ^+ transitions will be suppressed at the L_3 edge. Reversing the magnetisation of the sample, and hence the splitting, will reverse the suppression and enhancement of the helicities. The notation $I^{\pm}$ denotes the scattered intensity due to either a change of helicity of the incident beam or magnetisation of the sample, which provides magnetic information regarding the resonant energy transition and hence the element, as described below.

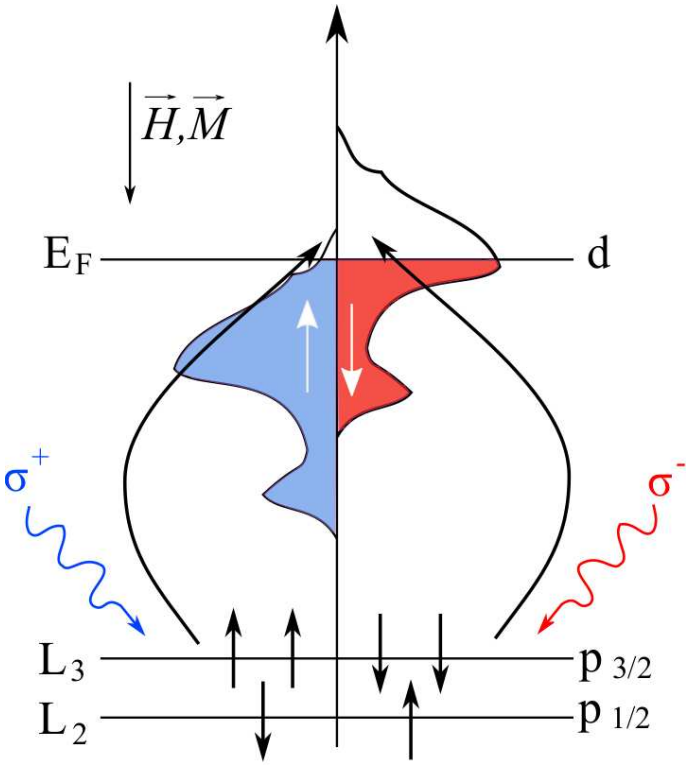

Figure 6.2: A schematic illustration of the two step model for XMCD at the L_2 and L_3 edges. In the first step, circularly polarised light preferentially drives a transition with angular momentum colinear to its own from the $p_{3/2}$ $(l + s)$ state, and vice versa from the $p_{1/2}$ $(l - s)$ state. Secondly, the imbalance of spin states in the d band acts as a spin detector.

X-Ray Fluorescence

High intensity x-rays can also excite core level electrons, resulting in x-ray fluorescence as described for electron beam driven fluorescence, in the previous chapter. The L_2 and L_3 absorption edges can be measured by varying the energy of the incident x-ray beam, and detecting the emitted x-rays using a fluorescence detector. In addition to observing the resonant atomic species within a sample, through the use of circularly polarised x-rays, both the orientation and size of the moment can be determined from measurements of the L_2 and L_3 edges and applying the *sum rules* [216], this measurement, however, was not undertaken on any samples considered in this thesis. A comparative qualitative study is given in later chapters concerning the orientation of the moments within a ferrimagnetic sample, in which the sign of the ratio of the intensities of x-rays emitted with different helicities of incident light, $I^{\pm}$, provides information regarding the direction of the magnetic moments with respect to the applied magnetic field in the scattering plane along the direction of the x-ray beam propagation. Details of these measurement are discussed in the next section.

6.2.2 Synchrotron Radiation and Measurements

XRMR measurements used in this thesis were performed at beamline 4-ID-D at the *Advanced Photon Source* (APS), Argonne National Lab. Here, XRR was undertaken at a magnetic field fixed in one direction to saturate the magnetisation and with the x-ray polarisation set using a diamond phase plate at each energy [217]. The intensity at each point was recorded for both helicities, I^+ and I^-. The sum of these two intensities provides structural information, while the difference is sensitive to the magnetic state of the material probed. By normalising to the sum, the asymmetry (or flipping) ratio can be defined as

$$R = \frac{I^+ - I^-}{I^+ + I^-}, \tag{6.6}$$

which removes the effect of pure charge scattering. For all samples measured in this thesis, I^+ and I^- correspond to the detected intensity of different helicities, at a fixed magnetisation state.

The measured difference in intensities obtained by either reversing the magnetisation or the polarisation helicity of the incoming x-ray beam is typically small, and thus requires an extremely high intensity, or brightness, of the incident radiation, in addition to the high precision to which both the energy and polarisation must be tuned. Synchrotron radiation facilities are therefore needed to carry out these

measurements.

Synchrotron radiation is based on the emitted radiation from circulating electrons. Electrons are accelerated to relativistic speeds in a linear accelerator, before being injected into a circular ring, emitting x-rays at sites of momentum change such as bending magnets and insertion devices. At the beamline 4-ID-D, an *undulator* inserted into the beamline, consisting of many alternating pole magnets, causes the electron beam to oscillate and emit radiation. The spacing between the alternating magnets determines the wavelength of the emitted light. The overall intensity of the beam is enhanced due to constructive interference from each of the emitted x-rays.

The setup for measurements is broadly similar to that for laboratory based XRR. Figure 6.3 shows a photograph of the setup, and figure 6.4 a simplified schematic. A monochromator selects a single wavelength to determine the energy of the beam, with phase retarders selecting a single, or combination of, helicities. Following this, slits and a bending mirror coated with rhodium narrow the beam down to a 10-20 μm beam size. Filters placed at the source and detector reduce the intensity of the full beam into the detector to prevent saturation.

Samples were held in vacuum in a cryostat with a beryllium cap which was transparent to x-rays at the wavelength used. An electromagnet was used to reverse the saturated magnetisation state of the sample, applied along the direction of the beam unless stated otherwise, as the scattered intensity contained information regarding the component of the moment in the direction of the beam, and hence the moments were required to lie along the same direction. For XRMR, standard specular coupled $\theta - 2\theta$ scans were performed by varying the angle of the sample stage and the main detector, with the incident beam fixed.

A typical XRMR measurement is shown in figure 6.5a for both positive and negative magnetisation states. The asymmetry ratio reverses sign with a corresponding reversal in the applied field, as expected. Figure 6.5b shows a typical absorption spectra at the Pt L_3 edge, with a corresponding XMCD signal, as determined by equation 6.6, in order to average values from different measurements as further detailed in chapter 9.

It is also possible to measure element specific hysteresis loops, and scans over the absorption edges using this technique, by measuring the difference in intensity of the two polarisation helicities as a function of applied magnetic field. For both of these cases, the fluorescence detector was used in place of the main detector. The hysteresis profile obtained arises only from the element on resonance at the selected x-ray energy. Figure 6.5c shows such a typical magnetic hysteresis loop. Similarly, the applied magnetic field could either be fixed, or removed, and the intensity of either, or both of, the two helicities recorded as a function of incident energy to

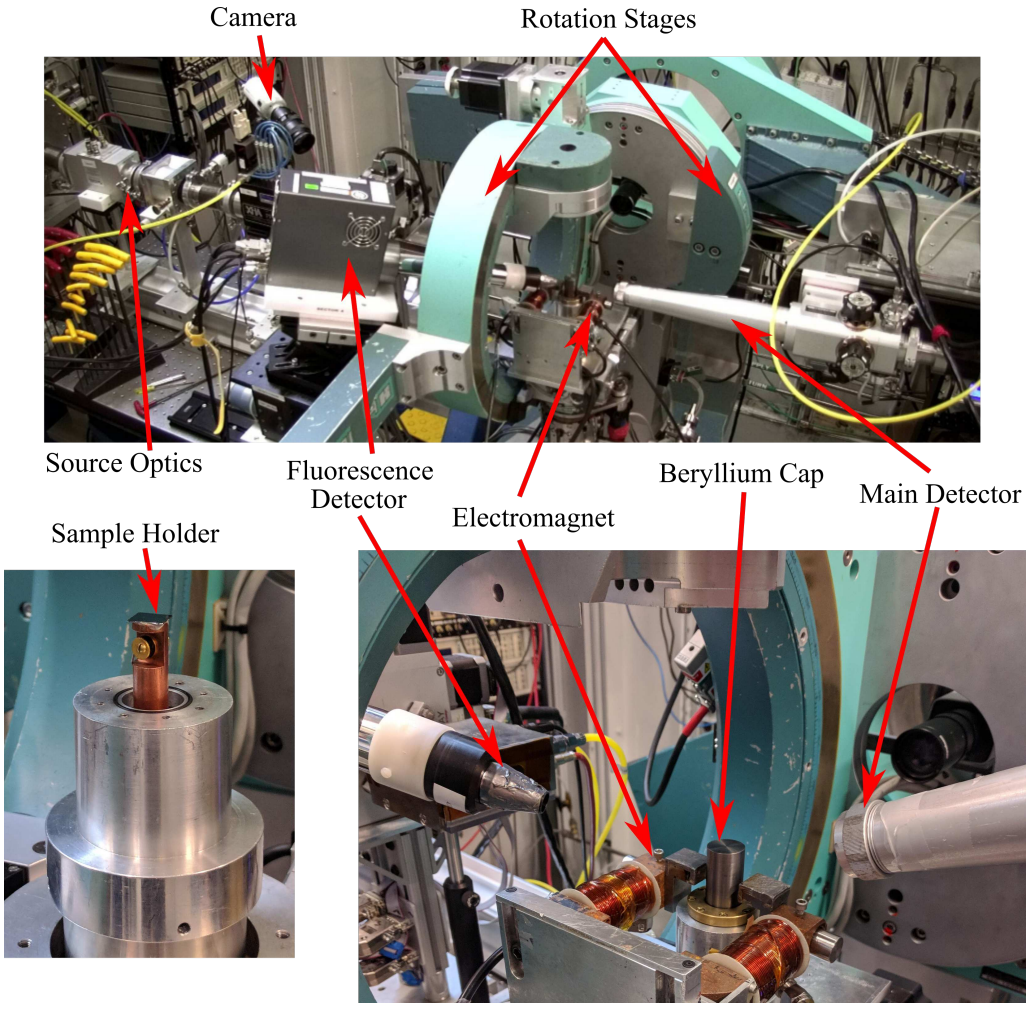

Figure 6.3: Annotated photographs of the x-ray measurement setup used on the bealime 4-ID-D at the APS to measure thin films using resonant x-rays.

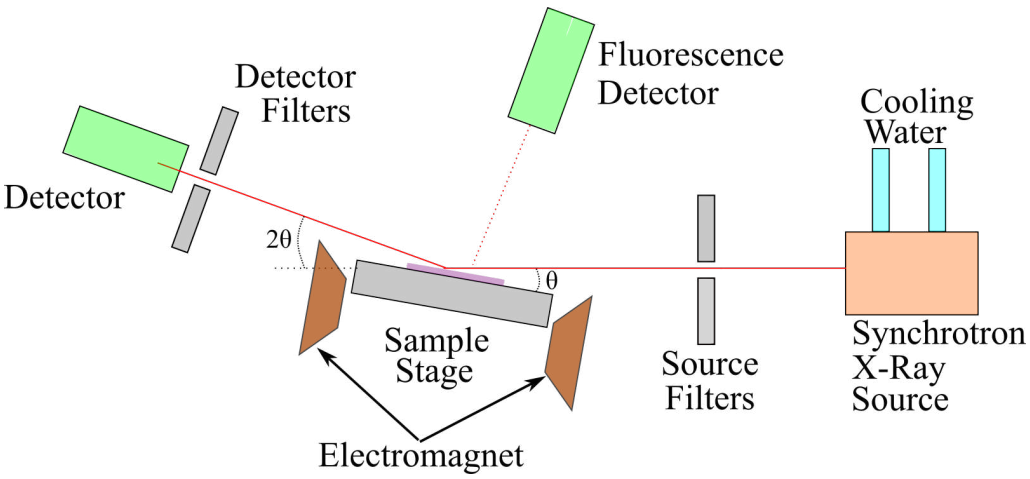

Figure 6.4: Simplified schematic illustration of the setup on the 4-ID-D beamline, for both specular reflectivity, and fluorescence measurements.

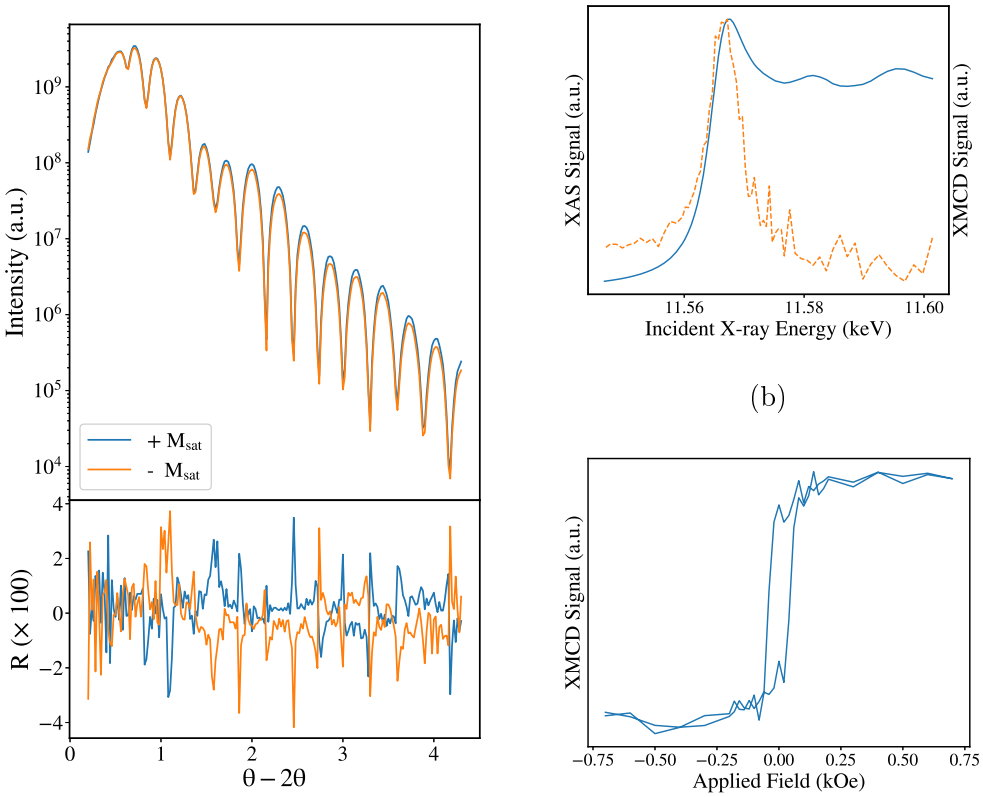

Figure 6.5: (a) Typical XRMR measurement showing x-ray reflectivity (top) and the mirrored difference in the asymmetry ratio for positive and negative magnetic states (bottom). (b) X-ray absorption spectra (solid blue) and XMCD signal (dashed orange) at the Pt L_3 edge in a Pt/CoFeGd/Pt system. (c) Element specific hysteresis loop obtained by measuring the asymmetry ratio as a function of applied field, taken at the Pt L_3 edge.

produce a scan over the absorption edges.

6.3 Magneto-Optical Kerr Effect

The interaction of polarised light with a material is not limited to the excitation of core electrons with high energy x-rays as detailed in the previous section. The rotation of the plane of polarised light passing through a magnetic material was first observed by Faraday in 1845 [218], with a similar effect observed for a reflected beam by Kerr in 1877 [219]. The latter effect, commonly known as the Magneto Optic Kerr Effect (MOKE), lacks the element specificity of XMCD, as the photon energy is not tuned to an absorption edge. However, the optics involved allows for a laser beam to be focused down to a small spot size, thereby only probing a microscale area. This section details the geometries and setup involved with MOKE.

6.3.1 Polarised Light and Magnetisation

Linearly polarised light which is used for MOKE measurements, is a combination of left and right circular polarisations. A phase difference between the two polarisation components produces linear polarisation rotated by an angle with respect to a defined plane of incidence, while a difference in intensity between the two components produces elliptical, rather than linear, polarisation. Linear polarisation can be further defined as either p-polarised, in which the electric field vector of the light is parallel to the plane of incidence, or s-polarised, in which the electric field vector is orientated perpendicular to the plane of incidence.

The Kerr effect results from a difference in the refractive indices of the two helicities of circularly polarised light within the magnetic medium. Following a reflection of initially linearly polarised light from a magnetised material, the linear polarisation of the outgoing beam is rotated due to this difference in the refractive indices. The effective refractive index for each helicity is also dependent upon the magnetisation of the sample. Hence by measuring the degree of rotation, or the associated intensity change due to polarisation rotation, measured with a fixed analysing polariser, as a function of applied magnetic field a magnetic hysteresis loop can be acquired [127].

6.3.2 Kerr Effect Geometries

The Kerr effect is sensitive not only to the magnetisation of a medium, but also the relative orientation of the magnetisation with respect to the scattering vector. Figure 6.6 shows the three possible geometries involved. For the longitudinal and polar geometries this can also be understood as a result of the Lorentz force between the magnetisation and electric field vector of the incident light, which produces a component of the polarisation of the reflected wave orthogonal to both.

In the polar geometry, with the magnetisation out-of-plane, both s and p polarisations experience a Kerr rotation, which is maximised at normal incidence. Both the longitudinal and transverse geometries are sensitive to changes of in-plane magnetisation. For transverse MOKE, no component of M lies within the scattering plane, hence no Kerr rotation occurs, but rather a modulation of the amplitude of p-polarised light [127]. With the longitudinal geometry, the magnetisation lies within the scattering plane, and therefore a Kerr rotation is observed [127]. Only the longitudinal measurement geometry was used within this thesis.

MOKE is a surface sensitive technique, as the light is attenuated within a magnetic thin film. The length scale over which the intensity falls to $1/e$ of the original value is known as the skin depth. This is typically between 10 and 20 nm for most metals [220] and hence the reflected light is not sensitive to depths much thicker

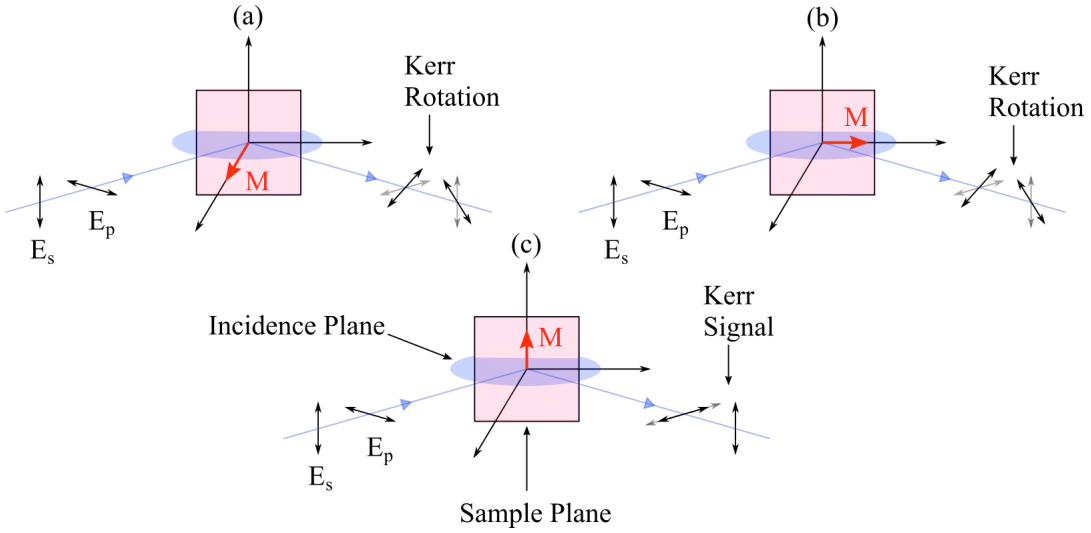

Figure 6.6: Schematic illustration of MOKE scattering for (a) Polar, (b) Longitudinal and (c) Transverse geometries.

than this value.

6.3.3 Longitudinal MOKE Setup

All samples investigated in this thesis had in-plane magnetisation, and therefore only longitudinal MOKE was used. A schematic of a typical setup is shown in figure 6.7. A diode laser produced light with a wavelength of 658 nm, which first passed through a beam expander, then a high quality polarising prism, before being focussed down onto the sample through a lens, at an angle of 45°. The reflected light was then passed through a second lens which focussed the beam through a $\lambda/4$ wave plate and an analysing polarising prism, onto a photodiode. The $\lambda/4$ wave plate removed any ellipticity from the reflected beam, and the analyser was initially set to extinction, then offset from extinction by rotating by 5°. This allowed any change in the Kerr rotation to be detected as an intensity change at the photodiode. The signal from the photodiode was then amplified and measured, and averaged to improve the signal to noise ratio, with an oscilloscope.

A white light source, flip mirror, neutral density attenuator (removed during normal operation), and camera focused on the sample surface allowed for direct visualisation of the beam spot on the sample surface. The sample was attached to a translation stage capable of xy motion as well as angular rotation within the plane of the magnetic field. This allows for the focussed beam to be positioned onto microscale patterns, should the user wish to measure a specific area. The sample was placed within a magnetic field, which was swept at a rate of 11.7 Hz, driven from a Kepco BOP power supply. A calibrated Hall probe placed within the field was

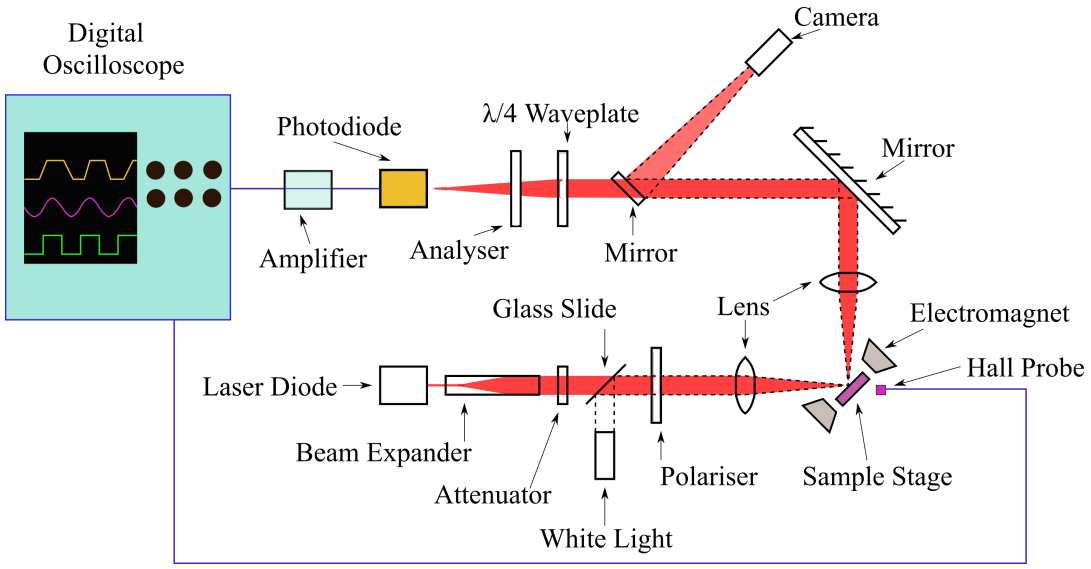

Figure 6.7: Schematic diagram of the experimental setup for longitudinal MOKE measurements.

also attached to the oscilloscope. The oscillating Kerr voltage, due to the oscillating magnetic field, was averaged over many field cycles by the oscilloscope, before being acquired by a *Python* programme over GPIB. Plotting the changing signal from the photodiode against the Hall probe signal was used to generate a magnetic hysteresis loop, an example of which can be seen in figure 6.8a.

Two main parameters of interest from MOKE loops for characterising the magnetisation behaviour are the *coercive field*, the field required to reverse the magnetisation state to zero, given by the half-width of the loop, and the *remanence ratio*, the ratio of signal remaining at zero applied field, compared to at magnetic saturation. For samples with an in-plane anisotropy, both of these properties can change as a function of in-plane angle, as can be seen in figure 6.8a, while full angular scans provide a simple visual picture of the degree of anisotropy in a sample, as shown in figure 6.8b. Along the hard axis, both the magnetic remanence and coercivity will be lowest, and both largest along the easy axis.

6.4 Superconducting Quantum Interference Device

A *superconducting quantum interference device* (SQUID) magnetometer is a device used to probe the magnetic moment of a whole sample, unlike the element or surface sensitive measurements described previously. SQUIDs can be broadly described as a high gain current (or flux) to voltage amplifier [221] and are capable of a resolution with a very high sensitivity down to 10^{-14} T [222]. This section briefly details the basic principles behind DC SQUID magnetometry and discusses the interpretation

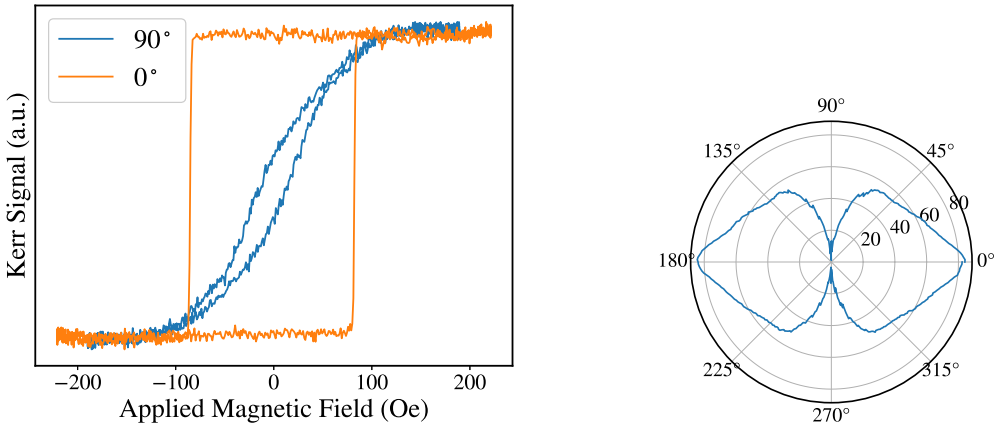

(a) (b)

Figure 6.8: (a) Typical magnetic hysteresis loops obtained from longitudinal MOKE along the hard and easy axes of a Co/Ru/Co trilayer. (b) Coercive field as function of in-plane rotation for the trilayer sample.

of the measurements. SQUID magnetometry was used in this thesis to understand the change in magnetisation of ferrimagnetic alloys with temperature, as discussed in a later results chapter. All measurements were undertaken by Ben Nicholson at *Diamond Light Source*, Oxfordshire, using a Quantum Design MPMS3 [223].

6.4.1 The Josephson Junction

A DC SQUID circuit consists of two superconductors separated by an insulating layer or weak link known as a Josephson Junction [224, 225], connected in parallel with a constant DC supply [21], as illustrated in figure 6.9a. In the absence of an external voltage, a current can tunnel across the barrier, the amplitude of which is sensitive to external magnetic fields. In addition, the magnetic flux contained within the loop is is quantised and can only exist in integer units of the flux quantum, $(h/2e)$. As the external flux changes, the critical current of the two junctions oscillates with a period equal to integers of the flux quantum, and hence there is a corresponding voltage change across the junction. An increasing external field, increases the number of flux jumps which occur, and produces a sinusoidal voltage wave, the period of which corresponds to one increase in the flux quantum [21]. Integrating this sinusoidal voltage from the SQUID produces a signal proportional to external flux.

A schematic of a SQUID-VSM (vibrating sample magnetometer) is shown in figure 6.9b. In a conventional VSM, a voltage is induced in a pick-up loop due to Faraday's law of induction, from a moving magnetic sample. The setup is similar

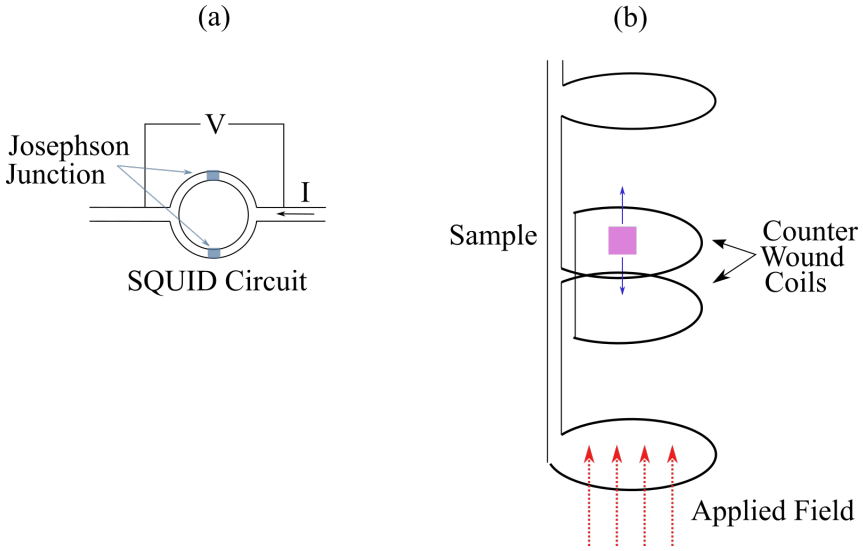

Figure 6.9: Schematic diagram of (a) the Josephson Junction used to form the SQUID circuit, and (b) the sample environment within the four pickup coils in the VSM.

for SQUID-VSM, but instead of merely recording, or amplifying the signal from the pickup coils, a flux transformer couples the pickup coils to the SQUID. As the pickup coils are superconducting, a current is induced rather than a voltage. Four coil windings are used in the detection coil. Any noise arising from fluctuations in the external magnetic field picked up by the two central coils, are cancelled by the top and bottom coils. However these do not remove all sources of noise, in particular residual fields in the magnet can lead to erroneous results [226].

6.4.2 Interpreting Results

SQUID magnetometry was primarily used in this thesis to characterise the temperature dependence of the magnetisation of the ferrimagnetic alloys discussed in later chapters. Two types of scan were undertaken, either measuring the magnetic moment as a function of temperature at a fixed field, or the moment as a function of applied field at a fixed temperature, producing magnetic hysteresis loops. For temperature dependence, most measurements were undertaken with the sample cooling from a high temperature down to a low temperature at a fixed field, a process known as *field cooling* (FC).

Samples were mounted in a weakly diamagnetic plastic straw to minimise the background contribution before being loaded into the system. However, as this technique measures the total moment of the sample, the diamagnetic component of the silicon substrate also produces a contribution to the measured signal. Figure 6.10 illustrates the raw data and the procedure for removing this diamagnetic component.

A straight line was fitted to between 5 and 10 data points at the two extremes of the applied magnetic field. The gradients of the two lines were then averaged and subtracted from the field dependent data to remove the background diamagnetic components. Converting from moment (emu) to magnetisation, the moment per unit volume, (emu/cm^3) requires the film thickness (measured using XRR) and the area (determined by the shadow mask used in deposition) to be known.

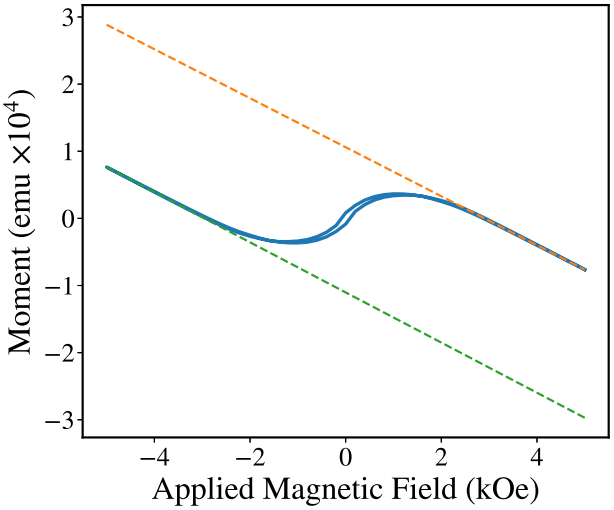

(a)

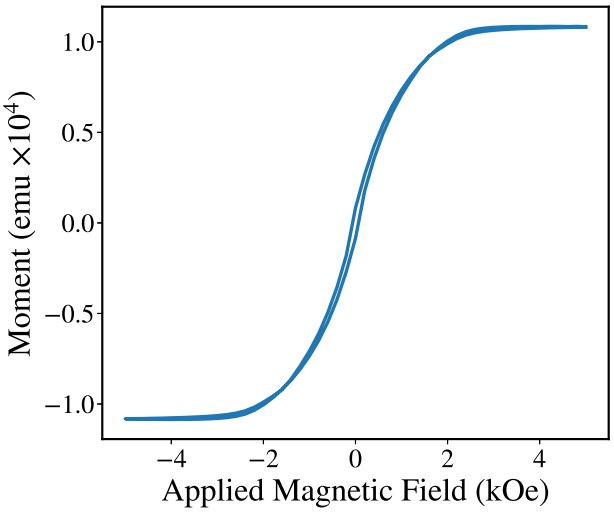

(b)

Figure 6.10: (a) Example of raw data from a thin-film taken as a function of field at a fixed temperature. To subtract the diamagnetic background a straight line was fitted to the extremes of the hysteresis loop (dashed lines), the gradients of which were averaged, then subtracted to produce (b), showing a hard axis of magnetisation.

Chapter 7

Development of a Dynamic Measurement System for Thin-film Analysis

7.1 Introduction

This chapter begins by introducing the techniques used to measure the dynamic properties of magnetic thin film systems. Various methods that probe ferromagnetic resonance exist, from frequency domain network analysis and free space cavity measurements methods, which measure the average properties of a sample, to time domain, spatially-resolved methods such as magneto-optic Kerr effect measurements and element specific techniques using synchrotron radiation. The focus of the discussion here, however, is directed to laboratory based frequency domain techniques.

Following this overview, the details of the design and performance of a system for measuring dynamic magnetic properties up to 15 GHz, developed as part of this study, is described. An initial system based on a vector network analyser (VNA) is first detailed, before the development of an integrated standalone system, capable of automated in-plane rotation analysis utilising lock-in techniques, is presented. Finally, a brief summary is given of measurements which show the capability of the system.

7.2 Dynamic Magnetisation Measurements

Frequency domain measurements of magnetic thin-films record the microwave energy absorbed within a magnetic thin film system, which reaches a maximum at the ferromagnetic resonance condition. These methods can be broadly split into two categories; cavity based measurements, in which the frequency is confined to a narrow selected band with ferromagnetic resonance observed as the applied magnetic field is swept, and broadband waveguide measurements, in which both the frequency and the applied magnetic field can be swept over a wide range of values, usually at a fixed angle of the sample with respect to the field. This section describes the operating principles of the two techniques. All samples examined in this thesis were measured using broadband techniques, either in Durham, or at the Institute for Molecular Physics, Polish Academy of Sciences (IFMPAN) in Poznań.

7.2.1 Cavity-based Measurements

Ferromagnetic resonance measurements undertaken within a metal microwave resonant cavity are closely related to another analytical technique known as electron paramagnetic resonance or electron spin resonance (ESR), where incident RF energy drives transitions between energy levels that are Zeeman split by an external magnetic field [227]. Figure 7.1 shows an illustration of a typical experimental arrangement used in both of these measurements. A microwave source injects RF energy into the cavity, the dimensions of which are determined by the frequency of operation. The *Q-factor* of the cavity parametrises the ratio of the energy stored to the energy dissipated. For a perfectly matched cavity (high Q), little to no energy is reflected back to the detector diode, and the energy density of the resonant RF radiation inside the cavity is high. By sweeping the applied magnetic field, the resonance condition of the sample can be tuned to match the cavity, and the sample absorbs a fraction of the RF energy, lowering the Q-factor [77]. This lowering of Q causes a change in impedance, and microwave energy is reflected to the detector diode [227]. Thus, by measuring the diode signal as a function of applied magnetic field, a microwave absorption profile can be obtained.

An advantage of the cavity-based technique is the ability to easily rotate the sample either in or out of the plane of the applied magnetic field, which allows for the angular dependence of the resonant condition to be probed and analysed using the equations detailed in chapter 3. Cavity-based systems can also be used to perform measurements in-situ during film growth, due to the ease of performing the measurements under vacuum. The main drawback is the limited range of frequency operation, as any large changes in frequency require a change of cavity size.

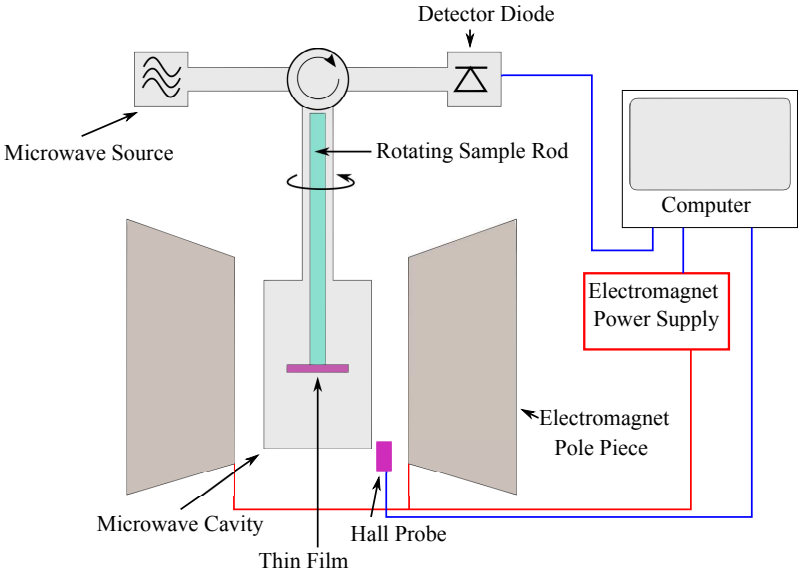

Figure 7.1: Schematic illustration of a cavity-based measurement for ferromagnetic resonance.

7.2.2 Broadband Waveguide Measurements

In order to investigate the dynamic response of magnetic thin films over a broad range of frequencies, it is necessary to use microwaves propagating across a transmission line waveguide, rather than free space. Various forms of transmission line can be used, with the two most common being the microstrip, a signal line separated from a ground plane by a dielectric, and a co-planar waveguide, in which the signal line is adjacent to additional grounded lines. The next section details some of the considerations taken when producing these waveguides.

Initial experiments investigating FMR using transmission lines used pulsed voltages across a waveguide with a sample in contact, and recorded the signal in the time domain with a fast oscilloscope [228]. Frequency domain measurements commonly use a commercial *vector network analyser* (VNA) as the microwave source and to measure the reflected and transmitted microwave power across a transmission line as a function of frequency. This signal is commonly described by the *s-parameters*, and presented in decibels [139]

$$S_{i,j} = 20 \log_{10} \left(\frac{V_i}{V_j} \right), \tag{7.1}$$

where i, j denote the port of the source and receiver, e.g. S_{11} measures the signal reflected back to port 1 from the source port 1, and S_{21} denotes the transmitted signal measured at port 2, from the source port 1. Around resonance, a portion of the RF energy is absorbed by the sample, and the signal, S_{21}, is reduced. Therefore by either sweeping the applied magnetic field or RF frequency, the dynamic

magnetisation response of the magnetic thin film can be probed.

Early measurements of FMR using a VNA involved hybrid fixed ESR cavity measurements with a broadband coaxial probe head [229]. Removing the cavity aspect and replacing the coaxial connection with a co-planar waveguide was shown to greatly improve the signal to noise ratio due to increased grounding [230]. Performing a single port reflection measurement also allows for an estimation of the permeability of the sample [231, 232], with a shorted co-planar waveguide providing greater signal to noise than shorted microstrips [233], again due to increased grounding. Advanced instruments are also capable of broadband measurements inside a cryostat, as a function of in and out of plane angles to the magnetic field and at frequencies up to 70 GHz [234]. Comparisons between broadband measurements in the literature show good agreement between various implementations of waveguide-based techniques [235], while analysis involving both reflection and transmission measurements using a VNA has been reported to provide greater precision than one component alone, the error due to neglecting the reflected component is small [236].

Figure 7.2 shows a simplified schematic of a typical broadband FMR measurement using a VNA. The VNA measures the microwave frequency signal transmitted through a waveguide with a thin-film sample placed faced down onto the transmission line, with a computer controlling the magnetic field by adjusting the current to the electromagnet. A Hall probe provides a measurement of the static magnetic field. At the resonance condition, a portion of the RF energy is absorbed, and the transmitted signal is reduced. The next section details typical FMR measurements using this technique. The disadvantage of broadband techniques is the difficulty in performing measurements as a function of magnetic field angle, as the sample is placed in contact with the waveguide.

7.3 The Development of a Measurement System

In order to investigate the dynamic properties of magnetic thin film systems a measurement system was developed. Initial system iterations were based on a vector network analyser as both the microwave source and for signal detection, before an integrated system was designed and developed that combined both the benefits of in-plane rotational behaviour of free space cavity techniques with the broadband frequencies of transmission line waveguides. The remainder of this chapter details the design and development of this latter system, and summarises its functional capabilities.

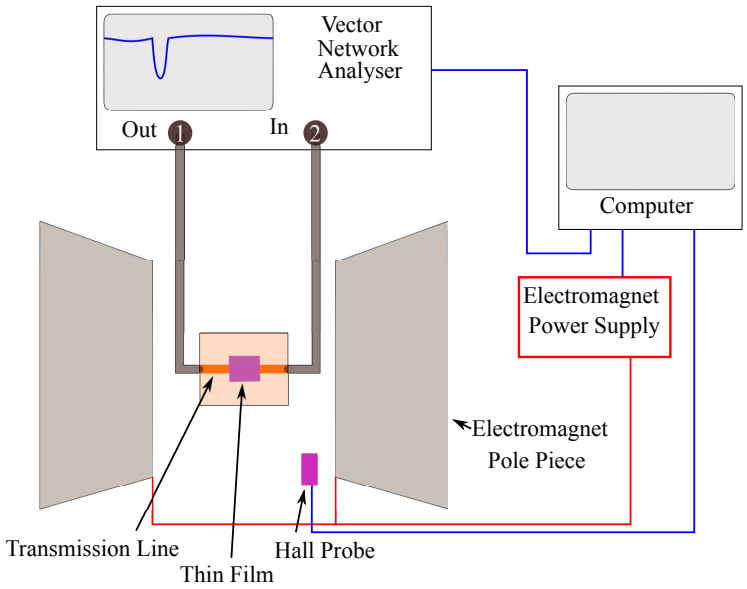

Figure 7.2: Schematic illustration of a typical setup for ferromagnetic resonance measured using a vector network analyser and a waveguide, in this case a microstrip.

7.3.1 Transmission Lines for FMR Measurements

The first component which must be considered when designing a broadband system to measure FMR, is the transmission line. Both a microstrip and co-planar waveguide transmission line were considered. Although the propagation loss is typically higher, a microstrip was chosen over a co-planar waveguide due to the simpler design being achievable with local production equipment. Co-planar waveguides often require via holes connecting the top and bottom ground planes and thus require additional processing, whereas a microstrip simply requires a controlled track width for a given dielectric thickness to obtain the standard 50 Ω impedance. Figure 7.3a shows a schematic cross section of a typical microstrip. Due to the orientation of the magnetic field, it is necessary to have the microstrip positioned parallel to the static applied magnetic field when undertaking FMR experiments, to ensure the magnetic component of the RF signal is perpendicular to that of the DC magnetic field.

For any transmission line operating at high frequency, the maximum energy is transferred between circuit components when there is no impedance mismatch, as was the case for incident EM waves in free space in chapter 4. In order to reduce the signal loss between components, all cables and transmission lines, must be matched to an impedance of 50 Ω. Specialist 50 Ω coaxial cables and connectors known as *SubMiniature version A* (SMA) typically have very low loss up to 18 GHz and were used here to carry microwave signals to and from the impedance matched microstrip

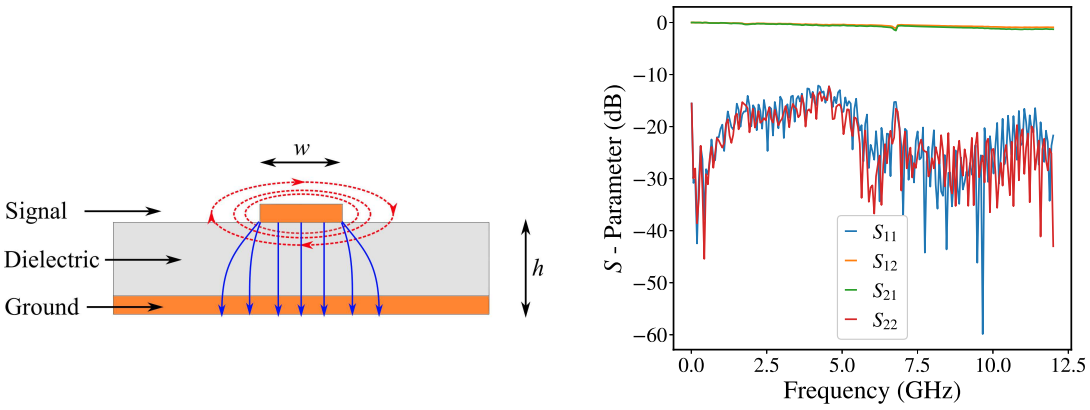

(a) (b)

Figure 7.3: (a) Schematic illustration of the cross-section of a microstrip transmission line, with a metallic signal line of width, w and dielectric of thickness, h. The dispersion of the electric field is illustrated in blue, and the magnetic field in red. (b) Measured S-parameters of the microstrip used to measure samples in Durham in this thesis with no sample present.

transmission line. The impedance of a microstrip is given by [237]

$$Z_{\text{ms}} = \begin{cases} \frac{Z_0}{2\pi\sqrt{\varepsilon_{\text{eff}}}} \ln\left(\frac{8h}{w} + \frac{w}{4h}\right), & \text{if } \frac{w}{h} < 1 \\ \frac{Z_0}{\sqrt{\varepsilon_{\text{eff}}}\left(\frac{w}{h} + 1.393 + 0.667 \ln\left(\frac{w}{h} + 1.444\right)\right)}, & \text{if } \frac{w}{h} \geq 1 \end{cases} \tag{7.2}$$

with Z_0 the impedance of free space, w the width of the signal line and h the thickness of the dielectric. It is assumed here that the thickness of the signal line exceeds the skin depth at microwave frequencies (10s of μm). The effective dielectric constant, ε_{eff} is given as [237]

$$\varepsilon_{\text{eff}} = \frac{\varepsilon_{\text{r}} + 1}{2} + \frac{\varepsilon_{\text{r}} - 1}{2} \left(\frac{1}{\sqrt{1 + 12\left(\frac{h}{w}\right)}}\right), \tag{7.3}$$

with ε_{r} the permittivity of the dielectric layer. It is therefore critical to use a material with a constant permittivity over the frequencies of operation. For this reason, *Rogers RT-Duroid 6002* (ε_{r}=2.94) was chosen [238]. The dielectric is coated with copper cladding, therefore for a simple straight 14 cm long microstrip, as used in this thesis, a milling machine is simply required to etch away the top copper cladding in all areas other than the signal line. For this material, and a dielectric thickness of 0.03 inches, the microstrip width is impedance matched to 50 Ω at 1.9 mm.

Figure 7.4 shows a 3D rendering of the design of the FMR system transmission

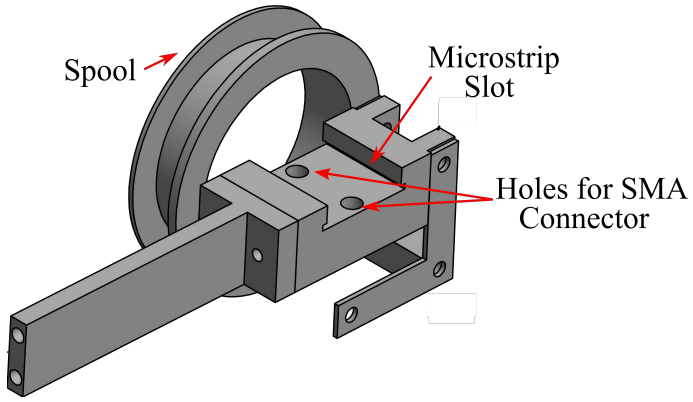

Figure 7.4: Annotated rendering of the design of the FMR system transmission line holder for the microstrip. Not shown is second spool for clarity.

line holder. SMA launchers connect to the underside, such that the signal pins come through the microstrip sitting on top and are electrically contacted with a small amount of solder. The spool in the figure is discussed in later sections.

7.3.2 Vector Network Analyser Based Measurements

The first iteration of the system to measure FMR in this work utilised an Agilent (now Keysight [239]) vector network analyser to generate the microwave frequencies and measure the transmission across a microstrip. Results obtained using this system form the first half of chapter 8, and were published in [109]. The system follows the form shown in figure 7.2, with an air-cooled Newport Pagnell electromagnet type C supplied by a 60 V, 1.5 A Thurlby Thandar TTi PL601 [240] power unit to provide the DC magnetic field. With the sample holder described, the electromagnet pole gap was 30 mm, providing a maximum field of 2 kOe with a 2 Oe step size. In this configuration the VNA was set to continuously sweep the frequency from 1 to 15 GHz, and a Raspberry Pi module [241] was used to send ASCII commands to the power supply to adjust the magnetic field and to the VNA to save the S-parameters at each field step, dwelling at each point for 3 s. The magnetic field was calibrated with a Hall probe, such that the applied current to the magnet could be converted to a magnetic field value. In order to avoid hysteretic effects in the electromagnet pole pieces, for each measurement the magnet was first saturated before the current was reduced back to 0 A. In this way, the resonance in terms of both the field and frequency domains could be measured.

Figure 7.5a shows a typical measurement of the S_{21} parameter as a function of frequency for two different applied magnetic fields. As can be seen in the frequency domain measurements, there is often a significant and complex background to the signal that makes identifying and fitting the ferromagnetic resonance peaks difficult.

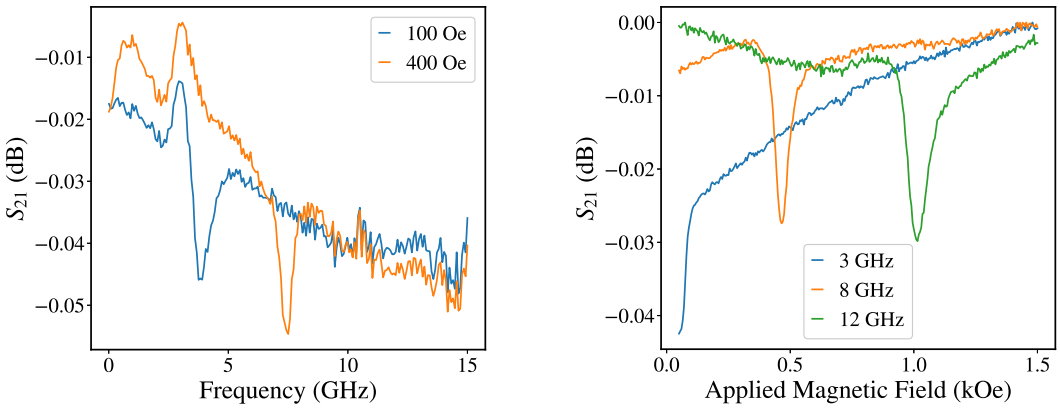

(a) (b)

Figure 7.5: (a) Measured S_{21} parameter as a function of frequency for a $Fe_{60}Co_{20}B_{20}$ (10 nm) / Pt (2 nm) sample using a VNA. (b) The S_{21} parameter for the same sample in the magnetic field domain, obtained by slicing the data.

In addition, as discussed in chapter 3, the interpretation of the linewidth in the frequency domain neglects inhomogeneous broadening. By taking a large number of small magnetic field steps, it is possible to transform the data into the field domain by slicing the data to give a fixed frequency. Figure 7.5b shows the results of this for the same sample. Assuming the background does not change significantly with the applied magnetic field, this approach removes a lot of noise in the measurement, allowing for clearer resonance peak identification. This can be further enhanced by either fitting to a window around the peak, and/or by taking a measurement of the microstrip with no sample to provide a background signal, that can be subtracted from the raw data. These approaches are discussed further in the next chapter. Figure 7.5b also shows one of the issues with the use of a unipolar power supply, which is that due to remanence in the electromagnet pole pieces, even at 0 A current, a significant remanent magnetic field is produced (around 60 Oe), which prevents resonances at lower frequencies from being accessed.

Measuring in both the field and frequency domains also allows for colour maps of the S-parameters to be produced, which can visually reveal the presence of additional resonant modes. Figures 7.6a and 7.6b show an example of this for a 50 nm thick $Ni_{80}Fe_{20}$ film divided into sub-units of 10 nm separated with a Ti layer. For the single thick film, an additional mode can be seen at high frequencies and low magnetic fields, corresponding to a perpendicular standing spin wave in the film, which vanishes to higher frequencies for the thinner film.

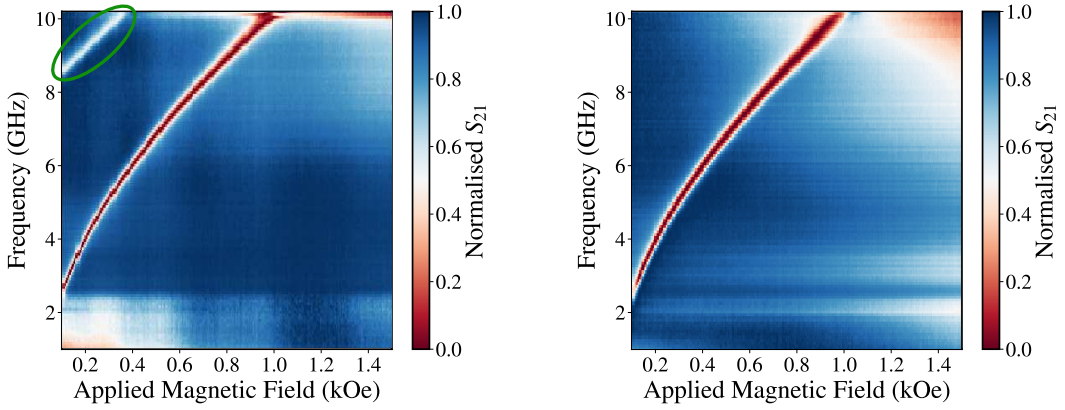

(a) (b)

Figure 7.6: Measured S_{21} as a function of both frequency and applied magnetic field for (a) $Ni_{80}Fe_{20}$ (50 nm) / Ti (5 nm) and (b) $[Ni_{80}Fe_{20}$ (10 nm) / Ti (5 nm)$]_5$. (a) also shows the presence of a signal indicating an additional spin wave mode in the thicker film (see green ellipse).

7.3.3 Development of Integrated RF System for FMR Measurements

While the system based on a VNA provides a quick measurement over large range of frequencies, it did not allow for the angular dependences of ferromagnetic resonance to be probed easily, and due to the unipolar power supply and magnetic remanence issue described earlier, the low fields and lower frequency resonances were inaccessible in the original system. These issues also prevented the FMR measurement system from being able to test 'field-free' resonance measurements of patterned synthetic structures. In order to overcome these problems, a stand-alone system was developed combining the benefits of magnetic field angle dependent measurements as in cavity-based measurements, with the broadband frequency response obtained with transmission-line techniques. Lock-in detection of the transmitted RF signal was also included to improve the sensitivity of measurements. The results obtained using this system form the second half of chapter 8, which were also published [242], and most of the results of chapter 10. Overall design of the system was undertaken by the author, with specific designs and production of the housing, microcontroller boards, and power regulation performed by Andrew Hunter of the Electronic Engineering Services Workshop in the Physics Department. Initial code to control the motors, and designs of the motor stands were produced by Katarina Henning, a RISE student, supervised by the author.

Schematic Diagram, Components and Photos

Figure 7.7 shows an illustrative schematic of the layout of the system. Here, the central control unit is responsible for all power regulation, microwave signal generation and detection as well as the control over the sample movement motors. Pre-set commands sent over a serial interface from the computer control each component and allow for the transfer of data to the computer. Figure 7.8 shows a schematic of the inside of the control unit. The role of key components will be discussed in further detail in this section. The basic mode of operation can be considered as a single-port VNA measurement, which measures only the magnitude of the signal across a transmission line.

Microwave frequencies are generated using a SynthHD RF signal generator [243], which is capable of generating frequencies from 10 MHz to 15 GHz, with a nominal power output of 10 dBm. The RF generator can also output both frequency modulated (FM) or amplitude modulated (AM) signals, with modulation frequencies up to 10 kHz. A USB connection allows for commands to set the desired output to one of two SMA connectors. The signal is propagated via an impedance matched SMA cable to the microstrip transmission line described previously, before transmission back to the control unit via a second SMA cable. The microwave power of the transmitted signal is detected using an impedance matched Schottky diode. The analogue power level can then either be directly converted to a digital signal and transferred to the computer, or used as the input to a lock-in amplifier, as detailed later in this section.

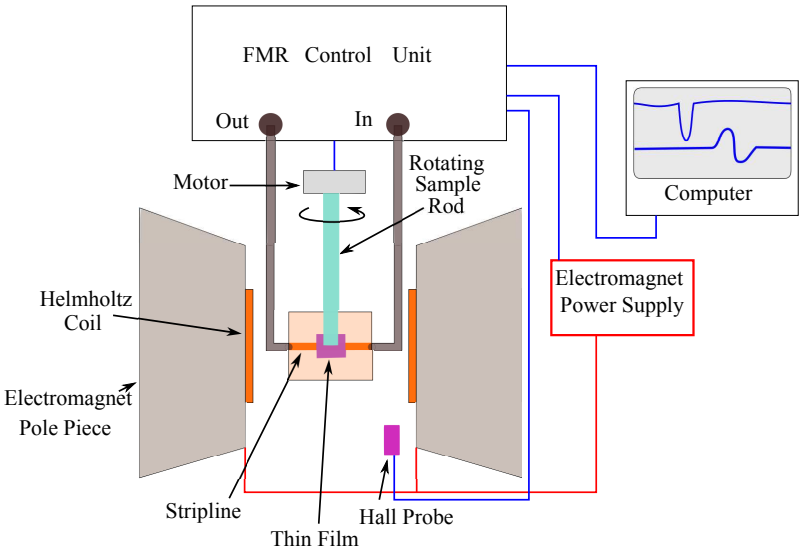

Figure 7.7: Schematic illustration of the components for the integrated FMR system, with the control unit responsible for power regulation, frequency generation and detection and rotational behaviour, rather than individualised components.

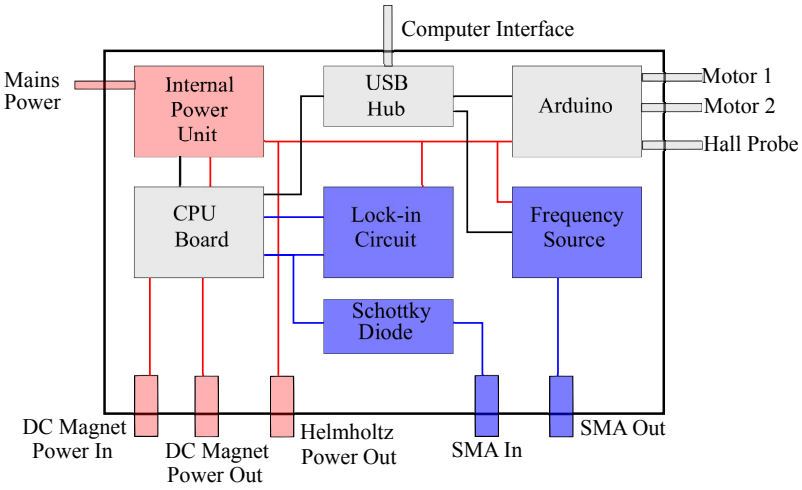

Figure 7.8: Schematic illustration of the components inside the central control unit. Blue indicates the microwave components and connections. The red components indicate power elements for the magnets. The grey units represent the control circuits.

A Cypress microcontroller [244] continuously digitised the RF diode output signal over a range -5 V to +5 V with 16 bit resolution. This value is transferred to the computer, with each measurement separated by a carriage return character. The detection of the microwave signal is only one role of the microcontroller, it also regulates the current to the electromagnet that produces the DC magnetic field and to the Helmholtz coils that generates the alternating magnetic field used to modulate the signal for lock-in detection. For both magnetic field sources, the current can be set from 0 to the maximum (1.3 A DC, 2 A AC), in 1024 steps with 10 bits resolution. This corresponds to a field step size of around 2 Oe, smaller than the field linewidths and changes in linewidth in later chapters. As the magnetic field is measured directly with a Hall effect sensor, the accuracy of magnetic field measurements is determined by the temperature characteristics of the Hall probe. For the Allegro Microsystems Hall probe used, a 10 Oe deviation occurs from the true value at the maximum operating temperature (150°) as opposed to the lab measurement temperature (25°), therefore the drift of the Hall probe is likely to be smaller than the measurement step size. The same unipolar power supply used for the DC electromagnet in the VNA-based system was used as the power source for the field controller. In this system, the power supply is set to maximum output and the microcontroller, with the aid of a heat sink, regulates the output power to the electromagnet. This is an improvement as the microcontroller allows for the polarity of the output current to be switched, which in turn, overcomes the remanence in the electromagnet pole pieces, enabling resonances at lower frequencies to be measured. The microcontroller also generates a 120 Hz voltage sine wave, which combines with

an internal power source to produce a sine wave current, with an rms current up to 2 A and 12 V. This sinusoidal current is used to drive the Helmholtz coils to produce a small sinusoidal magnetic field, in addition to the static magnetic field, to modulate the RF output for lock-in signal detection.

An Arduino Uno [245] with an Adafruit MotorShield [246], powered by an internal 12 V power source, provides the control for two stepper motors; one is used to raise and lower the sample vertically above the microstrip, and another to rotate the sample with respect to the microstrip and the electromagnet. Each motor, without adjusting the gearing ratio, provides 200 steps per full revolution (1.8° steps). In addition to the motor control, the Arduino has further analogue and digital input and output pins available. In this system, a 5 V digital output pin was used to power a Hall effect probe which provided a measurement of the magnetic field across the microstrip. The output voltage from the Hall probe is fed back to one of the analogue input pins. With no field, the output voltage of the probe is 2.5 V, half the supplied voltage. An increasing amplitude of positive or negative magnetic field then changes the output voltage until it is saturated at either 0 V or 5 V. The recorded voltage was calibrated with measurements taken using a commercial Gaussmeter at the same time, providing a conversion between Hall voltage and magnetic field at the microstrip. Figure 7.9 shows an example of a calibration curve. Commands must be first written to the Arduino's onboard memory before a computer is able to control the motors and read the Hall probe. For this system, such commands included stepping the motors forward and back, and reading the analogue input pin

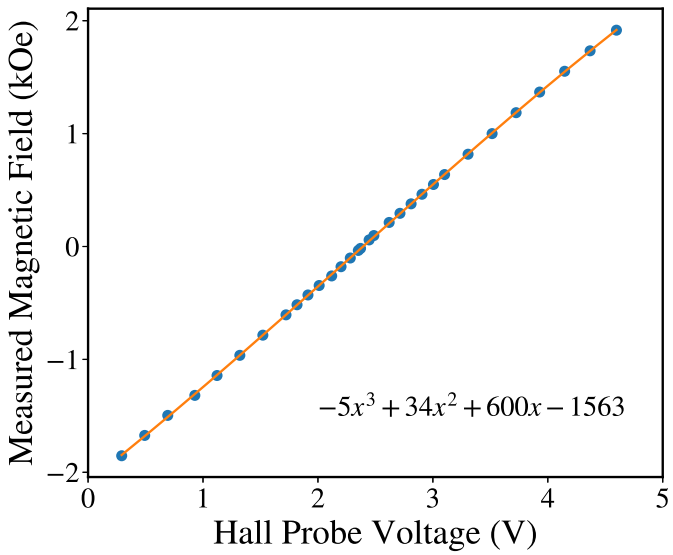

Figure 7.9: Calibration of Hall probe voltage to magnetic field across the transmission line, showing raw data with simple polynomial fit.

for a set amount of time. Once these commands are set, the Arduino can communicate with the computer over a serial interface. The interface between the Arduino and the peripheral components is via two 9-pin plugs for the motors, and an 18-pin plug for additional components, such as the Hall probe.

Figures 7.10a and 7.10b show labelled photographs of the front and back panel and figure 7.11 shows an annotated photograph of the inside of the control unit. The USB hub allows for a single point connection of the system to a computer, rather than via the individual components. The role of the gain controls and of the back panel outputs are discussed later in this section.

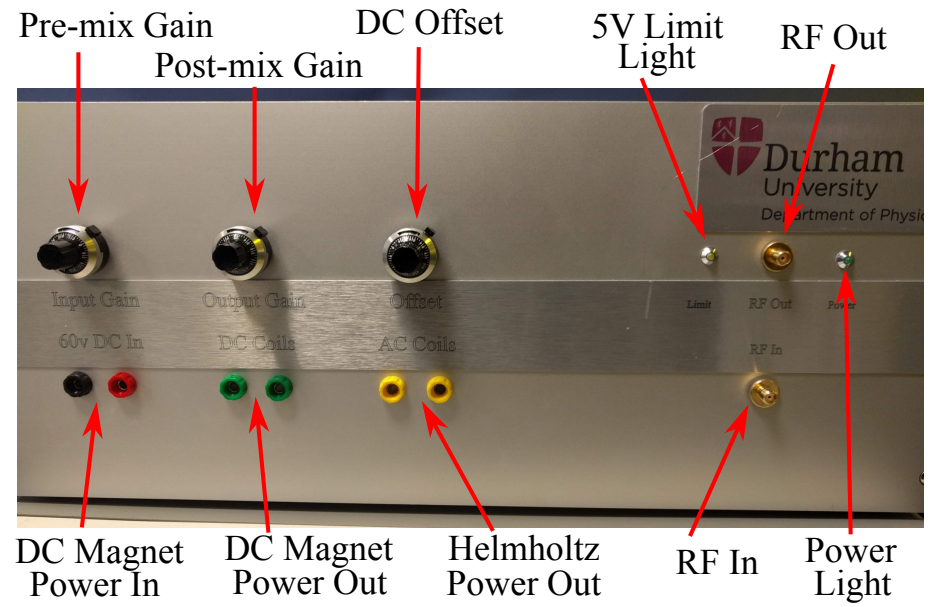

(a)

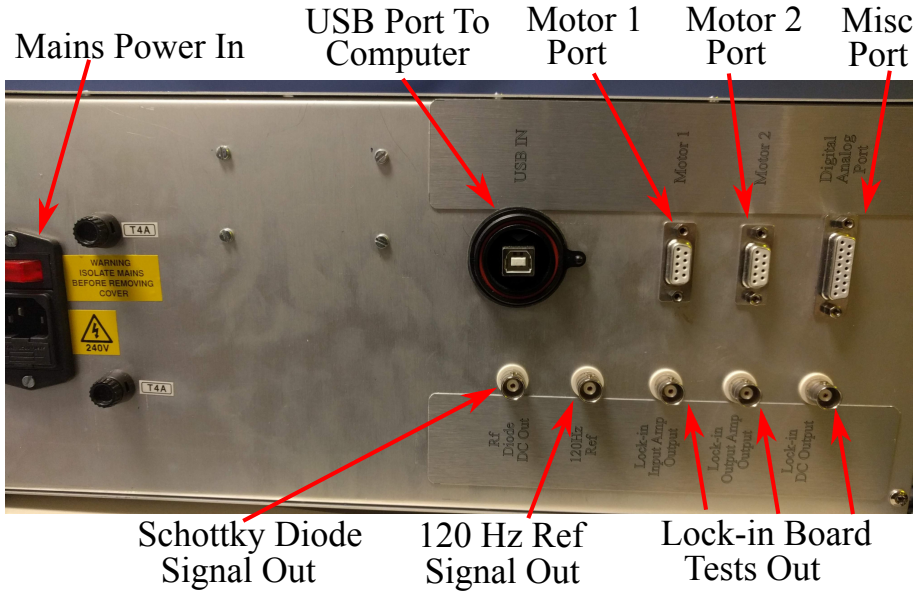

(b)

Figure 7.10: Annotated photographs of the (a) front and (b) back panels of the FMR control unit.

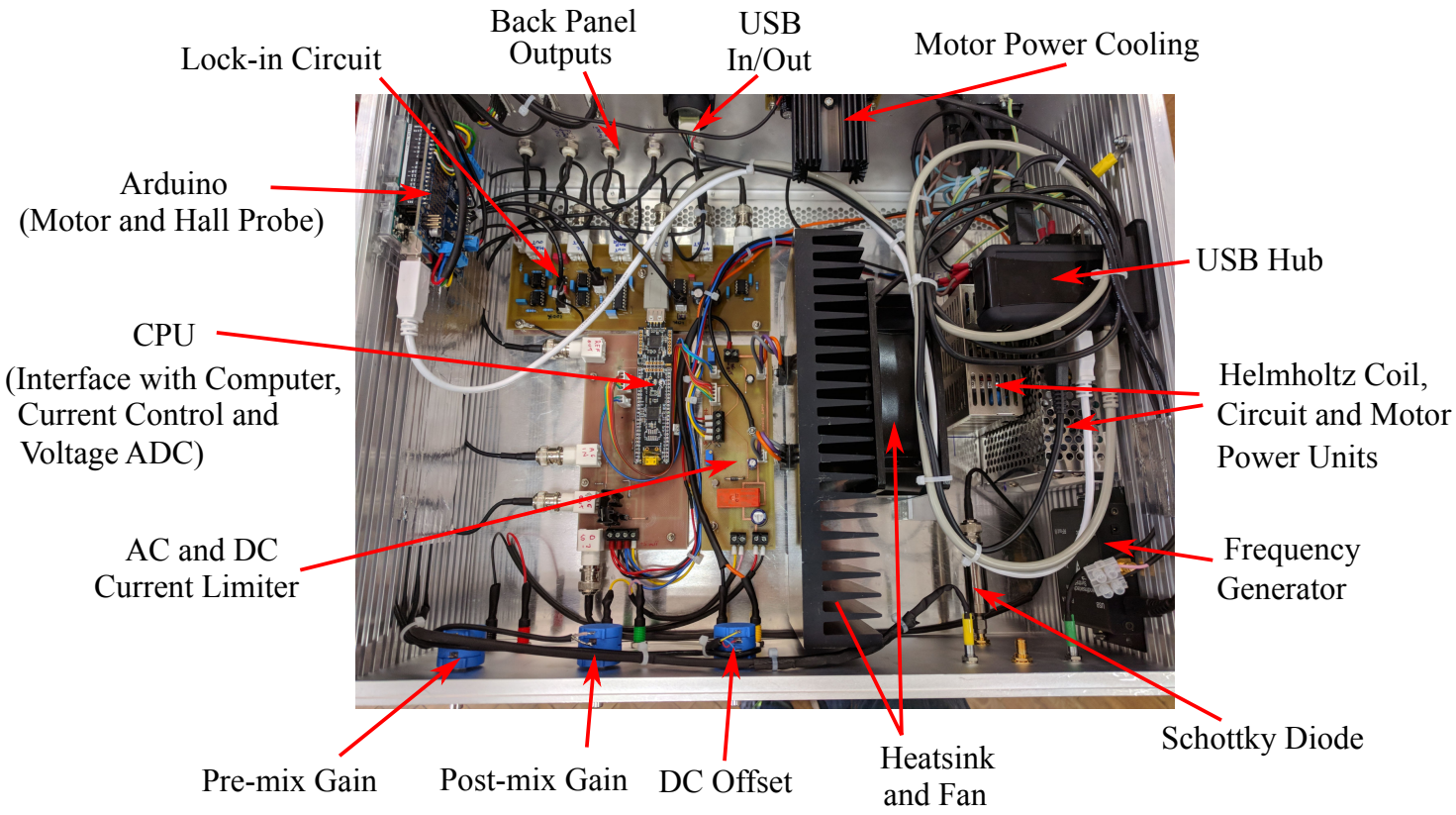

Figure 7.11: Annotated photograph of the inside of the FMR control unit.

Un-modulated RF Signal

In the simplest mode of operation, the FMR measurement can be thought of as a simple VNA operating in transmission only, where only the magnitude of the signal is recorded. At resonance, the ferromagnetic film absorbs some of the microwave energy, and hence the transmitted signal is reduced. Figure 7.12a shows a typical scan, utilising the bipolar magnetic field feature of the system, to access lower frequency resonances with low positive and negative magnetic fields. Unlike the VNA-based system, rather than continuously sweeping the frequency and stepping the applied magnetic field, the microwave frequency here is fixed and the magnetic field is stepped. Though this significantly increases the measurement time for a full frequency and magnetic field scan, it is possible to produce maps in both domains, as can be seen in figure 7.12b.

Above 7.5 GHz, an additional mode was observed in scans, as shown in figure 7.13 for a 15 nm film. This does not correspond to the standing spin waves observed with the VNA-based system as it occurs at too low a frequency for the thickness of film. In this case, the additional mode is an artefact of the SynthHD microwave source, which only has fundamental oscillations up to 7.5 GHz and above which requires a frequency doubler to generate higher frequencies. This was confirmed by measuring the output of the generator at 8 GHz using a fast oscilloscope, as shown in figure 7.14. One method to remove this artefact is to use a high pass filter before the transmission line, however, this requires scans to be stopped midway through, where

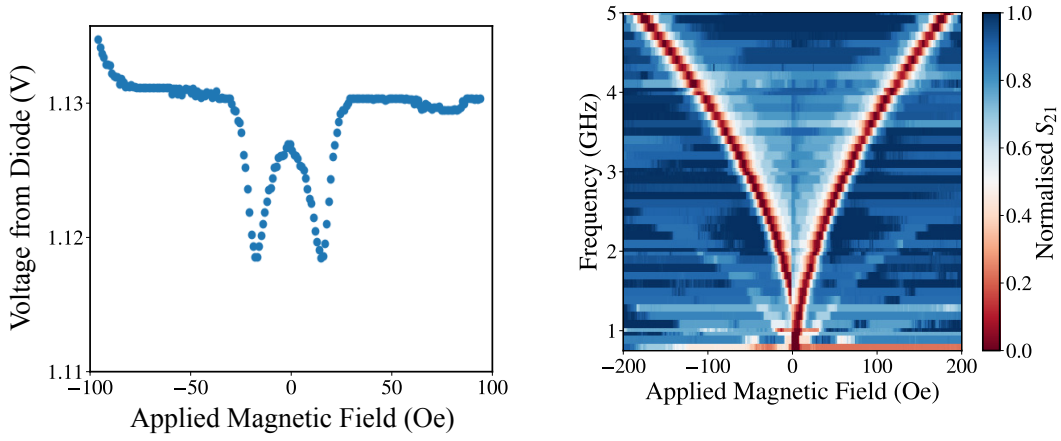

(a) (b)

Figure 7.12: (a) The measured transmission across the microstrip recorded as a voltage from a Schottky diode with a 30 nm thick $Fe_{60}Co_{20}B_{20}$ film on top of the microstrip. This was measured at a fixed frequency of 2 GHz. (b) The normalised transmission of the same film across a range of applied magnetic fields and frequencies.

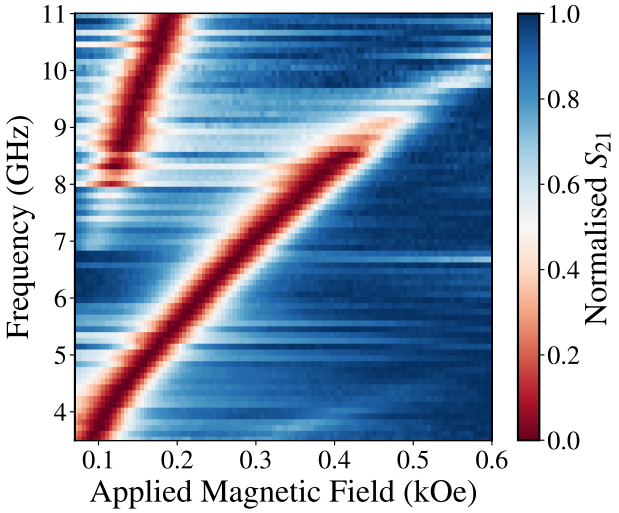

Figure 7.13: Frequency and magnetic field domain scan showing the presence of an additional mode at higher frequencies.

such scans span across the two frequency regimes. The scan window could also be adjusted to track only the resonance peak, but this requires some knowledge of the material, such as an estimation of the saturation magnetisation to use in the Kittel formula. Alternatively, when processing the data, scans with frequencies above 7.5 GHz can be split, providing an additional measurement of the lower frequency.

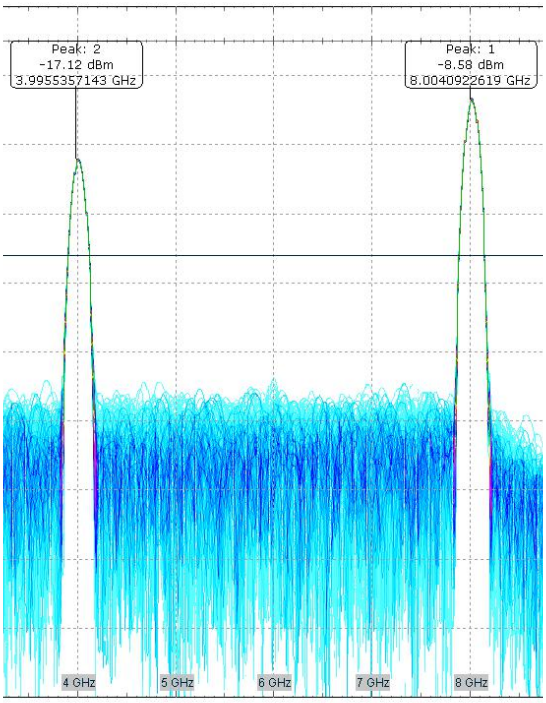

Figure 7.14: Measured output of the SynthHD generator set to 8 GHz measured using a fast Rohde and Schwarz oscilloscope, with the f/2 harmonic shown.

Modulated Output Signals and Lock-in Techniques

Lock-in detection can be utilised in order to improve the signal-to-noise ratio of any measurement by modulating and demodulating a detected signal, as the noise from frequencies other than the modulated frequency is effectively suppressed. This is most often achieved with commercial lock-in amplifiers, which operate over a wide range of frequencies and are usually costly. As only a single detection frequency was required here, a simple lock-in circuit was designed and produced for this system, based on the Analog Devices 630 chip (AD-630) [247] that uses a 120 Hz voltage wave, generated by the microcontroller, as a reference.

Figure 7.15 displays a schematic of the circuit used. The signal from the Schottky diode is first filtered before amplification with a low-noise amplifier, the gain of which is controlled manually using the left dial on the front panel of the control system. The signal is then mixed with the reference signal using the AD-630. The post-mixed signal is then passed through an integrator, the gain of which is controlled by the middle dial on the front panel, before the DC component is selected using a low pass filter. The time constant of this part of the circuit is set to 417 ms, sufficiently larger than the 120 Hz modulation time constant of 8.3 ms, such that multiple modulations are sampled, and the modulating component is suppressed by -34 dB. An offset to this DC component can be added using the right dial on the front panel, before the signal is passed to the microcontroller and converted to a digital output. If the signal exceeds the 5 V limit of the microcontroller, an LED on the front panel is illuminated as a warning.

A photograph of the circuit board without the chips populated is shown in figure 7.16. Additional outputs from the board allow for sampling of the signal at various points in the lock-in circuit, and are accessed externally through the back panel of the control system shown in figure 7.10b. The raw modulated diode output and reference are also available as outputs, allowing for the use of an external lock-in amplifier, if required.

Modulation of the transmitted RF signal can be achieved in either the magnetic field or the frequency domain. The SynthHD generator used allows for amplitude modulation of the output by producing a look-up table of amplitudes to scan over, which can be controlled with an external trigger. Figure 7.17 shows the main problem with this method, which is that small periodic voltage spikes occur each time the look-up table is started, and these are comparable in magnitude to the signal measured. Though these peaks could be removed either in data analysis by removing specific frequency components, or by better tuning of the lock-in circuit, amplitude modulation of the magnetic field provided a more robust method in this instance to modulate the signal for lock-in detection

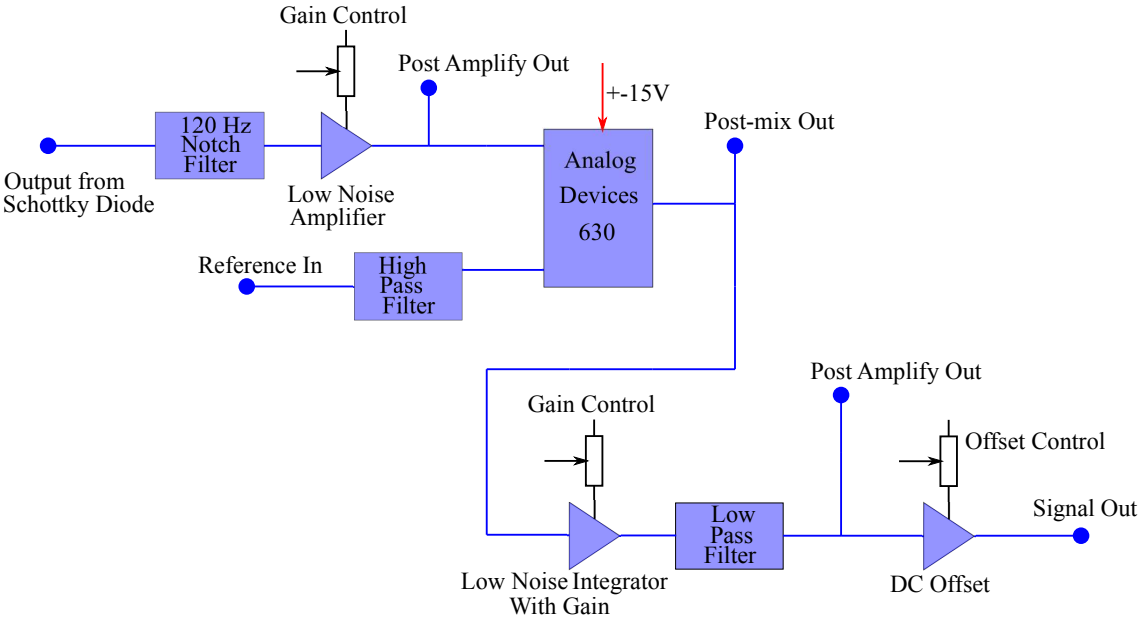

Figure 7.15: Schematic illustration of the lock-in circuit used in this system, based on the AD-630 chip.

Due to the large inductive impedance of the electromagnet it is difficult to produce a fast time-varying field superimposed on the static field. Therefore a pair of aluminium spools were designed that fit either side of the microstrip holder, as shown previously. These were wound with insulated copper wire to produce a pair of Helmholtz coils. These coils were used to generate a small alternating magnetic field modulation to the larger static magnetic field. To achieve a uniform AC field across the transmission line, the Helmholtz configuration requires a separation of the coils that is equal to the radius of the coils. A simple relation for the magnetic

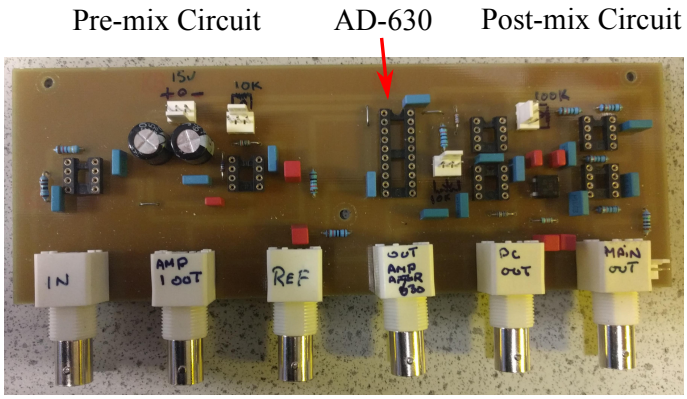

Figure 7.16: Annotated photograph of the un-populated lock-in circuit with the various outputs for each stage.

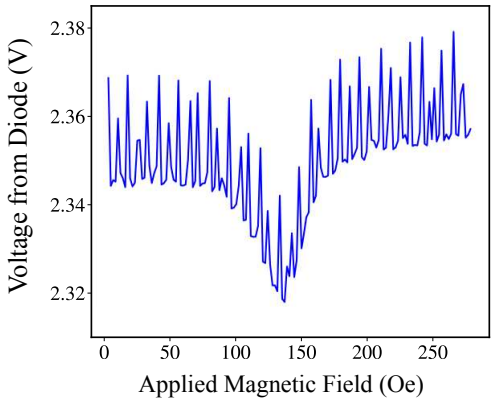

Figure 7.17: Lock-in output signal as a function of magnetic field at 4 GHz using the built-in look-up table of the SynthHD generator.

field produced at a distance, x, away from the centre of the coil, along its axis, is

$$B(x) = \frac{\mu_0 N I R^2}{2\left(x^2 + R^2\right)^{3/2}}, \tag{7.4}$$

with μ_0 the permeability of free space, N the number of coil windings, I the current, and R the radius of the coil. Ideally, to minimise heating the current should be kept as low as possible, and N maximised, however, due to the restrictions on space between the pole pieces, restricting the size of the microstrip, the separation of the centres of two spools was 26 mm, giving a diameter of 52 mm for the coil spools. Figure 7.18a shows the calculated magnetic field along the direction of the transmission line for two coils with a radius and separation of 26 mm, 100 turns of wire and a 1 A current. The calculated magnetic field is uniform to 3% over the 20 mm length covered by the sample measurement microstrip, indicated by the shaded region on the graph.

This calculation assumes there is no change in the coil diameter, or width, due to the windings. The aluminium spools designed have a width of 6 mm, which gives a depth of wire of around 4 mm with 100 turns of wire. A better approximation accounting for this difference was proposed by Crosser *et al.* [248]. Figure 7.18b shows the calculated magnetic field along the direction of the microstrip when these factors are accounted for. The actual change is minimal however, with a reduction of around 2 Oe compared to the previous model. Importantly, the field is also predicted to be uniform across the dimensions of the transmission line in this model.

Due to the modulation of the magnetic field, the output from the lock-in circuit provides the derivative of the signal with respect to the field, and thus the derivative of a Lorentzian profile must be fitted to the data to extract the physical parameters. Figure 7.19a shows example signals at three different frequencies, clipping the +-5

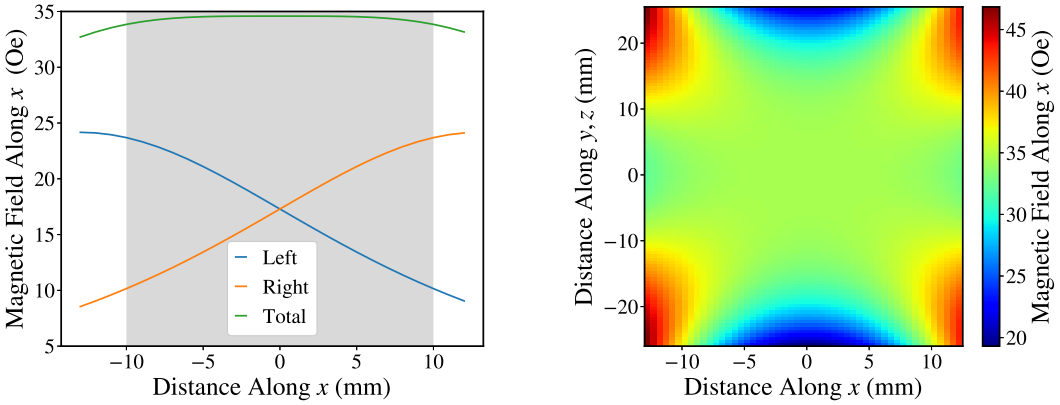

(a) (b)

Figure 7.18: (a) Calculated magnetic field across transmission line using equation 7.4 for two coils of 100 turns separated by 26 mm, with a current of 1 A. (b) Calculated magnetic field accounting for the increase in diameter due to coil winding.

V limit. It is also possible to produce a full colour map over both the frequency and field domains, as shown in figure 7.19b. However, as before with the un-modulated signal, the f/2 harmonic appears above 7.5 GHz, in addition the much smaller 2f harmonic from the frequency generator is also just visible.

The amplitude of the AC field is dependent upon the current to the coils, with the frequency set to 120 Hz, and is limited by the microcontroller to a maximum output of 2 A rms. Commands from the computer allow for 1024 steps between 0 and 2 A. The amplitude of the modulation is determined by the magnitude of the

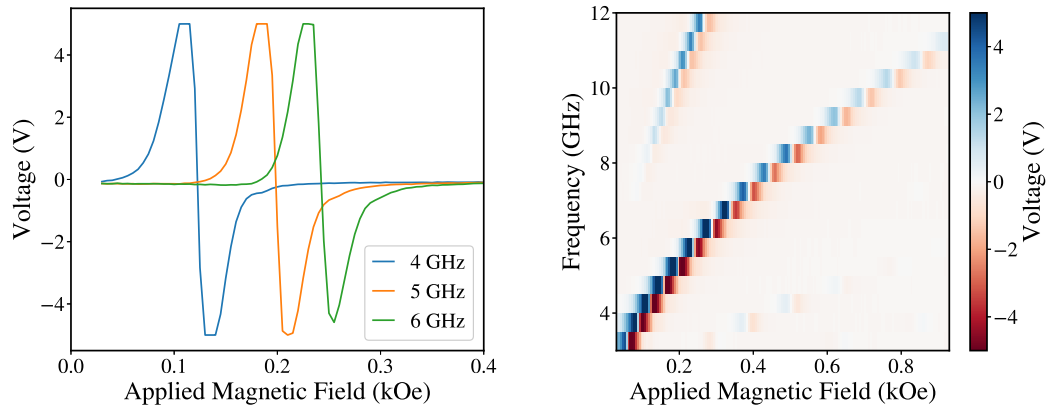

(a) (b)

Figure 7.19: (a) Measured ferromagnetic resonance signals as a function of applied magnetic field for a 30 nm $Fe_{60}Co_{20}B_{20}$ film at three frequencies using the lock-in technique. (b) The frequency and field map for a 20 nm $Fe_{40}Co_{40}B_{20}$ film measured using the lock-in technique.

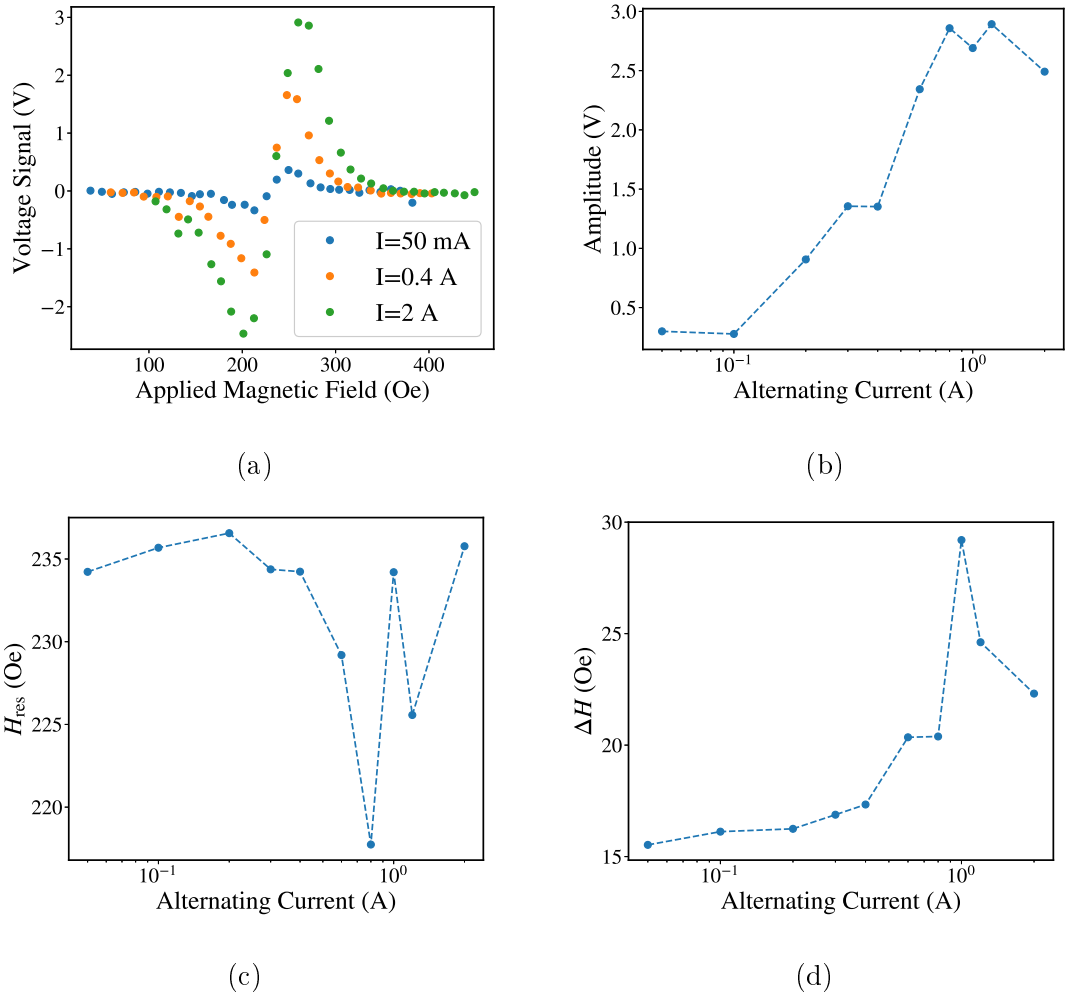

Figure 7.20: (a) Resonant signals as a function of magnetic field, for three different AC amplitudes in the Helmholtz coils. (b) The amplitude of the raw signal as a function of the current to the Helmholtz coils. (c) The resonance peak as a function of AC current. (d) The fitted linewidth as a function of AC current, assuming a first order derivative of a Lorentzian. Dashed lines are a guide.

AC magnetic field, as shown in figures 7.20a and 7.20b. For small fields, higher order expansion terms can be neglected and the profile obtained is simply the first derivative of a Lorentzian. However, for higher currents, the applied field approaches the fitted linewidth of the resonance and this approximation no longer holds. Figures 7.20c and 7.20d show the effect of increasing AC current amplitude on the fitting parameters, with both the resonant position and the linewidth decreasing in precision as the current approaches 1 A. For these reasons, it is favourable to reduce the AC current as much as possible, and amplify the measured signal using the lock-in circuit, where these parameters are unaffected.

Developing a System for Rotating the Sample in the Magnetic Field

In order to achieve similar rotational field orientation capabilities as for cavity-based systems, to enable the angular dependence of resonant behaviour to be measured, a two motor system was implemented. One motor performs the rotation of the sample itself and another is needed to raise and lower the thin film from the surface of the transmission line. The ability to control the vertical height of the sample also prevents the sample from being degraded by contact with the microstrip, and prevents damage to the copper signal line. Figures 7.21a and 7.21b show a 3D rendering of the housing and the finished aluminium housing for the motors.

For the rotation, a sample stick consisting of a 3D printed cylinder was directly attached to one of the stepper motors. The vertical motor required a drive shaft to raise and lower the rotational motor housing. An aluminium T-piece was designed to screw onto a threaded M6 brass rod coupled to the second stepper motor, such that as the motor rotated, the T-piece was raised or lowered. With the scale of the threading on the M6 rod, a full rotation of the stepper motor (200 steps), raises or lowers the T-piece by 1 mm. Without gearing, the stepper motors are capable of performing 1.8° angular steps, and therefore vertical steps of 5 μm in height control were obtained. The stand was also designed with a slot into which a portion of the T-piece fits, to minimise the translational movement of the rotational motor as it is raised or lowered. Figures 7.22a and 7.22b show photographs of the assembled motor structures with both motors attached.

Computer Control and the User Interface

Aside from the code onboard the Arduino that controls the motors, the Python programming language [249] was used for the control software. The PySerial module [250] allows for the transfer of ASCII commands across a serial interface within a Python script. A separate Python wrapper module was written by the author to provide simple instructions to be sent to the control unit, without the user having to understand the mechanics of the measurement itself. The three modular instruments which receive communication from the control software are the frequency generator, the Arduino, and the microcontroller.

The SynthHD frequency generator contains a multitude of preset commands. For the wrapper module, these were reduced to a `load`, `close`, and `set_frequency` function. The `load` function opens the serial connection, and initialises the frequency generator by setting the fundamental oscillator and turning any modulation off. The `set_frequency` function sets the desired output frequency, in MHz, and the `close` function sets the output power of the generator to the minimum, and closes the

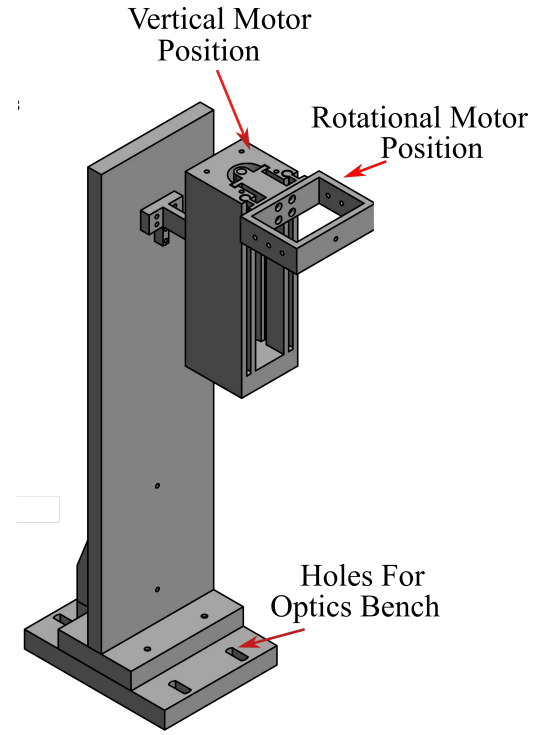

(a)

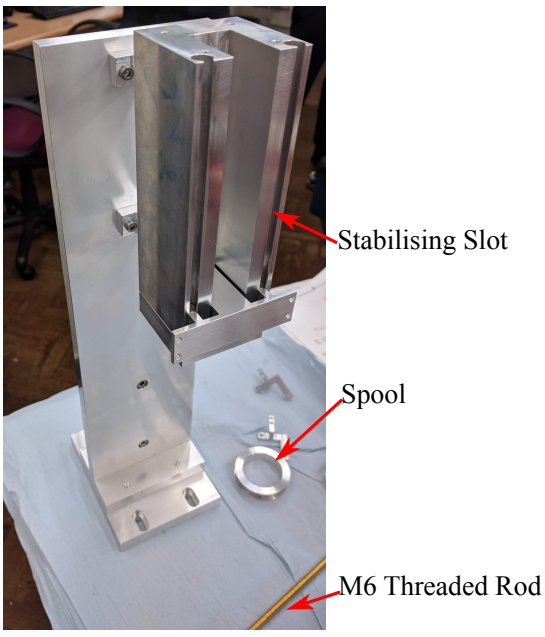

(b)

Figure 7.21: (a) 3D rendering of the aluminium structure supporting the two motors. (b) Annotated photograph of the partly assembled housing, without the rotational motor support.

connection.

The commands for the Arduino are written to the board in compiled C++. The Arduino strips the first character, a letter, corresponding to a function then reads

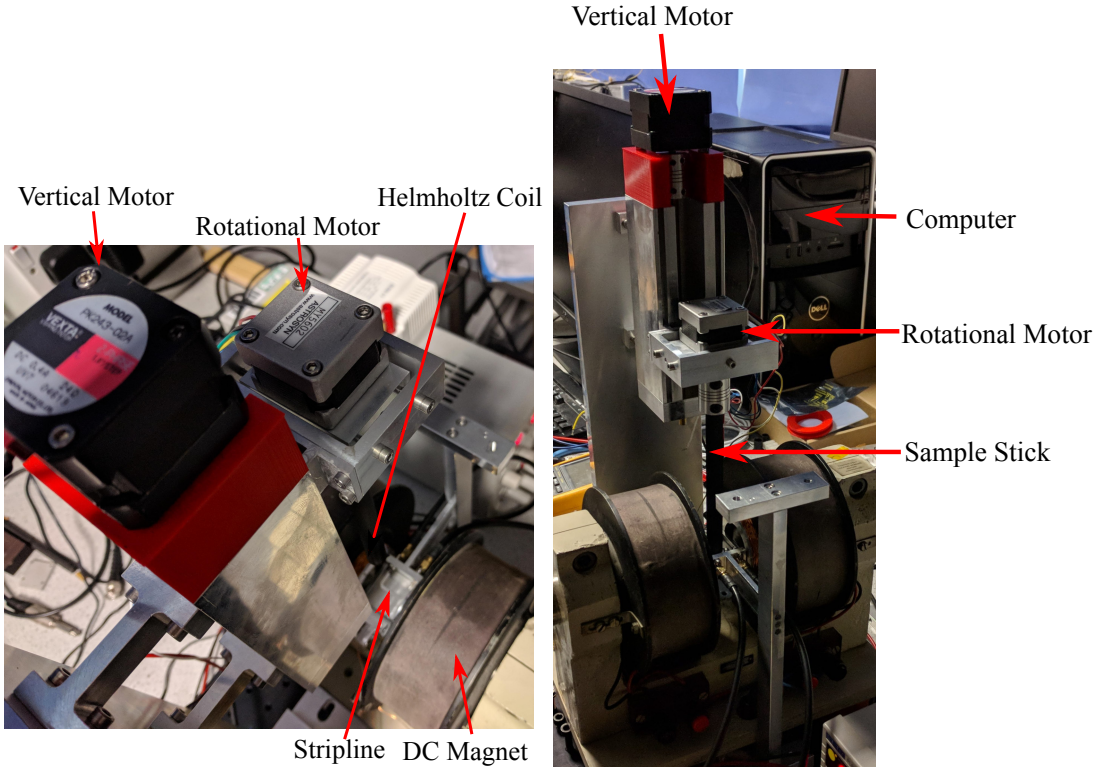

Figure 7.22: Annotated photographs of the (a) top and (b) side of the assembled sample support structure with the DC electromagnet visible.

the integer until the carriage return character, and carries out the given function a specified number of times given by a control integer, or until a stop command is received. For instance the command 'R200' will rotate the angular stepper motor by 200 steps. The wrapper function in Python simplifies this for the user into `load`, `move_x_motor`, `read_Hall_voltage` and `close` functions. The `load` and `close` functions initialise and terminate connections, the `move_x_motor` moves the corresponding motor a number of steps, and the `read_Hall_voltage` reads the input from the Hall sensor for a given time, converts it to a voltage and returns the average reading.

Commands to the microcontroller, much like the Arduino, are defined on the board itself and were written by Andrew Hunter of the Electrical Engineering Services. These also consist of a letter, followed by a 4 digit integer and a carriage return character. The DC magnetic field can be set in 1024 steps using 'DXXXX' with 'D0000' setting the output to 0 A, and 'D1024' setting it to the maximum. Similarly 'AXXXX' sets the 120 Hz current for the Helmholtz coil. The commands 'r0000' and 'R0000' reverse the polarity of the DC magnet, running the same command twice will have no effect, i.e. 'R0000' followed by 'R0000' will not reverse the polarity twice. Finally, the measured voltage direct from the Schottky diode

can be selected using 'c0000', and the signal from the lock-in circuit using 'C0000'. The board continuously sends either one of these voltages across the serial connection as long as it is open. The Python module simplifies these commands for the user into `load`, `set_AC_current`, `set_DC_current`, `measure_DC`, `measure_AC`, and `close_functions`. The two measurement functions take a dwell time as an input, and read the input from the microcontroller for the given time, returning an average value, as well as the standard error, given by the standard deviation divided by the square root of the number of measurements. This provides an error on each point in the magnetic field scan. To avoid damage to the circuit, the magnet current is first set to 0 A, before the polarity is switched.

Additional functions remove the need for user input to set these commands. The function `bipolar_field scan`, takes as inputs the minimum and maximum magnetic fields selected, a field step size, and a measurement dwell time. This function automates all of the necessary current setting and reversals of polarity, returning the field value at each point in Oe, the measured signal in volts, and the error on each point. As a fail-safe, in case any power cables become damaged, this function first applies a small DC field and attempts to measure it with the Hall probe. If a threshold value if not reached, due to cable failure or disconnection, the function sets all power to zero and closes all connections.

Finally, a user interface also was developed for general users not familiar with the Python scripting environment, a screenshot of which is shown in figure 7.23. In order to position the sample, the user has control over the vertical and rotational motors, with a stop function immediately stopping the movement. Checkboxes select either the direct DC signal input, or the use of the modulated signal with the lock-in detection and a slider is provided to set the AC current. The frequency and magnetic field boxes set the minimum, maximum and step size of the scan and a dwell time sets the number of seconds the signal is analysed at each point in the magnetic field scan. If more than one frequency is used then the frequency is fixed, and the `bipolar_field_scan` function is called at each frequency. Setting the rotational measurements and selecting a number of steps using the checkboxes performs a magnetic field sweep at each rotational angle for a fixed frequency. The data for all scans is saved as a .txt file, with the name of the file giving the frequency and the angular step, and the three columns within the file giving the measured magnetic field, output signal and the associated error on the signal. A window, shown in the top left of the screen, shows the results from the previous field scan, with a text box underneath showing the current scan number, scan completion and any error messages, such as unphysical values for the scan parameters.

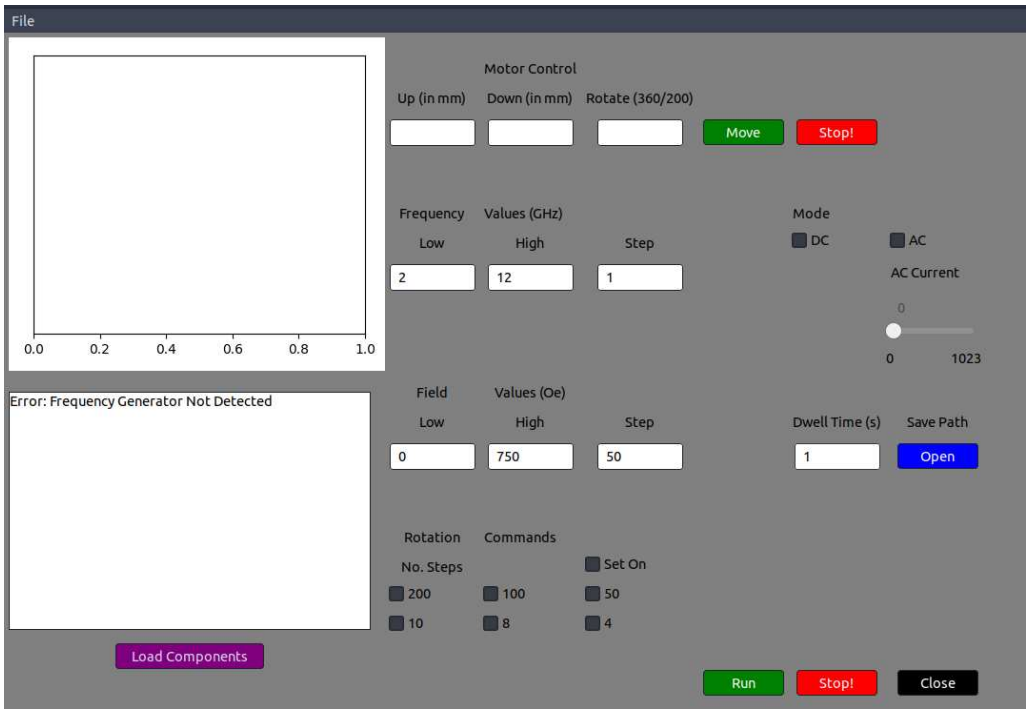

Figure 7.23: Screenshot of the user interface used to control the integrated FMR system. Details of the function of each box are in the text.

7.3.4 Testing and Demonstration of the Integrated FMR System

In order to verify the system produces an accurate response, several tests were performed, testing the accuracy, the sensitivity and ability to perform angular measurements. The results of these tests are summarised here.

Fitting Resonance Data

Un-modulated, field-swept FMR measurements in this thesis were fitted to an asymmetric Lorentzian function,

$$\chi = \chi' \sin(\phi) + \chi'' \cos(\phi) = A \frac{\frac{\Delta H}{2}\cos(\phi) + (H - H_{\text{res}})\sin(\phi)}{\left(\frac{\Delta H}{2}\right)^2 + (H - H_{\text{res}})^2} + B, \tag{7.5}$$

with χ' and χ'' representing the real and imaginary components and ϕ the mixing angle between the absorptive and dispersive components. A is the unitless amplitude, B the voltage offset, H_{res} the resonant field and ΔH the FWHM of the Lorentzian.

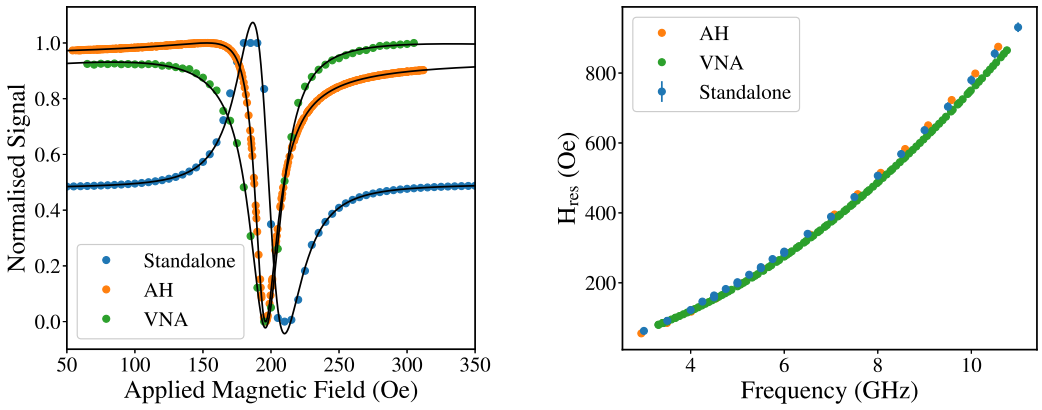

(a) (b)

Figure 7.24: (a) Measured FMR signal of the same 20 nm thick $Fe_{60}Co_{20}B_{20}$ film on three separate instruments, at 5 GHz with appropriate Lorentzian fitted. (b) Position of the resonance peak as a function of frequency for the same sample on the three systems, best fits are not shown for clarity.

For a field-modulated FMR response, the signal is fitted to the derivative, given by,

$$\frac{d\chi}{dH} = A\left(\frac{-2\left(H-H_{\text{res}}\right)\frac{\Delta H}{2}\cos\left(\phi\right)}{\left(\left(\frac{\Delta H}{2}\right)^2+\left(H-H_{\text{res}}\right)^2\right)^2} - \frac{\left(\left(\frac{\Delta H}{2}\right)^2-\left(H-H_{\text{res}}\right)^2\right)\sin\left(\phi\right)}{\left(\left(\frac{\Delta H}{2}\right)^2+\left(H-H_{\text{res}}\right)^2\right)^2}\right)+B, \tag{7.6}$$

with all terms as defined previously.

Comparison of FMR Measurement Systems

First, to test the accuracy and reliability of the integrated system, scans of a 20 nm thick $Fe_{60}Co_{20}B_{20}$ film were performed on two other systems over range of frequencies. The first was the original vector network analyser-based system, described previously, and the second a separate system designed by Dr Aidan Hindmarch (AH) based on similar principles, but with a Rohde and Schwarz frequency generator, capable of outputting frequencies up to 40 GHz. Figure 7.24a shows the raw data taken at 5 GHz for the same sample on the three systems, using the lock-in circuit for the integrated system developed here fitted with the appropriate Lorentzian. The integrated system gives $H_{\text{res}} = 197 \pm 2$ Oe and $\Delta H = 20.2 \pm 0.8$ Oe, the VNA system $H_{\text{res}} = 194 \pm 1$ Oe and $\Delta H = 21 \pm 1$ Oe, and the AH system $H_{\text{res}} = 196 \pm 2$ Oe and $\Delta H = 19.6 \pm 0.6$ Oe, which agree within error.

Fitting the data with the appropriate Lorentzian function allows for the extraction of the peak resonance as a function of frequency to be obtained, which can then be fitted to the Kittel equation. Figure 7.24b shows the results of this fitting,

with very good agreement between the three systems. With the effective magnetisation and an in-plane anisotropy as fitting parameters, the integrated system gives $4\pi M_{\text{eff}} = 14\pm2$ kG and $H_{\text{u}} = 4\pm7$ Oe, the VNA system gives $4\pi M_{\text{eff}} = 14.4\pm0.7$ kG and $H_{\text{u}} = 7.2\pm0.2$ Oe and the AH system $4\pi M_{\text{eff}} = 13.6\pm0.5$ kG and $H_{\text{u}} = 19.0\pm0.5$ Oe. The discrepancy between the values in the anisotropy may be attributed to the positioning of the sample on the transmission line, as the alignment may differ by a few degrees, which would shift the resonance position if the field was not aligned with any uniaxial anisotropy axis.

Measurement Sensitivity of the Integrated FMR System

The sensitivity of the integrated system was first tested by measuring progressively thinner films until the signal could no longer be measured above the noise using the highest gain settings. Figures 7.25a and 7.25b show the limits of the system, with two highly-damped films. With a 5 nm thick ferromagnetic layer, the signal is just discernible above the noise. It may be possible to enhance this further by undertaking background subtraction of the transmission line with no sample.

A second test of the sensitivity of the system involved raising a 20 nm thick $Fe_{60}Co_{20}B_{20}$ film above the microstrip and measuring the effects on the fitted linewidth and resonant peak centre. The sample was first placed in direct contact with the transmission line before the sample mount was lowered with double sided tape and bonded to the sample. Magnetic field scans were performed at increments in sample height above the transmission line at the same frequency. Figures 7.26a and 7.26b show the variation of the linewidth and resonant peak as the film was raised up to

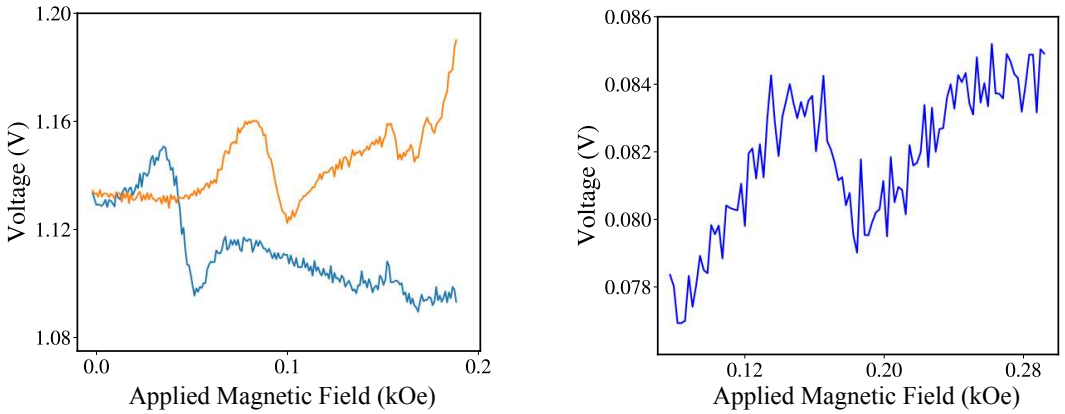

Figure 7.25: Ferromagnetic resonance magnetic field scans of (a) a Pt (2 nm)/ $Fe_{60}Co_{20}B_{20}$ (8 nm)/ Ta (3 nm) sample at two frequencies and (b) a Pt (2 nm)/ $Fe_{60}Co_{20}B_{20}$ (5 nm)/ Ta (3 nm) sample at a single frequency.

3 mm above the microstrip. There is little change in the fitted parameters until around a millimetre in height, which may be due to the calibration in the DC magnetic field no longer holding, or the inhomogeneities in the RF magnetic field at this height.

FMR Behaviour as a Function of Sample Angle

A final test of the integrated system was the testing of the ability to measure any angular dependence of ferromagnetic resonance resulting from anisotropies present within a sample. Patterned ellipses of 40 nm thick $Fe_{40}Co_{40}B_{20}$ with dimensions of 10 μm $\times$ 40 μm were produced using the photolithographic procedures detailed in chapter 5 in order to impose a uniaxial shape anisotropy. Figure 7.27a shows an image of these ellipses. Magnetic field scans were performed with the sample located 100 μm above the microstrip as a function of in-plane field angle, with 25 steps per full rotation (14.4°) at two frequencies, 4.5 GHz and 6.5 GHz. Figure 7.27b shows an example of the raw data obtained at two angles. The shift in resonance peak to a lower magnetic field at 90° is due to the external magnetic field aligning with the long axis of the ellipse, and hence reinforcing the magnetic anisotropy, which increases the effective field and therefore resonance occurs at a lower applied magnetic field.

The results of performing this scan over the full in-plane angular range are shown in figure 7.27c, where a clear sinusoidal behaviour is observed as a consequence of

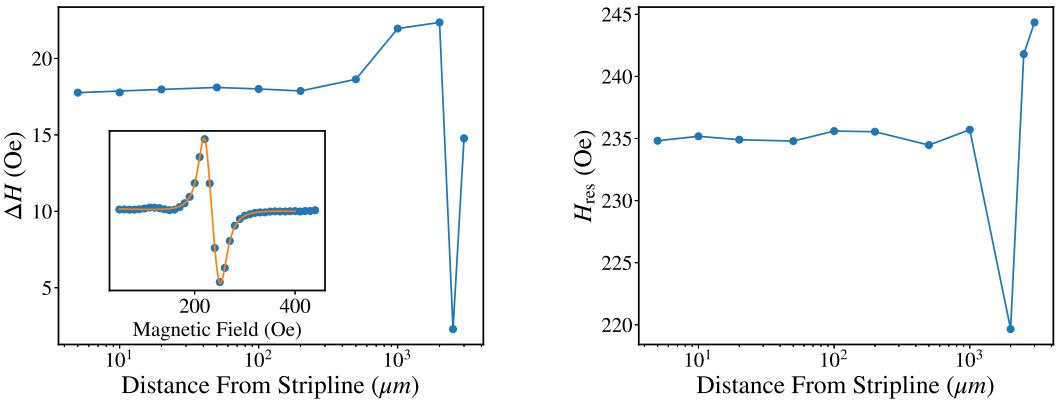

(a) (b)

Figure 7.26: (a) FMR linewidth determined as a function of sample height above the transmission line. Inset is an example of the FMR data measured with a magnetic field sweep (blue), with best fit to the derivative of a Lorentzian profile (orange). (b) Resonance peak value in the magnetic field domain as a function of height above the microstrip. The solid lines are a guide to the eye.

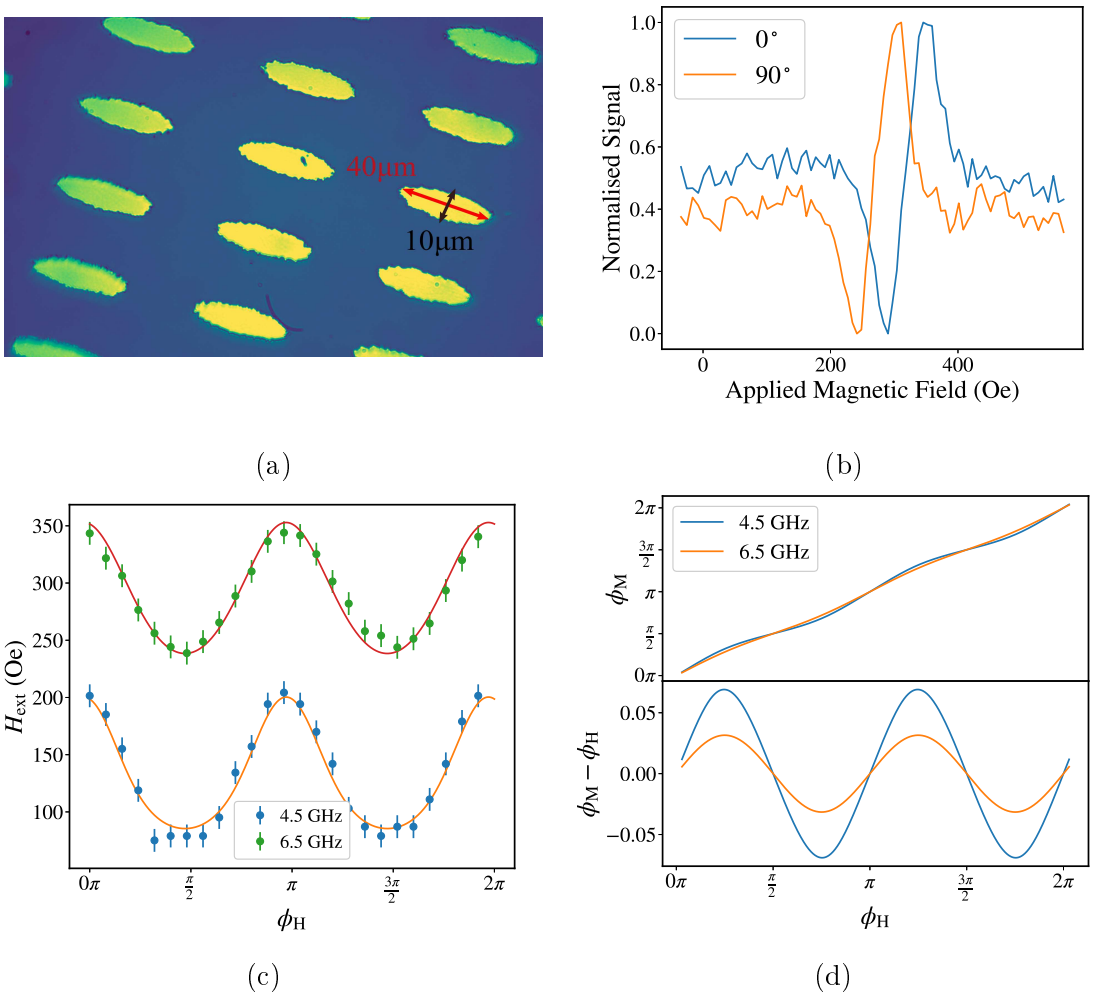

Figure 7.27: (a) Optical micrograph of the patterned ellipse shapes. (b) FMR data from a magnetic field sweep taken at 0° and 90° at 6.5 GHz. (c) Dependence of the fitted resonance peak centre as a function of angle, with associated best fit for two fixed frequencies. (d) Extracted direction of the angle of magnetisation as a function of angle of applied field, and the phase difference between the two at the two frequencies.

the field aligning along the long and short axes of the ellipse. Analysis of these datasets was undertaken by fitting simultaneously using the framework for angular behaviour, described in chapter 3 and shared the same free parameters (effective magnetisation and anisotropy field) with only the frequency changing between them. This fitting gives $4\pi M_{\text{eff}} = 18 \pm 1$ kG and $H_{\text{u}} = 58 \pm 5$ Oe, which corresponds to resonance without an external field present at 2.9 GHz. As a result of the equilibrium conditions, the angle of magnetisation, ϕ_{M}, is also determined as a function of the applied magnetic field angle, ϕ_{H}, shown in figure 7.27d. For 4.5 GHz frequency, the phase difference between ϕ_{M} and ϕ_{H} is larger as the external field is closer in magnitude to the anisotropy field and hence the magnetisation remains 'pulled'

towards the long axis of the ellipse for a greater angular range.

7.4 Summary

In conclusion, the two main methods of measuring dynamic magnetic materials in the frequency domain, cavity-based and vector network analyser-based, were introduced. For each technique, a brief description of the measurement process and the advantages to the technique were detailed. Following this, the development of a system to measure FMR based on a VNA was described. This system, while providing broadband frequency measurements, did not allow for angular behaviour, or low frequency responses to be probed.

A low-cost integrated system was therefore developed to measure ferromagnetic resonance. The system combines the benefits of angular measurements of cavity-based measurements with broadband transmission-line based measurements. The system operates from 10 MHz up to 15 GHz, is capable of 1.8° angular steps with respect to the in-plane magnetic field, and 5 μm vertical steps of the sample from the waveguide. Measurements can be undertaken using both direct transmission line and field-derivative techniques, provided by an integrated lock-in amplifier. The integrated system developed here produces comparable results with those obtained using other research systems, and has been used to obtain the results presented both in this thesis, and in published work.

Chapter 8

Interfacial Phenomena I: Spin Transport

8.1 Introduction

This chapter presents the results of two studies into controlling the damping via interfacial spin transport. The first half focuses on the methods and the underlying principles and parameters which enhance damping and control the frequency bandwidth response. One particular focus is directed towards discrepancies between the parameters of interest in the literature. Building upon a model explained in the literature, it is shown here that discrepancies between these reported parameters can be addressed [109].

The second half of the chapter discusses methods to suppress any interfacial enhancement of damping by the insertion of an insulating layer between the ferromagnetic layer and the heavy metal. By considering the interfacial structure, the thickness of insulating barrier required to treat each layer in a multilayered system as dynamically separate was determined. For the system under investigation, it was found that spin transport is fully suppressed once a complete layer of insulator has been formed [242].

8.2 Ferromagnetic/Heavy Metal Thin-film Systems

The bandwidth of the frequency response of a resonant ferromagnetic material is determined from the linewidth of the absorption, which, in turn, is directly linked to the Gilbert damping parameter. As discussed in chapter 3, by placing a suitable heavy metal layer in contact with a ferromagnetic layer, the overall damping is enhanced as an additional interfacial channel for energy loss becomes available. In the spin pumping formalism, a spin current is transmitted across the FM/HM interface, and the magnitude of the damping enhancement is determined by two key parameters associated with the heavy metal layer, i.e. the spin mixing conductance, which quantifies the number of conductance channels, and the spin diffusion length, which determines the lengthscale over which the coherent spin current propagates, as discussed previously. In order for broadband devices based on highly damped materials to be realised, the underlying physics and material parameters must first be understood. However, for common spintronic materials such as Pt, the values of the interfacial parameters vary greatly.

This section describes the results of a published study [109] that builds upon previous work and presents a resolution to these reported discrepancies. Concepts and previous measurements in the literature are first discussed before the functional analysis and the pitfalls associated with the analysis of damping in ultrathin films are presented. Finally, the key parameters and lengthscales in FM/HM systems with varying interfacial structure are shown.

8.2.1 Physical Mechanisms of Spin Transport and Conflicting Measurements

Spin transport across interfaces is determined by a combination of factors associated with the materials involved and details of the structure at the interface, which is often embodied by the effective spin-mixing conductance parameter, $g_{\mathrm{eff}}^{\uparrow\downarrow}$ [112, 251, 252], for which higher values are associated with more significantly enhanced damping, and hence a broader resonant response. The magnitude of the damping enhancement depends on both the FM layer parameters, such as the thickness and saturation magnetisation, and the HM layer parameters, including the thickness, spin-diffusion length and spin-flip probability [113, 126]. As this spin transport is strongly linked to the interface, the damping enhancement also depends on the transparency of the FM/HM interface, quantified by the spin-mixing conductance, or with the spin-flip scattering associated with the interfacial structure, which has often been termed spin-memory loss in this context [253, 254].

These key transport parameters remain the subject of debate, with the reported

values in the literature seemingly affected by the different experimental methods and analyses. In particular, values for the spin-diffusion length of the HM layer are inconsistent between techniques, while the role of the interface structure and its influence on the effective spin-diffusion length is not clear. The transport properties of FM/HM systems have been probed with several techniques, including but not limited to: magnetoresistance [253, 255, 256]; magneto-optics [9]; spin Hall angle [8, 133, 257]; ferromagnetic resonance (FMR) [17, 258–262] and combinations of these techniques [254, 263–265]. Despite, or perhaps because of, the wide range of experimental techniques and analyses, a range of values for the spin-diffusion length, λ_{sf}, have been reported for Pt at room temperature that varies by over an order of magnitude from 1.2 nm up to 11 nm [8, 9] from these different methods, with FMR measurements typically giving lower values for λ_{sf} than spin Hall measurements [8, 260, 266, 267].

The influence of crystallographic structure at the interface on the efficacy of spin-pumping and the spin-mixing conductance has also been reported [268–270], with recent experiments highlighting the importance of interfacial structure on the damping parameter measured with ultra thin HM layers (< 2 nm) [108]. Additional reports also suggest that proximity induced magnetisation of the HM layer may play a role [17, 271] in interfacial spin transport, with other work suggesting it is irrelevant [18]. This conflict forms the basis of part of the results detailed in the next chapter.

Despite the range of systems studied in the literature, the factors affecting spin transport across FM/NM boundaries remain the subject of debate. The contributions to $g_{eff}^{\uparrow\downarrow}$ related to interfacial structure, spin diffusion length and spin Hall angle are not clearly defined. Spin-mixing conductance is often measured and determined for a single HM thickness, which can lead to $g_{eff}^{\uparrow\downarrow}$ behaving as a catch-all term that then critically affects the determination of the spin diffusion length.

Transition metals such as Ru and Pt are particularly useful for enhancing damping in FM/HM systems via spin pumping mechanisms [259, 272], for control of perpendicular magnetic anisotropy (PMA) [273, 274], and for enhancing spin orbit torques when used in combination [275]. As described in chapter 3, it is expected that in these materials the dominant spin relaxation is the Elliot-Yafet (EY) mechanism [116–118]. The EY mechanism involves a probabilistic spin-flip scattering at each momentum scattering event, with the spin relaxation time, τ_s, and the λ_{sf} proportional to the momentum scattering time and the mean free path, τ_e and l_e.

Recently Sagasta *et al.* reported a dependence of λ_{sf} on the resistivity, ρ, for thin film Pt [276] and building on this Nguyen *et al.* reported the product $\lambda_{sf}\rho$ as a constant for a given HM layer [277]. In this thesis, this concept was developed

in a study on the *thickness* dependence of the HM layer, as a route to determining reliable values of λ_{sf} from FMR measurements of the damping. Additionally, the contribution of the spin diffusion length to $g_{eff}^{\uparrow\downarrow}$ were studied with an amorphous ferromagnet (CoFeB/Pt) and two different crystalline (Co/Pt and Co/Ru) interfacial textures as a function of the thickness of both the HM and the FM layers in order to understand the role of interfacial structure.

8.2.2 Static and Dynamic Magnetic Analysis of Ultrathin Films

The thin films used in this section were fabricated in Durham using magnetron sputtering onto thermally oxidised Si wafers, as detailed in chapter 5. For Pt HM layers, a series of samples with varying Pt thickness (0-2 nm) were grown in both HM/FM and FM/HM layer configurations, where the FM layer was either Co or $Co_{20}Fe_{60}B_{20}$ (CoFeB). For each Pt thickness the FM thickness was varied to create the fuller dataset needed to properly determine $g_{eff}^{\uparrow\downarrow}$. For Co, the thickness was varied from 2 to 5 nm. This range allowed for in-plane magnetisation and up to 5 nm maintains an fcc structure that forms during early stage growth [268]. For amorphous CoFeB, the thickness was varied from 2 to 15 nm. All Pt samples were capped with a protective 2 nm layer of Ta, which formed a surface oxide layer that has negligible contributions to the spin pumping, as reported elsewhere [258]. For Ru layers, the thickness was varied up to 9 nm. Ru has hcp texture, so for these samples only HM capped FM layers were grown, to prevent the hcp texture influencing the fcc growth of sub-5 nm Co. Fcc Co samples were obtained below 5 nm and hcp Co between 10 and 30 nm. The Ru samples were capped with 5 nm of Cu to prevent oxidation. Figure 8.1 shows a grazing incidence x-ray diffraction measurement on two of the Co samples, showing the presence of the two phases of Co above a thickness threshold, with peak positions comparable to previous studies [278–280].

In-plane angular static magnetic characterisation was undertaken using MOKE and examples of the coercivity and magnetic remanence data are shown in figure 8.2, for a 5 nm CoFeB FM layer. Although there are small variations in the magnitude of the coercivity with a Pt cap and buffer compared to the control sample without, the overall angular dependence remains the same, showing a typical in-plane anisotropy, which is largely unchanged by the introduction of a HM layer. The difference in magnitude is likely due to the growth mechanics of the FM on the Pt, compared to the FM without Pt. The magnetic easy axis was marked on the back of each sample, which provided a reference to measure the easy axis with FMR.

In order to measure the dynamic magnetisation frequency response of these ul-

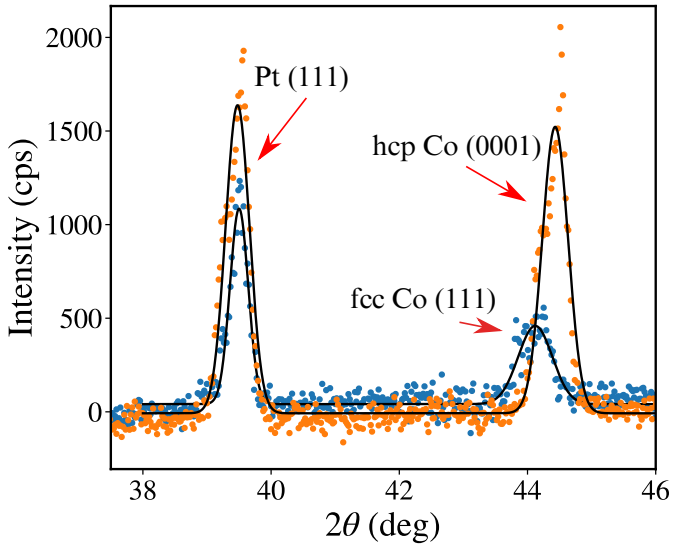

Figure 8.1: Grazing incidence x-ray diffraction for a Co (5nm) / Pt(2nm) (blue) and a Co (15 nm) / Pt (2 nm) film (orange), showing the two phases of Co present.

trathin FM layers, a VNA was set to undertake multiple averages of each frequency scan to reduce the background noise as much as possible. To fit the data efficiently it was necessary to iterate through datasets to generate an initial estimation of peak resonance position. However, in the presence of a large background signal, this becomes complex as shown in figure 8.3a, where the peak of the signal is no longer the minimum in the transmission data. Either by taking the gradient of the signal, or the maximum difference between datasets, (assuming that the background is largely constant), the peak position can be better identified.

Fitting the data to a window around the peak position provides a more accurate

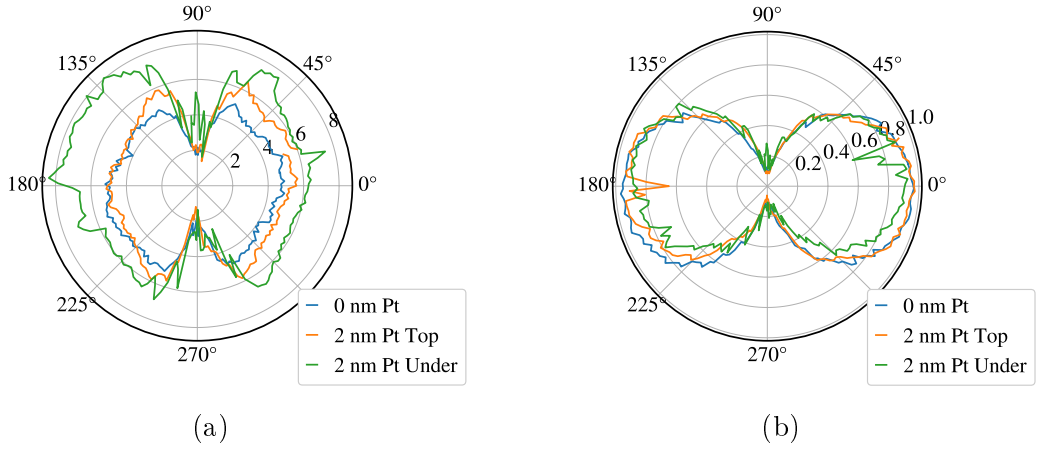

(a) (b)

Figure 8.2: Polar plots of (a) coercivity and (b) magnetic remanence ratio of a 5nm CoFeB layer with a Pt cap and buffer layer, measured using longitudinal MOKE.

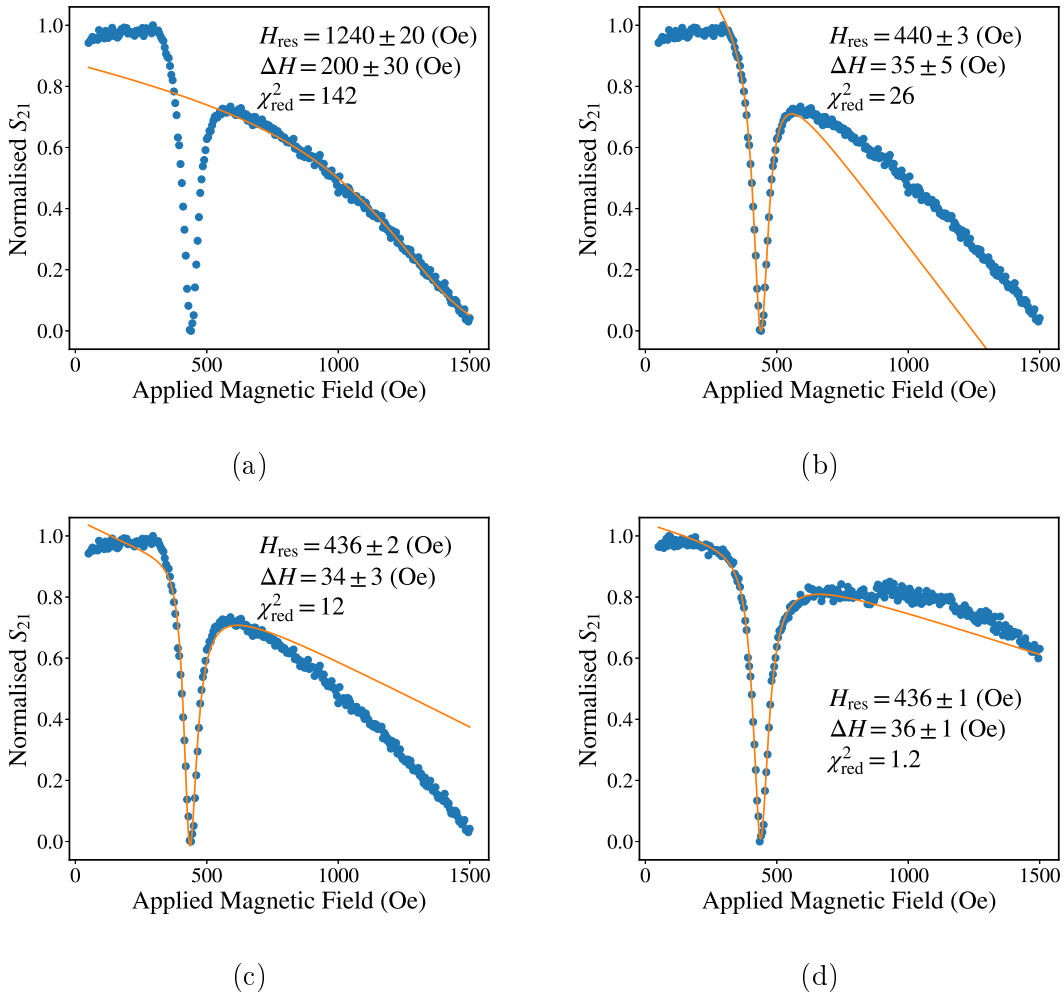

Figure 8.3: Measured S_{21} parameter as a function of the applied magnetic field for a 10 nm CoFeB sample with 8 GHz RF excitation. The raw data is in blue and best fits in orange, with (a) a best fit using the initial resonance position assumed as the minimum value in the signal, (b) the best fit using the maximum gradient with a 20 point window, (c) the best fit using the gradient with a 40 point window and (d) the best fit using a 40 point window with a background subtraction.

fit, however as shown in figures 8.3b and 8.3c, the size of the window alters the resultant fit. An additional procedure to improve the accuracy of the fit was to undertake a scan with no film present to provide a background which can then be subtracted from the data. Figure 8.3d shows the resultant fit for a single frequency using this procedure, while a comparison of figures 8.4a and 8.4b shows the increased clarity in both frequency and magnetic field domains, achieved with the removal of the background.

While figure 8.4b showed an example of the data at each frequency, the two parameters of interest from the fitting are the peak position of the resonance, to which the Kittel curve is fitted, and the linewidth. The resonant linewidth in mag-

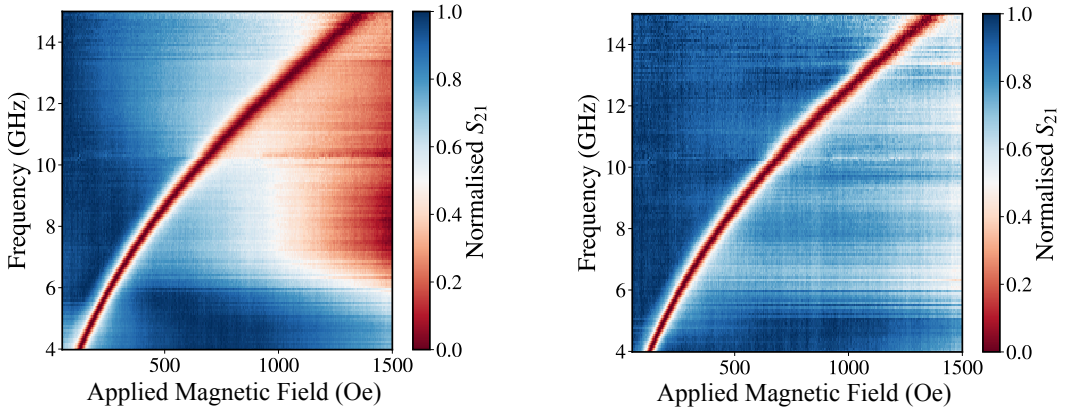

Figure 8.4: Full frequency and magnetic field domain map for the 10 nm CoFeB sample, showing (a) before and (b) after the background signal has been subtracted.

netic field, ΔH, as a function of frequency, f, allows the intrinsic and extrinsic contributions to damping to be extracted via

$$\Delta H = \Delta H_0 + \frac{4\pi\alpha}{\gamma} f, \tag{8.1}$$

where ΔH_0 is the extrinsic damping related to defects [108], α the intrinsic Gilbert damping parameter and γ the gyromagnetic ratio, as detailed in chapter 3. Figures 8.5 and 8.6 show the extracted field linewidths as a function of frequency with best fits for the systems used in this section.

8.2.3 Magnetisation-g-factor Relation and Interfacial Damping

The resonant condition for in-plane FMR of a thin film is given by the Kittel formula [74],

$$f = \frac{\gamma}{2\pi}\sqrt{H_{\text{res}}(H_{\text{res}} + 4\pi M_{\text{eff}})}, \tag{8.2}$$

with H_{res} the magnetic field at resonance, determined from the fit to the FMR data, and the effective magnetisation, M_{eff}, which takes into account any interfacial anisotropy terms. The spectroscopic g-factor, embodied via γ in equation 8.2 can complicate the fitting of resonance curves, due to its correlation with the effective magnetisation. As discussed in chapter 3, the g-factor is given by the ratio of the orbital, μ_{L}, to the spin, μ_{S}, magnetic moments commonly given as $g = 2\,(1 \pm \mu_{\text{L}}/\mu_{\text{S}})$ [28]. In bulk systems the orbital term is quenched by the crystal field, however, at interfaces the symmetry is broken, leading to an enhancement of μ_{L} that leads to variations in the magnitude of the g-factor, which is often one of

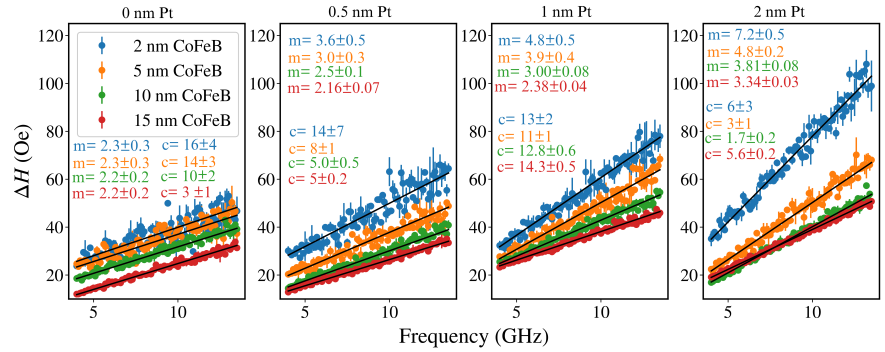

(a)

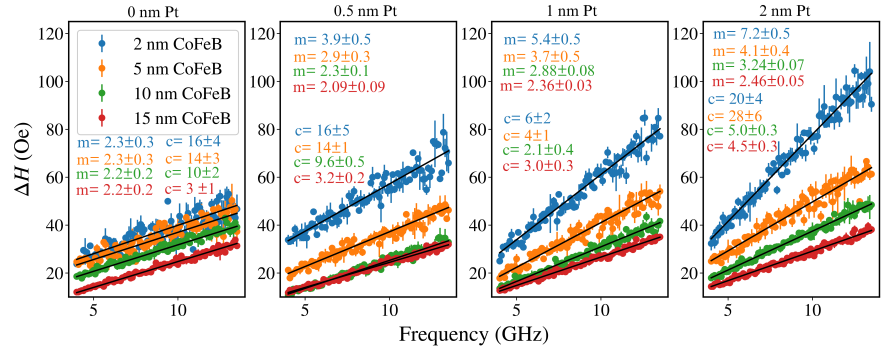

(b)

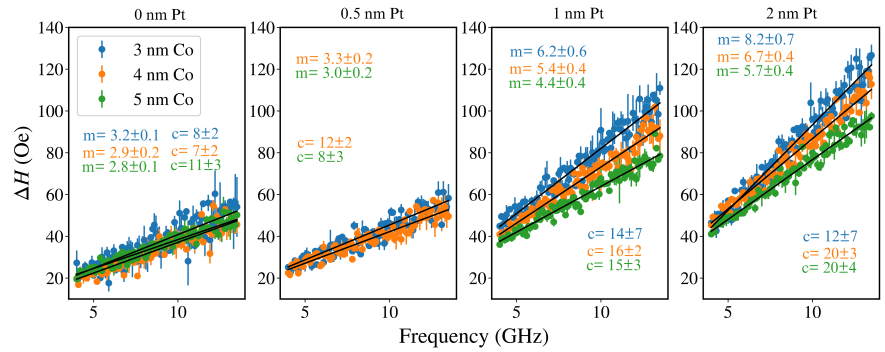

(c)

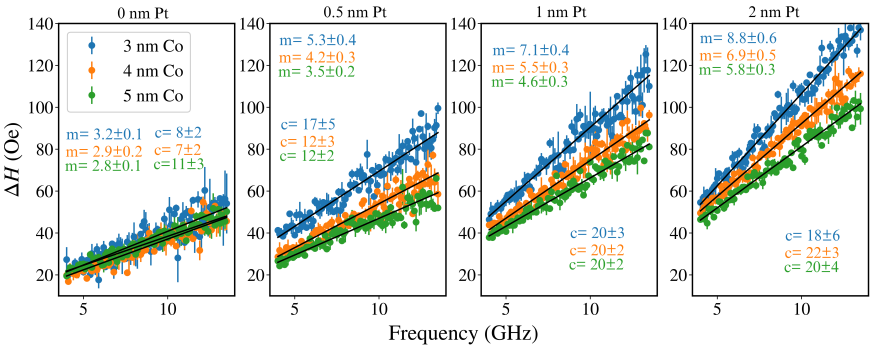

(d)

Figure 8.5: Data and best fits to the field linewidth as a function of frequency for (a) Pt/CoFeB, (b) CoFeB/Pt, (c) Co/Pt and (d) Pt/Co systems. The gradient of the best fitting straight lines in (b) are proportional to the Gilbert damping.

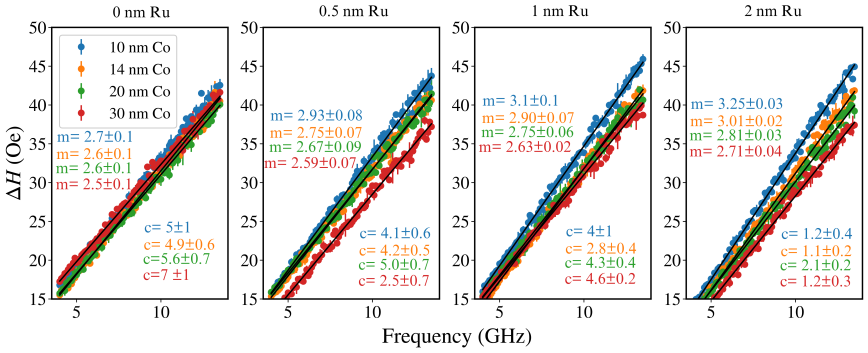

(a)

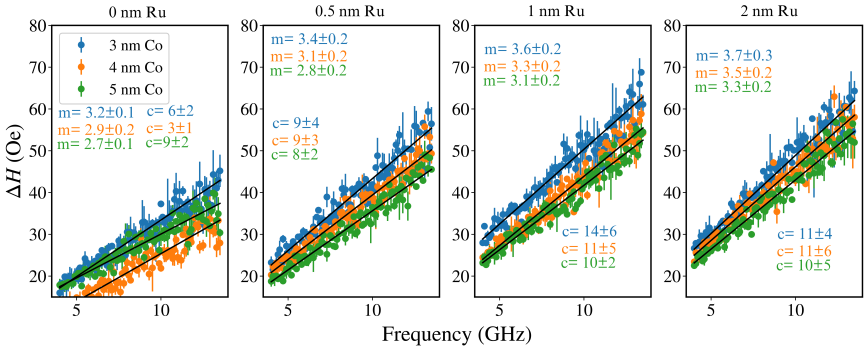

(b)

Figure 8.6: Data and best fits to the field linewidth as a function of frequency for (a) hcp Co and Ru and (b) fcc Co and Ru. The gradient of the best fitting straight lines in (b) are proportional to the Gilbert damping.

the parameters of interest in FMR experiments.

However, at low resonant frequencies, changing the g-factor in equation 8.2 produces the same response as changing M_{eff}. Figures 8.7a and 8.7b show an example of two different fits to the same data, both of which are visually 'good' fits, but yield unrealistic physical parameters for the 5 nm CoFeB film. A goodness of fit parameter, such as reduced chi squared, χ^2_{red}, is defined as [281]

$$\chi^2_{\text{red}} = \frac{1}{\nu} \sum_i \frac{\left(y_i - y\left(x_i\right)\right)^2}{\alpha_i^2}, \tag{8.3}$$

with $y_i - y\left(x_i\right)$ the difference between theory and raw data at each point, α_i the error at each point and ν the number of degrees of freedom. By using this goodness of fit, χ^2_{red} can be evaluated over a range of values of the g-factor and M_{eff}. Figure 8.8 shows an example of this for the same dataset as in figure 8.7. For the frequency range fitted here, there exists a broad range of values of both the g-factor and M_{eff} over which the fit can be considered 'good'. Shaw *et al.* [282], reported a similar result and determined that the dependence of the resonance condition on the two parameters can be separated by fitting at higher frequencies, where $H_{\text{res}} \geqslant M_{\text{eff}}$, which was not

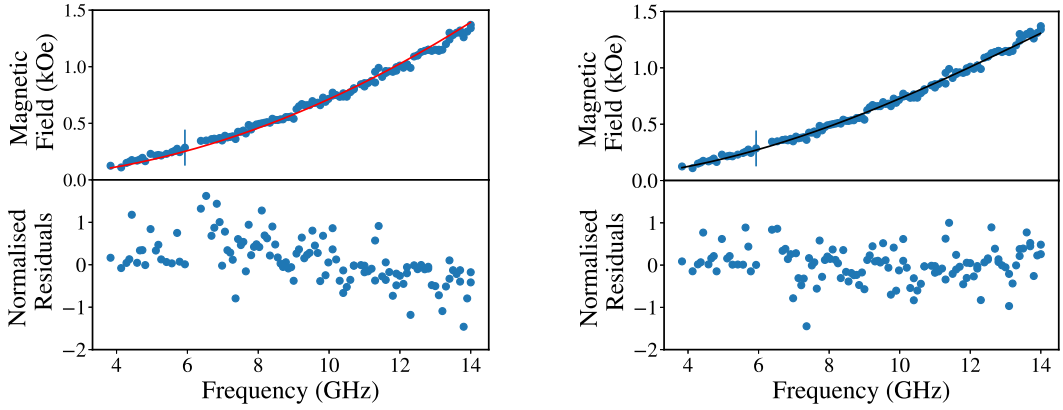

(a) (b)

Figure 8.7: Ferromagnetic resonance peak positions as a function of magnetic field and frequency for a 5 nm CoFeB film, fitted with the Kittel equation with two different sets of parameter, but which give a similar goodness of fit. Parameters from (a) $g = 1.80 \pm 0.06$, $4\pi M_{\text{eff}} = 21.8 \pm 0.3$ kG and (b) $g = 4.4 \pm 0.2$, $4\pi M_{\text{eff}} = 8.3 \pm 0.8$ kG.

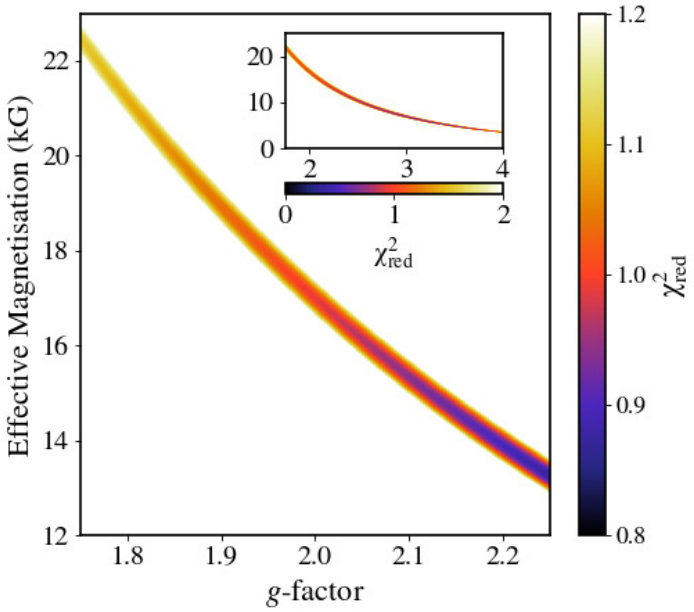

Figure 8.8: Calculated χ^2_{red} for a range of values for the g-factor and M_{eff} for the raw data in figure 8.7. Inset is χ^2_{red} over a wider range.

achievable with the VNA-based setup developed due to the higher magnetic field required. Furthermore, there are additional complications regarding the observed angular dependence of ΔH that has been attributed to a g-tensor originating from SOC [29, 76] or more recently to anisotropic Gilbert damping [283, 284]. In addition, both the g-factor [285] and M_{eff} are influenced by the thickness of surrounding layers [273, 274].

As discussed in chapter 3, the intrinsic damping parameter, α, can be described by a combination of bulk, α_0, and interface, $\Delta\alpha$, terms, with the latter given by

$$\Delta\alpha = \alpha - \alpha_0 = \frac{\gamma\hbar}{4\pi M_s t_{FM}} g_{eff}^{\uparrow\downarrow}, \tag{8.4}$$

which is dependent on the effective spin-mixing conductance. Importantly, in order to circumvent the difficulties associated with the correlation between the g-factor and M_{eff} that compromises analysis, equation 8.4 can be rearranged to give

$$\frac{g_{eff}^{\uparrow\downarrow}}{t_{FM}} = \frac{M_s}{\hbar}\left(\frac{4\pi\Delta\alpha}{\gamma}\right), \tag{8.5}$$

which allows direct extraction of $g_{eff}^{\uparrow\downarrow}$ using the second term of equation 8.1, which now depends only on the ratio of α and the g-factor. Therefore by measuring the intrinsic linewidth as a function of FM thickness, the effective spin-mixing conductance can be determined from the gradient, an example of which is shown in figure 8.9a for a CoFeB / Pt system. Figure 8.9b shows an example of the adjusted intrinsic linewidth determined from FMR as a function of the inverse of the FM thickness for the Pt / Co (fcc) system. The gradient of this provides the effective spin mixing conductance.

The measurement of $g_{eff}^{\uparrow\downarrow}$ as a function of the NM thickness allows the interfacial transport parameters to be extracted. Following Tserkovnyak *et al.* [113], interfacial

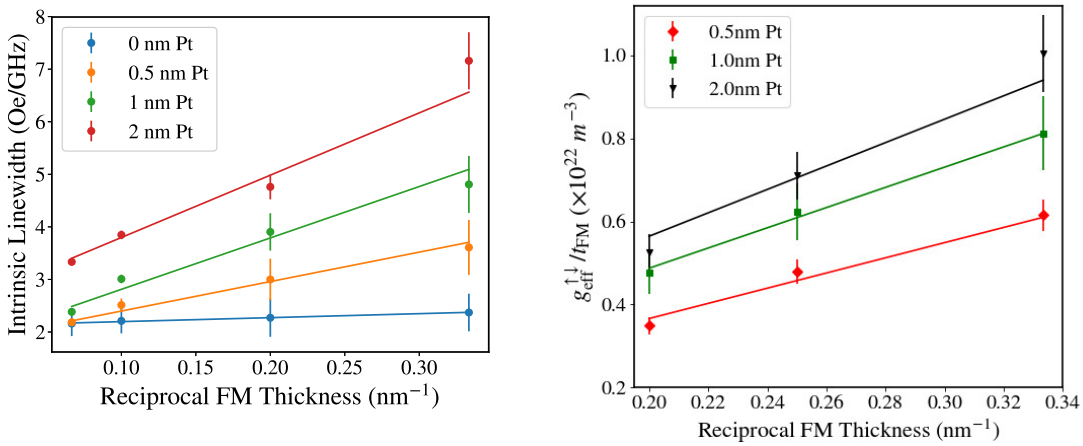

(a) (b)

Figure 8.9: (a) Intrinsic linewidth as a function of inverse FM thickness for a Pt/ CoFeB system, at various Pt thicknesses. The gradient gives the effective spin mixing conductance. (b) Adjusted intrinsic linewidth for a Pt / Co (FCC) system, at three Pt thicknesses.

damping depends on the NM thickness according to

$$\Delta\alpha = \frac{\alpha_{\mathrm{sp}}^{\infty}\sqrt{\epsilon}}{\sqrt{\epsilon} + \coth\left(\frac{t_{\mathrm{NM}}}{\lambda_{\mathrm{sf}}}\right)}, \tag{8.6}$$

where ϵ is the spin-flip probability in the NM layer. The FM and NM thickness dependences can be combined by considering the effective mixing conductance following the same form, due to the linear relationship between $g_{\mathrm{eff}}^{\uparrow\downarrow}$ and $\Delta\alpha$, i.e.,

$$g_{\mathrm{eff}}^{\uparrow\downarrow}(t_{\mathrm{NM}}) = \frac{g_{\infty}^{\uparrow\downarrow}\sqrt{\epsilon}}{\sqrt{\epsilon} + \coth\left(\frac{t_{\mathrm{NM}}}{\lambda_{\mathrm{sf}}}\right)}, \tag{8.7}$$

with a bulk term $g_{\infty}^{\uparrow\downarrow}$ at $t_{\mathrm{NM}} \gg \lambda_{\mathrm{sf}}$. Significantly, elsewhere the value of $g_{\mathrm{eff}}^{\uparrow\downarrow}$ is typically determined only using equation 8.7 with a single NM thickness, and therefore it is only valid at this single NM thickness. However, using eq 8.7 with 8.4 allows for $g_{\mathrm{eff}}^{\uparrow\downarrow}$ to be fully described, and this approach was developed in this work.

The spin diffusion length is usually assumed to be constant, however, as discussed earlier in this section and chapter 2, it has been shown to be proportional to the conductivity of the NM layer and therefore is expected to change for very thin films where the resistivity is known to increase rapidly in the ultrathin regime and, particularly for incomplete layers resulting from island-like growth. Following the model of Nguyen *et al.* [277], here the value of the product $\lambda_{\mathrm{sf}}\rho$ is taken as a constant. Using this constant and introducing an assumed empirical exponential dependence for ρ upon the NM thickness as introduced in previous chapters [69], a relationship for the thickness dependence of $\lambda_{\mathrm{sf}}(t)$ has been obtained as,

$$\lambda_{\mathrm{sf}}(t) = \frac{\lambda_{\infty}\rho_{\infty}}{\rho_{\infty} + \frac{\lambda_{\infty}\rho_{\infty}}{\lambda_0}e^{-t/\lambda_{\infty}}}, \tag{8.8}$$

where the bulk NM resistivity and the spin diffusion length are given by ρ_{∞} and λ_{∞} respectively. Here, λ_0, (or alternatively ρ_0 [69]) is a phenomenological scaling parameter, such that the spin diffusion length tends to zero in the limiting case of NM thickness tending to zero. The spin-flip probability ϵ is given by the ratio of the elastic scattering length to the spin diffusion length, $l_{\mathrm{e}}^2/3\lambda_{\mathrm{sf}}^2$, which are both linearly proportional to the conductivity, therefore ϵ will not vary with NM thickness.

For the case of a FM/NM_1(t)/NM_2 system, where the second interface between

the NM layers is important, the behaviour of $g_{\infty}^{\uparrow\downarrow}$ and $\Delta\alpha$ with t_{NM1} follows [113]

$$\alpha_{\mathrm{sp}} = \alpha_{\mathrm{sp}}^{\infty} \frac{4+\sqrt{3/\epsilon}}{4+\sqrt{3/\epsilon}\frac{4+\tanh\left(t_{\mathrm{NM}_1}/\lambda_{\mathrm{sf}}\right) r\sqrt{3/\epsilon}}{4\tanh\left(t_{\mathrm{NM}_1}/\lambda_{\mathrm{sf}}\right)+r\sqrt{3/\epsilon}}} \tag{8.9}$$

where r is the ratio of $g^{\uparrow\downarrow}_{\mathrm{NM}_1/\mathrm{NM}_2}/g^{\uparrow\downarrow}_{\mathrm{FM/NM}_1}$. With $r = 0$ the two systems are decoupled, giving the same result as eq. 8.6.

8.2.4 Interfacial Dependence of Spin Transport Parameters

Analysis of the damping from Pt and Ru interfaced with ferromagnetic layers involved fitting $\Delta\alpha/\gamma$ and $g_{\mathrm{eff}}^{\uparrow\downarrow}$ as a function of NM thicknesses for each fixed FM thickness simultaneously, to extract the best fitting values for λ_{sf} and ϵ, this thereby fits both the FM and NM thickness dependences. Table 8.1 summarises the fitted interfacial transport parameters used, which are discussed in the rest of this section for Co/Ru, Co/Pt and CoFeB/Pt systems.

For the Co/Ru/Cu system, $g_{\mathrm{eff}}^{\uparrow\downarrow}$ increases for Co(hcp)/Ru(hcp) structure with increasing Ru thickness relative to Co/Cu. This may be associated with the matching of crystal structures at the interface compared to Co(hcp)/Cu(fcc) system. Also, as the Ru thickness increases further, $\Delta\alpha$ and $g_{\mathrm{eff}}^{\uparrow\downarrow}$ tend to saturation as the HM thickness approaches the spin diffusion length as shown inset in figure 8.10.

For the Co(fcc)/Ru(hcp) case, the introduction of Ru results in a decrease of the effective spin-mixing conductance compared to Co(fcc)/Cu(fcc), indicating a more opaque interface to spin propagation. A similar reduction of damping with a hcp material between two fcc layers was observed by Yakata *et al.* [261] for NiFe/Ru/Pt. The $\mathrm{FM/NM_1/NM_2}$ system was fitted with equation 8.9. Whereas the previous study attributed the decrease in interfacial damping to a change of the $\mathrm{NM_1/NM_2}$ spin-mixing, (changing the r parameter), here the reduction is due to a difference in structure across the $\mathrm{FM/NM_1}$ interface. For the Co(hcp)/Ru(hcp)/Cu(fcc) case, r is reduced such that the system behaves as if it was effectively $\mathrm{FM/NM_1}$ only, while for the Co(fcc)/Ru(hcp)/Cu(fcc) case, r increases with t_{Ru} thickness

		Spin Diffusion Length			
Sample	Spin-flip Probability ϵ	Constant λ_{sf}	Thickness dependent λ_{∞}	$g_{\infty}^{\uparrow\downarrow}$ ($\times 10^{18}$)	r
Co(hcp)/Ru(hcp)/Cu	$3.8 \pm 0.4 \times 10^{-3}$	7.0 ± 0.5 nm	22 ± 1 nm	16 ± 4 m^{-2}	$5.6 \pm 0.2 \times 10^{-4}$
Co(fcc)/Ru(hcp)/Cu	$3.1 \pm 0.6 \times 10^{-3}$	7.0 ± 0.5 nm	22 ± 1 nm	0.6 ± 0.4 m^{-2}	$1.4 \pm 0.8 \times 10^{1}$
Pt(fcc)/Co(fcc)	$1.7 \pm 0.4 \times 10^{-1}$	1.6 ± 0.6 nm	9.4 ± 0.7 nm	90 ± 10 m^{-2}	-
Co(fcc)/Pt(fcc)	$2.6 \pm 0.7 \times 10^{-1}$	1.6 ± 0.6 nm	9.5 ± 0.6 nm	75 ± 6 m^{-2}	-
Pt(fcc)/a-CoFeB	$1.1 \pm 0.5 \times 10^{-1}$	1.6 ± 0.6 nm	6.6 ± 0.8 nm	47 ± 5 m^{-2}	-
a-CoFeB/Pt(fcc)	$1.0 \pm 0.3 \times 10^{-1}$	1.6 ± 0.6 nm	6.8 ± 0.7 nm	54 ± 7 m^{-2}	-

Table 8.1: Interfacial spin transport parameters extracted from fitting of the thickness dependence of both the NM and FM layers.

such that $g_{\text{eff}}^{\uparrow\downarrow}$ falls. Yakata *et al.* also observed a slight increase in damping for a NiFe(fcc)/Ru(hcp) system with larger Ru thickness, but the increase was much smaller than Co(hcp)/Ru(hcp). ϵ for both Ru cases is much lower than for Pt, and λ_{sf} is more than twice that of Pt, as expected [113]. However, in the study by Yakata, the observed decrease in damping was due to the Ru increasing in thickness between a FM and a Pt spin sink layer, which is different to the system here. Interfacial damping in the spin pumping formalism is dependent upon the mixing conductance and the properties of the NM layer - the thickness, spin diffusion length and spin flip probability. A possible interpretation of the results here is that although the increasing Ru layer increases the damping, the interface mismatch causes a small decrease in the effective spin mixing conductance at a given NM thickness, albeit at a smaller rate than the damping enhancement from the Ru. This interpretation is limited by the noise and error due arising from the thinner FCC samples. Nevertheless, it is clear the interface properties play a a key role in spin transport and the enhancement of damping.

The evolution of both $g_{\text{eff}}^{\uparrow\downarrow}$ and $\Delta 4\pi\alpha/\gamma$ as a function of Pt thickness is shown in figure 8.11 for Co(fcc) and amorphous CoFeB. The larger errors from the Co samples originate from the smaller signals, and hence larger fitting uncertainties, from determining the linewidth. An interfacial difference is observed in $g_{\text{eff}}^{\uparrow\downarrow}$ with

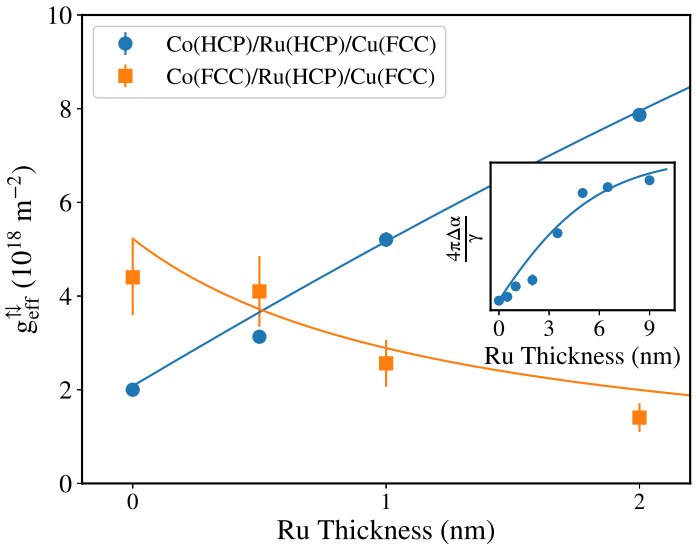

Figure 8.10: The variation in $g_{\text{eff}}^{\uparrow\downarrow}$ for Co/Ru interfaces as a function of Ru thickness with either hcp or fcc Co. The graphs are scaled by subtracting $g_{\text{eff}}^{\uparrow\downarrow}$ with no Ru, which is 4.8×10^{18} m^{-2} for fcc and 2.1×10^{18} m^{-2} for hcp. Inset shows the evolution of the measured linewidth for the hcp Co case, over the full range of Ru thickness studied. The data are fitted to equation 8.9, with a spin diffusion length from equation 8.8

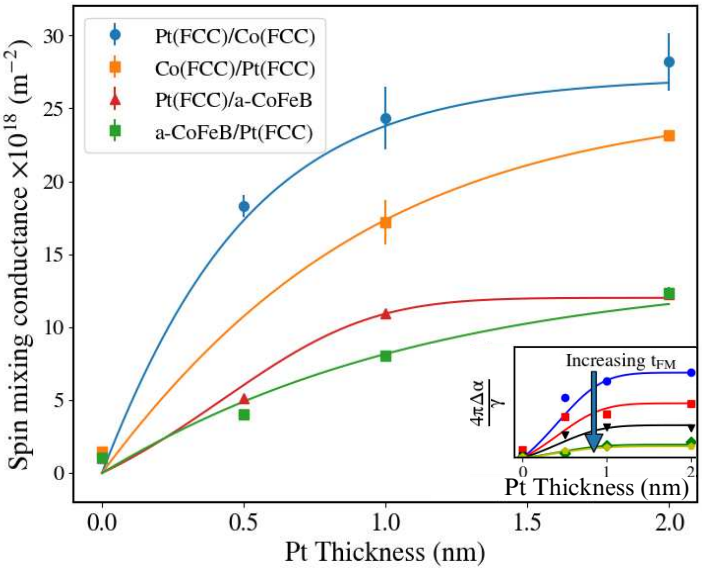

Figure 8.11: The evolution of $g_{\text{eff}}^{\uparrow\downarrow}$ with Pt thickness for fcc Co, and amorphous CoFeB, with Pt on different interfaces. Inset is $\Delta 4\pi\alpha/\gamma$ for Pt/CoFeB samples with increasing FM thickness from top to bottom. Data fitted to equation 8.7, with inset fitted to equation 8.6. In both cases the spin diffusion length fitted to equation 8.8.

Co(fcc)/Pt(fcc) and Pt(fcc)/Co(fcc), that is attributed to a subtle difference in local structure. Interface-structure-dependent behaviour in Co/Pt systems was also observed for the proximity induced moment in Pt [14], with a twofold difference in total moment between the interfaces.

With an amorphous FM layer, as shown in figure 8.11, there is a significant reduction in $g_{\text{eff}}^{\uparrow\downarrow}$ compared to interfacing with a crystalline Co layer, for the same NM thickness. The final value reached is also independent of interface, within error. However before a complete layer of Pt is formed, there is a higher spin-mixing conductance for the bottom interface. Structural studies of Pt on amorphous CoFeTaB layers showed a change in the texture of sub-2 nm Pt layers [286].

The effect of including a thickness dependent λ_{sf} in the analysis is shown in table 8.1. Fitting with a constant λ_{sf} gives values typical of previous FMR analyses between 1 and 2 nm [8, 260], here, the new inclusion of a NM layer thickness dependence gives λ_{sf} close to 10 nm, as reported elsewhere [266, 270, 287]; significantly this resolves the discrepancy between values of λ_{sf} from different methods highlighted earlier. The magnitude of ϵ for Pt supports reports that the EY mechanism is the dominant source of spin-flip scattering [277] and is of a similar order of magnitude (10^{-1}) to reported values [112].

A visual comparison of the raw intrinsic data for the FMR linewidth, with simulations based on the extracted parameters is shown in figures 8.12. The maximum increase in damping is achieved for thinner FM layers paired with NM layers above

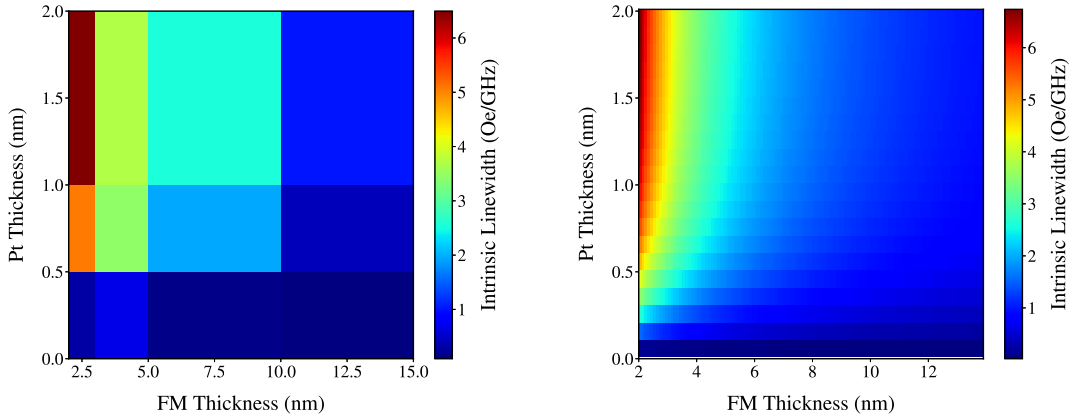

(a) (b)

Figure 8.12: (a) Measured intrinsic FMR linewidth contribution for a CoFeB / Pt system as a function of both FM and NM thickness. (b) Simulated damping surface using the parameters obtained from the fit, as given in table 8.1.

λ_{sf}. Therefore, for a broadband ferromagnetic frequency response based on spin transport, multiple sub-units of FM/HM layers would be required to maximise the intrinsic ferromagnetic loss. The next section reports an investigation into the thickness of an insulating barrier required to treat these sub-units as dynamically distinct.

To summarise, a detailed exploration of both FM and NM layers provides deeper insight into spin transport across interfaces in spintronic systems. Regardless of the interface, the transport properties of Ru and Pt layers are governed by the EY mechanism. For Ru, a lower spin-flip scattering probability compared to Pt and a longer spin-diffusion length were obtained, while most significantly the inclusion of a thickness dependent spin diffusion length resolves the discrepancies in the reported values of the spin diffusion length for Pt from FMR analysis.

8.3 Spin Transport with Insulating Barriers

In spintronic systems, insulating layers are commonly used as barriers between two ferromagnetic materials in a magnetic tunnel junction structure, where a charge current can propagate through the structure and the resistance depends on the relative alignment of the two FM layers. These insulating barriers have been well studied since the discovery of giant tunnelling magnetoresistance with insulating layers such as Al_2O_3 [288, 289] and MgO [290], where the magnitude of the difference in resistance also depends upon the composition of the FM material [291].

A multilayered synthetic magnetic system with a broadband frequency response based on large magnetic damping requires the pairing of structurally matched HM

layers, thicker than λ_{sf}, with thin FM materials, as shown in the previous section. In order to be able to treat each FM/HM bilayer in a multilayered system as separate, and to enhance both the impedance matching and the resistivity of a synthetic material, it is advantageous to insert insulating barrier layers to effectively subdivide the multilayered structure. It is therefore important to investigate the efficiency of such barrier layers with respect to controlling the flow of spin current.

The propagation of spin current through an insulating barrier has led to conflicting results in the literature. Initial theoretical predictions of spin pumping required a transparent interface between the FM and NM layers for a large increase in damping [122]. Conversely, early experimental results by Moriyama *et al.* [10] suggested an enhancement in the damping with an insulating barrier present, which contrasts with later works by Kim *et al.* [11] and Mosendz *et al.* [292], who observed the suppression of spin pumping with the insertion of nano-oxide and MgO layers respectively. Studies of both Si and oxide semiconductors [293], have also shown some suppression of spin pumping and suggest that the carriers may continue to allow spin diffusion through the barrier. Baker *et al.* [294] also observed suppression of spin pumping but with dynamic exchange between two FM layers across the insulating barrier, in CoFe/MgO/Ni trilayers. Most recently, Mihalceanu *et al.* [12] reported a rapid decrease in the damping due to reduced spin pumping with the addition of an ultra-thin MgO barrier layer between Fe and Pt, from which it was concluded that spin current can tunnel through a few monolayers of an insulating oxide barrier. That work was supported by transmission electron microscopy (TEM) imaging, which, however, is limited to sampling very small areas and provides a projection of a thin 3D sample volume that may not show pinhole defects, and any defects present may be difficult to directly image [295].

The discrepancies between these previous studies may be associated with the details of the multilayered structure. In particular, the nature of the interface structure in such systems is known to be important for spin-pumping [268, 296] and in the ultra-thin film regime the presence of a continuous intermediate layer needs to be established when studying such interlayer effects [14]. Spin pumping and $d-d$ hybridisation across a FM/NM interface both lead to additional magnetic energy loss and increased precessional damping. An increase in damping linked to spin pumping across a continuous insulating layer implies some form of spin current tunnelling, however, even small discontinuities, such as pinholes, within the insulating layer can allow for $d-d$ hybridisation between the ferromagnetic and heavy metal layers, leading to an increase in the damping [108, 115], and limited channels for spin current propagation. A detailed understanding of the role of structure at the interface is therefore needed to fully characterise dynamic magnetic behaviour with

an insulating barrier.

This section describes the results of a study, now published [242], investigating the evolution of spin-pumping from a thin-film ferromagnet into a heavy metal layer as a function of the thickness of an oxide spacer layer. The spin transport was determined from analysis of broadband FMR measurements and the sample structure was analysed using x-ray reflectivity (XRR) in order to characterise and understand the interfacial regions between the oxide and the FM and NM layers. The structural characterisation of FM/ Insulator / HM trilayers is presented, followed by the dynamic characterisation. The role of the insulating barrier was then further investigated by examining the behaviour in a multilayered system with multiple FM/oxide/HM repeated units.

8.3.1 FM/Oxide/HM Trilayer Structural Characterisation

As in the previous section, samples were grown in Durham using the RF magnetron sputtering process described in chapter 5 using a SiO_2 target. Due to the lack of an oxygen atmosphere this may result in some partial oxidation of the surrounding layers. Three series of samples were grown, the first consisting of a set in which the SiO_2 thickness in a $Co_{20}Fe_{60}B_{20}\,(10\,\mathrm{nm})$ / $SiO_2\,(0-5\,\mathrm{nm})$ / $Pt\,(10\,\mathrm{nm})$ structure was varied, along with a reference sample with no Pt but with a 5 nm SiO_2 layer. The second consisted of a further series varying the SiO_2 thickness in $Co_{40}Fe_{40}B_{20}\,(10\mathrm{nm})$ / $SiO_2\,(1-2\,\mathrm{nm})$ / $Pt\,(10\,\mathrm{nm})$, both with and without the Pt to verify the observed behaviour in the first set. Finally, the third set consisted of a multilayer structure of $[Co_{20}Fe_{60}B_{20}\,(x\,\mathrm{nm})$ / $Pt\,(10\,\mathrm{nm})$ / $SiO_2\,(5\,\mathrm{nm})]\times y$, such that the total FM thickness was held constant with $x \times y = 24$, while the number of multilayers was varied.

XRR was used to extract interfacial structure information. As discussed previously, this method measures over a large area, of the order of square centimetres, unlike transmission electron microscopy, and provides an averaged view of both the layers and interfaces within a sample and, with detailed model fitting, provides quantitative information regarding the structures. The unit cell size for SiO_2 is on the order of 0.5 nm [199], hence any layer below this thickness is likely to be incomplete, and due to the island-like growth of the insulating layer, there is likely to be voids up to a threshold thickness. However, this provides opportunity for the correlation between the interface profile and spin transport to be investigated, as the damping should reduce to the bulk FM value once the layer is complete, assuming no tunnelling.

Figures 8.13a, 8.13b and 8.13c show examples of both the measured reflectivity data and the best-fitting simulations obtained using the GenX code [209], for a SiO_2

thickness of 0.5 nm, 2 nm and 5 nm respectively, with fitted parameters in tables 8.2, 8.3 and 8.4, where the fitted densities are slightly lower than the bulk value, a expected with thin film growth.

The corresponding scattering length density (SLD) profiles were extracted from the best-fitting model for the three samples measured. The interface widths in such multilayered structures results from a combination of topographical roughness of interface between the layers and chemical intermixing between these different layers. Here the interface width between the insulating and FM layers largely reflects chemical intermixing across the interface, as determined from rocking curve analysis for the 0.5 nm barrier, the fits of which are shown in figure 8.15.

A value for the interface width has been estimated from both the slope of the scattering length density (SLD), where it changes from 90% to 10% of its value from one layer to the next, as shown in figure 8.14, and also from the width parameter of the error function to produce the SLD profile, used to parametrise the interface roughness. For the CoFeB and SiO_2 interface, both of these analyses gives an interface width of 2.4 nm, below this thickness the SiO_2 layer is discontinuous.

Layer	Thickness (Å)	σ (Å)	Density ($Å^{-3}$)	Bulk Density ($Å^{-3}$)
CoFeB	93.3 ± 0.3	6.1 ± 0.2	0.088 ± 0.001	0.0883
SiO_2	5.4 ± 0.3	7.3 ± 0.3	0.0246 ± 0.0002	0.0252
Pt 1	36.8 ± 0.4	21 ± 1	0.0637 ± 0.0001	0.0647
Pt 2	55.4 ± 0.3	7.0 ± 0.2	0.0641 ± 0.0002	0.0647

Table 8.2: Fitted XRR parameters for the 0.5 nm SiO_2 layer obtained from GenX.

Layer	Thickness (Å)	σ (Å)	Density ($Å^{-3}$)	Bulk Density ($Å^{-3}$)
CoFeB	91.2 ± 0.3	8.8 ± 0.2	0.0881 ± 0.0001	0.0883
SiO_2	22.0 ± 0.2	7.3 ± 0.2	0.0250 ± 0.0003	0.0252
Pt 1	34.1 ± 0.5	18 ± 1	0.0630 ± 0.0004	0.0647
Pt 2	57.7 ± 0.5	7.0 ± 0.2	0.0640 ± 0.0003	0.0647

Table 8.3: Fitted XRR parameters for the 2 nm SiO_2 layer obtained from GenX.

Layer	Thickness (Å)	σ (Å)	Density ($Å^{-3}$)	Bulk Density ($Å^{-3}$)
CoFeB	91.3 ± 0.2	10.2 ± 0.3	0.087 ± 0.001	0.0883
SiO_2	53.6 ± 0.2	8.2 ± 0.1	0.0249 ± 0.0001	0.0252
Pt 1	30.8 ± 0.3	11.5 ± 0.8	0.0627 ± 0.0001	0.0647
Pt 2	59.6 ± 0.3	7.6 ± 0.1	0.0640 ± 0.0003	0.0647

Table 8.4: Fitted XRR parameters for the 5 nm SiO_2 layer obtained from GenX.

Aside from being readily available, the wide interface width of the SiO_2 layer provides a suitable material to correlate the thickness dependence of the measured

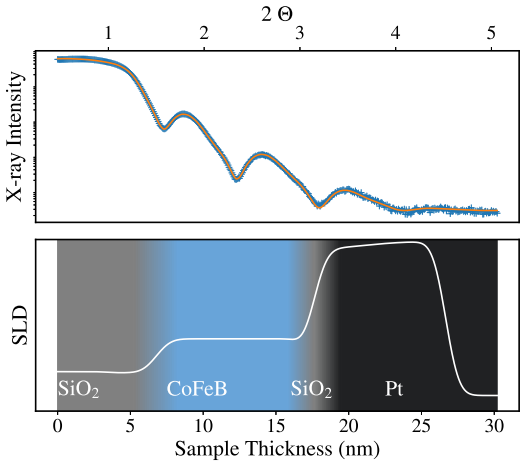

(a)

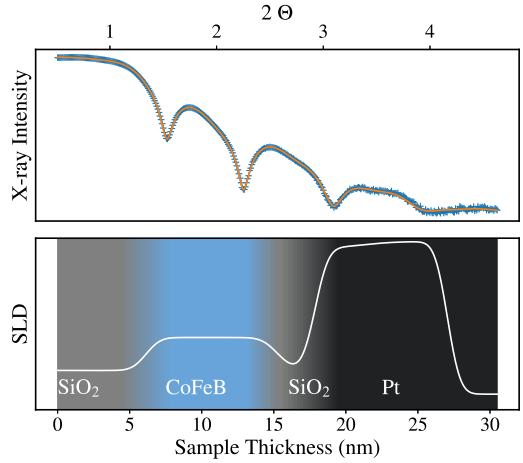

(b)

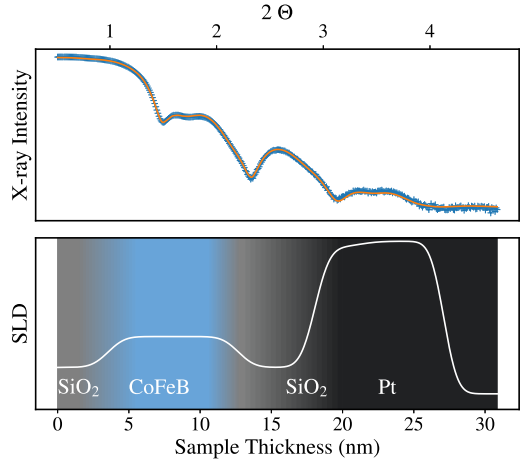

(c)

Figure 8.13: Raw XRR data with best fit, above, and corresponding colour coded scattering length density profile with a SiO_2 thickness below for (a) 0.5 nm, (b) 2 nm and (c) 5 nm in a $Fe_{60}Co_{20}B_{20}$ (10 nm) / SiO_2 (x nm) / Pt (10 nm) stack.

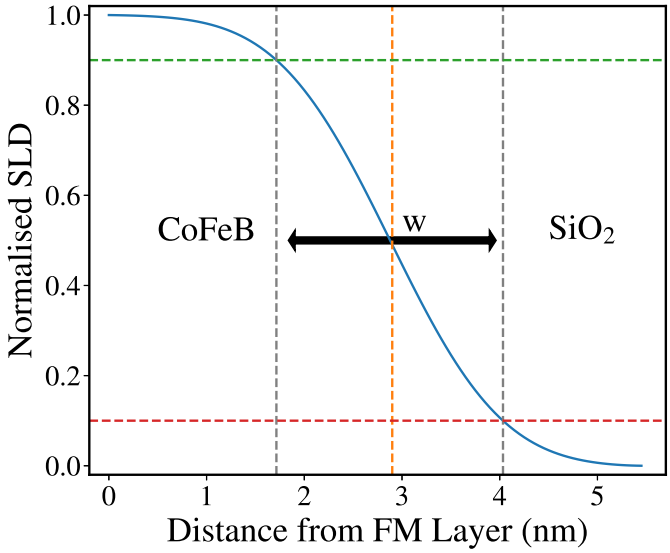

Figure 8.14: An approach to estimating the interface width by considering the lengthscale over which the SLD changes from 90% (green) of the peak value to 10% (red), shown here for the 5 nm SiO_2 layer, with the centre of the interface given by a dashed orange line, and interface width, w, given by difference between the two grey lines.

dynamic properties to the interface profile. This allows for both the verification of the lengthscale over which spin pumping is suppressed and to compare the reports of Mihalceanu *et al.* [12], of spin tunnelling across an insulating barrier.

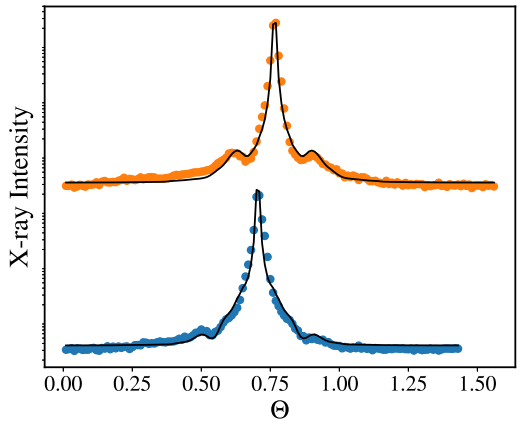

Figure 8.15: Rocking curves with best fit for the 0.5 nm barrier at two 2Θ angles for the 0.5 nm SiO_2 in a $Fe_{60}Co_{20}B_{20}$ (10 nm) / SiO_2 (0.5 nm) / Pt (10 nm) stack barrier, following the description of analysis in chapter 5.

8.3.2 Dependence of damping on SiO_2 Thickness in FM/Oxide/HM Systems

Dynamic characterisation of the spin transport as a function of SiO_2 thickness was undertaken for the trilayer samples using the integrated FMR system outlined in the previous chapter. The sample was suspended face down 0.5 mm above an impedance-matched microstrip, and the AC function of the system was used whereby the Helmholtz coils were used to provide a small field modulation on top of the larger DC magnetic bias field. The time-varying output voltage from a microwave diode power detector, connected across the transmission line, was proportional to the field derivative of the transmitted RF power, and hence the microwave absorption, χ'', of the sample was measured using the lock-in circuit of the integrated FMR system. Figure 8.16a shows typical spectra around resonance as a function of magnetic field for various excitation frequencies, f. An example of the fitting of the linewidth data to determine the intrinsic and extrinsic damping contributions to the measured linewidth is shown in figure 8.16b, with the deviation at 7 GHz due to destructive interference caused by the length of the waveguide.

The effect of increasing the thickness of a SiO_2 spacer layer on both the intrinsic and extrinsic contributions to the precessional damping in $Co_{20}Fe_{20}B_{20}$ (10 nm) / SiO_2 (x nm) / Pt (10 nm) trilayers is shown in figure 8.17. As the nominal thickness of the oxide layer between the ferromagnet and the heavy metal spin-sink increases, the intrinsic linewidth decreases. This decrease is at a similar rate to that observed for an MgO spacer layer in a similar study [12]. With increasing oxide thickness the

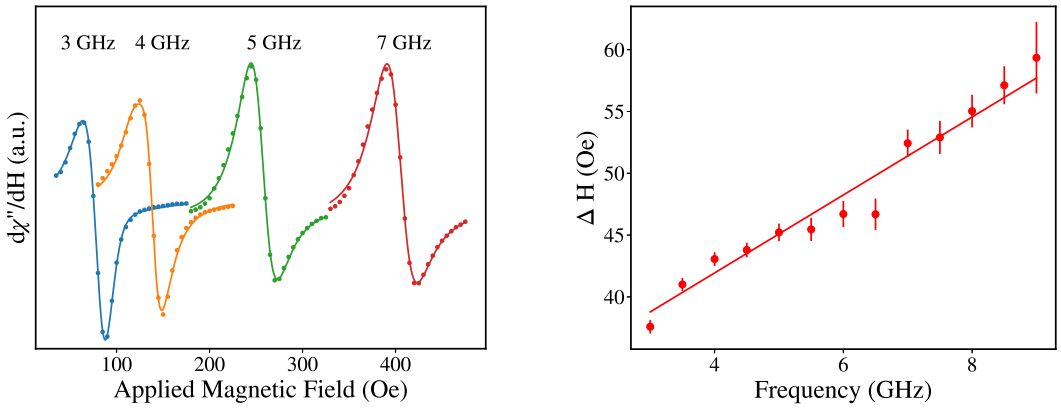

(a) (b)

Figure 8.16: (a) Typical absorption derivative profiles at four frequencies with fits, obtained from lock-in amplifier field-swept FMR for a CoFeB (10 nm) / Pt (10 nm) sample. (b) Measured linewidth from field-swept FMR with linear fit to determine both intrinsic and extrinsic damping contributions.

intrinsic damping decreases towards the value observed when no HM spin-sink layer is present, as indicated on the figure by the orange square data point. The large initial extrinsic damping may be attributed to increased scattering through voids as the spin current passes from the FM to the Pt layer.

In other research the continued enhancement of damping with increasing insulating barrier thickness was attributed to tunnelling of spin current through the insulating spacer layer [12]. The new results and detailed structural analysis show that an understanding of the interfacial structure is important for a robust interpretation of the spin transport behaviour.

The dynamic analysis of spin transport was repeated with a slightly different composition of FeCoB, with $Co_{40}Fe_{40}B_{20}$ used rather than to $Co_{20}Fe_{60}B_{20}$, in order to both verify the same trend in the behaviour and to confirm that no increase in damping occurs without a spin sink layer present. Figure 8.18 shows the results of both the intrinsic and extrinsic contributions to the damping as a function of SiO_2 thickness. The overall intrinsic linewidth is larger due to the different composition, in agreement with other work [297], however, no significant change was observed with intrinsic damping for samples without Pt while varying the SiO_2 thickness. For the extrinsic damping, a small increase was observed with partial coverage of the SiO_2, which may be attributed to some surface oxidation of the uncovered layer, and was reduced when the SiO_2 coverage increased.

The correlation between the dynamic properties and the interface structure is shown in figure 8.19. By plotting the normalised structural SLD profile of the

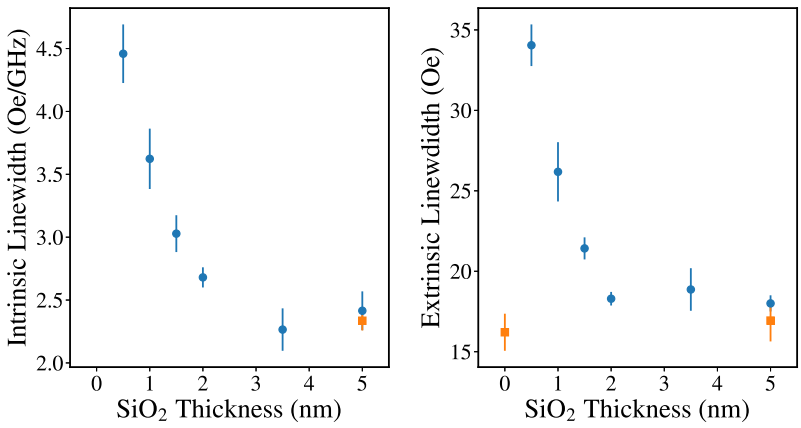

Figure 8.17: The variation of both intrinsic and extrinsic contributions to FMR linewidth as a function of SiO_2 thickness in $Co_{20}Fe_{60}B_{20}$ (10 nm) / SiO_2 (x nm) / Pt (10 nm) (blue circles). The orange square at 0 nm denotes a reference sample with no SiO_2 and the orange square at 5 nm denotes a reference sample with no Pt layer.

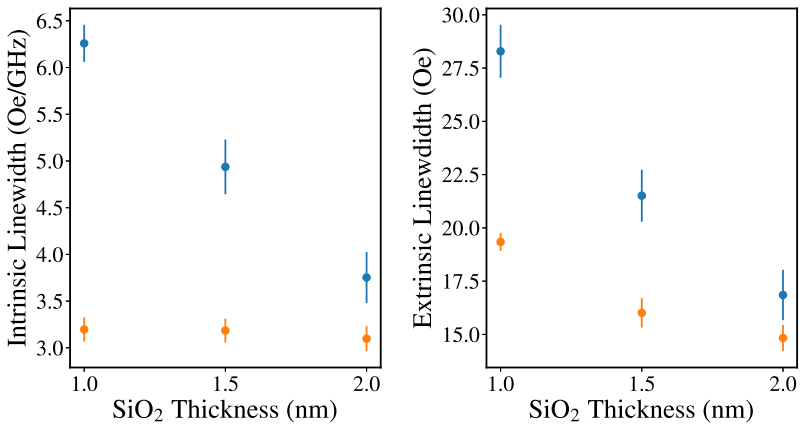

Figure 8.18: Intrinsic and extrinsic contributions to the FMR linewidth for a $Fe_{40}Co_{40}B_{20}$ (10 nm) / SiO_2 (x nm) system. The orange data is for FM and SiO_2 only and blue data denotes samples capped with 10 nm Pt.

CoFeB/SiO_2 interface onto the same nominal SiO_2 thickness-axis as for the damping, the relationship between the structure of the insulating layer and the measured damping response can directly be compared. At low SiO_2 thicknesses (below 2.4 nm) the SiO_2 layer is discontinuous, enabling some localised direct contact and $d-d$ hybridisation between the ferromagnet and the heavy metal (HM), where the spacer layer is incomplete, which it is proposed creates direct pathways for propagation of spin current from the ferromagnet into the heavy metal spin-sink. These two mechanisms enhance the damping above that of the pure ferromagnet [115], but this decreases rapidly as the area of HM in direct contact with the FM is reduced. However, when the insulating spacer layer continuously covers the ferromagnet, above 2.4 nm, there is no measurable enhancement of the intrinsic damping from the heavy metal layer.

The effects of the discontinuous interface is also observed in the SiO_2 thickness dependence of the extrinsic contribution to the damping, see figure 8.19b. An increase in the extrinsic contribution to the linewidth indicates an increase in defects that mediate two-magnon scattering processes. As a function of SiO_2 thickness the extrinsic contribution increases in a single large step with the thinnest oxide layer and then decreases as the thickness increases further, this decrease is comparable with the form of the scattering length density. The extrinsic contribution provides evidence further supporting the interpretation of the nominal thickness dependence as a consequence of the presence of a discontinuous insulating layer, as it has been previously shown that discontinuous coverage of a ferromagnet with a heavy metal layer leads to enhanced extrinsic damping [108]. A slight enhancement in extrinsic damping was also found without a Pt layer, which may be attributed to partial

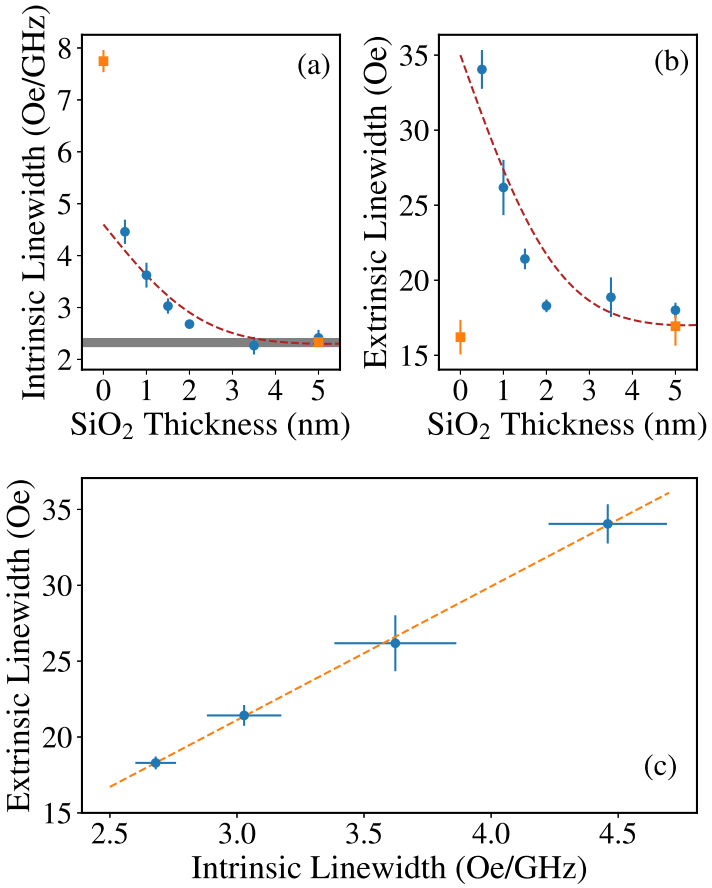

Figure 8.19: (a) Intrinsic and extrinsic contributions to the FMR linewidth as in figure 8.17 , but with extracted SLD for the 5 nm SiO_2 barrier from figure 8.13c superimposed shown in red dashed lines. The horizontal grey bar indicates the damping equivalent to that of the ferromagnetic layer only. (b) As figure 8.17 with SLD for a 5 nm SiO_2 barrier superimposed on top given by the red dashed line. (c) Correlation between the intrinsic and extrinsic contributions for samples without a full surface coverage of the insulating layer.

oxidation of the FM surface due to a discontinuous interface [298]. The common dependence of both the intrinsic and extrinsic damping upon the discontinuous SiO_2 layer is further evidenced by the linear correlation between the extrinsic and intrinsic contributions for samples lacking a full surface coverage of the SiO_2 layer (i.e. below 2.4nm), as shown in figure 8.19c. Here, as discussed, regions with a low surface coverage allow for a large increase in both the extrinsic and intrinsic contributions, which are both suppressed with the same functional form as the layer becomes complete. Direct surface measurements, such as Atomic Force Microscopy, are unable to distinguish between defects such as pinholes which would lead to this effect and topographical roughness, due to the lack of element specificity.

8.3.3 Damping in Multilayered Systems with SiO_2 Spacers

A test of the application of a thick insulating layer (5 nm) as a barrier to spin pumping was undertaken by comparing a series of multilayered samples with a single layered reference sample. The total FM thickness was the same in all these samples, but the FM material was sub-divided into a few thinner layers in the multilayered samples in a structure [$Co_{20}Fe_{60}B_{20}$ (x nm) / Pt (10 nm) / SiO_2 (5 nm)]$\times y$, with $x \times y = 24$. Figure 8.20 shows the structural characterisation of the 8 nm CoFeB layer, with three repeats of the sub-unit. As shown by the repeating uniform SLD profile, obtained from the fit to the XRR data, each of the repeating sub-units is structurally identical.

The dependence of the intrinsic linewidth on the thickness of the ferromagnetic material in the multilayered samples is shown in figure 8.21, for the multilayers with and without Pt. Without the heavy metal, the intrinsic linewidth increases very slightly for thinner FM layers. In contrast, with Pt, as expected the intrinsic damping is greatly enhanced due to spin pumping, but also the enhancement is larger for thinner FM layers. The solid lines shown are best fits to equation 8.4, which allows the effective spin mixing conductance for 10 nm of Pt to be extracted as $(30 \pm 4) \times 10^{18}\,\mathrm{m}^{-2}$, which is comparable to that found in a similar system in the previous section. The single layer reference sample of CoFeB (10 nm) / Pt (10 nm),

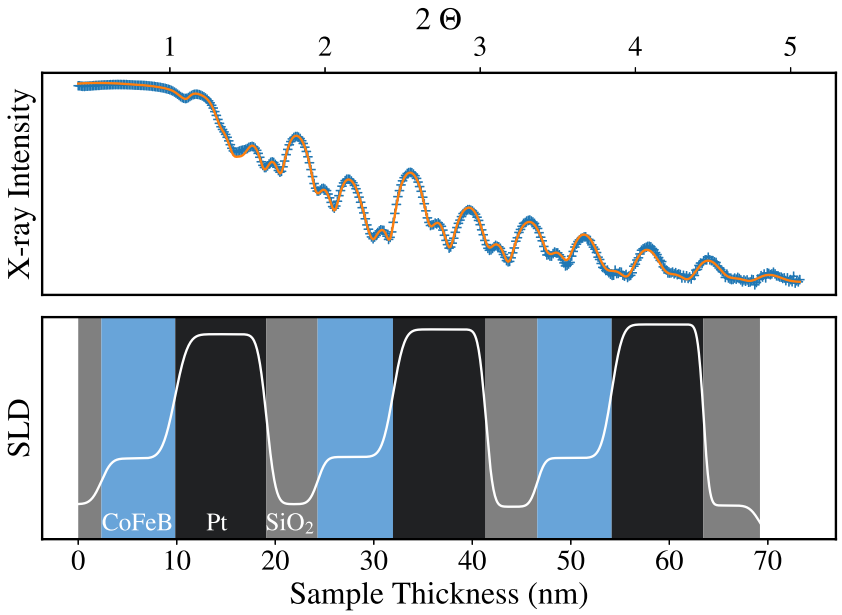

Figure 8.20: Structural characterisation of a [$Co_{20}Fe_{60}B_{20}$ (8 nm) / Pt (10 nm) / SiO_2 (5 nm)]$\times$3 sample, using XRR shown above, with best fit and corresponding colour coded structural length density, SLD, profile, below.

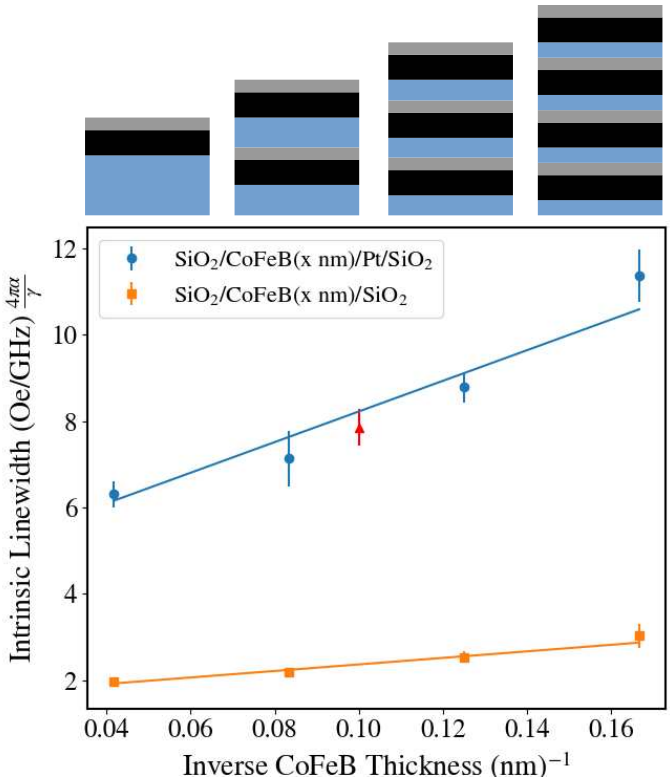

Figure 8.21: Dependence of the intrinsic damping contributions on the ferromagnetic thickness for [CoFeB (x nm) / Pt (10 nm) / SiO_2 (5 nm)] $\times\, y$ multilayers (blue circles) and without platinum (orange squares). Top shows a schematic of multilayered samples. The red triangle denotes intrinsic linewidth for single layer sample of CoFeB(10 nm)/Pt(10 nm). Straight line fits indicate increase in damping due to spin pumping, the gradient of which provides the spin mixing conductance.

marked as a red triangle on the figure, fits with the other data points, lying on the best-fitting line, indicating that the individual units of the multilayers that are separated by 5nm of SiO_2 are effectively isolated units in terms of spin transport. Had spin pumping through 5 nm thick SiO_2 been present, there would have been an enhancement in the damping from both interfaces, resulting in the best fitting line being significantly higher than the reference sample.

8.4 Summary

Spin transport from a ferromagnet to a non-magnetic heavy metal layer provides an additional energy loss channel for the damping of precessing magnetisation which manifests as an increase in the bandwidth of absorption. This chapter presented the results of two investigations into methods to both enhance and suppress the increase in magnetic damping due to interfacial spin transport. Maximal enhancement in the bandwidth was achieved by closely matching structures of FM materials with

suitable HM spin sinks, in particular Pt. By inserting insulating layers of a suitable thickness, these sub-units of a multilayered synthetic material can be treated as isolated.

Section 8.2 built upon the reported dependence of the spin diffusion length on the resistivity, to account for changes in resistivity in ultrathin films, it was demonstrated that the apparent discrepancies in the spin diffusion length for Pt from different techniques can be accounted for with this enhanced model. Additionally, regardless of the interface, the transport properties of Ru and Pt layers are governed by the EY mechanism. For Ru, a lower spin-flip scattering probability was obtained compared to Pt, agreeing with the literature, which corresponds to a longer spin-diffusion length due to the decreased SOC of Ru.

Section 8.3 correlated the structure of the interface with the spin transport from a FM layer into a HM across a SiO_2 spacer layer. Spin-pumping was observed for nominal SiO_2 thicknesses up to around 2 nm, which corresponds to the length-scale of the interface width of the oxide barrier, such that, structurally the insulating layer was discontinuous when enhanced damping was observed and no enhancement was measured when the SiO_2 layer was complete (i.e. a thickness $>$2.4 nm). Above this thickness, there is a significant barrier to spin transport, which suppresses the propagation of spin current between adjacent layers in multilayered structures. Though the prospect of spin tunnelling is not ruled out, aside from resonant tunnelling in thick layers, the experimentally observed spin-pumping signals with ultra thin insulators are more likely due to the discontinuous insulating layer rather than requiring models involving tunnelling of pure spin-current, as had been suggested previously [12].

Though these two investigations explored methods to enhance and suppress spin transport, and detailed some of the key parameters, questions remain regarding the underpinning physics. One such question is the nature of the HM which allows for interfacial enhancement of damping. As detailed in chapter 3, for the two mechanisms of interfacial damping described, it is unclear whether the enhancement occurs mainly due to increased d-d hybridisation, and hence proximity induced magnetism, or due to spin accumulation potentials. These questions form the basis of the next chapter.

Chapter 9

Interfacial Phenomena II: Heavy Metal Proximity Induced Magnetism and Damping

9.1 Introduction

The previous chapter focussed on methods to control the frequency bandwidth response of a synthetic material by engineering interfacial effects to either enhance or suppress additional energy loss channels. This chapter focuses on the underlying physical phenomena behind interfacial enhancement of damping by considering the role of induced magnetism in the heavy metal required for high magnetic damping. Both sections here detail investigations using measurements involving synchrotron light at the Advanced Photon Source, and hence provide a probe of element specific magnetism of the heavy metal.

The first section details the results of a published investigation [299] into the nature of proximity induced magnetism by considering the direction of the induced moment in Pt across the compensation transition in a Gd based ferrimagnet, and whether it aligns with the net magnetisation direction, or with the direction of an individual sub-lattice moment. Following this, the second section describes the results of inserting spacer layers to weaken the induced magnetism, and the resultant consequences for the measured dynamic behaviour. The effect of the number of interfaces with regards to spin transport is also considered using film thickness wedges grown at the IFMPAN.

9.2 Proximity Induced Magnetism in Rare Earth: Transition Metal Ferrimagnets

Heavy metals, such as Pt, can enhance the frequency bandwidth response of a material by providing an additional energy loss channel via the spin pumping mechanism, the magnitude of which depends upon the details of the interface, as detailed in the previous chapter and elsewhere [108–110, 133, 300, 301] . As discussed in chapter 2, electronic hybridisation at the interface between a ferromagnet and a material close to the Stoner criterion will also create a proximity induced moment (PIM) in the non-ferromagnetic material. PIM is known to enhance the magneto-optical response in Co/Pt systems [13] and the relationship between PIM and other interfacial phenomena has been explored [14, 302]. These interfacial effects are not limited to ferromagnetic materials, and have also been demonstrated in ferrimagnetic (FiM) systems [303, 304], in which there are two magnetically coupled and oppositely aligned sub-lattices. However, debate continues about the role of PIM in such spin transport physics, both with respect to metallic FM/NM systems [17, 18] and in insulating ferrimagnets layered with heavy metals (FiM/NM) [16, 305–309], in order to properly utilise heavy metal layers to enhance damping, it is therefore critical to understand the physics underpinning the details of the interface.

The presence of a proximity induced moment in heavy metals layered with ferromagnetic transition metals has been experimentally verified using element specific x-ray magnetic circular dichroism (XMCD) for almost two decades [310–313]. In contrast, debate remains for NM heavy metals layered with insulating ferrimagnetic oxides. XMCD studies of Pt layered with several different ferrimagnetic oxides, including Fe_3O_4 and $CoFe_2O_4$, show no measurable magnetic polarisation of the Pt layer [15, 16, 314], while for Pt in contact with yttrium iron garnet, XMCD confirms the presence of an induced moment in Pt, but conflicting reports remain regarding the magnitude of the moment induced [15, 315]. More recently, the absence of PIM in Pt in contact with $CoFe_2O_4$ has been contradicted by indirect evidence from anisotropic magnetoresistance measurements and supported by density functional theory, indicating a small induced moment in Pt [309, 316].

The differences in the PIM of Pt layered with either metallic ferromagnets or ionic ferrimagnets may be attributed to the ordering of the magnetic moments due to various forms of exchange, as outlined in chapter 2. For oxide ferrimagnets, the magnetic moments are localised to lattice sites and magnetic sub-lattices align antiparallel via superexchange, mediated locally by hybridisation of individual orbitals, while in transition metal ferromagnets the moments are less localised and $d-d$ exchange interactions, mediated by conduction electrons, give rise to parallel alignment

of moments. In contrast to both ferromagnetic metals and oxide ferrimagnets, the presence or absence of PIM in Pt in contact with ferrimagnetic rare-earth/transition metal alloys (RE:TM) is unknown. It is also not known whether any induced moment in Pt would be directly coupled to one of the ferrimagnetic sublattices or follows the net magnetisation of the alloy.

Ferrimagnetic rare-earth/transition metal thin-film systems have been extensively studied due to their potential in spintronic applications. With different temperature dependencies of the magnetic moments and antiparallel coupling between the TM and RE sublattices in multilayers [317] and alloys [32], compensation points occur with net zero magnetisation and angular momentum [33] at a given temperature or composition [318]. These compensation points lead to useful phenomena, such as fast domain wall motion [319, 320], thermally induced switching [321, 322], vanishing skyrmion Hall angles [323] and self-focusing skyrmion racetracks [324], while efficient spin-orbit torque switching around compensation has been observed in studies of RE:TM alloys with bulk perpendicular anisotropy (PMA) [325–329], the onset of which may be controlled by the RE content [330]. Recently, it has also been shown that the width of domain walls and compensation temperatures can be altered with ion bombardment [331].

This section details the results of a study into PIM in Pt layered with two RE:TM ferrimagnetic alloys with compensation points above and below room temperature respectively, in order to determine the presence and the orientation of the PIM in relation to the direction of RE or the TM sub-lattice moments and to the net magnetisation. Using element specific resonant x-ray analysis, both the direction of the induced Pt moment, with respect to the ferrimagnetic sub-lattices, and the profile of the Pt PIM as a function of distance from the interface with the ferrimagnet were determined. The results on the ferrimagnetic systems presented in this section provide a fuller of understanding of the nature and role of PIM, which is then applied to spin transport in the following section.

9.2.1 Sample and Measurement Details

Ferrimagnetic samples were grown by the author and Dr Oto-obong Inyang, using magnetron sputtering, with the alloys produced by co-sputtering from TM and Gd targets. Atomic compositions were determined using energy-dispersive x-ray spectroscopy by Dr Inyang. Trilayered structures were fabricated consisting of Pt (5 nm)/FiM alloy (15 nm)/Pt (5 nm), where the FiM alloy was either $Co_{77}Gd_{23}$ or $(Fe_{50}Co_{50})_{77}Gd_{23}$. SQUID magnetometry measurements were performed by Ben Nicholson, with hysteresis loops measured at a range of temperatures for both alloys.

Resonant x-ray studies at the Pt and Gd L_3-edges (11.56 and 7.24 keV respectively) were undertaken on the 4-ID-D beamline of the Advanced Photon Source at Argonne National Laboratory. X-ray magnetic circular dichroism (XMCD) was used to probe the magnetic moments of specific elements, as described in chapter 6. Although determining values for moments using the sum rules for Gd is not accurately applicable due to the 4f and 5d states [332], the sign of the dichroic spectra was used to determine the direction of the elemental magnetic moments, with respect to the probe beam and applied field. Samples were also studied with grazing incidence resonant reflectivity, at the Pt L_3 edge, to obtain structural and magnetic information. Both XMCD and reflectivity were performed with a magnetic field of ± 0.6 kOe applied in-plane and along the beam axis. Analysis of the magnetic component of the resonant reflectivity allows a depth profile of the induced Pt magnetisation to be determined. X-ray absorption spectroscopy (XAS) was measured using a fluorescence detector, with both left and right circularly polarised x-ray intensities measured at each point. The measured XMCD signal was given by $(I^+ - I^-)\,/\,(I^+ + I^-)$, where I^+ and I^- denote the spectra with opposite circular polarisations, for a fixed magnetic field. The polarisation averaged XAS is defined as $(I^+ + I^-)/2$.

9.2.2 Temperature Dependent Measurements

To verify the dominant sub-lattice for the CoGd and CoFeGd ferrimagnetic alloys, in-plane (IP) hysteresis loops and measurements of the moment as a function of temperature were performed using SQUID magnetometry. Figure 9.1 shows the results of these, with the inset showing the temperature dependence of the saturation moment. The CoGd shows both a minimum in the temperature dependence of the net moment that is characteristic of the magnetisation compensation point, here above room temperature, and a consistent increase in the moment below the compensation point. It is also noted that a divergence in the coercive field was observed at the compensation point in similar alloys, explaining the enhanced coercivity of the CoGd alloy observed at 300K [333]. At temperatures below compensation, the Gd moment dominates and the Gd sub-lattice will be aligned with the applied field, with the Co sub-lattice antiparallel. Therefore at room temperature the Gd is dominant in the CoGd alloy. Above the compensation temperature the TM moment dominates the net moment, which is the case for the CoFeGd sample, as evidenced by the consistent decrease in moment as a function of temperature, and shows no compensation point down to 20K, the lowest temperature studied. Therefore at room temperature the TM is dominant in the CoFeGd alloy.

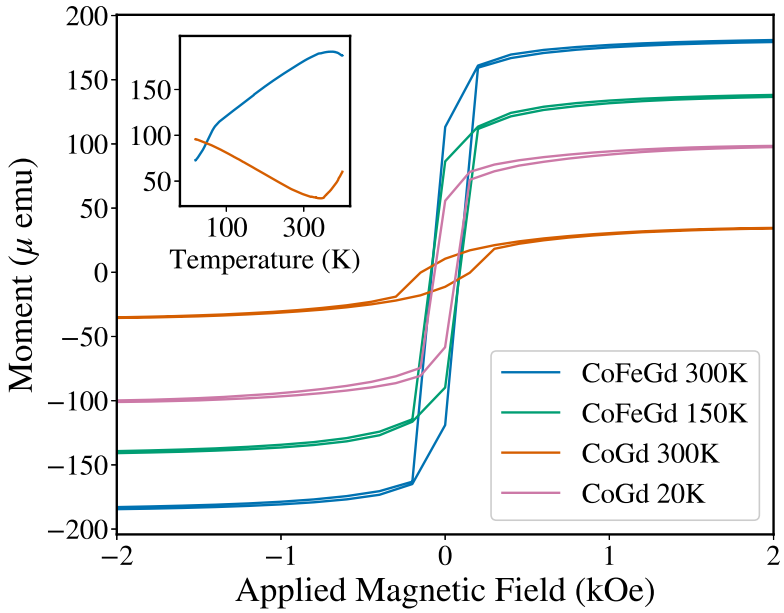

Figure 9.1: Magnetic hysteresis for the two Pt/RETM/Pt ferrimagnetic alloys at different temperatures. The inset shows the saturation moment as a function of temperature for Pt/CoGd/Pt (orange) and Pt/CoFeGd/Pt (blue), which indicates compensation points above and below room temperature respectively.

The magnitude of the Pt and Gd moments in the Pt/CoFeGd/Pt sample were also recorded by measuring the XMCD as a function of temperature, which acts as a proxy for the magnetic moments due to the proportional relationship between the two. Figure 9.2a shows the results of these measurements, with the surprising result of a decrease of the measured in-plane Gd moment as a function of temperature, which was not observed in the CoGd alloy. Although the net moment measured by SQUID also decreases as a function of temperature for the CoFeGd alloy, this is usually observed due to the competition between the competing RE and TM moments, which increase in magnitude at different rates as a function of temperature, leading to a net zero moment at the magnetisation compensation temperature, though each sub-lattice has a magnetic moment.

The decrease in Gd moment was further investigated by rotating the sample such that the applied field was now out-of-plane (OOP), with the probe beam perpendicular to the plane of the sample. This geometry allowed the magnitude of the OOP moment to be investigated, the results of which are also shown in figure 9.2a. An increase in the out-of-plane moment can be seen to accompany the reduction of the in-plane moment at both the Gd and Pt edges. To verify that the transition is a reorientation of the magnetism to out-of-plane, element specific hysteresis loops at the Gd edge with a sample temperature of 20 K, were measured in both of these ge-

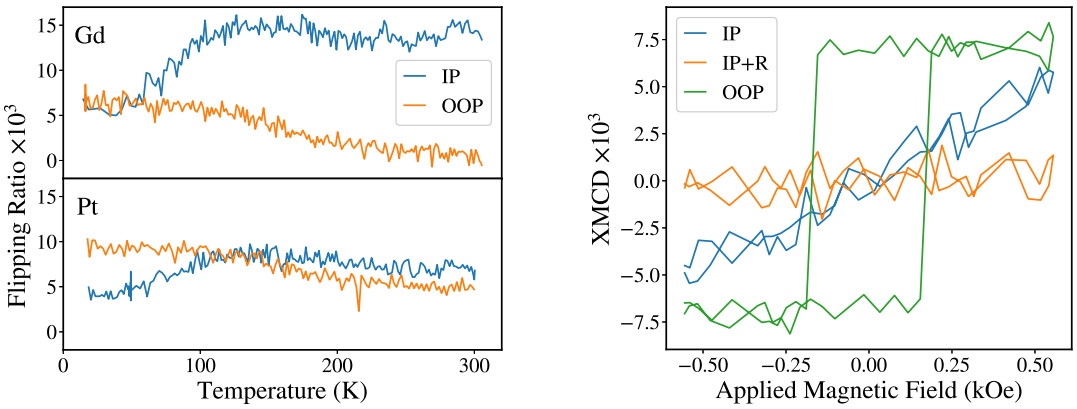

(a) (b)

Figure 9.2: (a) Flipping ratio as a function of temperature for the Pt/CoFeGd/Pt sample at both the Pt and Gd L_3 edges measured both in (IP) and out-of-plane (OOP), as defined in section 6.2.2. (b) Element specific hysteresis loops at 20 K at the Gd L_3 edge for the CoFeGd sample with in-plane (IP), out-of-plane (OOP) and in-plane, and rotated (IP+R) geometries.

ometries as well as a third with the same setup as usual in-plane measurements, but with the applied magnetic field rotated perpendicular to the probe beam direction while remaining in-plane. As XMCD is sensitive to the moment in the direction of propagation of the probe beam, this setup allowed for any spin-flop transitions to be ruled out, in which the Gd moment remains in-plane, but perpendicular to the applied magnetic field. Figure 9.2b shows the results in each of these geometries at 20 K, with a clear OOP easy axis, a hard IP axis, and no signal with the magnet rotated, eliminating the possibility of a spin-flop transition.

The transition of the Gd moment to out-of-plane, is also accompanied with a transition of the net moment, as shown in figure 9.3a, with hysteresis loops taken using SQUID magnetometry in both in and out-of-plane geometries. At 300 K, there is a clear magnetic easy axis in-plane, and a hard axis out-of-plane, which both reverse at 20 K. This transition is clearly observed in the calculated remanence ratio of the hysteresis loops as a function of temperature, shown in figure 9.3b, with the transition of the net moment to out-of-plane occurring at just over 100 K. Elsewhere, Gd on W was shown to have a temperature dependent spin reorientation transition [334] and the presence of a weak perpendicular magnetic anisotropy has been observed in FeGd alloys and not in CoGd of the same concentration [330]. For FeGd an out-of-plane transition was attributed to the weak anisotropy of the Gd arising due to the lack of orbital anisotropy from the half filled 4f orbital [335], where the difference in CoGd and FeGd may be attributed to the different anisotropy constants, and hence differences in magnetostriction ($Co_{17}Gd_2$: K_1=-5.1, K_2=-2.4

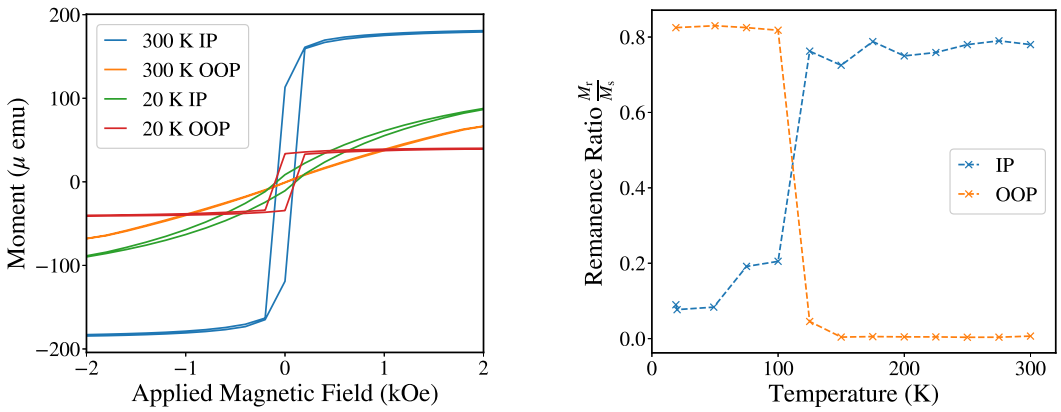

(a) (b)

Figure 9.3: (a) Magnetic hysteresis loops measured using SQUID magnetometry both in-plane and out-of-plane for the CoFeGd alloy, at two temperatures. (b) Magnetic remanence ratio as a function of temperature for two geometries calculated from the hysteresis loops. Dashed lines are a guide to the eye.

K/f.u., $Fe_{17}Gd_2$: K_1=-57.8, K_2=+4.6 K/f.u.) [57]. Further investigation into the out-of-plane transition of the iron rich ferrimagnetic alloy is beyond the scope of the work detailed in this thesis focusing on the induced magnetism in the Pt layer, and hence the remainder of the data presented in this section for the CoFeGd alloy is taken in the in-plane geometry, and hence is taken at temperatures above 150 K.

9.2.3 Energy and Field Scans at the Pt and Gd L_3 Edges

By considering the sign of the XMCD L_3 signal of the Gd sublattice and for the Pt, and knowing which sublattice dominates the magnetisation, the alignment of the induced moment in the Pt with respect to either the TM or RE sublattice can be determined. Figures 9.4a and 9.4b present the XMCD spectra, with the XAS inset, for the CoFeGd and CoGd alloys respectively, which show the maximum magnetic signals at the Pt and Gd L_3 edges. These spectra probe the p to d transitions and thus the Pt and Gd $5d$ moments. As can be seen for both alloys, the sign of the dichroic spectra is the same at the Gd and Pt edges with magnetisation either parallel or antiparallel to the probe beam. However, for a positive magnetisation, both Pt and Gd XMCD spectra are negative for the CoFeGd alloy, and positive for the CoGd alloy, due to the net moment being dominated by the CoFe in CoFeGd and Gd in CoGd.

Before any comparison can be made with the literature regarding the direction of the moments based on the sign of the XMCD spectra, the relationship between the sign of the Gd M_5 and L_3 dichroic edges and the direction of the magnetic moment

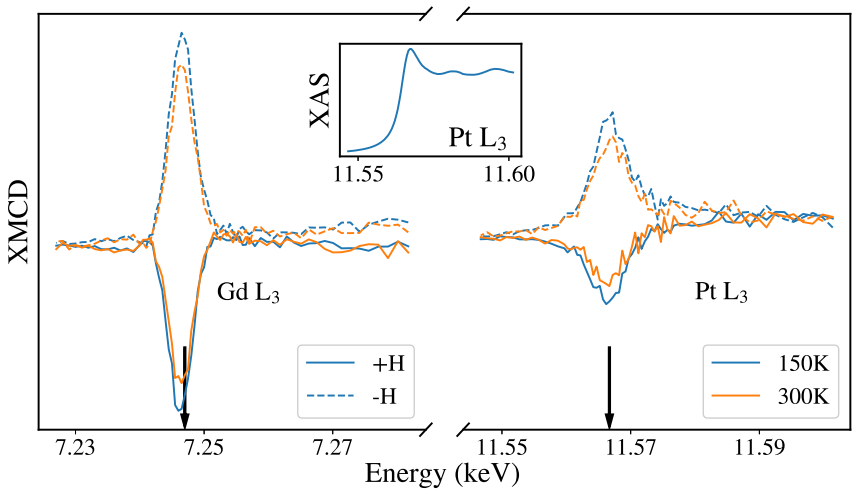

(a)

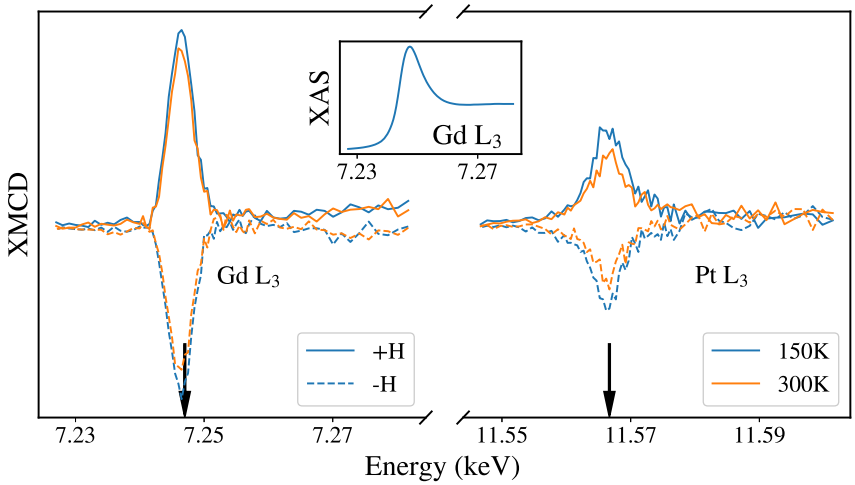

(b)

Figure 9.4: Energy scans at the L_3 edges of Pt and Gd in a Pt/FiM Alloy/Pt structure with $(Fe_{50}Co_{50})_{77}Gd_{23}$ (top) and $Co_{77}Gd_{23}$ (bottom). Vertical arrows on the energy scans denote the energies at which the Gd/Pt specific hysteresis loops were taken. Inset are the X-ray absorption spectra over the L_3 edge of Pt (top) and Gd (bottom).

needs to be briefly discussed, since other key works on XMCD of Gd have focused on the Gd M_5 edge. First, it was established in previous studies of ferromagnetic Gd that when the magnetisation was aligned with the field, the sign of the dichroic spectrum at the M_5 edge was negative and at the L_3 edge was positive [332, 336, 337]. Therefore, for the Gd L_3 edge, the sign of the dichroic spectrum is positive when the Gd magnetic moment is positively aligned with the magnetic field and the spectrum is negative when the Gd moment is antiparallel to the applied magnetic field. Second, in ferrimagnetic CoGd alloys, where Co dominates the magnetisation, the sign of the XMCD spectrum of the Gd M_5 edge was positive, while the Co L_3 edge was

negative [338], and across the compensation temperature, when the Gd moment dominates the magnetisation, both the Co and Gd XMCD signals were reversed, i.e. the Co L_3 edge becomes positive and Gd M_5 edge negative [32]. With this relationship, for an antiparallel ferrimagnetic coupling of Co and Gd, it is expected that the sign of both the Co L_3 edge XMCD spectrum and the Gd L_3 edge spectrum will be the same, even though the magnetic moments of the two sublattices are antiparallel.

For Pt, it was reported that the sign of the Pt L_3 edge in a Co/Pt system is the same as the Co L_3 edge, i.e. it is negative for positive orientation of the Co magnetisation [17, 339]. Therefore, in the case where Pt and Gd are aligned antiparallel, the L_3 XMCD spectra of both Gd and Pt will have the same sign. The sign of the spectra will depend on whether the Gd or the TM sublattice dominates the magnetisation, when Gd is dominant and aligned parallel with the saturating field, both the Gd and Pt XMCD L_3 spectra will be positive. A simplified summary of these alignments is presented in table 9.1.

As shown in figure 9.4, for Pt layered with the TM dominated CoFeGd alloy, for parallel alignment of the magnetisation and the beam, the dichroic spectra of both Pt and Gd are negative, therefore the Pt is aligned to the CoFe and antiparallel to the Gd. However, in the RE dominated CoGd alloy, for the same alignment of the net magnetisation (now Gd dominated), the signs of both the Gd and Pt dichroic spectra are reversed, indicating that, although the Gd moment is parallel to the magnetic field, the induced moment on the Pt is antiparallel and therefore aligned with the Co sublattice and opposite to the net magnetisation. Therefore in both cases, the Pt moment aligns with the transition metal sublattice regardless of which sublattice dominates the magnitude and direction of the net magnetisation.

A schematic illustration of the direction of the moments determined from the sign of the spectra is shown in figures 9.5a and 9.5b for the CoFeGd and CoGd alloys respectively. Also shown are the element specific hysteresis loops taken at both the Pt and Gd L_3 edges for both samples, the energies of which are indicated by black arrows in figure 9.4. The parallel and antiparallel alignments of the induced moment

Element Edges	Dichroic Signs	Moments	Ref
Gd M_5 - Gd L_3	Opposite	Parallel	[332, 336, 337]
Gd M_5 - Co L_3	Opposite	Antiparallel	[32, 338]
Co L_3 - Pt L_3	Same	Parallel	[17, 339]
Gd L_3 - Co L_3	Same	Antiparallel	
Gd L_3 - Pt L_3	Same	Antiparallel	

Table 9.1: A summary of the relations between the signs of dichroic spectra, and the alignment of moments.

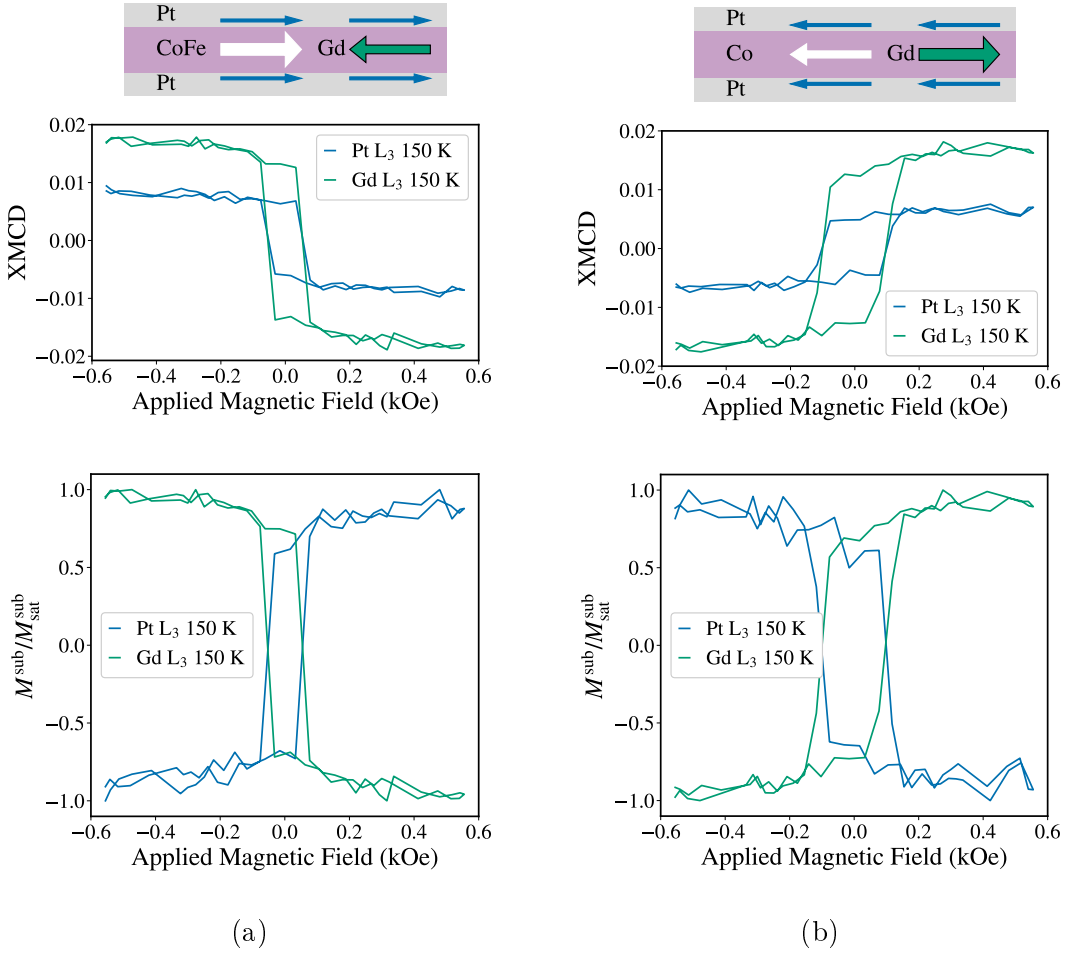

Figure 9.5: Schematic illustrations of the determined alignment of the moments and element specific hysteresis loops at the L_3 edges of Pt and Gd in a Pt/FiM Alloy/Pt structure for (a) $(Fe_{50}Co_{50})_{77}Gd_{23}$ and (b) $Co_{77}Gd_{23}$, with corrected hysteresis loops underneath showing the direction of the sublattice.

in Pt to the net magnetisation are evident in the element specific hysteresis loops, which reverse sign across the composition compensation transition. The coercivity is comparable with the bulk measurements in figure 9.1, and the fact that the Pt and Gd have the same shapes and coercivities demonstrates coupling of the Pt to the ferrimagnetic order.

Though there is a lack of an established first principles description of the magnetic properties of the $4f$ system in the RE [340], the coupling of the induced moment to the moment of the TM can be first considered using the approach proposed by Campbell [37], described in chapter 2. In this model, a direct $4f - 5d$ exchange in the RE splits and polarises the almost unoccupied $5d$ band [58, 59], resulting in an experimentally verified ferromagnetic coupling of the $4f - 5d$ states [45]. In both the Gd-TM and Pt-TM interactions, a direct $5d - 3d$ hybridisation occurs, the sign of which is determined by d band filling. For the RE-TM interaction, the hybridi-

sation leads to a slight occupation of the $5d$ band, with a larger occupation of the minority spin states, resulting in an antiferromagnetic coupling of the electrons [53]. Due to the ferromagnetic $4f - 5d$ exchange, the $4f$ *spin* moment is the same as the $5d$ moment and antiparallel to the $3d$ moment. The overall moment direction of the RE is thus determined by the orbital contribution, which for Gd is zero, and hence the total RE and TM moments are antiparallel. The Gd-Pt interaction can be understood by first ignoring the TM. In this system, the local spin moment in the $4f$ state through $4f - 5d$ exchange acts as field-like term which lowers the energy of the Gd $5d$ spin-down band, which preferentially hybridises with the nearly filled Pt d states producing an even larger Gd $5d$ moment, with a moment of equal but opposite magnitude induced in the Pt [58]. Therefore both the Gd-Pt and TM-Pt interactions act to induce a moment parallel to the TM and antiparallel to Gd as observed here.

The same conclusion can be reached within the RKKY framework, in which indirect exchange is mediated by conduction band electrons. For heavy RE elements, such as Gd, the $5d$ states in the conduction band are polarised by the localised $4f$ state. From Pauli exclusion this interaction produces a coupling which oscillates in sign as an electron moves away from the localised state. The integration of this oscillation provides a polarisation at the Fermi level in which there are more spin-up electrons. Hence, for heavy REs in the ground state, the *spin* momentum (and spin polarisation), and the *total* angular momentum are antiparallel to each other [341]. In the RE:TM alloy, the conduction band is a hybridisation of the TM $3d$ states and the RE $5d$ states, in which the total angular momenta are antiparallel, but the spin states of the Gd are aligned with the magnetisation direction of the TM alloy. Therefore the hybridised Pt $5d$ states are coupled to the spin polarised d orbitals in the RE and TM, which in this formalism are in the same direction.

9.2.4 XRMR at the Pt L_3 Edge

Though the presence of a Pt PIM and the ferromagnetic alignment with the transition metal moment has been demonstrated, the spatial relationship between the Pt PIM and the interface with the ferrimagnetic alloys was not revealed by the analysis so far. X-ray magnetic reflectivity, as detailed in chapter 6, provides knowledge of both the structural interface width and the PIM profile, allowing for insight into the lateral extent of the $d - d$ hybridisation that gives rise to the induced moment.

Examples of resonant reflectivity data at the Pt edge and the best fitting simulations of both the specular reflectivity and the dichroic asymmetry are shown in figure 9.6a. The simulations were performed using the *GenX* code [209], from which

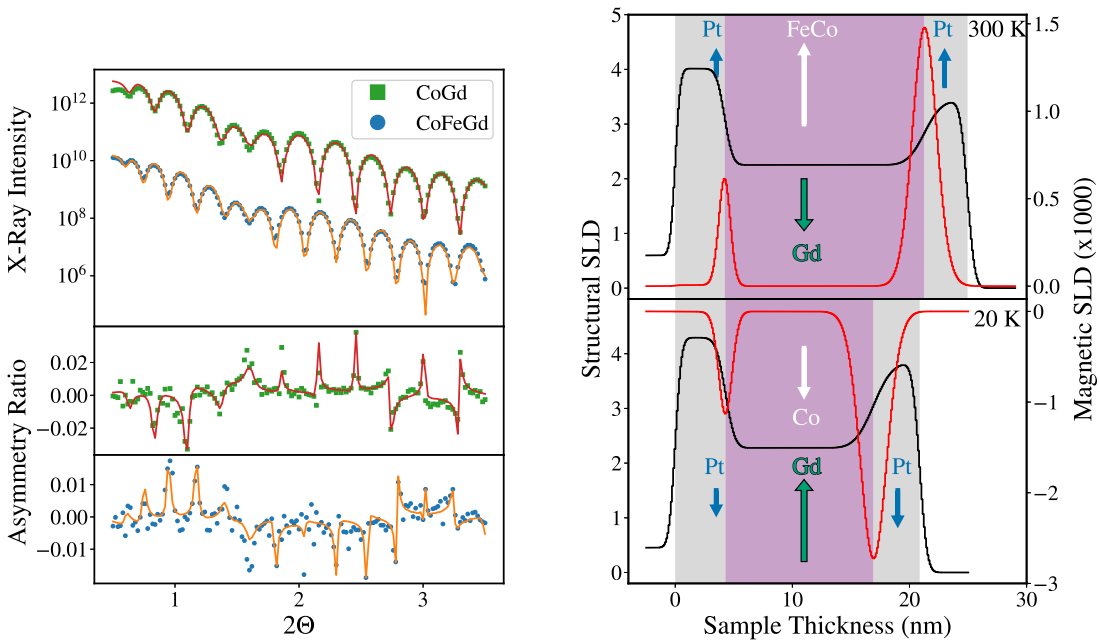

(a) (b)

Figure 9.6: Structural and magnetic characterisation of the two samples using resonant X-ray reflectivity at the Pt L_3 edge taken at $H = \pm 0.6$ kOe. (a) Measured reflectivity profiles with corresponding X-ray helicity asymmetry ratio below for CoGd (top) and CoFeGd (bottom). The asymmetry ratio is defined as $(R^+ - R^-)/(R^+ + R^-)$, where $R^{+,-}$ are reflected intensities with opposite circular polarisations. The solid lines represent best fitting models to both the structural and magnetic data. (b) Structural (black) and magnetic (red) scattering length densities from the model fits to the data for both RE:TM/Pt samples.

the best fitting structural (SLD) and magnetic (mSLD) scattering length densities were obtained, also shown in figure 9.6b. This analysis shows that the RE:TM alloy density is uniform indicating the Gd is uniformly distributed, in contrast to another observation [32].

The SLD and mSLD indicate the structural interface width and the extent of the PIM in Pt respectively, while the mSLD also shows the opposite signs of the induced Pt moments for the two FiM alloys, consistent with the earlier XMCD results described previously. The SLD shows the interface width between the Pt and the alloy extends over 1.9 nm (FWHM) and is associated with a combination of topographical roughness and intermixing across the interface. Additionally, the magnetic analysis shows that the interfacial profile of the PIM in Pt closely follows the structural width of the interface, supporting the notion that $d - d$ coupling is required between the Pt and the alloy components to create the PIM, consistent with other work in the literature on layer-resolved Pt moments in Ni/Pt mutlilayers [311]. Furthermore, it is also observed that the PIM in Pt at the lower Pt/FiM interface

is significantly smaller than at the upper interface, which agrees with observations in Pt/Co/Pt [14] and in Pd/Co/Pd [342], and indicates the sensitivity of the $d-d$ hybridisation to the local interfacial structure, which, in this case is narrower at the lower interface. The difference in interfacial behaviour was also observed in the previous chapter for spin transport. It is therefore of interest to compare the role of the induced moment in the Pt layer, with the dynamic interfacial transport which enhances the damping. This forms the basis of the rest of the investigations in this chapter.

To summarise, a resonant x-ray study determined for the first time that the moment in Pt aligns to the transition metal moment across the ferrimagnet magnetisation compensation point. Magnetic reflectivity measurements show that the spatial extent and amplitude of coupling which produces the induced moment are strongly tied to the details of the interfacial structure.

9.3 Proximity Induced Magnetism and Spin Transport

The previous section established that the induced magnetism in Pt is intrinsically linked to the interface with a magnetic material due to orbital hybridisation. It is also well known that Pt layered with a ferromagnetic material provides another energy loss channel, which acts to enhance the damping at resonance and hence increases the frequency bandwidth, as was detailed in the previous chapter. However, both the mechanism for the enhancement of damping and the relation between the dynamic behaviour and the static induced moment remain subjects of debate.

Chapter 3 introduced two theories of interfacial enhancement of damping. The first is the commonly used spin pumping formalism, in which a non-equilibrium spin accumulation from a precessing magnetisation in a ferromagnetic layer transfers a pure spin current across an interface with a NM material [113, 122, 124, 125]. The enhancement of damping is then determined by how efficiently spins transfer across an interface, which depends upon the matching of conductance channels, and the lengthscale over which spin currents de-phase inside the NM material, the spin diffusion length, which depends upon the SOC of the material [112]. Materials such as Pt and Pd are therefore good spin sinks. In this formalism, proximity induced magnetism plays no role, as the equilibrium enhanced spin susceptibility does not affect either the Sharvin conductance or the non-equilibrium transfer of spin current across an interface [123].

An alternative first principles approach was proposed by Barati, Cinal, Edwards

and Umerski [115], based on the model by Kamberskỳ [95] which considers magnon relaxation with inter and intraband transitions arising from SOC [343] across a FM/HM interface. Materials such as Pt and Pd lead to a large increase in damping due to strong SOC interactions and orbital hybridisation with $3d$ transition metals. This hybridisation is responsible for the induced moment in Pt, and hence this approach directly relates the damping with the hybridisation that gives rise to proximity polarisation.

This discrepancy is also apparent in experimental literature, with a recent report claiming an irrelevance of PIM to interfacial spin torques, measured by altering the induced moment through alloying Pt with Au [18]. On the other hand, spin pumping based studies have correlated a reduction in the damping enhancement with a reduction in the induced moment of Pt with a Cu spacer in a NiFe/Cu/Pt structure, measured using XMCD, with a moment no longer present with a 1 nm barrier [17, 260]. This conflict is not limited to transition metal / HM interfaces, PIM and spin transport measurements in ferrimagnetic YIG/Pt also claimed to either have no effect determined from spin pumping measurements [252] or a significant effect with temperature dependent spin Hall effect measurements [315] and angular FMR [303].

Within the spin pumping formalism there is also disagreement as to how to treat the measured interfacial parameters for Pt while considering the induced moment, if at all. Conca *et al.* proposed treating the damping enhancement from Pt as coming from two regions in a CoFeB/Pt systems measured using spin pumping; one confined to the interface, and another outside of the range of PIM [271]. Omelchenko *et al.* reported that PIM does not play any explicit role in the mathematical interpretation of spin pumping, but plays an essential part in determining the quantitative values of key interfacial parameters such as the spin mixing conductance. In particular, the PIM acts to dephase the spin current, leading to short spin diffusion lengths [344].

A common method to investigate the role of PIM in spin pumping experiments is to insert a thin spacer layer at a FM/HM interface. Studies have shown a clear reduction in damping with a spacer layer such as Al [345], attributed to a loss of induced moment. Cu and Au are also commonly used as it is assumed that due to the large spin diffusion and spin orbit interaction lengths, 100 nm for Cu [261, 266, 346] and 60 nm for Au [347], the effect they have on spin transport is negligible. Indeed Cu spacer layers were shown to have little effect on the measured spin Hall angle in Co/Cu/Pt [133], attributed to the long spin diffusion length and low SOC. However, XMCD studies showed a large decrease in both induced moment and damping arising from spin pumping with the insertion of a thin Cu layer [17]. This is further complicated by reports of an induced moment in ultra-thin ($<$0.4 nm) Cu

between perpendicularly magnetised Co/Pt [348]. It is therefore key to compare the interfacial structure with the induced moment and the resultant damping, a link which is lacking currently in the literature.

This sections details an investigation in collaboration with the IFMPAN into spin transport and PIM in Pt through samples with compositional wedges of Pt, Cu and Au. By comparing synchrotron measurements undertaken at the APS on the Pt edge, which provides exclusive magnetic information of the Pt, with dynamic broadband FMR measurements, along with lab based structural characterisation using x-ray reflectivity, the relation between PIM, dynamic behaviour and interfacial structure was determined.

9.3.1 Thickness Gradient Wedges and Calibrations

All samples measured in this section were grown at the IFMPAN by Dr Hubert Głowiński, using the same magnetron sputtering process and substrates as used in other sections, with the addition of a controllable shutter across the sample, allowing for the growth of layers of material with varying thickness in one dimension. Samples were grown on thermally oxidised silicon wafers, cut to 10×20 mm, with the thickness wedge along the long axis of the wafer. Dynamic FMR measurements discussed later in the section were undertaken at the IFMPAN by both the author and Dr Głowiński, with analysis solely by the author.

The first set of samples consisted of thickness varying wedges of Pt and Cu with $Co_{25}Fe_{75}$ as the FM, due to the reported low damping in this material [297], which would make any changes in the damping due to interfacial effects clearer. Within this, three series of samples were fabricated, the first consisted of a Pt wedge in a Cu(2 nm) / CoFe (7 nm) / [Cu (5 nm) / Pt (t nm)]×n structure, such that $t \times n = 24$, i.e. the total Pt thickness is 24 nm, to investigate the role of the number of interfaces. Following this, two Cu wedge samples were fabricated, one in direct contact with the FM, Cu (2 nm)/ CoFe (7 nm)/ Cu (wedge up to 10 nm) / Pt (10 nm), and one within the Pt layer, Cu (2 nm)/ CoFe (7 nm)/ Pt (1 nm)/ Cu (wedge up to 5 nm) /Pt (1 nm). Finally, an additional series of samples with a Pt thickness gradient in *direct* contact with the FM were produced, Cu(2 nm) / CoFe (7 nm) / [Pt (t nm) / Cu (5 nm)]×n, again with $t \times n = 24$.

The second set of samples were based on Au thickness gradients, which allowed for the dependence of the dynamic response with a more closely matched electronic structure between the spacer layer and the HM [349] to be investigated, with both Pt and Pd as the spin sink. Both the same CoFe alloy as before and $Ni_{80}Fe_{20}$ were used as the FM, in order to verify the role of interfacial structuring, as the CoFe

alloy was expected to have bcc structure [297], while the NiFe, Pt, Pd, Au and Cu layers were expected to have fcc structure [199]. Samples in this set consisted of FM (7 nm) / Au (wedge up to 3 nm) / NM (4 nm), with CoFe and NiFe as the FM, and Pd, Pt and Cu as the NM. In addition two samples were produced with the NM in direct contact with the FM, in a FM (7 nm) / NM (2 nm) / Au (wedge up to 3 nm) / NM (2 nm) structure, with Pd and Pt again as the NM.

All thickness gradient wedges were grown such that the wedge started 4 mm from the edge of the cut wafer, which allowed for reference measurements to be taken without the wedge present. Calibration of the thickness wedges was undertaken using lab based XRR. Slits were placed at the x-ray source to narrow the beam to 1 mm in size, comparable with the transmission line used for the FMR measurements. The centre of the sample was first aligned, before a scan along the length at a specular condition of $\theta = 0.2°$, $2\theta = 0.4°$ was undertaken to determine the location of the sample edges. Figure 9.7a shows an example of this for the Cu(2 nm) / Co25Fe75 (7nm) / Au (wedge) / Cu (4nm) sample. The sample was measured to be 20 mm long, hence the corresponding position on the x-ray scan was taken to be where the recorded intensity is the same to within 10%, but separated by 20 mm. For this sample this occurred at 35 mm and 55 mm.

X-ray reflectivity measurements were undertaken at five positions across the measured samples, for the example here these were at positions of 52, 48, 44, 40 and 37 mm. Figure 9.7b shows the resultant reflectivity profiles and best fits obtained using the *GenX* code [209], which were used to determine the Au thickness. The corresponding SLD profiles, shown in figure 9.7c show a clear reduction of the Au signal as the Au thickness is reduced.

The Au thickness determined using XRR compared to the expected thicknesses based on the deposition parameters, knowing that the thickness gradient starts 4 mm from the edge and increases up to 3 nm, is shown in figure 9.7d. A simple linear fit to the measured data shows good agreement with the expected thickness, and therefore there is confidence that the Au thickness is as expected at other positions on the sample. It should be noted that this method works in part due to the differences in the electron densities between the layers of CoFe, Au and Cu, whereas the calibration would be inaccurate for thickness gradients with too similar x-ray scattering factors to the surrounding layers, as there would be no well defined, layer resolved SLD profile, which *GenX* uses to fit the reflectivity data.

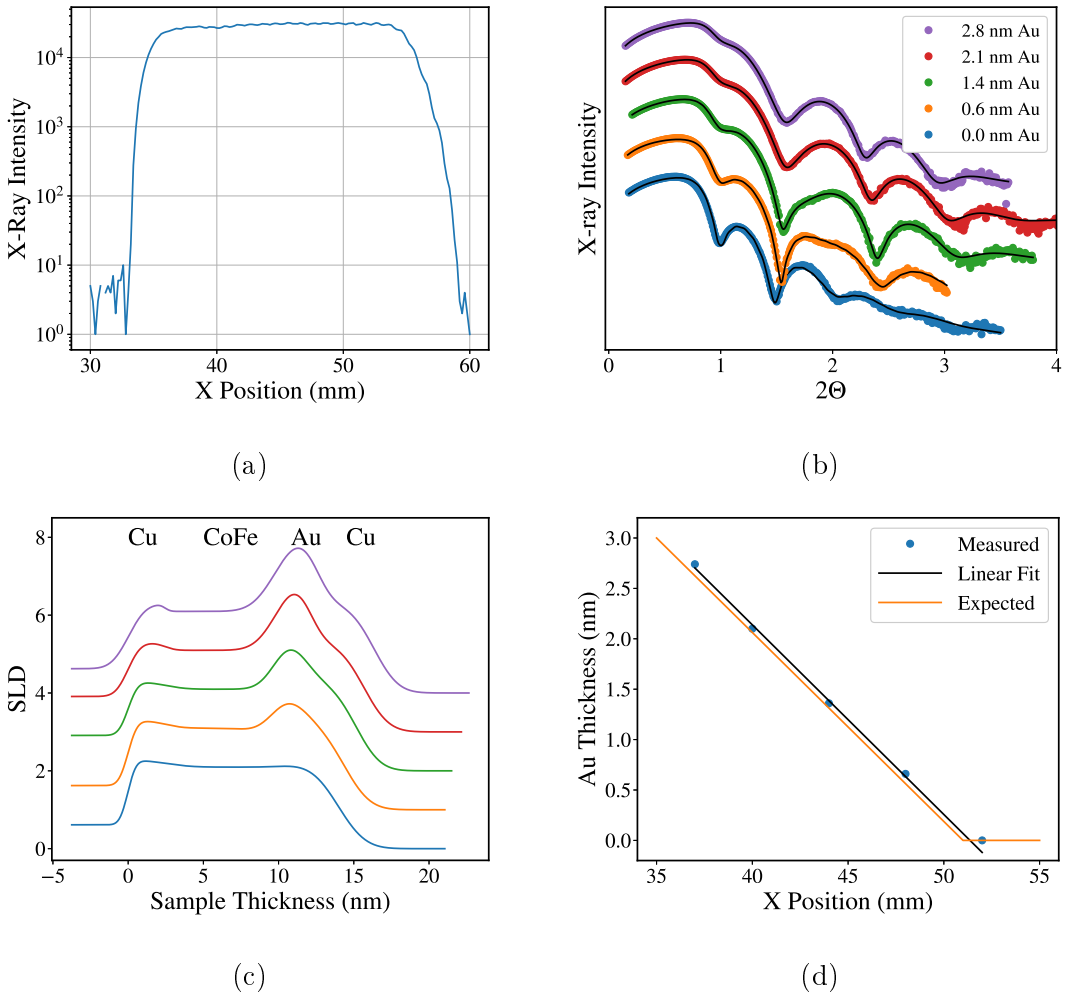

Figure 9.7: (a) Scan over the CoFe / Au (wedge) / Cu sample at a fixed specular condition. (b) Reflectivity curves with best fits at 5 locations along the sample, with determined Au thickness indicated. (c) Corresponding SLD determined from best fits to XRR data at the same Au thicknesses. (d) Expected experimental thickness (solid orange) and measured (blue dots) Au thickness with linear fit, as a function of sample position.

9.3.2 Dynamic Measurements with Pt and Cu Wedges

Dynamic measurements were undertaken using the broadband VNA based FMR at IFMPAN, which operates almost identically to the VNA based system described in chapter 7, with a co-planar waveguide as the transmission line, with a 1 mm wide central conductor. Thickness gradient samples were measured by performing magnetic field scans at various frequencies at different positions across the sample. The more confined magnetic field of the co-planar waveguide compared to the microstrip allowed for a 1 mm wide area to be excited for each scan, rather than the whole sample. Due to the large external magnetic fields available, resonance was able to be excited up to 40 GHz, figures 9.8a and 9.8b show examples of the raw S_{21} pa-

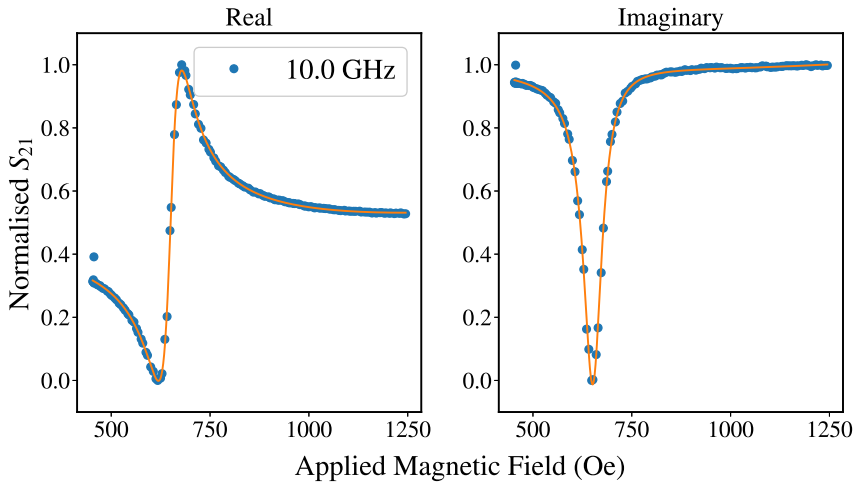

(a)

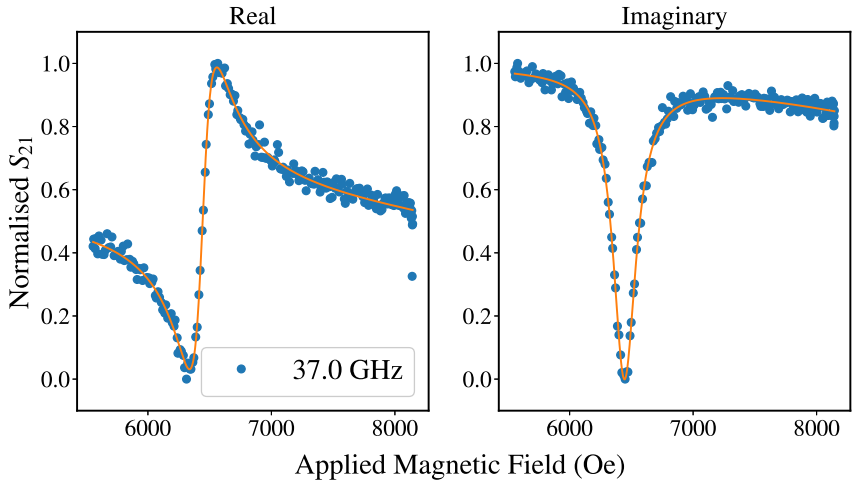

(b)

Figure 9.8: VNA based FMR measurements showing the real and imaginary components of the S_{21} parameter in a magnetic field scan on a CoFe (7 nm)/ Pt (4 nm) sample with an excitation frequency of (a) 10 GHz and (b) 37 GHz. Solid lines indicate best fits.

rameter in terms of both the real and imaginary components, fitted concurrently to determine the resonance position and linewidth.

Figures 9.9a and 9.9b show the resonance peak position at each frequency (the Kittel curve) and the magnetic field linewidth at each frequency respectively from the fitted S_{21} parameters. Best fits using the Kittel equation for the resonance position, and a straight line for the linewidth show good agreement over the full frequency range. A discussion of the measured damping for each of the sample series in the first set now follows.

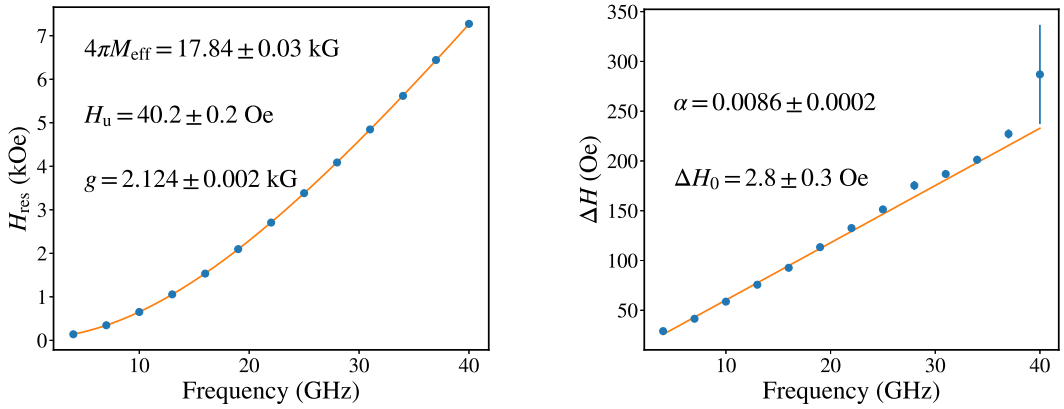

(a) (b)

Figure 9.9: Representative (a) Kittel curve and (b) linewidth plots with the data from the CoFe/Pt sample with best fits (solid lines) to determine the key dynamic parameters, such as the damping.

Pt Thickness Gradient with Cu Spacer

Initial investigations with the thickness gradients were designed to probe the role of the interface, and hence by increasing the number of interfaces, n, in a Cu(2 nm) / CoFe (7 nm) / [Cu (5 nm) / Pt (t nm)]$\times n$ structure, where the total HM thickness was held constant. Through this, it was thought that the interfacial contribution, if any, to the damping could be determined. As discussed previously, Cu was chosen as a spacer as it was reported to have a low SOC and large spin diffusion length, which would not have contributed to the interfacial damping enhancement in the material itself, but rather the interface may have some effect, such as an additional de-phasing of the spin current in the spin pumping formalism.

Figures 9.10a and 9.10b show the extracted damping parameters and effective magnetisation, respectively, for these samples. It was expected that the damping should increase with Pt thickness, as observed in the previous chapter. However, as observed in figure 9.10a there is no significant change for the simplest sample structure, consisting of Cu(2 nm) / CoFe (7 nm) / Cu (5 nm) / Pt (wedge). Although the damping is lower, there is also no significant change in the sample with an additional 5 nm Cu in the middle of the Pt thickness gradient. Within the spin pumping framework, the lower overall damping with an additional Cu spacer could be a consequence of the Pt thickness in the first Pt which the spin current reaches. The lack of a significant trend in the effective magnetisation is attributed to the Cu spacer preventing any induced surface anisotropies between the Pt and FM layers, as observed for Co/Pt [110].

The lack of a trend in the damping measurements indicates that either the Cu is

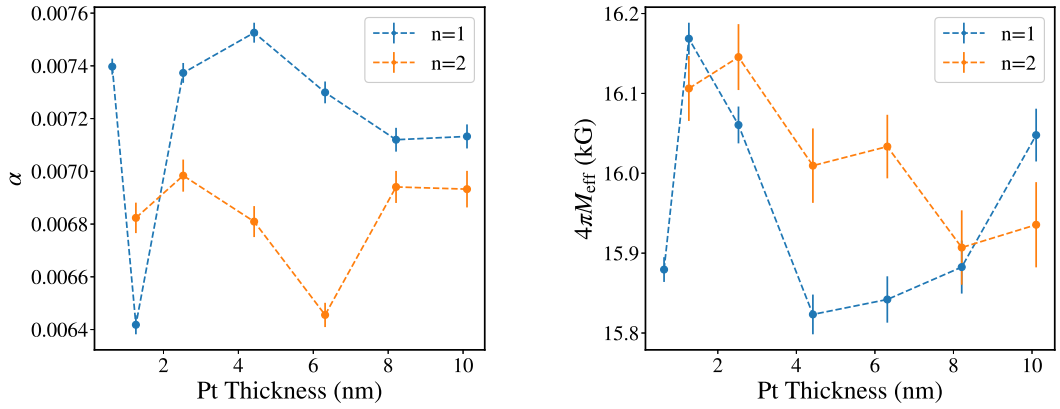

(a) (b)

Figure 9.10: (a) Damping parameter determined from fits to the FMR linewidth for a Pt thickness wedge following a Cu spacer layer in a Cu(2 nm) / CoFe (7 nm) / [Cu (5 nm) / Pt (t (nm)/n)]$\times n$ structure. (b) Effective magnetisation for the same sample, determined from fitting to the Kittel curve. Dashed lines are guide to the eye.

suppressing any interfacial enhancement of the damping by blocking the transfer of spin angular momentum, or that due to the 5 nm barrier, there is no induced moment in the Pt, which is evidence for the relation between the dynamic magnetisation behaviour and PIM. It is therefore of interest to determine the behaviour of a Pt wedge in *direct* contact with the FM.

Pt Thickness Gradient at the Interface with a Ferromagnet

Figure 9.11a shows the measured damping for Cu (2 nm) / CoFe (7 nm) / [Pt (t (nm)/n) / Cu (5 nm)]$\times n$ samples, with $n = 1, 2$. For these samples, the Pt is in direct contact with the FM, and for both sets a clear increase in damping is measured as a function of Pt thickness, which plateaus at Pt thicknesses above the spin diffusion length. For nearly all Pt thicknesses, the addition of a Cu spacer midway within the Pt thickness results in higher damping. This is shown directly in figure 9.11b, in which the difference between the two datasets is plotted. This additional damping is attributed to the Cu which, as the thickness is constant, would be expected to be linear with Pt thickness. However there is a slight enhancement at low Pt thicknesses, which may be due to increased interfacial disorder, as has been observed previously for FM/HM bilayers with low HM coverage [108]. These results suggest that there is an additional role that the interface plays with regard to damping enhancement.

In order to investigate any relation between PIM and the dynamic magnetisation

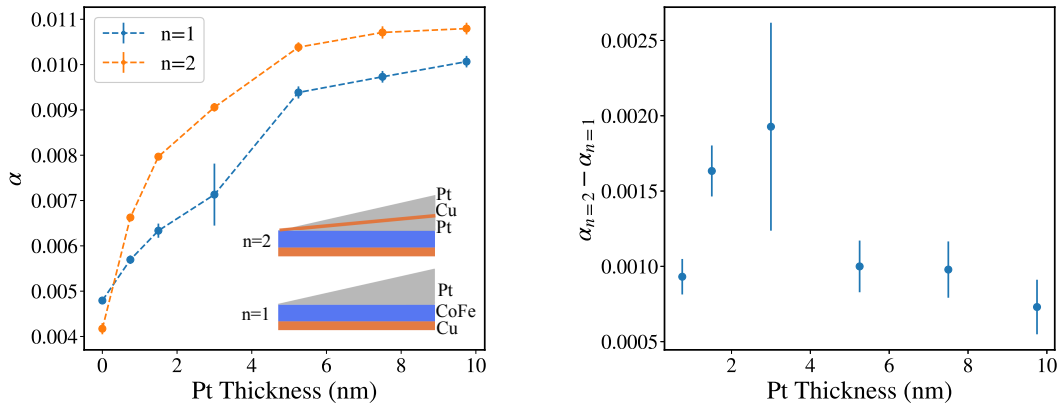

(a) (b)

Figure 9.11: (a) Measured damping parameter from the FMR linewidth for Cu(2 nm) / CoFe (7 nm) / ⌊Pt (t (nm)/n) / Cu (5 nm) ⌋$\times n$ samples. (b) Difference in the damping parameter between the two samples. Dashed lines are a guide to the eye.

behaviour further, measurements were undertaken on samples with a spacer layer of increasing thickness between a FM and HM layer.

Effect of Cu Spacer Layer Thickness Gradient on Damping

The damping parameter as a function of Cu spacer layer thickness is shown in figure 9.12, for a spacer layer directly between the FM and HM layers, Cu (2 nm)/ CoFe (7 nm)/ Cu (wedge up to 10 nm) / Pt (10 nm), and one within the Pt layer itself, Cu (2 nm)/ CoFe (7 nm)/ Pt (1 nm)/ Cu (wedge up to 5 nm) /Pt (1 nm). The difference in damping at zero Cu is attributed to the different thicknesses of Pt (2 nm and 10 nm). In both cases, the measured damping decreases sharply with the addition of the Cu layer, which is in conflict with previous measurements in the literature, which showed no change in spin Hall angle with a thin Cu layer. A simple exponential function was fitted to provide a quantitative comparison of the lengthscale of the decay in the damping enhancement, results in 0.44 ± 0.04 nm for the Cu wedge in the Pt, and 0.66 ± 0.06 nm for the Cu wedge between the FM and HM.

For the Cu wedge within the Pt, it is assumed that a moment is still induced in the first layer of the Pt, however, a sharp decrease in damping is still observed, implying that the interface with the Cu is the dominant factor in reducing the damping, rather than the induced moment. It may still be the case that both processes, that is the reduction in induced moment and additional interfacial loss, are present in the system and cannot be disentangled. Replacing the Cu with Au,

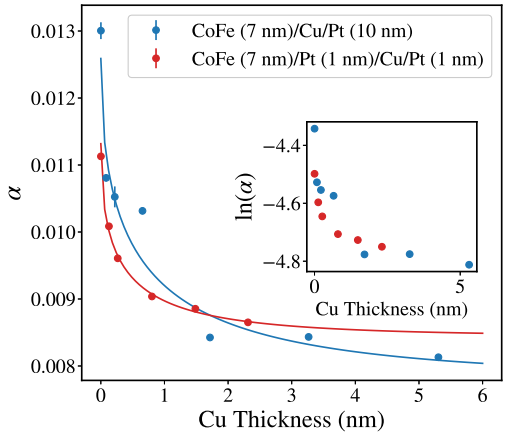

Figure 9.12: Damping parameter as a function of Cu spacer wedge thickness for two samples, as detailed in the legend. The solid lines are best fitting exponential functions.

the electronic structure of which is more similar to Pt, may provide insight into the reduction in damping. This is detailed later in this section. To properly correlate the reduction in Pt moment with the reduction in interfacial damping with Cu thickness, it is important to consider the relation magnitude and spatial variations of the induced moment with spacer layers.

9.3.3 Pt Proximity Magnetisation with Cu Spacer Layers

The extent of the induced moment in Pt as a function of Cu spacer layer thickness in the CoFe/ Cu(wedge) /Pt sample, was determined using magnetic reflectivity. Additional Pt element specific hysteresis loops, and scans of the XMCD signal as a function of position across the sample also provided information regarding the reduction in the induced moment as a function of Cu thickness. Similarly to the previous section, measurements were taken at the Pt L_3 edge at the 4-ID-D beamline of the Advanced Photon Source, using the setup detailed in chapter 6.

Magnetic reflectivity data and best fitting simulations of both the specular reflectivity and asymmetry are shown in figure 9.13a. As in the previous section, simulations were undertaken using *GenX* [209], from which the structural (SLD) and magnetic (mSLD) scattering length densities were obtained, as shown in figure 9.13b. Both the magnitude of the asymmetry ratio, and the mSLD substantially decrease with the introduction of a small amount of Cu between the CoFe and the Pt, and are over 100 times smaller after the insertion of 1 nm of Cu.

The induced moment in Pt is also highly localised to the interface in all three thicknesses measured. Figure 9.14 shows the normalised mSLD of all three Cu

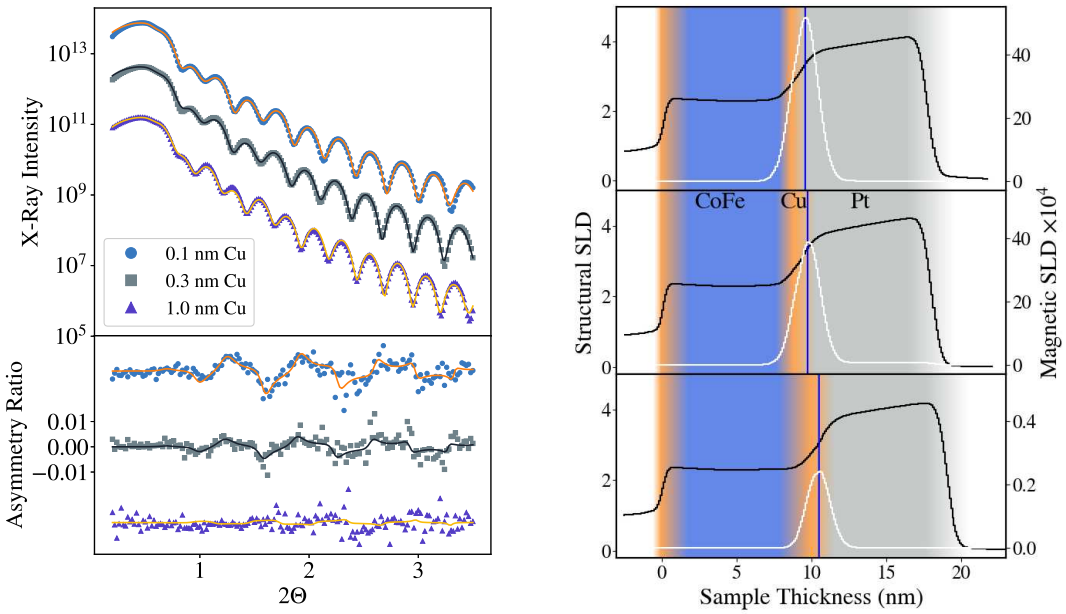

(a) (b)

Figure 9.13: (a) Top graph shows measured reflectivity profiles at the Pt L_3 edge with corresponding X-ray helicity asymmetry ratio below for three nominal thicknesses of Cu spacer layer in a CoFe/Cu/Pt structure. The asymmetry ratio is as defined in the previous sections. The solid lines represent best fitting models to both the structural and magnetic data. (b) Structural (black) and magnetic (white) scattering length densities from the model fits to the data for all three Cu thicknesses, the blue line indicates peak centre of Pt magnetic moment.

thicknesses, in which there is little variation in the spatial extent of the PIM, which is attributed to the direct hybridisation needed between the HM and the FM to induce the moment. The induced moment at the thickest Cu spacer could be attributed to small regions of intermixing which allow for direct hybridisation between the FM and Pt, rather than coupling through the Cu.

Figure 9.15 shows the measured XMCD across the Cu spacer thickness gradient for the CoFe/Cu/Pt sample, which confirms the decrease in moment at the onset of the wedge. Also marked is the integrated mSLD determined from the reflectivity, which serves as a proxy for the total moment induced. The decrease in the induced moment is also observed in the magnitude of the three element specific hysteresis loops, with the signal at 1 nm of Cu just discernable above noise.

The exponential fit to the XMCD as a function of Cu thickness, allows for a correlation between the XMCD, a proxy for the moment, and measured damping to be plotted. This is shown in figure 9.16, where there is a clear trend between the damping and induced moment. However, taking into account the dependence of the damping on the Cu spacer thickness introduced previously, it is evident that

the reduction in damping with Cu does not come solely from the reduction in $d-d$ hybridisation, which the induced moment is dependent on, but rather the combination of orbital hybridisation and reduction in interface transparency, the spin mixing conductance in the spin pumping formalism. Losses in the Cu itself attributed to the dephasing of spins are unlikely due to weak SOC and large spin diffusion lengths. This is in agreement with the work of Omelchenko *et al.* [344], in that the two contributions are entwined, and not irrelevant.

9.3.4 Dynamic Magnetisation Measurements in FM/SL/HM Systems with Au Spacer Layer Wedges

To further investigate the effect of the interface spin transparency, a series of samples was grown in which the spacer layer was Au. In addition, NiFe as a FM and Pd as a HM were also used, as all are expected to have fcc structure. Figures 9.17a and 9.17b show the extracted intrinsic and extrinsic damping contributions in a FM (7 nm) / Au (wedge) / Cu (4 nm) structure, for both NiFe and CoFe. In the spin pumping framework, the slight increase in intrinsic damping can be attributed to spin pumping into the Au layer [350]. Interestingly, the extrinsic damping remains mostly constant with NiFe as the FM, but increases with CoFe. This increase is most probably due to increased scattering associated with the greater structural mismatch between bcc CoFe and fcc Au, compared to fcc NiFe and fcc Au, which can lead to increased structural defects occurring during growth and hence a greater number of scattering centres. Growth of fcc Au on bcc Fe was shown to form a complex island structure beyond a few monolayers of Au [351].

The effect of replacing the Cu with Pd, a material with stronger SOC and the

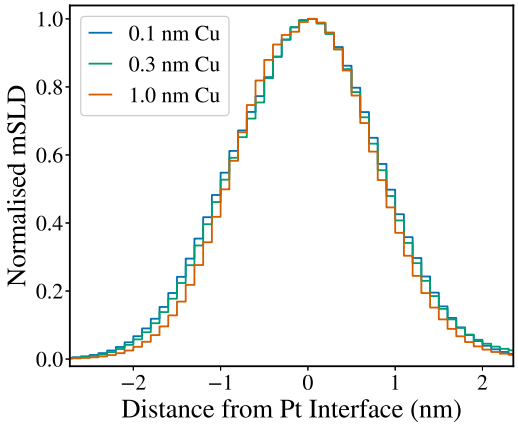

Figure 9.14: Normalised mSLD of the induced moment in Pt for all three Cu thicknesses in a CoFe/Cu/Pt structure.

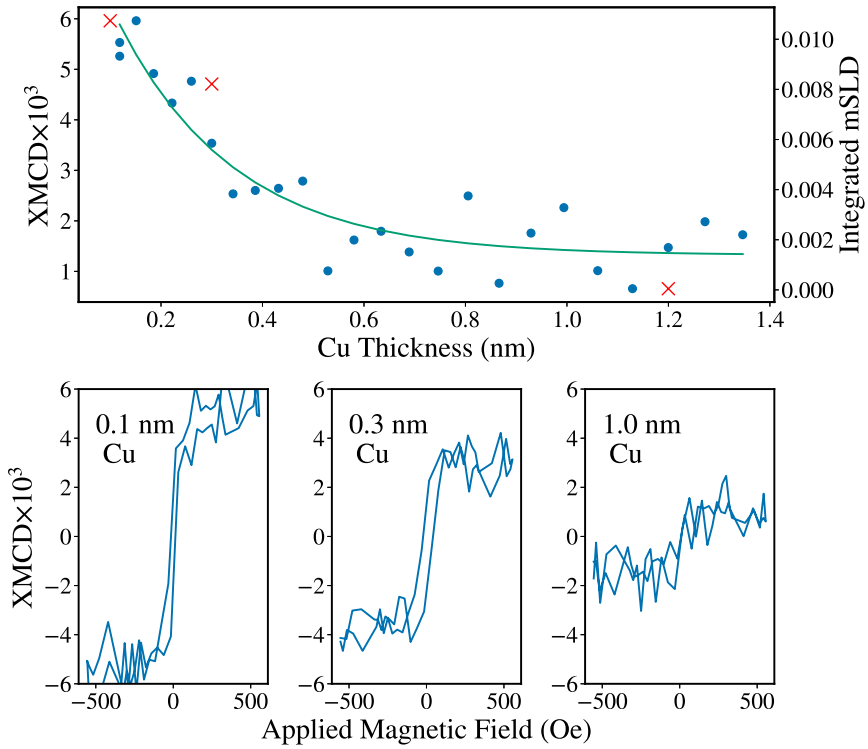

Figure 9.15: Measured XMCD as a function of Cu spacer wedge thickness (blue dots) with best fitting exponential (solid green). Red crosses mark the integrated mSLD value at the three Cu thicknesses from figure 9.13, with Pt hysteresis loops at each thickness.

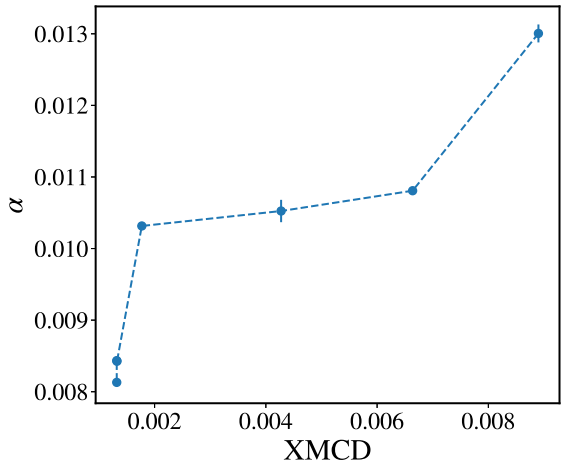

Figure 9.16: Damping and XMCD signal at the same points on the Cu spacer wedge for the CoFe/Cu/Pt sample. Dashed lines are a guide to the eye.

potential for $d-d$ hybridisation with a FM, on the intrinsic and extrinsic damping contributions is shown in figures 9.18a and 9.18b. Pd contains fewer electrons than Pt and hence has a smaller SOC, and therefore the corresponding interfacial damping

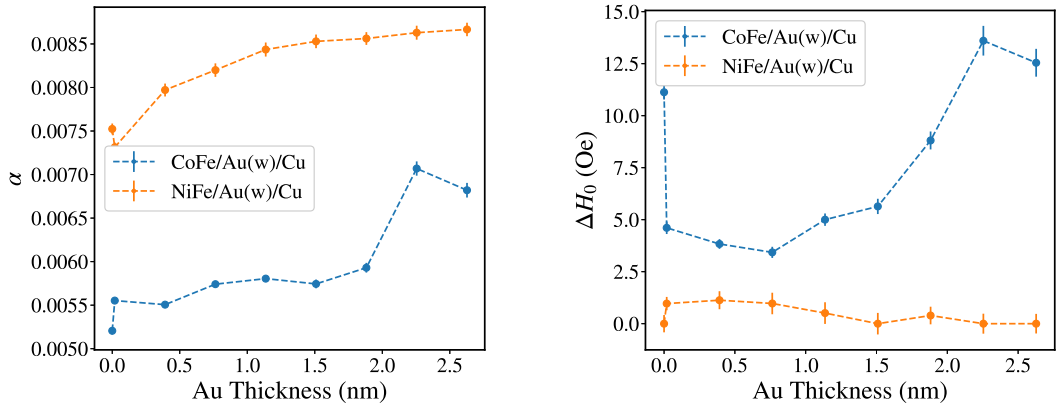

(a) (b)

Figure 9.17: (a) Intrinsic damping, α, and (b) Extrinsic damping, ΔH_0, contributions to the FMR linewidth as a function of Au thickness in a FM (7 nm) / Au (t nm) / Cu (4 nm) structure. Dashed lines are a guide to the eye.

enhancement is smaller than for Pt. This is reflected in the smaller increase in intrinsic damping with NiFe as the FM, with no Au. As with the Cu spacer layer, a small layer of Au is enough to reduce the damping, with the slight increase at thicker Au likely to arise from the spin pumping enhancement with thicker Au. Unlike NiFe, almost no change is observed in the intrinsic damping with CoFe as the FM, whereas the situation is reversed with regards to the extrinsic damping, in a similar manner to figure 9.17b. These results highlight the importance of close structurally matched interfaces for a controlled enhancement of damping [110].

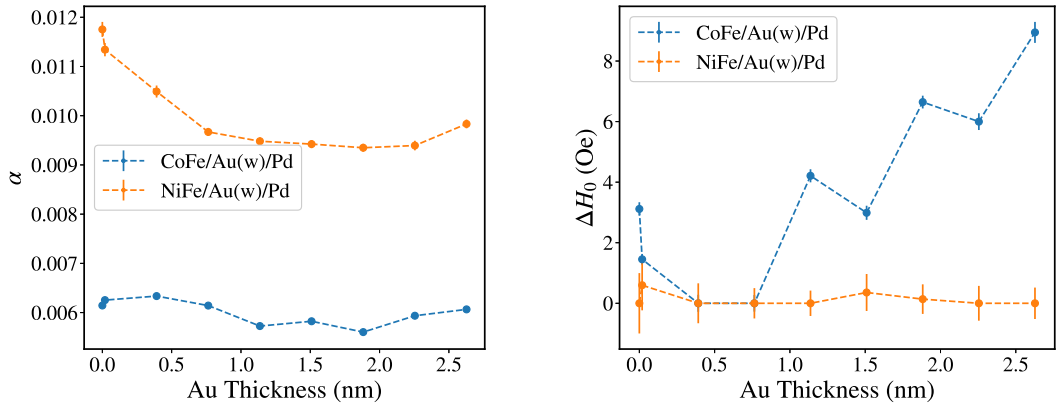

(a) (b)

Figure 9.18: (a) Intrinsic damping, α, and (b) Extrinsic damping, ΔH_0, contributions to the FMR linewidth as a function of Au thickness in a FM (7 nm) / Au (t nm) / Pd (4 nm) structure. Dashed lines are a guide to the eye.

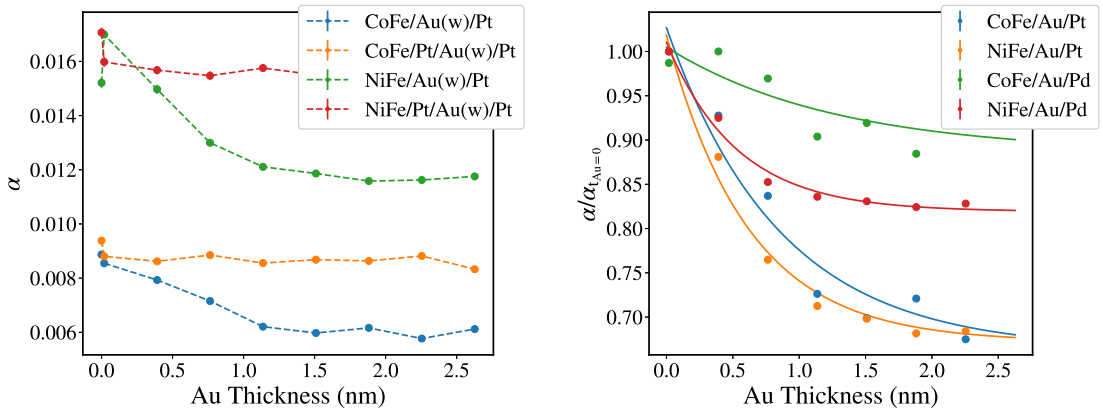

(a) (b)

Figure 9.19: (a) Intrinsic damping contributions, α, to the FMR linewidth as a function of Au thickness with structures as detailed in the legend. Dashed lines are a guide to the eye. (b) Intrinsic damping as a function of Au spacer layer for Pd and Pt HM trilayer stacks, normalised to the value with no Au present. Solid lines are best fitting simple exponential functions.

The effect on the measured intrinsic damping with Pt as the HM layer is shown in figure 9.19a for two sample structures, one with the Au wedge between the FM and HM layers, FM (7 nm) / Au (wedge up to 3 nm) / HM (4 nm) and one in the HM layer, with the total HM thickness constant, FM (7 nm) / HM (2 nm) / Au (wedge up to 3 nm) / HM (2 nm). Here, as with Pd, a decrease in intrinsic damping is observed for both the NiFe and CoFe trilayer samples with Pt as the HM. It has been reported that Pt has a larger interfacial exchange energy, and hence a stronger orbital hybridisation compared to Pd [17], which accounts for the differences in datasets here. In contrast to the Cu spacer, no change in damping is measured with the Au wedge within the HM layer, for both NiFe and CoFe. This is likely due to either: (i) that the first Pt layer is thick enough such that there is no enhancement after 2 nm, and hence the subsequent layers play no role or (ii) the close structure of Au results in a transparent interface when grown within a similar structured material. While scenario (i) is consistent with smaller reported values of the spin diffusion length [8], many estimates for λ_{sf} are $\sim$10 nm [9], furthermore a clear enhancement was observed in figure 9.11a with Pt thicknesses above 2 nm. For scenario (ii), although the Sharvin conductances and densities of states for Pt and 3*d* transition metals are similar, the lattice constants are not. CoFe has a lattice constant of 0.28 nm [352], for NiFe it is 0.35 nm [353], closer to Cu 0.36 nm, Pt 0.39 nm, Pd 0.39 nm and Au 0.41 nm [199, 354]. These differences in lattice constants emphasise the role of the interfacial structure *in addition* to the electronic ordering at the interface in enhancing damping. A possible consequence of scenario (ii), is

that orbital hybridisation, and therefore PIM, established in the initial interfacial layers is key to the additional damping enhancement from the rest of the HM later. This was observed in the tight-binding Barati-Umerski model, in which the largest contribution to damping in the HM layer originated from the first monolayer [115].

In order to compare the Pd and Pt data, the intrinsic damping for each trilayer dataset was normalised to the value with no Au present, and fitted with the same simple exponential function as the Cu data ($A\exp(-x/L)+c$) to compare lengthscales. Figure 9.19b shows the results of this, with fitted lengthscales of 0.85 nm for CoFe/Au/Pt, 0.62 nm for NiFe/Au/Pt, 1.3 nm for CoFe/Au/Pd and 0.53 nm for NiFe/Au/Pd. The shorter lengthscale for the decrease in damping in NiFe compared to CoFe for both Pt and Pd may be attributed to the more closely matched lattice constants, which gives a shorter interface roughness of $\sigma = 0.5$ nm for NiFe/Au and $\sigma = 1.2$ nm for CoFe/Au, as determined from XRR fits shown in figures 9.20a and 9.20b. The difference in the reduction of damping at the thickest Au values between the Pd and Pt spacer layers arises due to the larger SOC of the Pt. Additionally, neither the damping for the NiFe or CoFe with both Pt or Pd HM layers falls to the same level as the FM/Au/Cu data, indicating that there is still some damping enhancement, i.e. spin transport across the Au in the spin pumping formalism. This difference with the Au spacer and a HM layer is smaller than with a Cu layer, indicating the important, and not irrelevant, role of orbital hybridisation, and therefore proximity induced magnetism, to the first few layers of HM, and further to the interfacial damping enhancement of the whole HM layer. However, to confirm the pattern observed here, the induced moment across an Au spacer must be considered.

9.3.5 Pt and Au Proximity Magnetisation with Au Spacer Layers

As with the Cu spacer layer, the proximity induced moment in the CoFe/Au/Pt and NiFe/Au/Pt samples was investigated through energy specific hysteresis loops and scans of the XMCD signal as a function of position across the sample, at both the Pt and Au L_3 edges (11.564 keV and 11.919 keV respectively). Though the $5d$ states in Au are full, and hence should have no magnetic moment, hybridisation with a FM leads to $5d$ holes, which results in a spin polarisation and hence a small induced magnetic moment [313, 355, 356]. Figure 9.21a shows an example of the XMCD signal obtained at two positions on the wedge for the CoFe/Au/Pt sample, at both the Pt and Au edges, which both reverse dichroic sign upon reversal of the FM magnetisation with respect to the probe beam. As expected, the signal for Au

is much smaller compared to the Pt, due to the full 5*d* state.

The peak XMCD signal as a function of sample position for both the energy scans and element specific hysteresis loops, taken at both Pt and Au edges for the CoFe sample, is shown in figure 9.21b. Similar to the Cu wedge samples, a clear decrease in Pt signal, and hence induced Pt moment, is observed as the Au thickness increases and the hybridisation between the FM and the Pt is removed. Interestingly, the small induced moment in the Au increases to a peak in the transitional range between the maximum and minimum Pt induced moment. It is suggested that this is likely to correspond to the region where the Au layer is incomplete, resulting in hybridisation between both the FM and HM layers, and between the Pt and Au 5*d* states, where the Pt/Au hybridisation increase the holes in Au 5*d* and partially fills the Pt 5*d* orbitals. To correlate the sample position with the start of the Au thickness wedge, a scan of x-ray intensity as a function of sample position was undertaken at an energy above the L_3 edge (11.934 keV). Figure 9.21c shows the results of this for the CoFe/Au/Pt sample, with an increase in counts from $x = -6$ mm marking the beginning of the Au thickness wedge.

The averaged peaks of XMCD for both Au and Pt L_3 edges obtained from the energy scans and the hysteresis loops, as a function of Au thickness are shown in figure 9.22a for CoFe/Au/Pt and figure 9.22b for NiFe, correcting for the sample position as described previously. For both the CoFe and NiFe samples, both the XMCD and hysteresis loops show that the presence of a magnetic moment in Au peaks at a thickness below the interface width between the FM and Au layers, where hybridisation with both the FM and Pt may occur, and reaches an almost constant

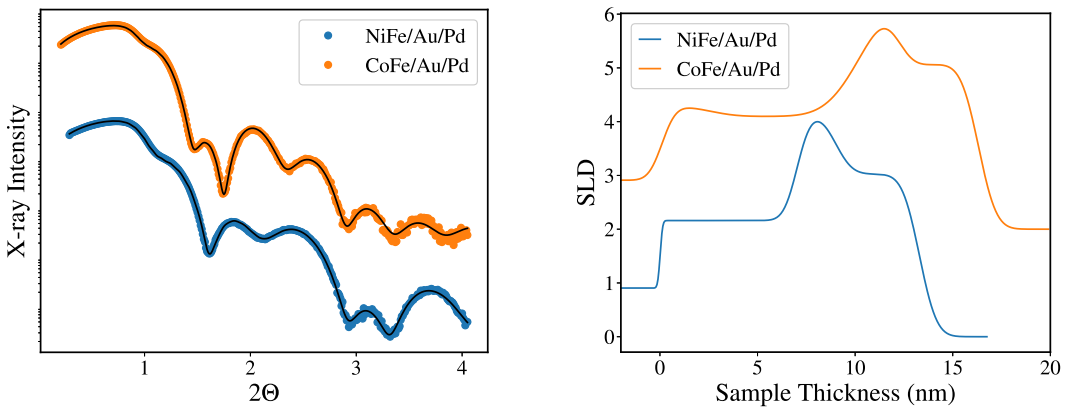

(a) (b)

Figure 9.20: (a) X-ray reflectivity profiles with best fitting simulations (solid lines) for NiFe (7 nm) / Au (2.0 nm)/ Pd (4 nm) and Cu (2 nm) / CoFe (7 nm) / Au (1.8 nm) / Pd (4 nm). (b) The SLD profiles extracted from the best fits to x-ray data.

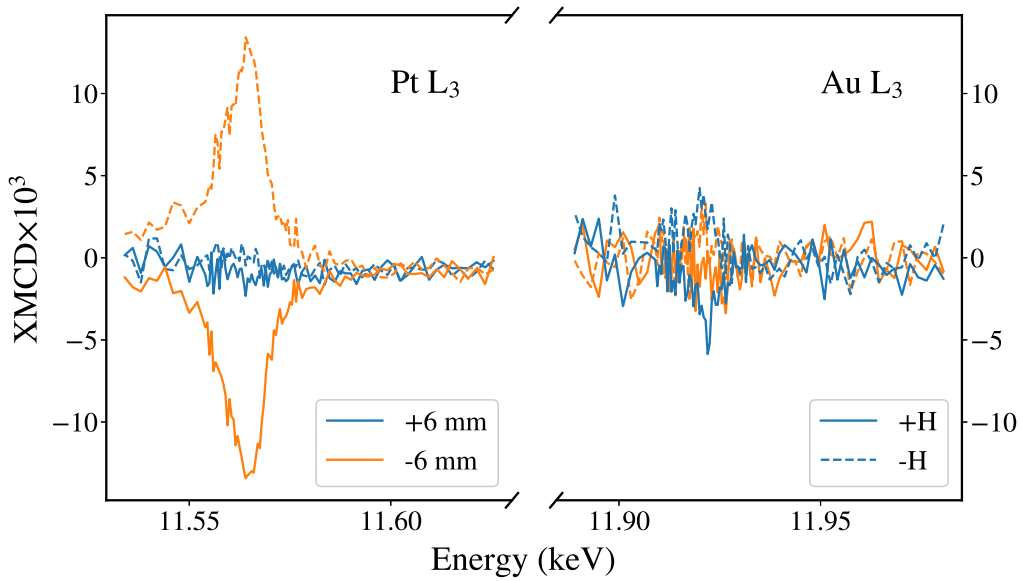

(a)

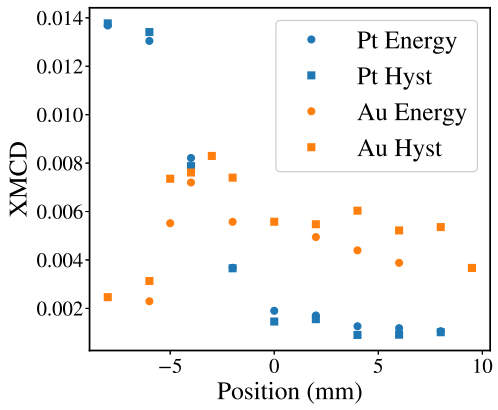

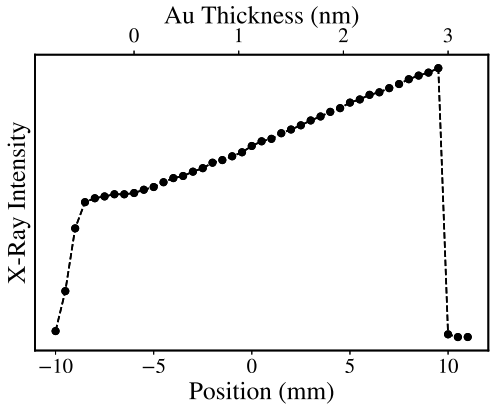

(b) (c)

Figure 9.21: (a) X-ray energy scans at the L_3 edges of Pt and Au at two positions on a thickness wedge of Au in a Cu (2 nm)/ CoFe (7 nm)/ Au / Pt (4 nm) sample. Solid and dashed lines indicate reversal of FM magnetisation state. (b) Peak XMCD signal of both hysteresis loops and energy scans as a function of sample position, for both Pt and Au edges. (c) Measured fluorescence signal as a function of sample position, taken 11.934 keV (above Au edge), with corresponding Au thickness assuming the wedge begins at -6 mm.

value at thicker Au spacer layers. Additionally, the decrease of the induced moment in the Pt occurs over a similar length scale (1.8 ± 0.2 nm) for both NiFe and

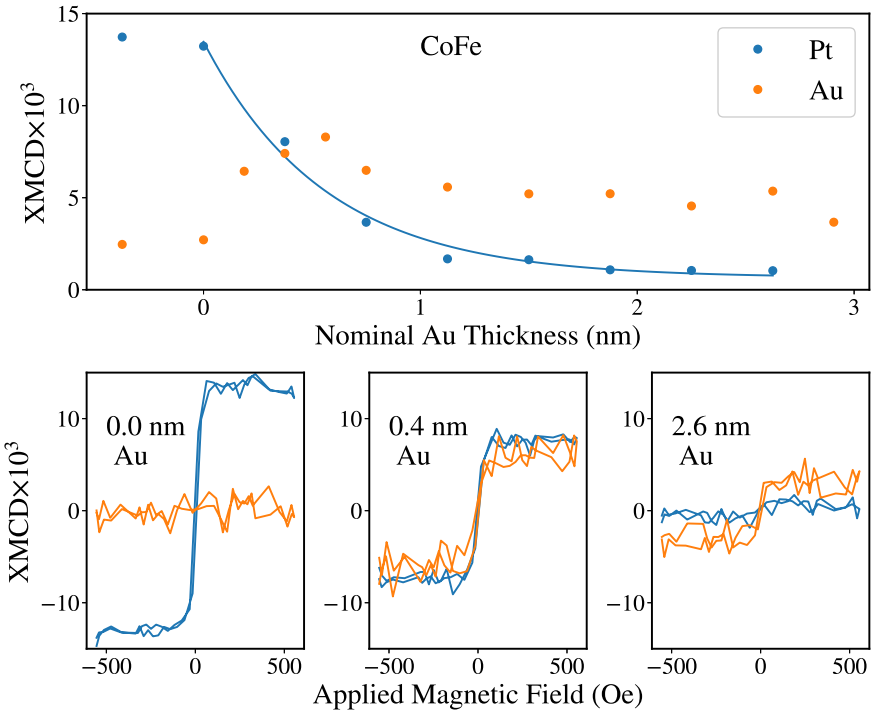

(a)

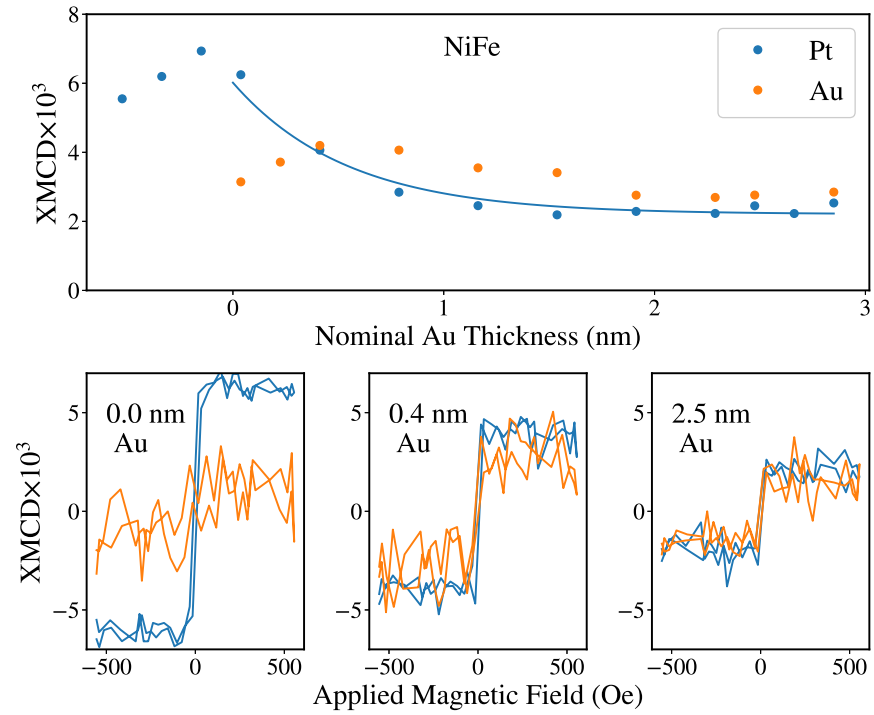

(b)

Figure 9.22: Measured XMCD as a function of Au spacer thickness at both the Pt (blue) and Au (orange) L_3 edges, with element specific hysteresis loops at three positions across the wedge, for (a) Cu (2 nm)/ CoFe (7 nm)/ Au / Pt (4 nm) and (b) NiFe (7 nm)/ Au / Pt (4 nm). Solid lines are best fitting exponential functions.

CoFe systems. However, though the general trend is similar, the magnitude of the induced moment is smaller for the NiFe sample, as expected from phenomenological models of a moment induced from interfacial effects, in which the moment is linearly proportional to the saturation magnetisation of the FM material [286].

Though the induced moment in the Pt layer is smaller in the NiFe sample, a moment is still measurable above the instrument noise at the thickest Au spacer layer investigated, and is comparable in magnitude to the induced Au moment, whereas at similar Au thicknesses for the CoFe sample, the Pt moment is no longer measurable. This is evident in the hysteresis loops show in figure 9.22. The persistence of a Pt moment at thicker Au is a surprising result, given that the Pt moment was shown to be confined to the interface for the Cu spacer layer. One possible explanation for the observed difference may be the structure of the two samples; for the NiFe sample, all layers are expected to be fcc, whereas the lattice mismatch between bcc CoFe and fcc Au and Pt may result in growth defects which prevent a strong hybridisation in the first few layers which then persists through the HM layer.

The resulting effect of the persisting moment on the measured damping as a function of Au spacer layer is shown in figure 9.23, in which the bulk damping term, determined from figure 9.17 (0.0075 for NiFe and 0.0055 for CoFe), is subtracted. For the CoFe sample, at thicker Au spacer layers, the interfacial damping contribution falls to almost zero, while the contribution with NiFe as the FM persists. This directly correlates with the observed induced moments in the Pt layer, which remain at equivalent thicker Au layers for the NiFe sample in contrast to the CoFe. These measurements suggest that even without *direct* FM-Pt hybridisation, as long as a

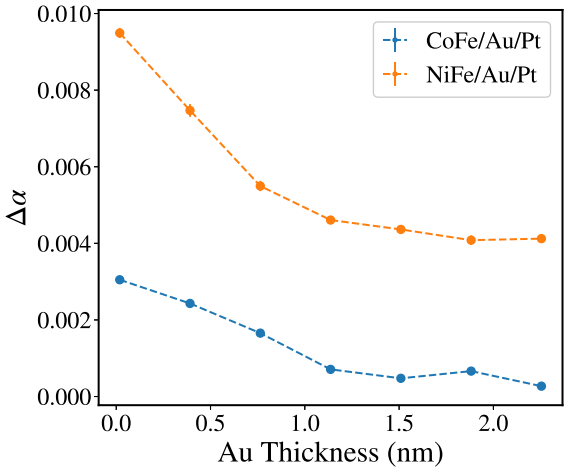

Figure 9.23: Decrease in interfacial damping as a function of Au spacer thickness for the Cu (2 nm)/ CoFe (7 nm)/ Au / Pt (4 nm) and NiFe (7 nm)/ Au / Pt (4 nm) samples. Dashed lines are a guide to the eye.

moment is induced in the Pt, then there is a measurable increase in the magnetic damping. It is therefore of importance to determine the spatial extent of the induced Au and Pt moments.

Figures 9.24 and 9.25 show the fitted reflectivity profiles and asymmetry ratios at various points across the Au spacer wedge on the Pt and Au L_3 edges for the NiFe and CoFe samples respectively. Each simulated fit, based on the same multilayer model across the wedge for each FM material, incorporates both the reflectivity and asymmetry profiles, as was the case for the Cu spacer wedge. The decrease in magnitude of the asymmetry ratios at the Pt L_3 edge are indicative of the reduced Pt moment with the increase of the Au spacer layer thickness. The maximum resolution for SLD and mSLD from the fits can be found by considering the maximum Q vector,

$$Q = \frac{4\pi}{\lambda} \sin\left(\frac{2\theta}{2}\right), \tag{9.1}$$

with λ the wavelength. For the Pt and Au edges and angles here, this results in a maximum resolution of 1.6 Åfor Pt and 3.2 Åfor Au, which is likely to be below any interface widths.

The resulting structural and magnetic scattering length density profiles from the fits are shown in figure 9.26 for the NiFe and CoFe samples respectively with increasing Au spacer thickness. For both the NiFe and CoFe samples, with no Au present, the induced Pt moment is confined to the interface, as was observed with the Cu spacer. As the Au thickness is increased for the CoFe sample, the magnitude of the induced Au moment increases and remains confined to the interfacial regions, peaking at intermediate Au thickness values as was observed with the XMCD measurements. The induced Pt moment, however, sharply drops and broadens away from the interface, while the peak induced moment remains at the interface. For the NiFe sample, as the Au thickness is increased, the magnitude of the induced Au moment increases, but remains confined to the interface until the final thickness, where the spread of the induced moment increases. In contrast to the CoFe sample, the spread of the induced Pt moment with NiFe is much larger, with an additional drop in magnitude corresponding to the peak in the Au moment. At thicker Au spacer layers, the Pt moment both peaks away from the Au interface, and extends to the FM layer even at 2.5 nm of Au. This tail extension of the Pt moment may explain the clear XMCD signal observed at thicker Au spacer layers in the NiFe case, indicating that some form of direct hybridization remains, though it is unclear as to why this is not observed in the CoFe case. However, although the Q resolution provides a nominal resolution lower smaller then the mSLD profile widths, the main source of uncertainty which arises from the signal to noise of ratio

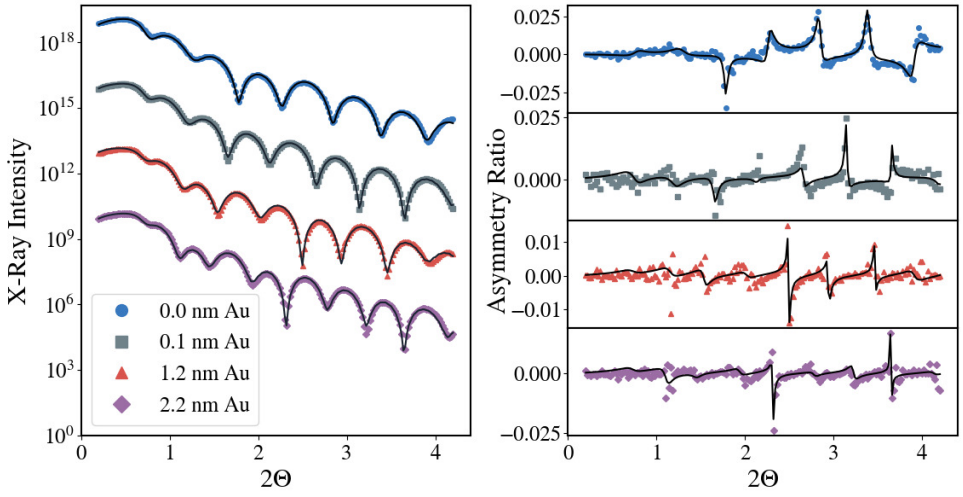

(a)

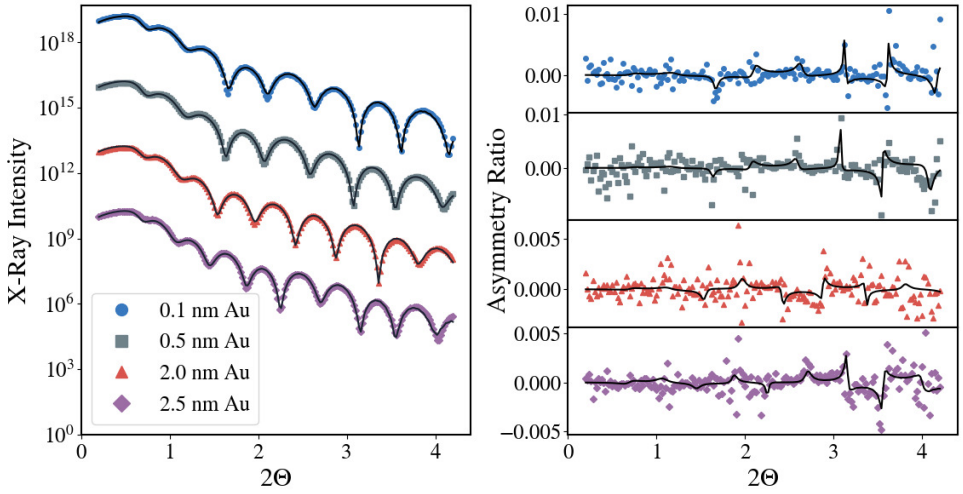

(b)

Figure 9.24: (a) Measured reflectivity profiles (left) at the Pt L_3 edge with corresponding X-ray helicity asymmetry ratio (right) for four nominal thicknesses of Au spacer layer in a NiFe/Au/Pt structure. (b) The same measurements at the Au L_3 edge. The asymmetry ratio is as defined in the previous sections. The solid lines represent best fitting models to both the structural and magnetic data.

of the magnetic asymmetry signal limits the accuracy of this interpretation of extended magnetic moments. Further work investigating the real space profile would verify whether intermixing, leading to orbital hybridisation and extended moments, is present. Nevertheless, there is a clear correlation between the induced moment and the enhancement in magnetic damping.

Finally, the correlation between the damping and Pt XMCD signal at the same point on the Au spacer wedge, for both CoFe/Au/Pt and NiFe/Au/Pt is shown in figure 9.27. A clear trend is shown, in which a larger induced moment is directly proportional to a larger enhancement in the damping. For the NiFe sample, the

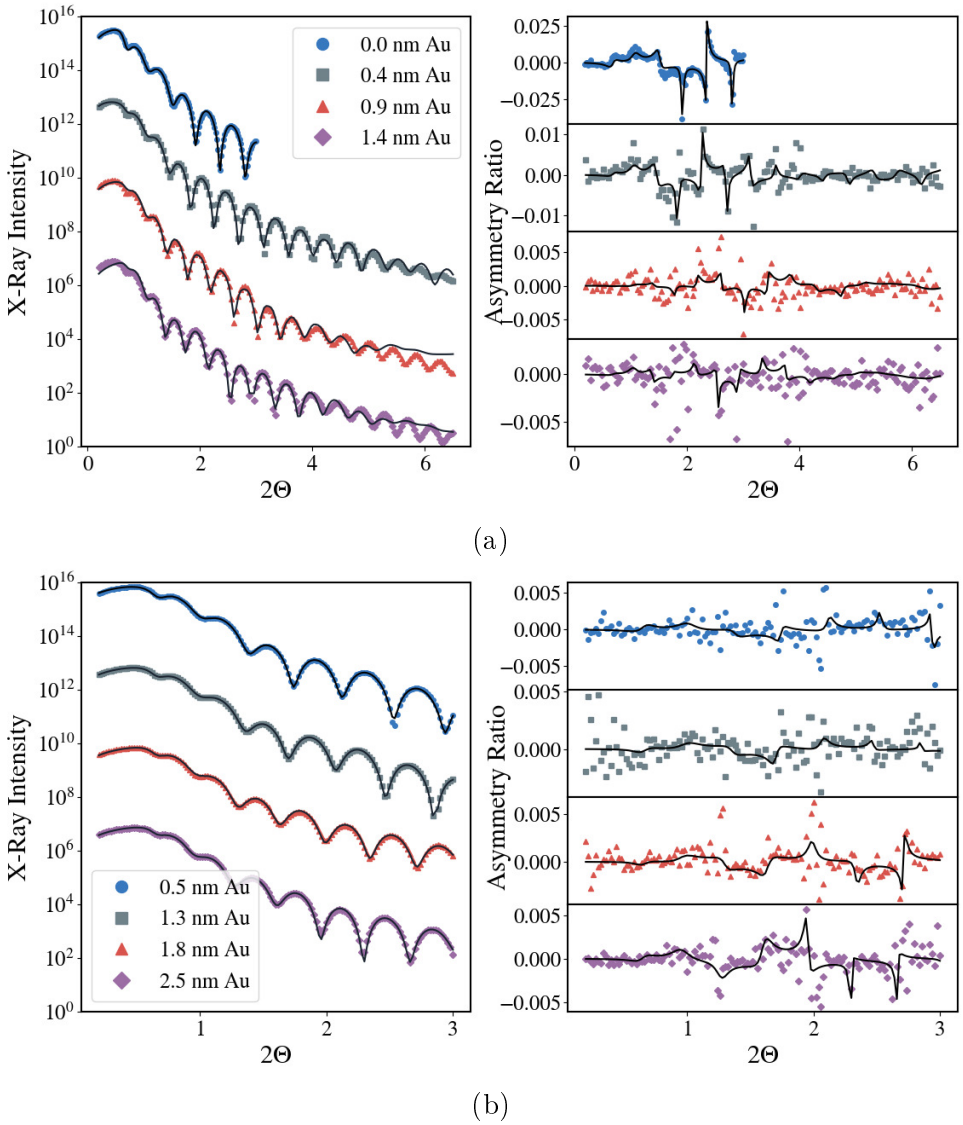

Figure 9.25: (a) Measured reflectivity profiles (left) at the Pt L_3 edge with corresponding X-ray helicity asymmetry ratio (right) for four nominal thicknesses of Au spacer layer in a Cu/CoFe/Au/Pt structure. (b) The same measurements at the Au L_3 edge. The asymmetry ratio is as defined in the previous sections. The solid lines represent best fitting models to both the structural and magnetic data.

high damping values at low XMCD, compared to the CoFe, remain attributed to the Pt layer, due to the small contribution (≈ 0.001) from the thickest Au spacer wedge, as was observed for the NiFe/Au/Cu sample shown in figure 9.17.

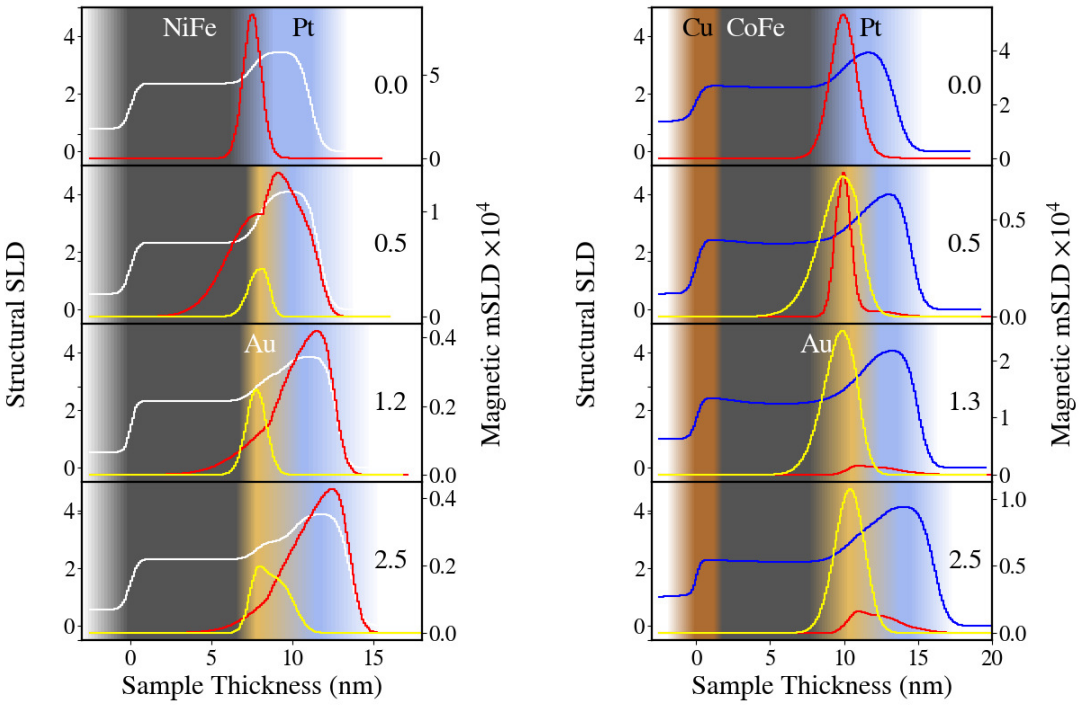

(a) (b)

Figure 9.26: Structural and magnetic scattering length densities from the model fits to the magnetic reflectivity data for varying Au spacer layer thicknesses, indicated on the figure, for (a) the NiFe sample and (b) the CoFe sample. The red line indicates the extent of the induced Pt moment, and the yellow the extent of the induced Au moment.

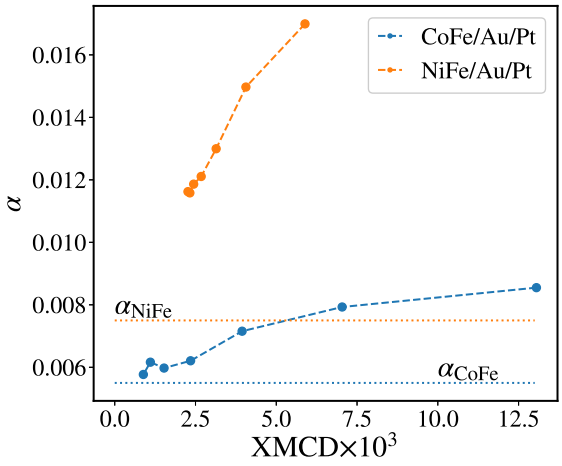

Figure 9.27: Damping and Pt XMCD signal at the same points on the Au spacer wedge for the CoFe/Au/Pt and NiFe/Au/Pt samples. Dashed lines are a guide to the eye. Dotted lines indicate bulk damping contributions from the ferromagnetic layer.

9.4 Summary

In conclusion, investigations into the relation between the induced moment in Pt and the consequences for interfacial enhancement of damping, and therefore the maximal frequency bandwidth response, were presented. First, the nature of the induced moment was revealed using resonant x-ray studies of proximity induced moment in Pt thin films layered with two rare earth:transition metal alloy ferrimagnets with compositions either side of ferrimagnetic magnetisation compensation at room temperature. The presence of a significant proximity induced moment in the Pt layered with these ferrimagnetic alloys was shown, and that the PIM is aligned parallel to the transition metal moments irrespective of the direction of the net magnetisation. The close interfacial localisation of the proximity induced moment showed that interfacial coupling is required for the PIM in heavy metallic layers, and therefore in RE:TM alloys, the induced moment is intricately determined by the detailed exchange coupling between individual orbitals rather than the net alloy moment.

The second half of the chapter then applied this interfacial basis of PIM, by comparing the induced moment and the dynamic magnetisation behaviour with a thickness gradient wedge between the HM and FM layers, using samples grown at the IFMPAN. Additional magnetic reflectivity measurements across Cu spacer wedges showed that the spatial extent and the magnitude of the PIM are strongly tied to the details of the interfacial structure, with the moment vanishing abruptly

with 1 nm Cu. The continued decrease in the damping with a Cu spacer in a Pt layer revealed that PIM is not solely responsible for the magnitude of damping enhancement, however the lack of a change with Au wedges before and in Pt layers indicated that both the electronic and structural details of the interface are key for large interfacial damping. An induced moment in Au as a function of Au spacer layer thickness between FM and Pt layers was found, which was maximal below the interface width, i.e. the thickness below which a continuous film layer was formed. The persistence of a PIM in the Pt layer at thicker Au spacer layers directly correlated with the measured interfacial damping, which remained non-zero in samples with PIM present.

By comparing the two different spacers, it was determined that PIM in the first few monolayers is crucial to achieve an enhancement in the damping from the rest of heavy metal layer. Therefore, for a large frequency bandwidth response of a thin film based on interfacial damping, a material capable of PIM is required. Damping is not the only parameter of synthetic magnetic thin films which allows for control of the dynamic resonant response, the next chapter details methods and results of controlling the effective magnetic field through lithographic patterning.

Chapter 10

Dynamic Magnetisation Response of Patterned Films

10.1 Introduction

Previous chapters have focused on describing the underpinning physics and methods to enhance magnetic damping using interfacial phenomena in order to produce a more broadband response. In this chapter, the thin films of ferromagnetic metals were patterned into microscale arrays of elongated structures to produce an effective self-biasing magnetic field, which aims to enable ferromagnetic resonance to be observed in the absence of an external magnetic field.

The first section of this chapter presents the results of varying the aspect ratio of uniform arrays of patterned stripes to induce different magnitudes of effective magnetic fields, before then considering the resonance behaviour observed with arrays of stripes orientated orthogonal to one another. The second section details the results of tessellated patterns composed of varying aspect ratios in order to produce an isotropic, field-free and broadband ferromagnetic resonance behaviour.

10.2 Arrays of Microscale Magnetic Stripes

The resonant frequency of a magnetic material system, described by the Kittel equation [74], is determined by the saturation magnetisation of the sample and the effective magnetic field. As discussed in chapters 3 and 4, the effective magnetic field can be tuned through numerous methods, however, photolithographic methods can be used to achieve large scale patterning of magnetic material with good uniformity in terms of the dynamic magnetisation response. Photolithography is also an industrially compatible process.

The magnitude of the effective magnetic field of patterned magnetic thin film structures is dependent upon the aspect ratio, as this determines the size of the demagnetising field. However, this dependence on the aspect ratio is reliant on the energy cost of forming long domain walls being larger than the energy cost of no flux closure, and hence patterns must be microscale or below, rather than on the order of millimetres or centimetres, where domains become favourable [357].

As detailed in chapter 4, patterned arrays of stripes of magnetic materials have been studied extensively in the literature, for various materials not limited to; NiFe [183, 184, 188] FeCoN [185] CoFeB [187], CoFeBSi [186], with the shape-induced magnetic anisotropy fields achieving ferromagnetic resonance at frequencies up to 10 GHz without an external magnetic field for 1 μm wide stripes [20]. More complex spin waves beyond the fundamental mode, have also been observed due to edge effects, within a 100 nm region [358–360], in submicron patterned films [361] and in dot and antidot arrays [362]. While these additional resonances provide additional energy loss channels, due to the feature sizes of samples used here only the main resonant mode was the focus of the study.

The rest of this section details the results of a study into the dynamic response of lithographically patterned arrays of magnetic structures with varying aspect ratios. The magnetic anisotropy values extracted from the best fits to the angular dependence of the resonance provide a guide for the design of novel structural arrays in the subsequent section, aimed at isotropic, field-free, broadband resonance. The feature sizes used here are limited by the feature resolution of the acetate sheets used as the photolithographic mask, and hence do not reflect the highest induced effective magnetic fields and external field-free resonant frequencies achievable using this patterning approach, but rather act as a proof of concept.

10.2.1 Sample Structural Preparation and Angular Ferromagnetic Resonance Measurements

All of the samples developed in this chapter were grown and patterned in Durham using the techniques and processes described in chapter 5. Thermally oxidised Si wafers were first cut to 12×12 mm, before the desired pattern from an acetate mask was transferred using photolithography. The acetate masks used had a manufacturer claimed minimum feature size of 5 μm, however the acetate sheets of most striped mask patterns with a 5 μm width did reliably transmit the UV lithographic illumination, resulting in stripes with distorted shapes and with the exception of one pattern, as discussed later, were not investigated further. Patterns based on 10 μm wide stripes were produced with aspect ratios: 1:1, 1:5, 1:25 and 1:73, with 30 μm spacing between each element. A 40 nm film of $Co_{20}Fe_{60}B_{20}$ was deposited at the same time onto all of the patterned wafers to produce all of the samples used in this section. Figures 10.1a and 10.1b show images of the 1:1 and 1:25 patterned final samples with the photoresist removed.

Ferromagnetic resonance measurements were undertaken using the purpose built integrated FMR system, with an external magnetic field sweep undertaken at each angular step as each sample was rotated within the applied magnetic field at a fixed microwave frequency. Figure 10.2 shows a representative scan at two orientations for the 10×250 μm sample obtained using the AC modulation and the lock-in amplifier in the FMR measurements. In the first orientation (0°), the long axis of the stripes, and hence the induced magnetic anisotropy easy axis, was aligned with the external magnetic field, and therefore a lower external field was required to excite ferromagnetic resonance. At 90°, the short axis of the stripes was aligned with the external magnetic field, and therefore a higher external field was required to excite resonance, as there is no additional contribution from the shape anisotropy. The position of

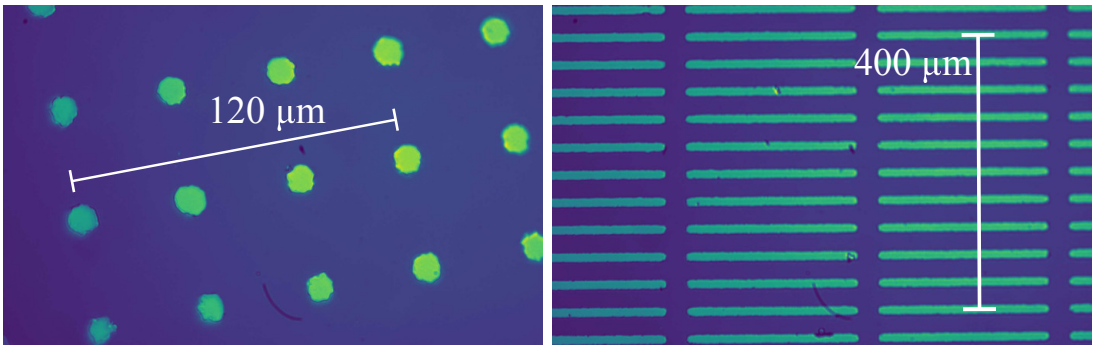

(a) (b)

Figure 10.1: Optical micrographs of arrays of 40 nm CoFeB patterned into (a) 10 μm dots and (b) 10×250 μm stripes, both with 30 μm spacing.

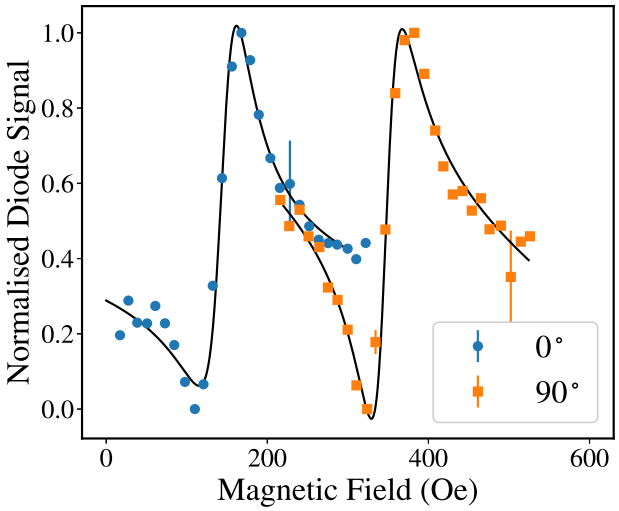

Figure 10.2: Normalised signal from lock-in amplifier and best fitting Lorentzian derivative for the array of 10×250 μm, 40 nm thick CoFeB sample, at a fixed frequency of 6 GHz, for two different sample orientations.

the resonance peak in the magnetic field domain, as a function of angle, is shown in figures 10.3a and 10.3b. For both samples at higher frequencies, where the external magnetic field is much greater than the induced anisotropic field, the plotted shape becomes more elliptical, whereas at lower frequencies for the sample with the larger anisotropy, there is a region at which almost no external magnetic field is required to excite ferromagnetic resonance. It is therefore necessary to determine the size of

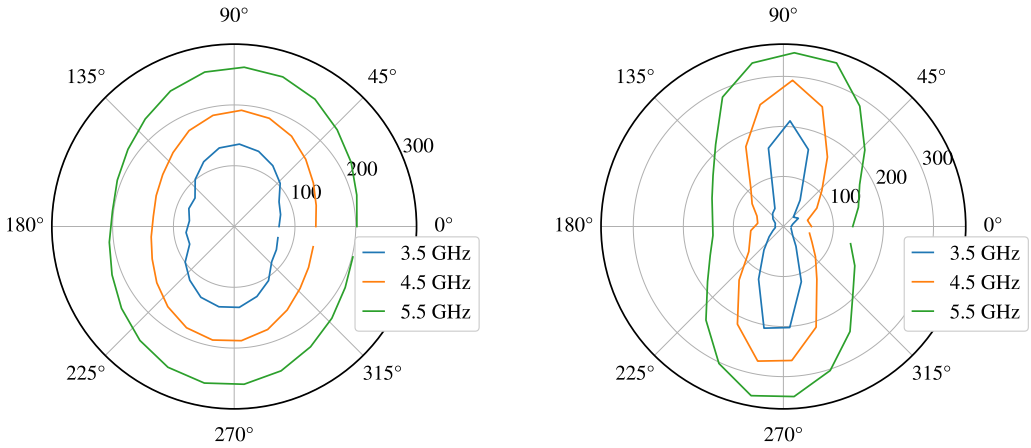

(a) (b)

Figure 10.3: Polar plots of the external magnetic field (in Oe) required to excite ferromagnetic resonance as a function of sample orientation angle with respect to the external magnetic field for 40 nm CoFeB striped arrays with (a) 1:5 and (b) 1:25 aspect ratios, at three frequencies.

the induced anisotropic field.

Previous studies investigated the reduction in the frequency linewidth with increasing aspect ratio due to the change of the effective magnetisation [363], however the focus here is on quantifying the magnitude of the induced anisotropy, in order to determine the frequency at which resonance occurs without the presence of an external field. As discussed in chapter 3, due to the shape of the stripes, the induced anisotropy can be treated as a uniaxial term, with the resonance condition,

$$\begin{aligned}\left(\frac{\omega_{\mathrm{res}}}{\gamma}\right)^2 &= \left[H_{\mathrm{ext}}\cos\left(\phi_{\mathrm{H}}-\phi_{\mathrm{M}}\right)+H_{\mathrm{u}}\cos 2\phi_{\mathrm{M}}\right] \\ &\times\left[H_{\mathrm{ext}}\cos\left(\phi_{\mathrm{H}}-\phi_{\mathrm{M}}\right)+4\pi M_{\mathrm{eff}}+H_{\mathrm{u}}\cos^2\phi_{\mathrm{M}}\right]\end{aligned} \tag{10.1}$$

where γ is the gyromagnetic ratio, H_{ext} is the external magnetic field at which resonance occurs, H_{u} is the uniaxial anisotropic field, $4\pi M_{\mathrm{eff}}$ is the effective magnetisation, ϕ_{H} is the angle of the sample with respect to the external magnetic field, and ϕ_{M} is the angle of the sample magnetisation, which is determined by solving the equilibrium condition at each angle,

$$H_{\mathrm{u}}\sin\phi_{\mathrm{M}} \;=\; 2H_{\mathrm{ext}}\sin\left(\phi_{\mathrm{H}}-\phi_{\mathrm{M}}\right). \tag{10.2}$$

By determining the external magnetic field required for resonance, H_{ext}, via fitting of the data as shown in figure 10.2 as a function of angle, the size of the anisotropy field was determined using these two equations. For the data in this section, a multivariate fit was used, where the data for each fixed frequency was fitted simultaneously, with only H_{u}, $4\pi M_{\mathrm{eff}}$ and a phase offset, ϕ_0, (to account for sample misalignment), as the free parameters.

10.2.2 Enhancing Shape Anisotropy by Tuning the Aspect Ratio

The angular dependence of ferromagnetic resonance with respect to the stripe angle to the external magnetic field, H_{ext}, is shown in figure 10.4. The associated angle of magnetisation, ϕ_{M}, as a function of the angle of applied field, ϕ_{H}, is also shown, which was determined from the equilibrium condition. For all figures, the long axis of the striped arrays was aligned with the external magnetic field at 0°. The increase in the peak-to-peak amplitude of the oscillating external magnetic field with increasing aspect ratio observed in the three left figures is indicative of an increasing magnetic anisotropy.

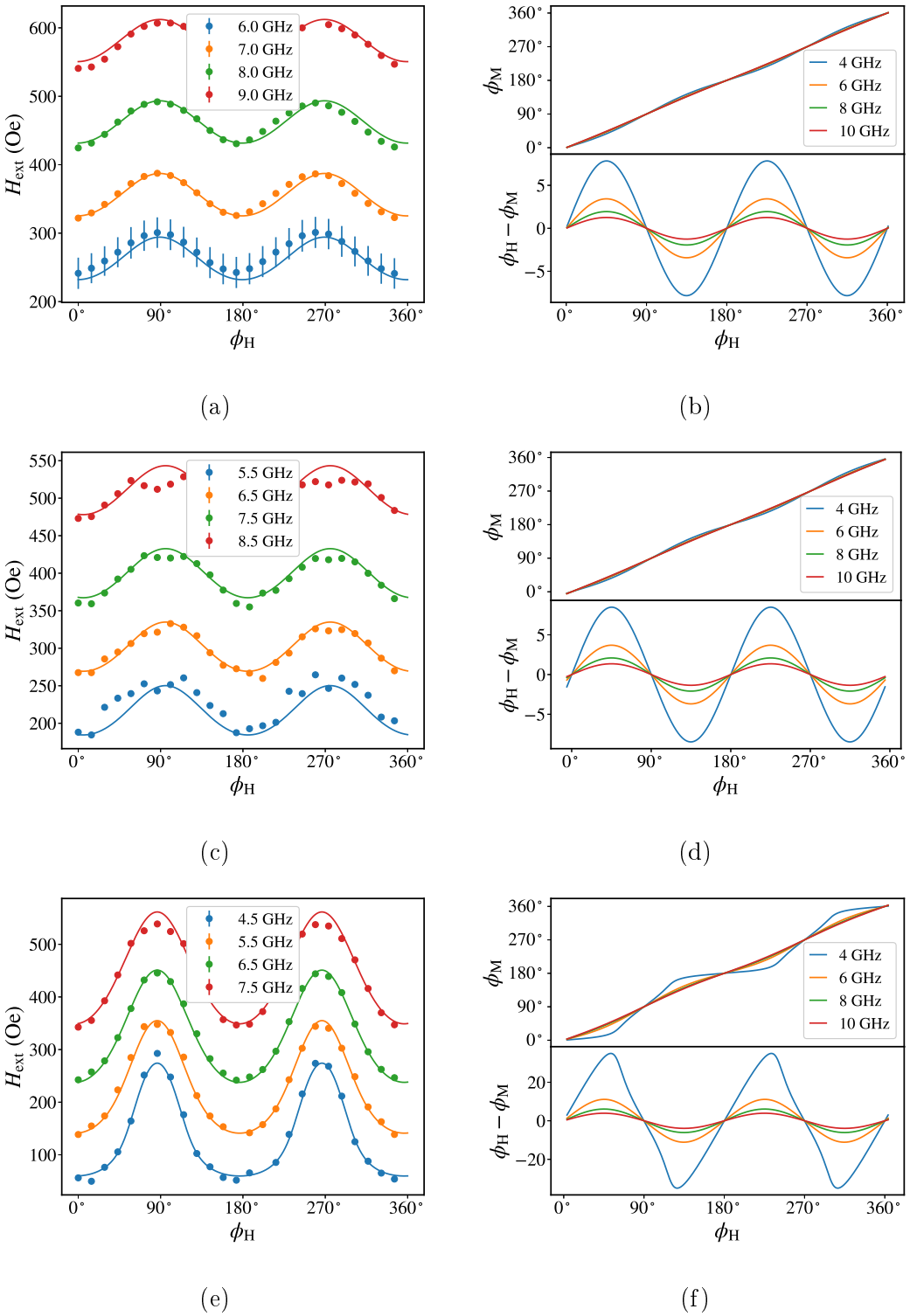

Figure 10.4: Angular dependence of the external magnetic field required to excite ferromagnetic resonance for different aspect ratio 40 nm CoFeB striped arrays. Angular data with best fits (left) and direction of magnetisation determined from the equilibrium condition for the fitted data (right) for: (a) and (b) an unpatterned thin film, (c) and (d) arrays of 10×50 μm stripes (1:5) and (e) and (f) arrays of 10×250 μm stripes (1:25)

In figure 10.4e, a flattening of the 'sinusoidal behaviour' is observed at 4.5 GHz, which can be better understood by considering the orientation of the magnetisation as a function of the orientation of the external magnetic field, and the phase difference between them, which is shown in the right hand column of figure 10.4. Again, as the aspect ratio is increased, the phase difference between the magnetisation and the external magnetic field increases. When the external field is aligned with the long axis of the stripe, at 0°, 180° and 360°, there is no phase difference between the two angles. However, as the sample is rotated, the external field competes with the shape induced anisotropy field, and hence a phase lag occurs as the magnetisation lies along the effective magnetic field, which is a sum of the two magnetic field contributions. This phase lag reaches a maximum when the external magnetic field is aligned with the short axis of the stripe, orthogonal to the shape anisotropic field. Beyond 90°, the external magnetic field now competes with the reversed anisotropy field, and hence the sign of the phase lag switches, as the direction of the external magnetic field *approaches* the long axis once more. This phase lag decreases for higher frequencies, as a larger external field is required for resonance, and hence the effective magnetic field, along which the magnetisation lies, is dominated by the external field, which becomes much larger then the induced anisotropic field.

For larger aspect ratios, e.g. 1:73, for the 10 μm width stripes, the peak to peak amplitude, and the phase difference both decrease compared to the 1:25 ratio case, as shown in figures 10.5a and 10.5b. This is likely due to the large length of the stripe resulting in it being energetically favourable for the formation of multiple magnetic domains, such that the enhancement of the anisotropy from the increased demagnetising field is removed [357].

In order to investigate the magnitude of the anisotropy at larger aspect ratios, a 5 μm width sample of the same aspect ratio was used. Figures 10.6a and 10.6b show images of two samples with the same aspect ratio, but different widths. Though the 5 μm width array has significantly rougher edges and less defined shapes, the large number of arrays allows for the average response to provide insight into higher aspect ratio samples.

As shown in figures 10.5c and 10.5d, the 1:73 aspect ratio 5 μm width sample has the highest peak-to-peak amplitude, and the largest phase difference between the angle of magnetisation and the angle of external magnetic field, confirming that the largest aspect ratio results in the largest induced magnetic anisotropy. In this case, the short axis of the stripes are aligned along 0°.

From the angular dependent behaviour, it is clear that there will be ferromagnetic resonance at a frequency at which no external magnetic field is required along the long axis, as the induced anisotropy field is sufficient. The anisotropy values

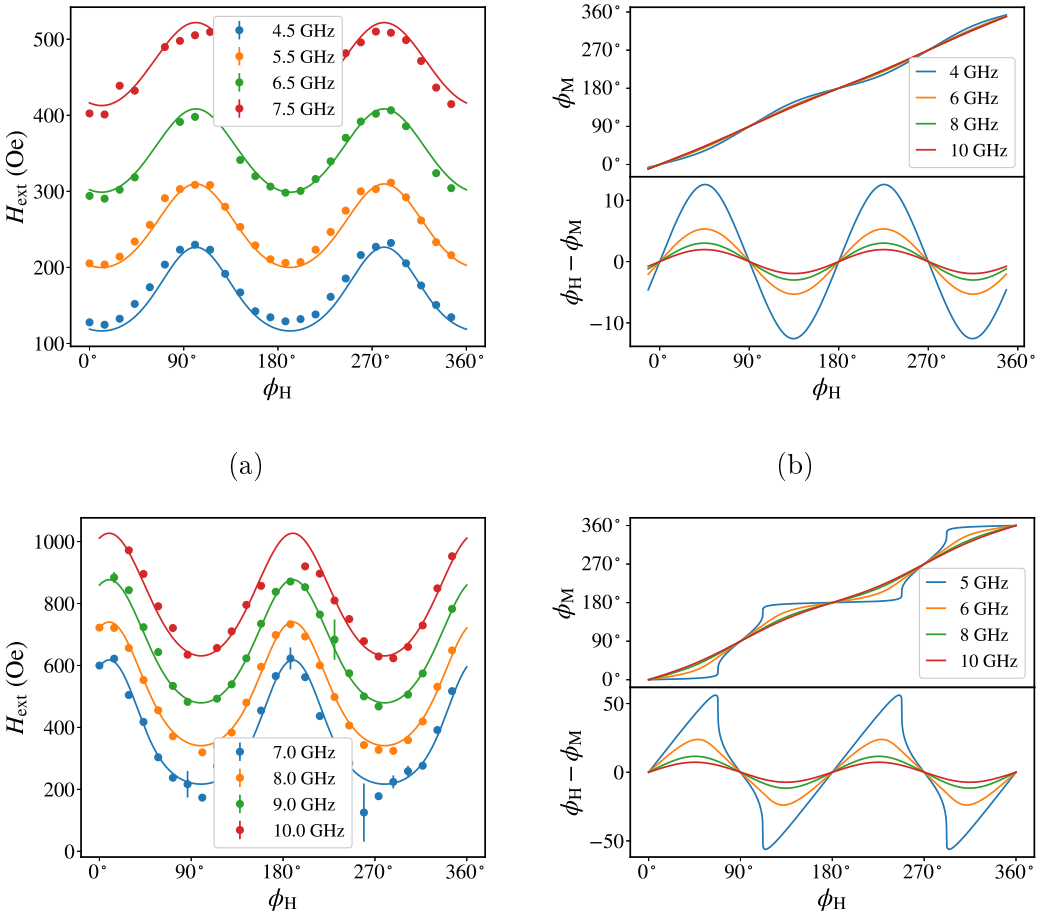

(a) (b)

(c) (d)

Figure 10.5: Angular dependence of the external magnetic field required to excite ferromagnetic resonance for the same aspect ratio 40 nm CoFeB striped arrays, with two different widths. Angular data with best fits (left) and direction of magnetisation determined from the equilibrium condition for the fitted data (right) for: (a) and (b) arrays of 10×730 μm stripes and (c) and (d) arrays of 5×365 μm stripes (1:73).

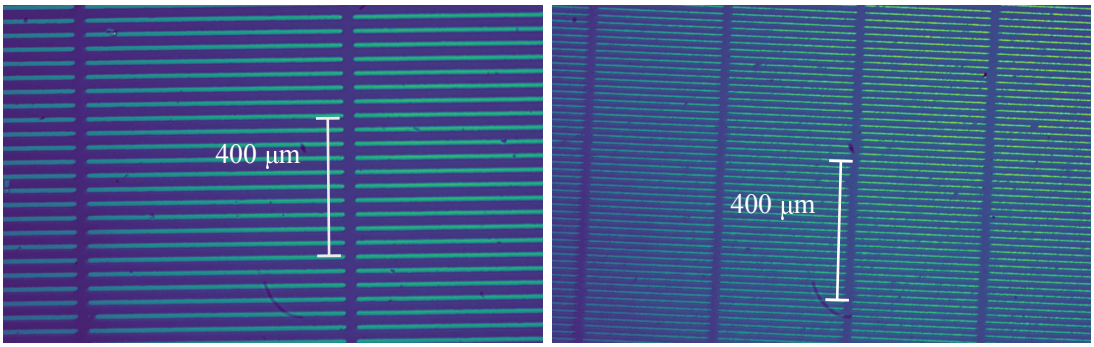

(a) (b)

Figure 10.6: Optical micrographs of arrays of patterned 40 nm CoFeB with (a) 10×730 μm stripes with 30μm spacing and (b) 5×365 μm stripes with 15μm spacing.

extracted from the best fits to the data as a function of the aspect ratio of the magnetic stripes are shown in figure 10.7. For all samples, $4\pi M_{\text{eff}}$ was determined to be 16.8 kG within error, which is comparable with other measurements on the same ferromagnetic material [364–366]. Using these values for anisotropy and effective magnetisation, the resonant frequency was determined from the Kittel equation, which is shown in black in figure 10.7. The shape of the frequency curve resembles the Kittel curve due to the linear relationship between the aspect ratio and the induced anisotropy. The external field-free resonance is dependent upon the magnetisation, and hence will increase or decrease if the magnetic material is changed.

10.2.3 Multiple Resonances from Orthogonal Stripes

The dynamic behaviour described thus far is from arrays of stripes with the long axes of all elements in the same orientation, with the induced anisotropy enhancing the effective magnetic field principally along the long axis. However, for a more isotropic response based on patterned thin films, it is more desirable for a uniform dynamic response to be achieved over a range of angles. By positioning blocks of the striped arrays orthogonal to one another, the angular response can be further enhanced. Figure 10.8 shows an image of the 10×250 μm striped arrays patterned into such an orthogonal array.

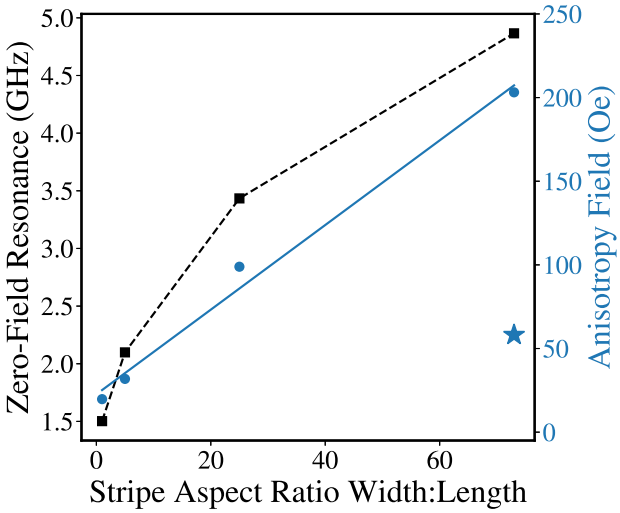

Figure 10.7: Anisotropy values from the best fits to the resonance data (blue circles) and the corresponding frequency at which ferromagnetic resonance can be expected with no external magnetic field (black squares) for 10 μm wide, 40 nm thick CoFeB stripe samples. The solid line is a linear fit and the dashed line a guide to the eye. The blue star denotes the 10×730 μm sample, for which it is suggested the additional domain structure modifies the FMR response.

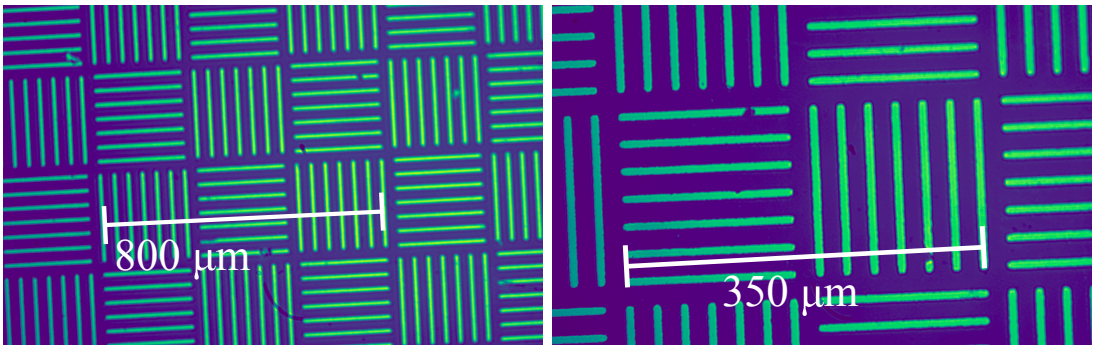

(a) (b)

Figure 10.8: Optical micrographs of orthogonal arrays of 40 nm CoFeB patterned into 10×250 μm stripes with 30μm spacing at two different magnifications.

The dynamic magnetisation behaviour as a function of external magnetic field at a fixed frequency of 6 GHz is shown in figure 10.9 for four angular positions between 0° and 90°. The sample was positioned such that one set of stripes was aligned parallel to the external magnetic field at 0°. Two distinct resonances can be seen clearly in figure 10.9a, with the resonance at the lower field corresponding to the stripes aligned with the field axis, where the presence of the anisotropy means a smaller external field is required to excite resonance, as compared to the orthogonal stripes with the short axis aligned with the field.

At 90°, as shown in figure 10.9d, the positions are reversed such that the stripe which had the long axis aligned with the external magnetic field now has the short axis aligned, and hence requires a larger external field to excite resonance. Figures 10.9b and 10.9c show the measured signal at intermediate angles between the swapping of the resonance positions. At 45°, the two resonances merge to produce a response which appears a single resonance with a larger linewidth. Therefore, to produce an isotropic response, patterns must be designed with varying angles of stripes, this forms the basis of the rest of this chapter.

10.3 Field Free Resonance through Microscale Tessellated Patterning

The previous section introduced methods to produce an effective magnetic field through lithographic patterning, the magnitude of which is determined by the aspect ratio. Whereas previous chapters have focused on ways to increase the bandwidth by increasing the loss mechanisms by enhancing the magnetic damping, this section details the dynamic response of tessellated patterned films, with a varying aspect ratio to produce both an isotropic and a broadband response.

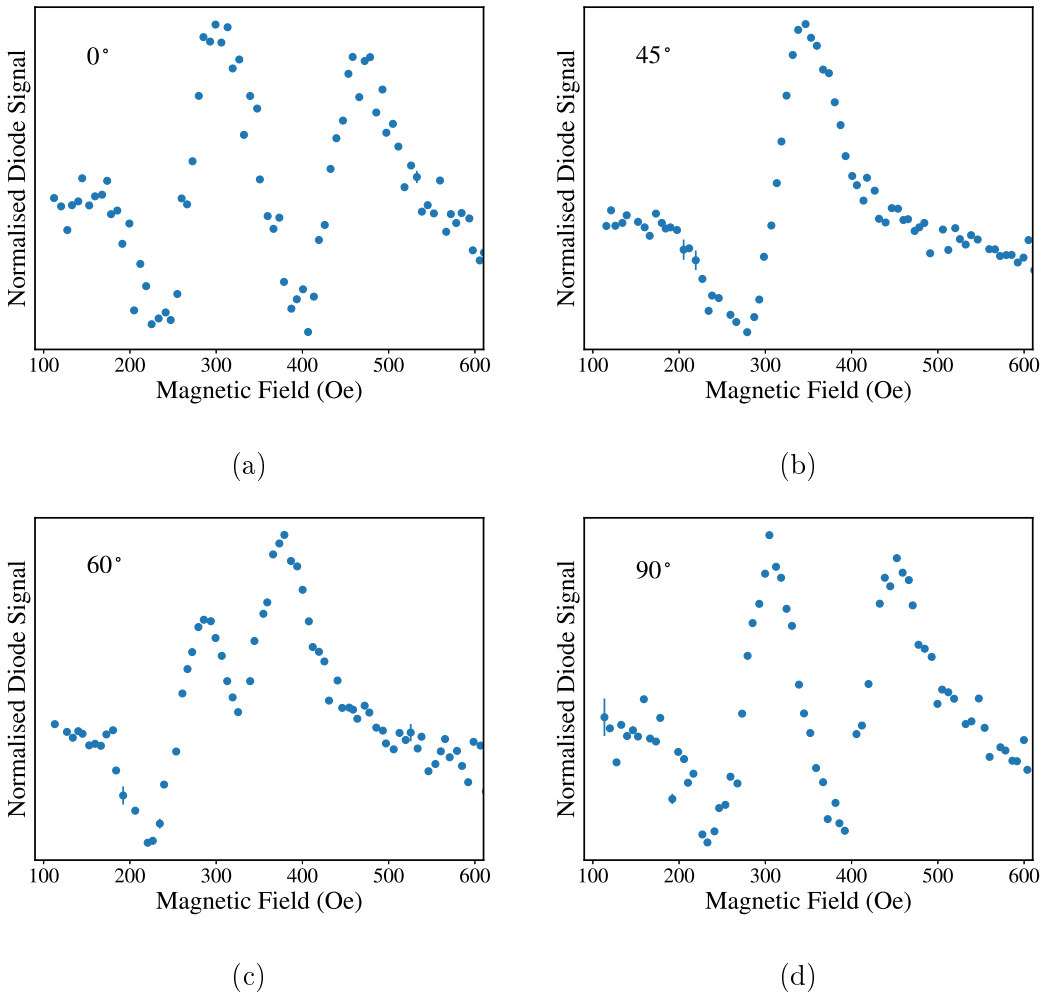

Figure 10.9: Normalised signal from lock-in FMR circuit for the 40 nm CoFeB samples patterned into 10×250 μm orthogonal arrays for four angular positions, at a fixed frequency of 6 GHz.

10.3.1 Pattern Design and Fabrication

The samples fabricated in this section followed the same process used in the previous section and outlined in chapter 5. In order to investigate methods to achieve an isotropic response, tessellated patterns of an increasing number of vertices were designed. The tessellated arrays produced consisted of repeated tiles of (in increasing complexity): striped tiles, square tiles, hexagonal tiles and octagonal tiles. For each tile, the width of each stripe was 10 μm, with 1:15 the largest aspect ratio used, i.e. 10×150 μm stripes, and with each stripe separated by 30 μm. For the square, hexagonal, and octagonal tiles, the outer stripes consisted of the 1:15 aspect ratio, with the aspect ratio decreasing towards the centre of the tile.

The magnetic thin-films of these patterned samples were all fabricated concurrently, using magnetron sputtering on 12×12 mm substrates, with 100 nm $Ni_{80}Fe_{20}$

deposited. Assuming the same conversion between aspect ratio and induced anisotropy field presented in figure 10.7, and a saturation magnetisation of 10 kG for $Ni_{80}Fe_{20}$ [21, 259, 296], the largest aspect ratio was predicted to induce a 50 Oe anisotropy field, giving a field-free resonance at 1.9 GHz. It should be noted that this is not the highest field free resonance frequency achievable, but rather a proof of concept of the isotropic response.

Unlike the previous section, samples were measured using a vector network analyser (VNA) in order to measure the broadband frequency response utilising the VNAs ability to produce a fast and constant power output as a function of frequency. Angular control of the sample measurement orientation was provided by the sample controller in the integrated FMR system, in these measurements the electromagnet was removed to ensure no remnant magnetic field from the pole pieces.

10.3.2 Angular Dynamic Magnetisation Response with Increasing Pattern Complexity

Measurements on each tessellated pattern were undertaken as a function of angle with respect to the RF field from the microstrip, with a frequency sweep performed at each angular step. Before each sample measurement, an uncoated silicon wafer was measured to allow for normalisation of the measured signal to a background, hence any large changes as a function of angle would be as a result of the magnetic material. In order to provide a quantitative description of the isotropic nature of each pattern, the area under each curve was integrated and plotted as a function of angle, normalised to the maximum value. The frequency responses as a function of angle for each tessellated tile are presented below, with the angle of sample rotation relative to the fixed waveguide.

Striped Tile

The simplest tessellated pattern was an array of 10×150 μm stripes, similar to those in the previous section. Figure 10.10a shows the measured S_{21} parameter with the striped array aligned along the short and long axes, with no external magnetic field applied. Along the long axis, where the induced shape anisotropy easy axis lies, a clear resonant peak is observed at around 1.9 GHz as predicted, whereas no clear peak is seen when the long axis is orthogonal to the magnetic component of the RF excitation.

The angular dependence of the measured resonant signal is clearly seen in figure 10.10b, with the integrated area shown as a function of angle. The shape of the integrated area is indicative of a uniaxial anisotropy, which is expected from the

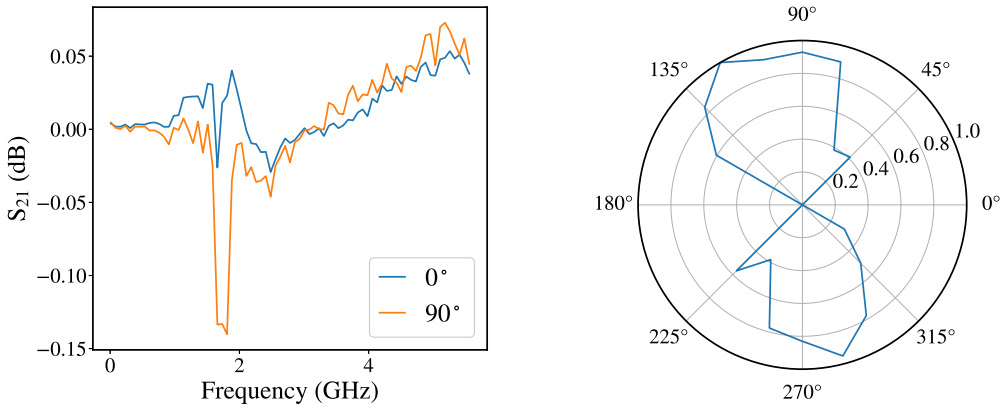

(a) (b)

Figure 10.10: (a) Magnetic field-free S_{21} measured as a function of frequency, with the sample aligned along the short (0°) and long (90°) axes of the 100 nm NiFe striped array of 10 × 150 μm. (b) Normalised integrated area of the array as a function of angle as it rotates above the transmission line.

patterning. Along the long axis at an angle of 90° between the long axis and the transmission line, the torque between the RF excitation across the stripline and the effective magnetic field from the induced anisotropy is largest, and hence at the resonance condition a larger proportion of the energy is absorbed by the sample, with the contrary true along the short axis at 0°.

Square Tile

The striped tile consisted of a single aspect ratio, and hence a single induced shape anisotropy value with an associated single resonance frequency. In order to achieve a broadband response using this method, multiple aspect ratio stripes are required, each with a different resonant frequency determined by the saturation magnetisation and shape. Figure 10.11a shows an image of the tessellated pattern consisting of orthogonal stripes with varying aspect ratio over a large area, with 10.11b highlighting a single tile used to create the pattern. The largest aspect ratio was 1:15, which is the same as that used for the simple striped array.

Examples of the measured S_{21} parameter as a function of frequency are shown in figure 10.12a for the square pattern orientated such that the magnetic component of the RF excitation was either aligned along one of the long axes of the square, or along the diagonal of the square. As with the single stripe array, a resonance peak is observed at around 1.9 GHz, when the long axis of the stripes with the largest aspect ratio (10×150 μm) are aligned with the RF excitation from the transmission line. However due to the orthogonal arrangement of the stripes, the resonance is

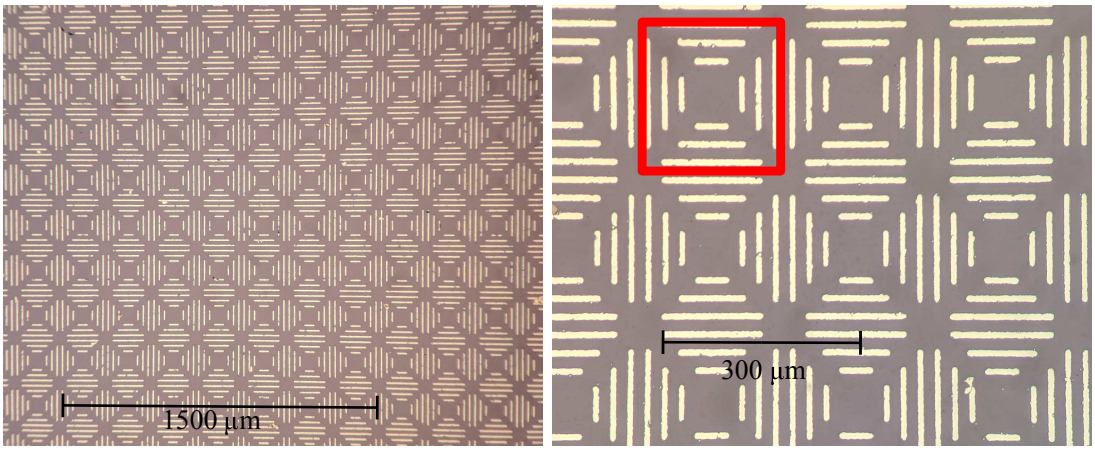

(a) (b)

Figure 10.11: Optical micrographs of the tessellated square tiles of 100 nm NiFe at (a) low magnification and (b) higher magnification with an individual tile highlighted in red.

only fully suppressed when the sample is rotated 45° such that there is a minimal torque between the effective magnetic field and the RF energy.

This angular behaviour is further shown by the integrated area as a function of angle, as shown in figure 10.12b, in which two additional lobes appear compared to the striped array due to the orthogonal alignment of the square tile. The difference in magnitude of the lobes may be attributed to the non-uniformity of the sample height above the waveguide, and coverage of the waveguide, as it rotates. This would produce peaks with the same shape, but a difference in magnitude in signal, and

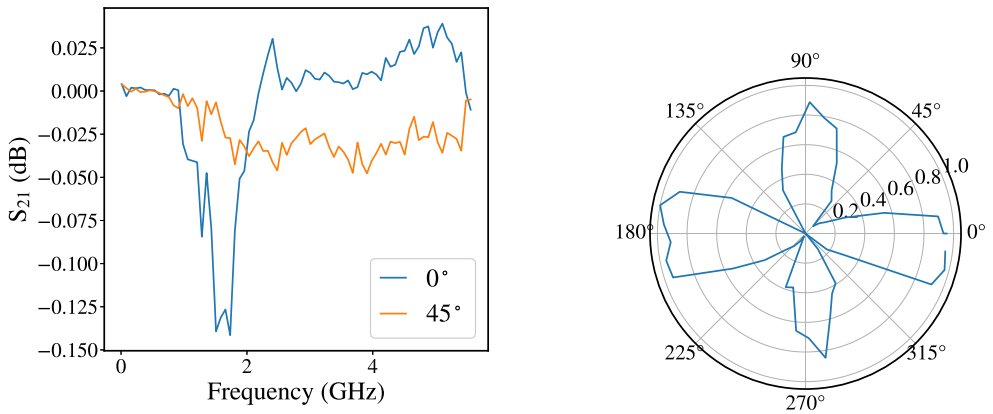

(a) (b)

Figure 10.12: (a) Field-free S_{21} as a function of frequency aligned along the one of the long axes of the square (0°), and along the diagonal (45°) with respect to the transmission line for the square tile of 100 nm NiFe. (b) Normalised integrated area of the square tiles as a function of angle.

hence a smaller integrated area.

An additional benefit of the different aspect ratios is that the effective resonance response extends over a wider frequency range, compared to the simple stripe array. Figure 10.13a shows a comparison between the square tiles and the single lines. Though both peaks occur around at 1.9 GHz, the smaller aspect ratio stripes, which have lower induced anisotropy and hence a lower resonance frequency, produce a wider frequency response, which is not due to an increase in the damping parameter. For confirmation that the dynamic behaviour measured so far was as a result of the lithographic patterning, an unpatterend film, grown at the same time, was measured with a small bias magnetic field to excite a 1.9 GHz resonance. Figure 10.13b shows the integrated area of this sample as a function of angle, which shows only a weak angular dependence, confirming that the significant angular behaviour is as a result of the patterning. It is worth noting that the weak anisotropy of the continuous film may be induced during deposition [367, 368].

Hexagonal Tile

Though the square tiling produced a more broadband frequency response, it did not produce an isotropic response to the RF excitation. Figures 10.14a and 10.14b show a pattern produced with an increased number of vertices based on hexagonal tiling. As with the previous patterns, the outer stripes consist of 10×150 μm stripes, with decreasing aspect ratios towards the centre, with 30 μm spacing.

The measured S_{21} parameter along two orientations is shown in figure 10.15a,

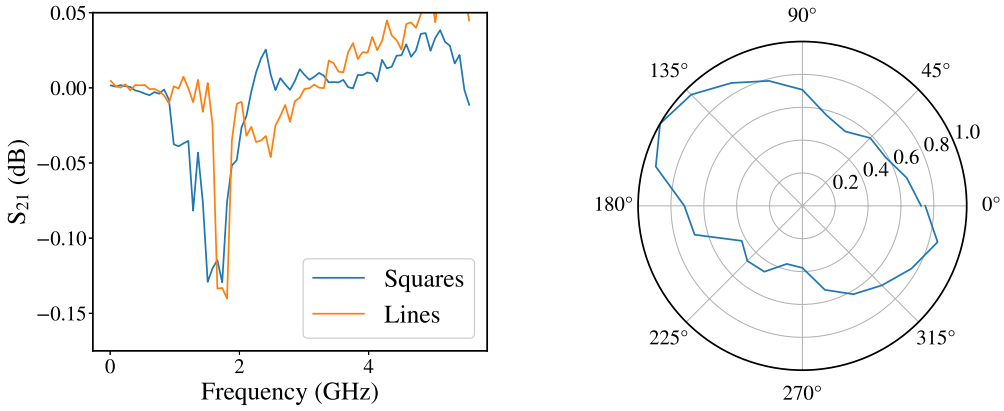

(a) (b)

Figure 10.13: (a) Field-free S_{21} as a function of frequency showing the comparison between 100 nm NiFe patterned into both the single stripes and the square tiles. (b) Normalised integrated area of an unpatterned film as a function of angle, grown at the same time.

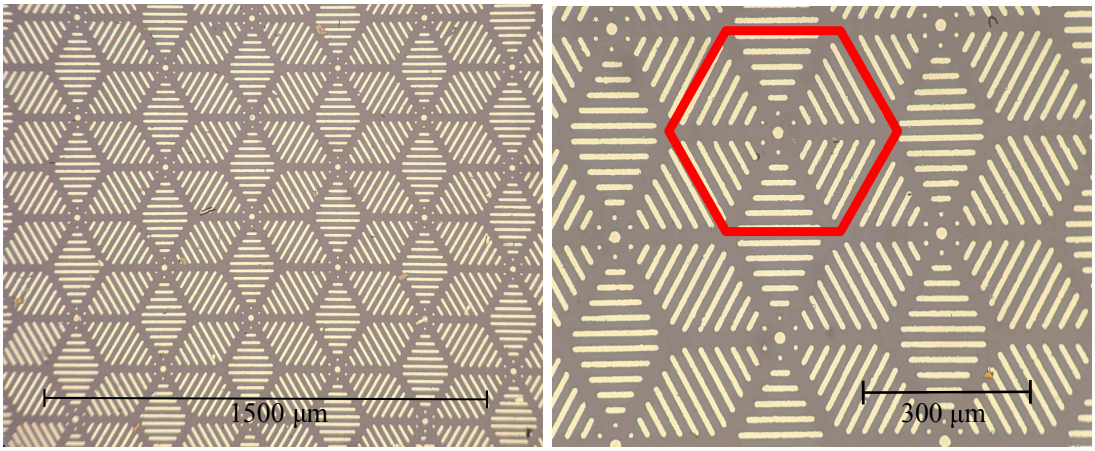

(a) (b)

Figure 10.14: Optical micrographs of the tessellated hexagonal tiles of 100 nm NiFe at (a) low magnification and (b) higher magnification with an individual tile highlighted in red.

with the main 1.9 GHz resonance and the wider bandwidth resulting from the multiple aspect ratios again clearly observed. The effect of increasing the order of the polygon used to produce the tiling pattern is shown in figure 10.15b, which indicates a much more isotropic integrated area.

Octagonal Tile

Increasing the polygon order of the tiling can further enhance the angular response. Figures 10.16a and 10.16b show images of a sample design based on an octagonal

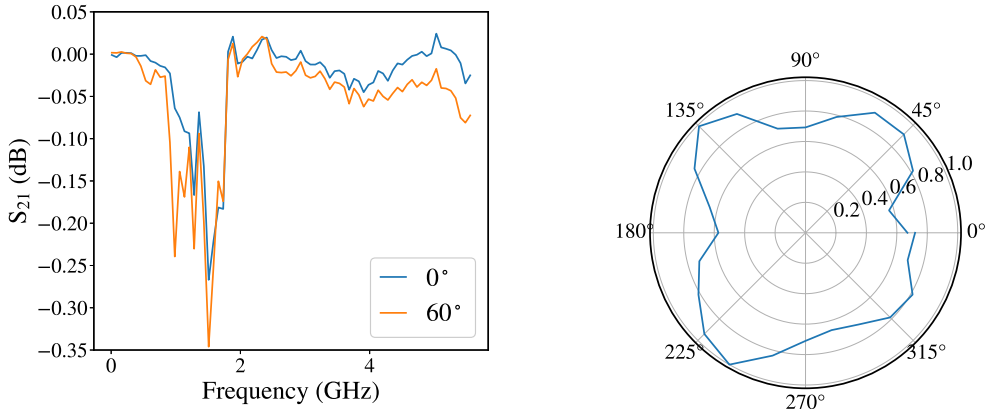

(a) (b)

Figure 10.15: (a) Field-free S_{21} as a function of frequency for 100 nm NiFe patterned with the hexagonal tiling aligned along two sample orientations with respect to the transmission line. (b) Normalised integrated area of the hexagonal tiles as a function of angle.

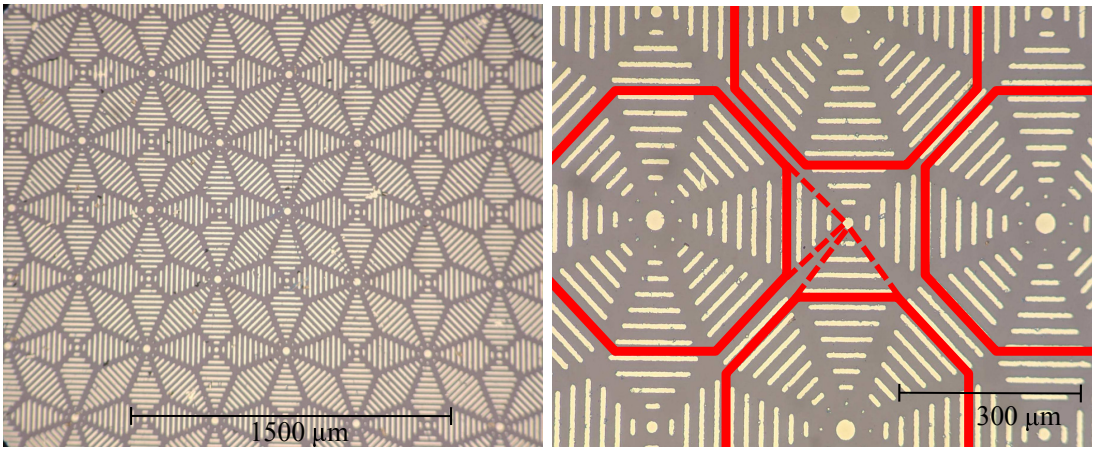

(a) (b)

Figure 10.16: Optical micrographs of the tessellated octagonal tiles of a 100 nm NiFe film at (a) low magnification and (b) higher magnification with an individual tile highlighted in red. Dashed lines indicate the extended tile, which can be tessellated.

tiling, which in this case do not simply tessellate and require an additional square tile occupying the space between the octagonal tiles or four triangular extensions to the octagonal tile. The outer edge consists of a 10×150 μm stripe, with decreasing aspect ratio down to a central 10 μm dot, with 30 μm spacing between each shape.

Figure 10.17a shows the dynamic response at two angular orientations for the octagonal pattern. The increased bandwidth and 1.9 GHz peak from the largest aspect ratio are again present, however unlike the square tiling, field-free resonance is maintained at a 45° orientation with respect to the RF excitation, due to the

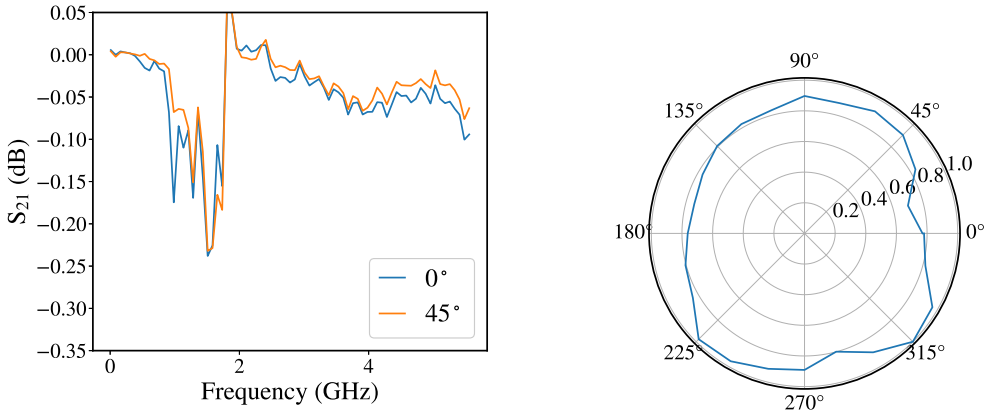

(a) (b)

Figure 10.17: (a) Examples of field-free S_{21} response as a function of frequency for alignment along two sample orientations with respect to the transmission line for a 100 nm NiFe film patterned with octagonal tiling. (b) Normalised integrated area of the octagonal tiles as a function of angle.

additional stripes at intermediate angles. The normalised integrated area, shown in figure 10.17b, is almost isotropic, again due to the multiple orientations of the stripes that create multiple induced anisotropic fields at different angles, which allow for the creation of a torque between the RF excitation and some components of the sample at almost all angles of orientation with respect to the RF excitation. This produces for a uniform dynamic response, regardless of the angle between incident RF and the sample.

10.3.3 Towards a Broadband FMR Response

The samples measured here were based on a 10 μm wide strip, with 1:15 the largest aspect ratio. In order to achieve external magnetic field free resonances at higher frequencies it is necessary to use either a smaller width, or a longer length, to increase the shape anisotropy further. However, to ensure a broadband response, multiple aspect ratios must still be used. Performing RF measurements in the magnetic field domain further highlights this. Figure 10.18 shows a scan as a function of the external magnetic field at 6 GHz for the octagonal tessellated pattern and for an unpatterned thin film. Two things are evident from the figure, firstly the position of the resonance is shifted to lower external fields, as the larger aspect ratio patterns enhance the effective field more, such that smaller external fields are required to excite resonance, as was observed in the previous section. Secondly, the linewidth is greatly enhanced in the magnetic field domain as well. However this is not as a result of increasing the magnetic damping, as was the case in previous chapters, but rather is the result of the overlap of multiple resonances due to the multiple effective fields from the stripes of varying aspect ratio.

10.4 Summary

This chapter presented the results on novel lithographic patterning of magnetic structures that aimed to use aspect ratios and orientations of the patterned elements to produce a magnetic system with a broadband field-free resonant response that also was isotropic with respect to the incident RF radiation.

The resonance frequency of magnetic thin films depends on two factors, the saturation magnetisation and the effective magnetic field. Therefore in order to achieve resonance free of an external magnetic field, it is necessary to induce a magnetic anisotropy by controlling the shape of the magnetic components, which produce the effective field needed for ferromagnetic resonance.

The first section detailed the results of angular measurements on arrays of stripes

with varying aspect ratio. Due to mask constraints, this was limited to microscale features, however a linear relation between the aspect ratio and induced anisotropy was determined. The largest aspect ratio (1:73), with microscale patterning, produced an anisotropy field of 200 Oe which corresponded to a field-free frequency of almost 5 GHz. It was shown that an array of orthogonal stripes could produce distinct resonances which merge to form a broader response.

The second section used the relation between the aspect ratio and the induced anisotropy field, to produce and measure patterned samples with resonances without the presence of an external magnetic field. Based on the largest aspect ratio of 1:15, a peak field-free resonance was observed at around 2 GHz. This is not the highest field-free resonance which can be achieved, but rather is a proof of concept of the capability of lithographic patterning. With initial tessellated patterns based on square tiling, consisting of varying aspect ratio stripes, a more broadband frequency response could be engineered compared to simple arrays of single dimensioned stripes. It was then shown that by tessellating higher order polygon tiles composed of varying aspect ratios, an isotropic, broadband and field free resonance could be achieved.

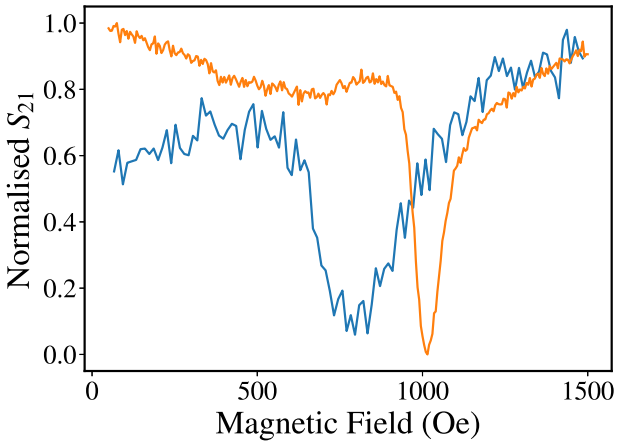

Figure 10.18: Comparison of normalised S_{21} as a function of external magnetic field at a fixed excitation 6 GHz for the octagonal pattern (blue) and an unpatterned film (orange). Both samples of 100 nm NiFe were grown simultaneously.

Chapter 11

Conclusions and Further Work

This thesis presented an investigation into methods to manipulate the dynamic magnetisation behaviour of thin film magnetic structures, in order to control the RF response. The details of the design and development of an instrument for measuring the high frequency response of magnetic thin films were presented first. The focus was then directed towards investigating both the underpinning physics and the methods to control two parameters of interest with thin films; the damping of magnetisation, enhanced through interfacial effects, and the induced effective magnetic field, determined by the shape imposed through lithographic processing. It was shown that both of these methods separately can be used to engineer structures with a wider frequency bandwidth response.

11.1 Thesis Summary and Conclusions

Following a brief introduction into the theory underpinning static (chapter 2) and dynamic (chapter 3) magnetic behaviour used throughout the thesis, chapter 4 presented a short review of existing magnetic materials for RF applications, providing a brief overview of the broad range of systems in the literature. A model for the frequency response of a multilayered magnetic system, developed by Wallace [81], based on wave impedance matching was detailed. The dynamic permeability, and hence the frequency response, was shown to depend on three key parameters: the *saturation magnetisation*, the *damping parameter*, and the *effective magnetic field*. Though the saturation magnetisation can be modified through methods such as doping [99], it is mostly determined by material choice, and hence the rest of the thesis focused on understanding and controlling the latter two parameters. For the damping parameter, interfacial effects were exploited to provide an additional energy loss channel, increasing the frequency bandwidth response. For the effective magnetic field, though several other methods exist, photolithography was utilised as it was an

industrially compatible process which was suitable to produce large uniform areas.

The model introduced in chapter 4 was used to highlight the effects of changing each of the three parameters in turn. A further development in this work allowed for the increase in damping due to interfacial effects to be modelled within the layered impedance model. The largest increase in damping was given by thinner ferromagnetic materials layered with heavy metals with a thickness above the spin diffusion length, the lengthscale over which the spin current injected from the ferromagnetic layer de-phases.

Chapters 5 and 6 detailed structural and quasi-static magnetic characterisation techniques, before chapter 7 presented a brief introduction to two frequency domain methods: Free-space cavity methods and vector network analyser (VNA) transmission line based methods, both of which can be used to probe the dynamic magnetisation response of thin film systems. The development of an initial system to measure ferromagnetic resonance based on a VNA was then detailed. While this system provided a broadband frequency measurement, and has contributed to published results [109], it did not allow for the angular dependence of ferromagnetic resonance to be examined. Additionally, the remanent field in the pole pieces of the electromagnet, combined with the unipolar power supply, did not allow for low frequency resonances to be investigated. The remainder of chapter 7 described the design and development of a low-cost integrated system to measure ferromagnetic resonance. The system outputs RF energy from 10 MHz up to 15 GHz, and was designed with an *Arduino* [245] and two motor stages to adjust the sample height and rotation above the microstrip transmission line. Without adjusting gear ratios, samples can be moved vertically in 5 μm steps, and rotated with 200 steps per full revolution, i.e. 1.8° angular steps. The system features two modes of operation, either measuring the RF power transmitted across the transmission line, as a function of magnetic field or RF frequency, in a similar manner to a VNA, or using an onboard lock-in amplifier circuit and external Helmholtz coils to measure the derivative of the signal with respect to the magnetic field, which improves the signal-to-noise ratio for smaller signals. Commands written in the *Python* [249] programming language allow for simple control of the equipment, in addition to a bespoke graphical user interface designed for the equipment. Testing of the integrated system in chapter 7 showed the current performance limits of the system, which showed the system can produce comparable results with those obtained using other research systems. The system was used both to obtain the results presented in this thesis, and in published work.

Chapter 8 presented the results of two published investigations into enhancing [109] and suppressing [242] the interfacial contribution to magnetic damping.

The first half of the chapter examined the underpinning spin pumping model and interpretation of FMR data, in order to better understand the role of the interface and robustly determine values for the key interfacial parameters using standard FMR methods. Reported discrepancies of these interfacial parameters in the literature were identified, in particular the spin diffusion length, which for a typical heavy metal such as Pt had reported values over an order of magnitude from 1 to 10 nm. FMR measurements using the VNA setup were undertaken on HM/FM and FM/HM systems, with varying FM and HM thicknesses, in order to fully investigate interfacial transport parameters. Here, the FM was chosen as Co (both fcc and hcp) or CoFeB (amorphous), with either Ru and Pt (fcc) as the HM, to explore the role of interfacial structure.

By developing a new aspect of the model that incorporates a dependence of the spin diffusion length on the resistivity of the heavy metal (HM) layer [300], which accounts for changes in the resistivity of ultrathin films, the spin diffusion length of Pt determined from this new FMR analysis was shown to increase by an order of magnitude (1.6 nm to ≈9 nm) compared to the earlier work of other groups. This accounts for previously reported discrepancies in the spin diffusion length between different experimental methods. Due to the smaller spin-orbit coupling (SOC) of Ru, a longer spin diffusion length was determined, 22 nm, compared to 9 nm for Pt. The highest increase in damping, and hence frequency bandwidth, was found in the more closely matched interfacial structures, i.e. hcp Co/ hcp Ru compared to fcc Co/ hcp Ru and fcc Co/ fcc Pt compared to amorphous CoFeB/ fcc Pt. This increase was reflected in the larger spin-mixing conductance values for crystallographically matched interfaces determined from FMR analysis.

The remainder of chapter 8 discussed methods to suppress the interfacial enhancement of damping through the insertion of an insulating layer, in order to be able to model the sub-units as separate from each other in a multilayered system, as was assumed in the modelling in chapter 4. Additionally, open questions were present regarding interfacial phenomena with thin insulating layers, with conflicting reports suggesting a complete suppression of interfacial transport [11], or tunnelling of spin-current through an insulating layer [12]. The interfacial structure with a SiO_2 spacer layer of varying thickness in a CoFeB/SiO_2/Pt system was first characterised using x-ray reflectivity, where it was determined that the insulating layer was discontinuous at thicknesses below 2.4 nm. This structural information was correlated with the measured interfacial damping as a function of the nominal insulating layer thickness, where spin-pumping was observed for nominal SiO_2 thicknesses up to around 2 nm, while no enhancement was measured when the SiO_2 layer was complete. Hence it was determined that a complete insulating layer in this case

fully suppresses spin transport. Although tunnelling of spin current is not ruled out, the observed spin pumping can be explained by discontinuous insulating layers, rather than invoking models involving tunnelling of pure spin-current, as had been suggested previously [12].

The results outlined in chapter 8 showed that the interfacial damping of a magnetic thin film system can be tuned through material choice and thickness in a multilayered system. However, the physics underpinning the mechanism behind the interfacial enhancement is still unclear. Chapter 3 outlined two models of damping enhancement, the first being the the spin-pumping model [123], in which a spin current is driven by a non-equilibrium spin accumulation in the FM layer which then de-phases and is absorbed in the HM, where the lengthscale is determined by SOC in the HM and the magnitude of enhancement is determined by the matching of conductance channels. The second is an electronic tight-binding model, developed further for damping by Barati and Umerski [115], in which interfacial $d-d$ hybridisation is the key mechanism. This hybridisation is also associated with proximity induced magnetism, which is not a feature of the spin-pumping model.

Chapter 9 investigated the role of proximity induced magnetism (PIM) in heavy metal layers on the damping parameter, by first considering the nature of PIM across the compensation point in rare-earth (RE) transition metal (TM) ferrimagnetic alloy systems, in which the RE and TM sublattices align antiparallel to one another, to ascertain whether the PIM in Pt follows the net moment, or is aligned with one of the sublattices. The results of this investigation formed the basis of a published article [299]. Synchrotron resonant x-rays measurements taken at the Advanced Photon Source, USA, allowed for element specific magnetism of both the Pt and Gd in Pt/CoGd/Pt and Pt/CoFeGd/Pt thin film systems. These alloys were chosen such that the magnetisation compensation of the CoGd alloy was above room temperature, and for the CoFeGd was below, and therefore at 300 K, the dominant sub-lattice in CoGd was the RE, and in CoFeGd was the TM. Temperature dependent scans of the XMCD signal and moment from MPMS (SQUID) measurements revealed a transition to out-of-plane for the CoFeGd alloy at low temperatures, and confirmed a magnetisation compensation point above room temperature for the CoGd alloy. By considering the sign of the dichroic spectra in energy scans and element specific hysteresis loops over the L_3 edges of Pt and Gd, it was determined, for the first time, that the induced moment in Pt aligns with the TM moment regardless of the net ferrimagnetic moment. Fits to the x-ray magnetic reflectivity (XRMR) at the Pt L_3 edge revealed that the induced moment is highly localised to the interface between the ferrimagnetic alloy and Pt, highlighting the role of coupling between individual orbitals, rather than the importance of the net moment.

Once the interfacial moment of Pt aligned with the TM was established, the second half of chapter 9 considered the impact of the magnitude of the moment on damping with the insertion of Cu and Au spacer layers between a FM and HM layer. Samples in this section contained thickness gradient wedge samples, grown at the Institute of Molecular Physics in Poznan, Poland (IFMPAN), to allow for a thickness dependence to be measured on a single sample. XMCD and magnetic reflectivity measurements on the Pt L_3 edge across a varying thickness Cu spacer in a CoFe/Cu/Pt system showed the induced moment vanishes with a 1 nm Cu spacer, and, correlating this with the continued decrease in the measured damping beyond 1 nm suggests that PIM is not solely responsible for an interfacial damping enhancement. This is supported by the almost constant increase in damping with a Cu spacer midway through a 12 nm Pt layer in a CoFe/Pt/Cu/Pt system, at which location there should be no induced moment, compared to the case without Cu.

This is not to say that PIM has no role in damping. Energy scans and hysteresis loops over the Au and Pt L_3 edges in NiFe/Au/Pt and CoFe/Au/Pt samples with varying Au thickness, revealed an induced moment in the Pt which decays with Au thickness, and a moment in Au, which was maximum below the interface width, when hybridisation with both the FM and Pt was possible. For the CoFe sample, both the induced Pt moment and the interfacial damping contribution were reduced to negligible levels with a thickness of 3 nm of Au, while a smaller Pt PIM and enhanced interfacial damping persisted in the NiFe sample at the same nominal 3 nm thickness of Au. While the difference in behaviour of both the interfacial damping and Pt PIM between the two FMs may be attributed to the difference in structure (bcc CoFe compared to fcc NiFe, Pt and Au), the direct correlation between the persistence of an induced moment with the damping highlight the role of $d-d$ hybridisation and the associated PIM.

Comparing the Au and Cu spacers, it is evident that PIM in the first few monolayers is key to achieving a large interfacial damping enhancement. For applications requiring a large frequency bandwidth response, layering ferromagnetic materials with materials capable of a large PIM is therefore necessary. However, this is not the only method to achieve a broadband response using magnetic thin film systems.

Chapter 10 introduced methods to control the dynamic magnetisation response of thin film systems through lithographic patterning. In order to produce structures capable of ferromagnetic resonance without an external magnetic field, the effective magnetic field must be enhanced intrinsically with the material. The frequency of resonance is then determined both by the saturation magnetisation of the magnetic material used, and the magnitude of the induced anisotropic field. Both the magnitude and direction of the effective magnetic field induced through photolithography

are dependent upon the aspect ratio and orientation of the resultant pattern.

The first half of chapter 10 described the results of an investigation into angular ferromagnetic resonance measurements on arrays of patterned stripes of varying aspect ratio, and hence varying effective magnetic fields. With the acetate masks available, only microscale features were achievable, however the analysis of the resulting patterns of 40 nm CoFeB films showed an almost linear relation between the aspect ratio of the stripes. Best fits to the data of the largest aspect ratio (1:73), determined an induced anisotropy field of 200 Oe, corresponding to a field-free resonance at almost 5 GHz. The dynamic response of a pattern based on orthogonal alignment of stripes showed two distinct resonances, when the external magnetic field was aligned along the long axis of one stripe, and the short axis of another, these merged and swapped peak positions as the sample was rotated in the magnetic field.

The second half of chapter 10 built upon this, and examined striped patterns with both varying aspect ratio (and hence effective magnetic fields) and varying orientation. Measurements in this section were performed in the absence of an external magnetic field. Patterns were designed based on a tessellated tile, with 10×150 μm (1:15) the largest stripes. For the 100 nm NiFe thick structure studied, a peak ferromagnetic resonance was both predicted and observed at 1.9 GHz. Due to the feature sizes available, this is not the highest field-free resonance achievable, but rather a proof of concept, highlighting the ability of photolithographic patterning to produce large areas of thin films with induced magnetic fields. Field-free measurements on the tessellated patterns based on a square tile revealed two distinct resonances as the sample was rotated with respect to the transmission line, when the RF field was aligned along either of the long axes, and orthogonal to the effective magnetic field. Additionally, the multiple aspect ratios in the square tile each produced a different effective magnetic field, and hence a much wider frequency response compared to the single aspect ratio striped array. Finally, it was shown that higher order polygon tiling (hexagonal and quasi-octagonal) produced a much more isotropic frequency response, due to the additional orientations of the anisotropic field. Through photolithographic patterning of magnetic thin film with a tessellated patten of varying aspect ratios, an isotropic, broadband and field free resonance was achieved.

11.2 Future Work

This thesis presented an investigation into some of the methods and underpinning physics in order to manipulate magnetic thin films for RF applications. Focus was directed to understanding and enhancing the damping through interfacial effects,

and manipulating the effective magnetic field through shape anisotropy induced via lithographic patterning. Though several important questions and issues were addressed, almost all aspects of the work could be extended further.

The modelling introduced in chapter 4 provides an easy way to model the frequency and field response of a layered structure in terms of impedances, which requires knowledge of the material parameters beforehand. The simulations currently assume an isotropic thin film system, one further addition could be to account for the angular dependence of the effective magnetic field, as was demonstrated with the striped arrays in chapter 10. Another immediate extension would be to run the simulation in reverse, i.e. in order to minimise the reflectance at a given frequency, or in order to produce the ideal dynamic response over a range of frequencies, what would be the ideal parameters? It would also be of interest to compare outputs with more established magnetic computational modelling, such as micromagnetics.

The integrated FMR system, detailed in chapter 7, can be extended in a number of ways. The current frequency output has a maximal fundamental value of 7.5 GHz, which is then doubled to 15 GHz, however more recent voltage oscillator microchips are capable of fundamental frequencies of up to 15 GHz, which in principle could be doubled up to 30 GHz. This would require likely require additional power extenders to achieve measurable signals at the higher limit, and would also require a larger electromagnet to excite resonance at these frequencies. A simpler upgrade to the system would be to replace the microstrip with a co-planar waveguide, to provide better signal to noise at higher frequencies. This, accompanied with adjustments to the lock-in circuit, would likely greatly improve the resolution of the system. Further upgrades to the system could include additional motors to allow for out-of-plane measurements, or the use of the auxiliary outputs to undertake simultaneous Hall effect measurements.

Chapter 8 detailed improvements in the understanding and quantification of the spin pumping model through the inclusion of a thickness dependence to the spin diffusion length via the thickness dependence of the resistivity. Open questions remain regarding the modification of other key interfacial parameters for Pt, such as the spin Hall angle. It may also be of interest to apply the method to other spin sink materials such as Pd. In light of the results presented in chapter 9, regarding the sudden drop in damping with a Cu spacer, it is clear that a detailed investigation is needed into what was thought of as a material to which spin current was transparent. This could involve matching the interfacial structure, e.g. with NiFe as the FM, in order to observe any changes to important parameters, such as the spin mixing conductance, spin Hall angle, or spin diffusion length.

Open questions also remain following the results presented in chapter 9. The

transition to out-of-plane magnetisation at low temperatures for the CoFeGd alloy could be better understood through magneto-torque measurement to give a detailed picture of the anisotropies involved. Verification of the alignment of the Pt moment with that of the transition metal would also be more concrete with a ferrimagnetic alloy with a magnetisation compensation point just below room temperature. It was recently shown that PIM required a threshold FM magnetisation, and hence could be turned 'off' with temperature with CoFeTaB alloys [286]. A further investigation into PIM and damping could use a material such as this to measure the damping with and without an induced moment in the Pt. The change, if any, of the spin diffusion length either side of a ferrimagnet magnetisation compensation may also provide further insight into links between PIM and dynamic behaviour.

There are multiple ways in which the study in chapter 10 could be extended. Firstly, higher frequencies could be achieved with smaller feature sizes in the lithographic mask, allowing for larger aspect ratios. An alternative technique, such as nano-imprint lithography, may be able to produce large scale structures at feature sizes beyond those limited by the wavelengths used in photolithography. A possible replacement for the different lateral aspect ratios required for a broadband response detailed in chapter 10, is to taper the film to produce a pyramidal structure, resulting in different effective magnetic fields in the same stripe. Silicon was used as the substrate throughout this thesis, however, it may be useful to produce the patterned structures on either flexible substrates in order to better fit to a surface, or onto substrates which can be dissolved into solution, resulting in structures with a defined effective magnetic field, and hence a defined resonant frequency, which could be added to other material. Finally, benefits of the multilayered structures detailed in earlier chapters could be combined with lithographic processing to produce a truly synthetic material, capable of a broadband frequency response.

Fin.

References

[1] M. N. Baibich, J. M. Broto, A. Fert, F. N. Van Dau, F. Petroff, P. Etienne, G. Creuzet, A. Friederich, and J. Chazelas, Phys. Rev. Lett. **61**, 2472 (1988).

[2] G. Binasch, P. Grünberg, F. Saurenbach, and W. Zinn, Phys. Rev. B **39**, 4828 (1989).

[3] M. D. Stiles and A. Zangwill, Phys. Rev. B **66**, 014407 (2002).

[4] S. Aggarwal, H. Almasi, M. DeHerrera, B. Hughes, S. Ikegawa, J. Janesky, H. Lee, H. Lu, F. Mancoff, K. Nagel, *et al.*, in *2019 IEEE International Electron Devices Meeting (IEDM)* (IEEE, 2019) pp. 2–1.

[5] A. Haldar, D. Kumar, and A. O. Adeyeye, Nat. Nanotechnol. **11**, 437 (2016).

[6] A. Haldar, C. Tian, and A. O. Adeyeye, Sci. Adv **3**, e1700638 (2017).

[7] J. Bass and W. P. Pratt Jr, J. Phys. Condens. Matter **19**, 183201 (2007).

[8] W. Zhang, V. Vlaminck, J. Pearson, R. Divan, S. Bader, and A. Hoffmann, Appl. Phys. Lett. **103**, 242414 (2013).

[9] C. Stamm, C. Murer, M. Berritta, J. Feng, M. Gabureac, P. Oppeneer, and P. Gambardella, Phys. Rev. Lett. **119**, 087203 (2017).

[10] T. Moriyama, R. Cao, X. Fan, G. Xuan, B. K. Nikolić, Y. Tserkovnyak, J. Kolodzey, and J. Q. Xiao, Phys. Rev. Lett. **100**, 067602 (2008).

[11] D. H. Kim, H. H. Kim, and C. Y. You, Appl. Phys. Lett. **99**, 072502 (2011).

[12] L. Mihalceanu, S. Keller, J. Greser, D. Karfaridis, K. Simeonidis, G. Vourlias, T. Kehagias, A. Conca, B. Hillebrands, and E. T. Papaioannou, Appl. Phys. Lett. **110**, 252406 (2017).

[13] E. Moog, J. Zak, and S. Bader, J. Appl. Phys. **69**, 4559 (1991).

[14] R. Rowan-Robinson, A. Stashkevich, Y. Roussigné, M. Belmeguenai, S. Chérif, A. Thiaville, T. Hase, A. Hindmarch, and D. Atkinson, Sci. Rep. **7**, 16835 (2017).

[15] M. Collet, R. Mattana, J.-B. Moussy, K. Ollefs, S. Collin, C. Deranlot, A. Anane, V. Cros, F. Petroff, F. Wilhelm, *et al.*, Appl. Phys. Lett. **111**, 202401 (2017).

[16] H. Wu, Q. Zhang, C. Wan, S. S. Ali, Z. Yuan, L. You, J. Wang, Y. Choi, and X. Han, IEEE Transactions on Magnetics **51**, 1 (2015).

[17] M. Caminale, A. Ghosh, S. Auffret, U. Ebels, K. Ollefs, F. Wilhelm, A. Rogalev, and W. Bailey, Phys. Rev. B **94**, 014414 (2016).

[18] L. Zhu, D. Ralph, and R. Buhrman, Phys. Rev. B **98**, 134406 (2018).

[19] N. N. Phuoc, F. Xu, and C. K. Ong, Appl. Phys. Lett. **94**, 092505 (2009).

[20] Y. Ren, X. Li, Y. Wang, J. Ren, Y. Zhang, B. Dai, H. Yan, G. Sun, and S. Peng, Sci. Rep. **6**, 31773 (2016).

[21] D. Jiles, *Introduction to magnetism and magnetic materials* (CRC press, 2015).

[22] K. Y. Bliokh, Y. P. Bliokh, S. Savel'Ev, and F. Nori, Phys. Rev. Lett. **99**, 190404 (2007).

[23] S. Lloyd, M. Babiker, G. Thirunavukkarasu, and J. Yuan, Rev. Mod. Phys. **89**, 035004 (2017).

[24] B. J. McMorran, A. Agrawal, P. A. Ercius, V. Grillo, A. A. Herzing, T. R. Harvey, M. Linck, and J. S. Pierce, Philos. Trans. R. Soc. A **375**, 20150434 (2017).

[25] M. E. McHenry and D. E. Laughlin, "Magnetic moment and magnetization," in *Characterization of Materials* (Wiley, 2012) pp. 1–25.

[26] S. Blundell, *Magnetism in Condensed Matter* (Oxford University Press, 2009).

[27] F. Hund, *Line spectra and Periodic Table of the Elements* (Springer, 1927).

[28] J. Pelzl, R. Meckenstock, D. Spoddig, F. Schreiber, J. Pflaum, and Z. Frait, J. Phys. Condens. Matter **15**, S451 (2003).

[29] A. Anisimov, M. Farle, P. Poulopoulos, W. Platow, K. Baberschke, P. Isberg, R. Wäppling, A. Niklasson, and O. Eriksson, Phys. Rev. Lett. **82**, 2390 (1999).

[30] C. Kittel *et al.*, *Introduction to solid state physics*, Vol. 8 (Wiley New York, 1976).

[31] P. Weiss, Comptes Rendus **143**, 1136 (1907).

[32] N. Bergeard, A. Mougin, M. Izquierdo, E. Fonda, and F. Sirotti, Phys. Rev. B **96**, 064418 (2017).

[33] M. Binder, A. Weber, O. Mosendz, G. Woltersdorf, M. Izquierdo, I. Neudecker, J. Dahn, T. Hatchard, J.-U. Thiele, C. Back, *et al.*, Phys. Rev. B **74**, 134404 (2006).

[34] M. A. Ruderman and C. Kittel, Physical Review **96**, 99 (1954).

[35] T. Kasuya, Progress of Theoretical Physics **16**, 58 (1956).

[36] K. Yosida, Physical Review **106**, 893 (1957).

[37] I. A. Campbell, J. Phys. F Met. Phys. **2** (1972).

[38] W. Heisenberg, Zeitschrift für Physik A **49**, 619 (1928).

[39] J. C. Slater, Physical Review **36**, 57 (1930).

[40] A. Bethe H, Sommerfeld, *Handbook der Physik*, Vol. 724 (Springer, 1933).

[41] R. Cardias, A. Szilva, A. Bergman, I. Di Marco, M. Katsnelson, A. Lichtenstein, L. Nordström, A. Klautau, O. Eriksson, and Y. O. Kvashnin, Sci. Rep. **7**, 1 (2017).

[42] M. Wu, "Nonlinear spin waves in magnetic film feedback rings," in *Solid State Physics*, Vol. 62, edited by R. E. Camley and R. L. Stamps (Academic Press, 2010) pp. 163 – 224.

[43] A. Fuss, S. Demokritov, P. Grünberg, and W. Zinn, J. Magn. Magn. Mater **103**, L221 (1992).

[44] P. Kurz, G. Bihlmayer, and S. Blügel, J. Phys. Condens. Matter **14**, 6353 (2002).

[45] S. Anilturk and R. Koymen, Phys. Rev. B **68**, 024430 (2003).

[46] K. J. Buschow, *Concise encyclopedia of magnetic and superconducting materials* (Elsevier, 2005).

[47] Y. Wei, *Ferromagnetic Resonance as a Probe of Magnetization Dynamics: A Study of FeCo Thin Films and Trilayers*, Ph.D. thesis, Acta Universitatis Upsaliensis (2015).

[48] E. C. Stoner, The London, Edinburgh, and Dublin Philosophical Magazine and Journal of Science **15**, 1018 (1933).

[49] J. C. Slater, Physical Review **49**, 537 (1936).

[50] J. Santiago, C. Huang, and E. Morosan, J. Phys. Condens. Matter **29**, 373002 (2017).

[51] T. Moriya, *Spin fluctuations in itinerant electron magnetism*, Vol. 56 (Springer Science & Business Media, 2012).

[52] P. Rhodes and P. Wohlfarth, Proc. R. Soc. A **273**, 247 (1963).

[53] M. Richter, J. Phys. D **31**, 1017 (1998).

[54] G. J. Long and F. Grandjean, *Supermagnets, hard magnetic materials*, Vol. 331 (Springer Science, 2012).

[55] P. Gubbens, "Chapter four - rare earth mössbauer spectroscopy measurements on lanthanide intermetallics: A survey," in *Handbook of Magnetic Materials*, Vol. 20, edited by K. Buschow (Elsevier, 2012) pp. 227 – 335.

[56] A. Szytula and J. Leciejewicz, *Handbook of crystal structures and magnetic properties of rare earth intermetallics* (CRC press, 1994).

[57] K. H. J. Buschow, *Handbook of magnetic materials*, Vol. 7 (Elsevier, 1993).

[58] M. Brooks, O. Eriksson, and B. Johansson, J. Phys. Condens. Matter **1**, 5861 (1989).

[59] M. Brooks, L. Nordström, and B. Johansson, Physica B Condens. **172**, 95 (1991).

[60] A. Clogston, B. Matthias, M. Peter, H. Williams, E. Corenzwit, and R. Sherwood, Physical Review **125**, 541 (1962).

[61] N. F. Mott, Proc. R. Soc. A **153**, 699 (1936).

[62] R. C. O'handley, *Modern magnetic materials: principles and applications* (Wiley, 2000).

[63] K. Fuchs, Math. Proc. Camb. Philos. Soc **34**, 100 (1938).

[64] E. H. Sondheimer, Advances in physics **1**, 1 (1952).

[65] A. Mayadas and M. Shatzkes, Phys. Rev. B **1**, 1382 (1970).

[66] B. Feldman, S. Park, M. Haverty, S. Shankar, and S. T. Dunham, Phys. Status Solidi B **247**, 1791 (2010).

[67] R. Smith, E. Ryan, C.-K. Hu, K. Motoyama, N. Lanzillo, D. Metzler, L. Jiang, J. Demarest, R. Quon, L. Gignac, *et al.*, AIP Advances **9**, 025015 (2019).

[68] D. Alcer and D. Atkinson, Nanotechnology **28**, 375703 (2017).

[69] R. Rowan-Robinson, A. Hindmarch, and D. Atkinson, Phys. Rev. B **90**, 104401 (2014).

[70] S. V. Von Sovskii, *Ferromagnetic resonance: the phenomenon of resonant absorption of a high-frequency magnetic field in ferromagnetic substances* (Elsevier, 2016).

[71] L. Landau and L. EM, Phys. Z. Sowjetunion **8**, 153 (1935).

[72] C. Kittel, Physical Review **70**, 281 (1946).

[73] C. Kittel, Physical Review **71**, 270 (1947).

[74] C. Kittel, Physical Review **73**, 155 (1948).

[75] T. L. Gilbert, Physical Review **100**, 1243 (1955).

[76] K. Baberschke, J. Phys. Conf. Ser. **324**, 012011 (2011).

[77] S. Azzawi, A. Hindmarch, and D. Atkinson, J. Phys. D **50**, 473001 (2017).

[78] E. Olsen, *Applied magnetism: a study in quantities* (Centrex, 1966).

[79] B. Heinrich, J. Cochran, and R. Hasegawa, J. Appl. Phys **57**, 3690 (1985).

[80] Y. Wei, S. L. Chin, and P. Svedlindh, J. Phys. D **48**, 335005 (2015).

[81] J. L. Wallace, IEEE Trans. Magn **29**, 4209 (1993).

[82] O. Chubykalo-Fesenko, U. Nowak, R. W. Chantrell, and D. Garanin, Phys. Rev. B **74**, 094436 (2006).

[83] A. Lyberatos, D. V. Berkov, and R. W. Chantrell, J. Phys. Condens. Matter **5**, 8911 (1993).

[84] F. Bloch, Physical Review **70**, 460 (1946).

[85] N. Bloembergen, Physical Review **78**, 572 (1950).

[86] H. Suhl, IEEE Trans. Magn **34**, 1834 (1998).

[87] D. A. Garanin, Phys. Rev. B **55**, 3050 (1997).

[88] H. Suhl, Physical Review **97**, 555 (1955).

[89] J. Smit, Philips Res. Rep. **10**, 113 (1955).

[90] S. Vonsovskii, *The Phenomenon of Resonant Absorption of a High-Frequency Magnetic Field in Ferromagnetic Substances* (Pergamon Press, Oxford, 1966).

[91] A. Hirohata and K. Takanashi, J. Phys. D: Appl. Phys. **47**, 193001 (2014).

[92] Y. Wang, R. Ramaswamy, and H. Yang, J. Phys. D: Appl. Phys. **51**, 273002 (2018).

[93] B. Heinrich, D. Fraitová, and V. Kamberskỳ, Phys. Status Solidi (b) **23**, 501 (1967).

[94] K. Gilmore, M. Stiles, J. Seib, D. Steiauf, and M. Fähnle, Phys. Rev. B **81**, 174414 (2010).

[95] J. Kunes and V. Kamberskỳ, Phys. Rev. B **65**, 212411 (2002).

[96] K. Gilmore, Y. Idzerda, and M. D. Stiles, Phys. Rev. Lett. **99**, 027204 (2007).

[97] K. Gilmore, Y. U. Idzerda, and M. D. Stiles, J. Appl. Phys **103**, 07D303 (2008).

[98] I. Barsukov, F. Römer, R. Meckenstock, K. Lenz, J. Lindner, A. Banholzer, M. Körner, J. Grebing, J. Fassbender, and M. Farle, Phys. Rev. B **84**, 140410 (2011).

[99] J. Rantschler, R. McMichael, A. Castillo, A. Shapiro, W. Egelhoff Jr, B. Maranville, D. Pulugurtha, A. Chen, and L. Connors, J. Appl. Phys **101**, 033911 (2007).

[100] K. Zakeri, J. Lindner, I. Barsukov, R. Meckenstock, M. Farle, U. Von Hörsten, H. Wende, W. Keune, J. Rocker, S. Kalarickal, *et al.*, Phys. Rev. B **76**, 104416 (2007).

[101] R. D. McMichael, D. Twisselmann, and A. Kunz, Phys. Rev. Lett. **90**, 227601 (2003).

[102] V. T. Synogach, Y. K. Fetisov, C. Mathieu, and C. E. Patton, Phys. Rev. Lett. **85**, 2184 (2000).

[103] H. Schultheiss, X. Janssens, M. van Kampen, F. Ciubotaru, S. Hermsdoerfer, B. Obry, A. Laraoui, A. Serga, L. Lagae, A. Slavin, *et al.*, Phys. Rev. Lett. **103**, 157202 (2009).

[104] A. Boardman and S. Nikitov, Phys. Rev. B **38**, 11444 (1988).

[105] H. Schultheiss, K. Vogt, and B. Hillebrands, Phys. Rev. B **86**, 054414 (2012).

[106] B. Heinrich, K. Urquhart, A. Arrott, J. Cochran, K. Myrtle, and S. Purcell, Phys. Rev. Lett. **59**, 1756 (1987).

[107] S. Mizukami, Y. Ando, and T. Miyazaki, Jpn. J. Appl. Phys. **40**, 580 (2001).

[108] S. Azzawi, A. Ganguly, M. Tokac, R. Rowan-Robinson, J. Sinha, A. Hindmarch, A. Barman, and D. Atkinson, Phys. Rev. B **93**, 054402 (2016).

[109] C. Swindells, A. Hindmarch, A. Gallant, and D. Atkinson, Phys. Rev. B **99**, 064406 (2019).

[110] M. Tokac, S. Bunyaev, G. Kakazei, D. Schmool, D. Atkinson, and A. Hindmarch, Phys. Rev. Lett. **115**, 056601 (2015).

[111] L. Zhu, D. C. Ralph, and R. A. Buhrman, Phys. Rev. B **99**, 180404 (2019).

[112] Y. Tserkovnyak, A. Brataas, and G. E. Bauer, Phys. Rev. Lett. **88**, 117601 (2002).

[113] Y. Tserkovnyak, A. Brataas, and G. E. Bauer, Phys. Rev. B **66**, 224403 (2002).

[114] E. Simánek and B. Heinrich, Phys. Rev. B **67**, 144418 (2003).

[115] E. Barati, M. Cinal, D. Edwards, and A. Umerski, Phys. Rev. B **90**, 014420 (2014).

[116] R. Elliott, Physical Review **96**, 280 (1954).

[117] Y. Yafet, Solid State Phys. **14**, 1 (1963).

[118] L. Szolnoki, B. Dóra, A. Kiss, J. Fabian, and F. Simon, Phys. Rev. B **96**, 245123 (2017).

[119] M. I. Dyakonov and V. I. Perel, Sov. Phys. Solid State **13**, 3023 (1972).

[120] R. Freeman, A. Zholud, Z. Dun, H. Zhou, and S. Urazhdin, Phys. Rev. Lett. **120**, 067204 (2018).

[121] Y. Otani and T. Kimura, Philos. Trans. R. Soc. A **369**, 3136 (2011).

[122] A. Brataas, Y. Tserkovnyak, G. E. Bauer, and B. I. Halperin, Phys. Rev. B **66**, 060404 (2002).

[123] Y. Tserkovnyak, A. Brataas, G. E. Bauer, and B. I. Halperin, Rev. Mod. Phys **77**, 1375 (2005).

[124] A. Brataas, Y. Tserkovnyak, and G. E. Bauer, Phys. Rev. Lett. **101**, 037207 (2008).

[125] K. Ando, Semicond. Sci. Technol. **29**, 043002 (2014).

[126] V. P. Amin and M. D. Stiles, Phys. Rev. B **94**, 104419 (2016).

[127] Y. Xu, D. D. Awschalom, and J. Nitta, *Handbook of Spintronics* (Springer, 2015).

[128] Y. Liu, Z. Yuan, R. J. Wesselink, A. A. Starikov, and P. J. Kelly, Phys. Rev. Lett. **113**, 207202 (2014).

[129] S. Zhang, P. Levy, and A. Fert, Phys. Rev. Lett. **88**, 236601 (2002).

[130] J. Sinova, S. O. Valenzuela, J. Wunderlich, C. Back, and T. Jungwirth, Rev. Mod. Phys **87**, 1213 (2015).

[131] M. D'yakonov and V. Perel, Sov. Phys. JETP **13**, 467 (1971).

[132] J. Hirsch, Phys. Rev. Lett. **83**, 1834 (1999).

[133] W. Zhang, W. Han, X. Jiang, S.-H. Yang, and S. S. Parkin, Nat. Phys. **11**, 496 (2015).

[134] Y. K. Kato, R. C. Myers, A. C. Gossard, and D. D. Awschalom, Science **306**, 1910 (2004).

[135] K. Ando, S. Takahashi, J. Ieda, Y. Kajiwara, H. Nakayama, T. Yoshino, K. Harii, Y. Fujikawa, M. Matsuo, S. Maekawa, *et al.*, J. Appl. Phys. **109**, 103913 (2011).

[136] S. A. Cavill, C. Huang, M. Offidani, Y.-H. Lin, M. A. Cazalilla, and A. Ferreira, Phys. Rev. Lett. **124**, 236803 (2020).

[137] L. Liu, O. Lee, T. Gudmundsen, D. Ralph, and R. Buhrman, Phys. Rev. Lett. **109**, 096602 (2012).

[138] L. Liu, T. Moriyama, D. Ralph, and R. Buhrman, Phys. Rev. Lett. **106**, 036601 (2011).

[139] F. R. Connor, *Wave Transmission* (Edward Arnold, 1972).

[140] T. Wang, H. Wang, G. Tan, L. Wang, and L. Qiao, IEEE Trans. Magn. **51** (2015).

[141] M. Green and X. Chen, J. Mater. **5**, 503 (2019).

[142] R. Panwar and J. R. Lee, Aerosp. Sci. Technol. **66**, 216 (2017).

[143] F. Qin and C. Brosseau, J. Appl. Phys. **111**, 061301 (2012).

[144] B. Quan, X. Liang, G. Ji, Y. Cheng, W. Liu, J. Ma, Y. Zhang, D. Li, and G. Xu, J. Alloys Compd. **728**, 1065 (2017).

[145] B. A. Munk, *Frequency selective surfaces: theory and design* (John Wiley & Sons, 2005).

[146] S. Kingsley and S. Quegan, *Understanding radar systems*, Vol. 2 (SciTech Publishing, 1999).

[147] J. Ramprecht and D. Sjoberg, Progress In Electromagnetics Research **75**, 85 (2007).

[148] G. M. Ettinger, *Magnetic amplifiers* (Methuen, 1957).

[149] J. Ramprecht, *Electromagnetic Waves in Media with Ferromagnetic Losses*, Ph.D. thesis, KTH, Sweden (2008).

[150] C. Song, X. Yin, M. Han, X. Li, Z. Hou, L. Zhang, and L. Cheng, Carbon N. Y. **116**, 50 (2017).

[151] C. Wang, X. Han, P. Xu, X. Zhang, Y. Du, S. Hu, J. Wang, and X. Wang, Appl. Phys. Lett. **98**, 072906 (2011).

[152] Y. Qing, W. Zhou, F. Luo, and D. Zhu, J. Mater. Chem. C **1**, 536 (2013).

[153] K. B. Alici, F. Bilotti, L. Vegni, and E. Ozbay, J. Appl. Phys. **108**, 083113 (2010).

[154] D. Yi, X. C. Wei, and Y. L. Xu, IEEE Trans. Microw. Theory Tech. **65**, 2819 (2017).

[155] J. Zhao, S. Wei, C. Wang, K. Chen, B. Zhu, T. Jiang, and Y. Feng, Opt. Express **26**, 8522 (2018).

[156] S. Zhong and S. He, Sci. Rep. **3**, 2083 (2013).

[157] C. Zhang, Q. Cheng, J. Yang, J. Zhao, and T. J. Cui, Appl. Phys. Lett. **110**, 143511 (2017).

[158] F. Ding, Y. Cui, X. Ge, Y. Jin, and S. He, Appl. Phys. Lett. **100**, 103506 (2012).

[159] W. Li, T. Wu, W. Wang, P. Zhai, and J. Guan, J. Appl. Phys. **116**, 044110 (2014).

[160] J. Y. Shin and J. H. Oh, IEEE Trans. Magn. **29**, 3437 (1993).

[161] A. N. Yusoff, M. H. Abdullah, S. H. Ahmad, S. F. Jusoh, A. A. Mansor, and S. A. Hamid, J. Appl. Phys. **92**, 876 (2002).

[162] Y.-B. Feng, T. Qiu, C.-Y. Shen, and X.-Y. Li, IEEE Trans. Magn. **42**, 363 (2006).

[163] S. S. Kim, S. T. Kim, Y. C. Yoon, and K. S. Lee, J. Appl. Phys. **97**, 10F905 (2005).

[164] B. Zhang, Y. Feng, J. Xiong, Y. Yang, and H. Lu, IEEE Trans. Magn. **42**, 1778 (2006).

[165] R. B. Yang and W. F. Liang, J. Appl. Phys. **109**, 07A311 (2011).

[166] C. Long, B. Xu, C. Han, Z. Chen, and J. Guan, J. Alloys Compd. **709**, 735 (2017).

[167] M. A. Abshinova, A. V. Lopatin, N. E. Kazantseva, J. Vilvcáková, and P. Sáha, Compos. Part A Appl. Sci. Manuf **38**, 2471 (2007).

[168] G. Wu, Y. Cheng, Z. Yang, Z. Jia, H. Wu, L. Yang, H. Li, P. Guo, and H. Lv, Chem. Eng. J. **333**, 519 (2018).

[169] X. F. Zhang, X. L. Dong, H. Huang, Y. Y. Liu, W. N. Wang, X. G. Zhu, B. Lv, J. P. Lei, and C. G. Lee, Appl. Phys. Lett. **89**, 053115 (2006).

[170] J. Liu, J. Cheng, R. Che, J. Xu, M. Liu, and Z. Liu, J. Phys. Chem. C **117**, 489 (2013).

[171] H. L. Xu, H. Bi, and R. B. Yang, J. Appl. Phys. **111**, 07A522 (2012).

[172] T. Wu, Y. Liu, X. Zeng, T. Cui, Y. Zhao, Y. Li, and G. Tong, ACS Appl. Mater. Interfaces **8**, 7370 (2016).

[173] X. Zhao, Z. Zhang, L. Wang, K. Xi, Q. Cao, D. Wang, Y. Yang, and Y. Du, Sci. Rep. **3**, 3421 (2013).

[174] N. Li, G. W. Huang, Y. Q. Li, H. M. Xiao, Q. P. Feng, N. Hu, and S. Y. Fu, ACS Appl. Mater. Interfaces **9**, 2973 (2017).

[175] P. Lunkenheimer, V. Bobnar, A. V. Pronin, A. Ritus, A. Volkov, and A. Loidl, Phys. Rev. B **66**, 052105 (2002).

[176] S. Krohns, P. Lunkenheimer, C. Kant, A. Pronin, H. Brom, A. Nugroho, M. Diantoro, and A. Loidl, Appl. Phys. Lett. **94**, 122903 (2009).

[177] J. Sebald, S. Krohns, P. Lunkenheimer, S. Ebbinghaus, S. Riegg, A. Reller, and A. Loidl, Solid State Commun. **150**, 857 (2010).

[178] Z. Ma, C. Cao, J. Yuan, Q. Liu, and J. Wang, Appl. Surf. Sci. **258**, 7556 (2012).

[179] W. Li, J. Lv, X. Zhou, J. Zheng, Y. Ying, L. Qiao, J. Yu, and S. Che, J. Magn. Magn. Mater. **426**, 504 (2017).

[180] Y. Zou, L. Jiang, S. Wen, W. Shu, Y. Qing, Z. Tang, H. Luo, and D. Fan, Appl. Phys. Lett. **93**, 261115 (2008).

[181] Y. Xu, W. Yuan, S. Bie, H. Xu, Q. Chen, and J. Jiang, J. Electromagn. Waves Appl. **29**, 2420 (2015).

[182] W. Ren, Y. Nie, X. Xiong, C. Zhang, Y. Zhou, and R. Gong, J. Appl. Phys. **111**, 07E703 (2012).

[183] G. R. Aranda, G. N. Kakazei, J. González, and K. Y. Guslienko, J. Appl. Phys. **116**, 093908 (2014).

[184] Z. Zhu, H. Feng, X. Cheng, H. Xie, Q. Liu, and J. Wang, J. Phys. D. Appl. Phys. **51**, 045004 (2018).

[185] Y. Wu, Y. Yang, F. Ma, B. Zong, Z. Yang, and J. Ding, J. Magn. Magn. Mater. **426**, 467 (2017).

[186] L. Zhang, H. Zheng, W. Zhu, M. Li, M. Zhang, Y. Liu, X. Wang, N. Wang, V. G. Harris, J. Xie, and L. Deng, J. Alloys Compd. **706**, 318 (2017).

[187] H. Feng, Z. Zhu, R. Gao, Y. Huang, X. Li, Q. Liu, and J. Wang, J. Magn. Magn. Mater. **497**, 166008 (2019).

[188] L. M. Malkinski, M. Yu, A. Y. Vovk, D. J. Scherer, L. Spinu, W. Zhou, S. Whittenburg, Z. Davis, and J. S. Jung, J. Appl. Phys. **101**, 09J110 (2007).

[189] Y. Yang, Z. Li, C. Neo, and J. Ding, J. Phys. Chem. Solids **75**, 230 (2014).

[190] S. S. Maklakov, A. N. Lagarkov, S. A. Maklakov, Y. A. Adamovich, D. A. Petrov, K. N. Rozanov, I. A. Ryzhikov, A. Y. Zarubina, K. V. Pokholok, and D. S. Filimonov, J. Alloys Compd **706**, 267 (2017).

[191] R. Stuart, *Vacuum Technology, Thin Films, and Sputtering: an Introduction* (Academic Press, 1983).

[192] P. J. Kelly and R. D. Arnell, Vacuum **56**, 159 (2000).

[193] F. Penning, Physica **3**, 873 (1936).

[194] F. Frank and J. H. van der Merwe, Proc. R. Soc. Lond. A **198**, 205 (1949).

[195] E. Bauer, Z. Kristallogr. Cryst. Mater **110**, 372 (1958).

[196] I. N. Stranski and L. Krastanow, Monatsh Chem Verw Teile Anderer Wiss **71**, 351 (1937).

[197] K. Oura, V. Lifshits, A. Saranin, A. Zotov, and M. Katayama, *Surface science: an introduction* (Springer Science & Business Media, 2013).

[198] A. Bravais, J. Ecole. Polytech. **19**, 1 (1850).

[199] D. R. Lide, *CRC handbook of chemistry and physics*, Vol. 85 (CRC press, 2004).

[200] M. D. Levenson, N. Viswanathan, and R. A. Simpson, IEEE Trans. Electron Devices **29**, 1828 (1982).

[201] A. Adeyeye and N. Singh, J. Phys. D **41**, 153001 (2008).

[202] *Microposit Positve Tone Resist: S1813*, DOW Chemical Company.

[203] *AZ 351B General Purpose Developer*, Microchemicals GmbH.

[204] J. Singh, C. Lamberti, and J. A. van Bokhoven, Chem. Soc. Rev. **39**, 4754 (2010).

[205] J. Als-Nielsen and D. McMorrow, *Elements of modern X-ray physics* (John Wiley & Sons, 2011).

[206] L. G. Parratt, Physical Review **95**, 359 (1954).

[207] H. Kiessig, Annalen der Physik **402**, 715 (1931).

[208] J. Kortright, J. Appl. Phys **70**, 3620 (1991).

[209] M. Björck and G. Andersson, J. Appl. Crystallogr. **40**, 1174 (2007).

[210] G. Schütz, W. Wagner, W. Wilhelm, P. Kienle, R. Zeller, R. Frahm, and G. Materlik, Phys. Rev. Lett. **58**, 737 (1987).

[211] J. Stöhr and H. C. Siegmann, *Magnetism: from fundamentals to nanoscale dynamics*, Vol. 152 (Springer Science & Business Media, 2007).

[212] B. L. Henke, E. M. Gullikson, and J. C. Davis, Atomic data and nuclear data tables **54** (1993).

[213] C. Kapusta, P. Fischer, and G. Schütz, J. Alloys Compd **286**, 37 (1999).

[214] A. S. Committee *et al.*, ANSI/IEEE Std (1979).

[215] E. Hecht, *Optics*, Vol. 4 (Addison Wesley San Francisco, 2002).

[216] B. Thole, P. Carra, F. Sette, and G. van der Laan, Phys. Rev. Lett. **68**, 1943 (1992).

[217] C. Giles, C. Malgrange, J. Goulon, F. De Bergevin, C. Vettier, E. Dartyge, A. Fontaine, C. Giorgetti, and S. Pizzini, J. Appl. Crystallogr **27**, 232 (1994).

[218] M. Faraday, Philos. Trans. Royal Soc. **136**, 1 (1846).

[219] J. Kerr, Philos. Mag **3**, 321 (1877).

[220] J. Bland, M. Padgett, R. Butcher, and N. Bett, J. Phys. E: Sci. Instrum **22**, 308 (1989).

[221] M. Farle, Rep. Prog. Phys. **61**, 755 (1998).

[222] W. Webb, IEEE Trans. Magn **8**, 51 (1972).

[223] Quantum Design, Inc., 10307 Pacific Center Court, San Diego, CA 92121, USA, see www.qdusa.com .

[224] B. D. Josephson, Phys. Lett **1**, 251 (1962).

[225] B. D. Josephson, Rev. Mod. Phys **46**, 251 (1974).

[226] M. Buchner, K. Höfler, B. Henne, V. Ney, and A. Ney, J. Appl. Phys **124**, 161101 (2018).

[227] J. A. Weil and J. R. Bolton, *Electron paramagnetic resonance: elementary theory and practical applications* (John Wiley & Sons, 2007).

[228] T. J. Silva, C. Lee, T. Crawford, and C. Rogers, J. Appl. Phys. **85**, 7849 (1999).

[229] V. Denysenkov and A. M. Grishin, Rev. Sci. Instrum **74**, 3400 (2003).

[230] Y. Ding, T. Klemmer, and T. Crawford, J. Appl. Phys. **96**, 2969 (2004).

[231] Y. Liu, L. Chen, C. Tan, H. Liu, and C. Ong, Rev. Sci. Instrum **76**, 063911 (2005).

[232] J. Wei, J. Wang, Q. Liu, X. Li, D. Cao, and X. Sun, Rev. Sci. Instrum **85**, 054705 (2014).

[233] J. Wei, H. Feng, Z. Zhu, Q. Liu, and J. Wang, Rev. Sci. Instrum **86**, 114705 (2015).

[234] I. Harward, T. O'Keevan, A. Hutchison, V. Zagorodnii, and Z. Celinski, Rev. Sci. Instrum **82**, 095115 (2011).

[235] S. S. Kalarickal, P. Krivosik, M. Wu, C. E. Patton, M. L. Schneider, P. Kabos, T. J. Silva, and J. P. Nibarger, J. Appl. Phys. **99**, 093909 (2006).

[236] C. Bilzer, T. Devolder, P. Crozat, C. Chappert, S. Cardoso, and P. Freitas, J. Appl. Phys. **101**, 074505 (2007).

[237] E. O. Hammerstad, in *1975 5th European Microwave Conference* (IEEE, 1975) pp. 268–272.

[238] Rogers Corp., 2225 W. Chandler Blvd. Chandler, AZ 852241, USA, see www.rogerscorp.com .

[239] Keysight Technologies, 610 Wharfedale Road, Winnersh Triangle, Wokingham, Berkshire, RG41 5TP, see www.keysight.com/ .

[240] Aim and Thurlby Thandar Instruments, Glebe Rd, Huntingdon, Cambridgeshire, PE29 7DR, UK, see www.aimtti.com .

[241] Rapberry Pi, Rapberry Pi Foundation, see www.raspberrypi.org .

[242] C. Swindells, A. Hindmarch, A. Gallant, and D. Atkinson, Appl. Phys. Lett. **116**, 042403 (2020).

[243] Windfreak Technologies, LLC., New Port Richey, Florida 34652 USA, see www.windfreaktech.com/ .

[244] Cypress Semiconductor Corp., 198 Champion Court San Jose, CA 95134 USA, see www.cypress.com/ .

[245] Arduino Uno, Arduino, see www.arduino.cc .

[246] Adafruit MotorShield V2, Adafruit Industries, see www.adafruit.com .

[247] Analog Devices, One Technology Way PO BOX 9106 Norwood, MA 02062 USA, see www.analog.com/ .

[248] M. Crosser, S. Scott, A. Clark, and P. Wilt, Rev. Sci. Instrum **81**, 084701 (2010).

[249] Python, Python Software Foundation, see https://www.python.org/ .

[250] Chris Liechti, pySerial, see pythonhosted.org/pyserial// .

[251] O. Sulymenko, O. Prokopenko, V. Tiberkevich, A. Slavin, B. Ivanov, and R. Khymyn, Phys. Rev. Appl. **8**, 064007 (2017).

[252] M. Weiler, M. Althammer, M. Schreier, J. Lotze, M. Pernpeintner, S. Meyer, H. Huebl, R. Gross, A. Kamra, J. Xiao, Y. Chen, H. Jiao, G. Bauer, and S. Goennenwein, Phys. Rev. Lett. **111**, 176601 (2013).

[253] H. Kurt, R. Loloee, K. Eid, W. Pratt, and J. Bass, Appl. Phys. Lett. **81**, 4787 (2003).

[254] J. Rojas-Sánchez, N. Reyren, P. Laczkowski, W. Savero, J. Attané, C. Deranlot, M. Jamet, J. George, L. Vila, and H. Jaffr'es, Phys. Rev. Lett. **112**, 106602 (2014).

[255] M. Khasawneh, C. Klose, W. Pratt, and N. Birge, Phys. Rev. B **84**, 014425 (2011).

[256] D. Bozec, M. Howson, B. Hickey, S. Shatz, N. Wiser, E. Tsymbal, and D. Pettifor, Phys. Rev. Lett. **85**, 1314 (2000).

[257] D. Wei, M. Obstbaum, M. Ribow, C. Back, and G. Woltersdorf, Nat. Commun. **5**, 3768 (2014).

[258] E. Montoya, P. Omelchenko, C. Coutts, N. Lee-Hone, R. Hübner, D. Broun, B. Heinrich, and E. Girt, Phys. Rev. B **94**, 054416 (2016).

[259] A. Ruiz-Calaforra, T. Brächer, V. Lauer, P. Pirro, B. Heinz, M. Geilen, A. Chumak, A. Conca, B. Leven, and B. Hillebrands, J. Appl. Phys. **117**, 163901 (2015).

[260] M. Belmeguenai, M. Gabor, F. Zighem, N. Challab, T. Petrisor, R. Mos, and C. Tiusan, J. Phys. D. Appl. Phys. **51**, 045002 (2018).

[261] S. Yakata, Y. Ando, T. Miyazaki, and S. Mizukami, Jpn. J. Appl. Phys **45**, 3892 (2006).

[262] A. Ghosh, S. Auffret, U. Ebels, and W. Bailey, Phys. Rev. Lett. **109**, 127202 (2012).

[263] K. Kondou, H. Sukegawa, S. Mitani, K. Tsukagoshi, and S. Kasai, Appl. Phys. Expr. **5**, 73002 (2012).

[264] J. Sánchez, L. Vila, G. Desfonds, S. Gambarelli, J. Attané, D. J.M., C. Mag'en, and A. Fert, Nat. Commun. **4**, 2944 (2013).

[265] A. Berger, E. Edwards, H. Nembach, O. Karis, M. Weiler, and T. Silva, Phys. Rev. B **98**, 024402 (2018).

[266] Y. Niimi, D. Wei, H. Idzuchi, T. Wakamura, T. Kato, and Y. Otani, Phys. Rev. Lett. **110**, 016805 (2013).

[267] M. Morota, Y. Niimi, K. Ohnishi, D. Wei, T. Tanaka, H. Kontani, T. Kimura, and Y. Otani, Phys. Rev. B **83**, 174405 (2011).

[268] M. Tokac, S. Bunyaev, G. Kakazei, D. Schmool, D. Atkinson, and A. Hindmarch, Phys. Rev. Lett. **115**, 056601 (2015).

[269] A. Cahaya, A. Leon, and G. Bauer, Phys. Rev. B **96**, 144434 (2017).

[270] O. Mosendz, J. Pearson, F. Fradin, G. Bauer, S. Bader, and A. Hoffmann, Phys. Rev. Lett. **104**, 046601 (2010).

[271] A. Conca, B. Heinz, M. Schweizer, S. Keller, E. Papaioannou, and B. Hillebrands, Phys. Rev. B **95**, 174426 (2017).

[272] N. Behera, M. Singh, S. Chaudhary, D. Pandya, P. Muduli, N. Behera, M. Singh, S. Chaudhary, D. Pandya, and P. Muduli, J. Appl. Phys. **117**, 17A714 (2015).

[273] A. Kolesnikov, M. Stebliy, A. Ognev, A. Samardak, A. Fedorets, V. Plotnikov, X. Han, and L. Chebotkevich, J. Phys. D. Appl. Phys. **49**, 425302 (2016).

[274] J. Miyawaki, D. Matsumura, H. Abe, T. Ohtsuki, E. Sakai, K. Amemiya, and T. Ohta, Phys. Rev. B **80**, 020408 (2009).

[275] X. Qiu, W. Legrand, P. He, Y. Wu, J. Yu, R. Ramaswamy, A. Manchon, and H. Yang, Phys. Rev. Lett. **117**, 217206 (2016).

[276] E. Sagasta, Y. Omori, M. Isasa, M. Gradhand, L. Hueso, Y. Niimi, Y. Otani, and F. Casanova, Phys. Rev. B **94**, 060412 (2016).

[277] M.-H. Nguyen, D. Ralph, and R. Buhrman, Phys. Rev. Lett. **116**, 126601 (2016).

[278] M. Tokac, *Investigation of Interfacial Effects in Ferromagnetic Thin-Films*, Ph.D. thesis, Durham University (2016).

[279] S. Ansari, R. Bhor, K. Pai, D. Sen, S. Mazumder, K. Ghosh, Y. Kolekar, and C. Ramana, Appl Surf Sci **414**, 171 (2017).

[280] Y.-M. Hwang, C.-T. Pan, Y.-X. Lu, S.-R. Jian, H.-W. Chang, and J.-Y. Juang, Micromachines **11**, 180 (2020).

[281] I. Hughes and T. Hase, *Measurements and their uncertainties: a practical guide to modern error analysis* (Oxford University Press, 2010).

[282] J. M. Shaw, H. T. Nembach, T. J. Silva, and C. T. Boone, J. Appl. Phys **114**, 243906 (2013).

[283] A. Baker, A. Figueroa, C. Love, S. A. Cavill, T. Hesjedal, and G. Van Der Laan, Phys. Rev. Lett. **116**, 047201 (2016).

[284] L. Chen, S. Mankovsky, S. Wimmer, M. Schoen, H. Körner, M. Kronseder, D. Schuh, D. Bougeard, H. Ebert, D. Weiss, and C. Back, Nat. Phys. **14**, 490 (2018).

[285] J. Nibarger, R. Lopusnik, Z. Celinski, and T. Silva, Appl. Phys. Lett. **83**, 93 (2003).

[286] O. Inyang, L. Bouchenoire, B. Nicholson, M. Tokac, R. Rowan-Robinson, C. Kinane, and A. Hindmarch, Phys. Rev. B **100**, 174418 (2019).

[287] H. Nguyen, W. Pratt, and J. Bass, J. Magn. Magn. Mater. **361**, 30 (2014).

[288] T. Miyazaki and N. Tezuka, J. Magn. Magn. Mater **139**, L231 (1995).

[289] Y. Sakuraba, a. M. Hattori, M. Oogane, Y. Ando, H. Kato, A. Sakuma, T. Miyazaki, and H. Kubota, Appl. Phys. Lett. **88**, 192508 (2006).

[290] S. S. Parkin, C. Kaiser, A. Panchula, P. M. Rice, B. Hughes, M. Samant, and S.-H. Yang, Nat. Mater. **3**, 862 (2004).

[291] Y. Lee, J. Hayakawa, S. Ikeda, F. Matsukura, and H. Ohno, Appl. Phys. Lett **90**, 212507 (2007).

[292] O. Mosendz, J. E. Pearson, F. Y. Fradin, S. D. Bader, and A. Hoffmann, Appl. Phys. Lett. **96**, 022502 (2010).

[293] C. H. Du, H. L. Wang, Y. Pu, T. L. Meyer, P. M. Woodward, F. Y. Yang, and P. C. Hammel, Phys. Rev. Lett. **111**, 247202 (2013).

[294] A. A. Baker, A. I. Figueroa, D. Pingstone, V. K. Lazarov, G. Van Der Laan, and T. Hesjedal, Sci. Rep. **6**, 35582 (2016).

[295] A. Thomas, V. Drewello, M. Schäfers, A. Weddemann, G. Reiss, G. Eilers, M. Münzenberg, K. Thiel, and M. Seibt, Appl. Phys. Lett. **93**, 152508 (2008).

[296] A. Ganguly, S. Azzawi, S. Saha, J. A. King, R. M. Rowan-Robinson, A. T. Hindmarch, J. Sinha, D. Atkinson, and A. Barman, Sci. Rep. **5**, 17596 (2015).

[297] M. A. Schoen, D. Thonig, M. L. Schneider, T. Silva, H. T. Nembach, O. Eriksson, O. Karis, and J. M. Shaw, Nat. Phys. **12**, 839 (2016).

[298] O. Ozatay, P. Gowtham, K. Tan, J. Read, K. Mkhoyan, M. Thomas, G. Fuchs, P. Braganca, E. Ryan, K. Thadani, *et al.*, Nat. Mater. **7**, 567 (2008).

[299] C. Swindells, B. Nicholson, O. Inyang, Y. Choi, T. Hase, and D. Atkinson, Phys. Rev. Res. **2**, 033280 (2020).

[300] M.-H. Nguyen, C.-F. Pai, K. X. Nguyen, D. A. Muller, D. C. Ralph, and R. A. Buhrman, Appl. Phys. Lett. **106**, 222402 (2015).

[301] C.-F. Pai, Y. Ou, L. H. Vilela-Leão, D. Ralph, and R. Buhrman, Physical Review B **92**, 064426 (2015).

[302] K.-S. Ryu, L. Thomas, S.-H. Yang, and S. Parkin, Nat. Nanotechnol. **8**, 527 (2013).

[303] S. Rezende, R. Rodríguez-Suárez, M. Soares, L. Vilela-Leão, D. Ley Domínguez, and A. Azevedo, Appl. Phys. Lett. **102**, 012402 (2013).

[304] S. Dushenko, M. Hokazono, K. Nakamura, Y. Ando, T. Shinjo, and M. Shiraishi, Nat. Commun **9**, 1 (2018).

[305] S. Y. Huang, X. Fan, D. Qu, Y. P. Chen, W. G. Wang, J. Wu, T. Y. Chen, J. Q. Xiao, and C. L. Chien, Phys. Rev. Lett. **109**, 107204 (2012).

[306] S. Geprägs, S. Meyer, S. Altmannshofer, M. Opel, F. Wilhelm, A. Rogalev, R. Gross, and S. T. Goennenwein, Appl. Phys. Lett. **101**, 262407 (2012).

[307] S. Shimizu, K. S. Takahashi, T. Hatano, M. Kawasaki, Y. Tokura, and Y. Iwasa, Phys. Rev. Lett. **111**, 216803 (2013).

[308] H. Nakayama, M. Althammer, Y.-T. Chen, K. Uchida, Y. Kajiwara, D. Kikuchi, T. Ohtani, S. Geprägs, M. Opel, S. Takahashi, *et al.*, Phys. Rev. Lett. **110**, 206601 (2013).

[309] W. Amamou, I. V. Pinchuk, A. H. Trout, R. E. Williams, N. Antolin, A. Goad, D. J. O'Hara, A. S. Ahmed, W. Windl, D. W. McComb, *et al.*, Phys. Rev. Mater. **2**, 011401 (2018).

[310] J. Vogel, A. Fontaine, V. Cros, F. Petroff, J.-P. Kappler, G. Krill, A. Rogalev, and J. Goulon, Phys. Rev. B **55**, 3663 (1997).

[311] F. Wilhelm, P. Poulopoulos, G. Ceballos, H. Wende, K. Baberschke, P. Srivastava, D. Benea, H. Ebert, M. Angelakeris, N. Flevaris, *et al.*, Phys. Rev. Lett. **85**, 413 (2000).

[312] F. Wilhelm, P. Poulopoulos, H. Wende, A. Scherz, K. Baberschke, M. Angelakeris, N. Flevaris, and A. Rogalev, Phys. Rev. Lett. **87**, 207202 (2001).

[313] F. Wilhelm, M. Angelakeris, N. Jaouen, P. Poulopoulos, E. T. Papaioannou, C. Mueller, P. Fumagalli, A. Rogalev, and N. Flevaris, Phys. Rev. B **69**, 220404 (2004).

[314] M. Valvidares, N. Dix, M. Isasa, K. Ollefs, F. Wilhelm, A. Rogalev, F. Sánchez, E. Pellegrin, A. Bedoya-Pinto, P. Gargiani, *et al.*, Phys. Rev. B **93**, 214415 (2016).

[315] Y. Lu, Y. Choi, C. Ortega, X. Cheng, J. Cai, S. Huang, L. Sun, and C. Chien, Phys. Rev. Lett. **110**, 147207 (2013).

[316] S. Nodo, O. Shimpei, T. Yanase, T. Shimada, and T. Nagahama, Appl. Phys. Express (2020).

[317] L. Frackowiak, P. Kuświk, M. Urbaniak, G. D. Chaves-O'Flynn, and F. Stobiecki, Sci. Rep. **8**, 16911 (2018).

[318] Y. Hirata, D. H. Kim, T. Okuno, T. Nishimura, D. Y. Kim, Y. Futakawa, H. Yoshikawa, A. Tsukamoto, K. J. Kim, S. B. Choe, and T. Ono, Phys. Rev. B **97**, 220403(R) (2018).

[319] K. J. Kim, S. K. Kim, Y. Hirata, S. H. Oh, T. Tono, D. H. Kim, T. Okuno, W. S. Ham, S. Kim, G. Go, Y. Tserkovnyak, A. Tsukamoto, T. Moriyama, K. J. Lee, and T. Ono, Nat. Mater. **16**, 1187 (2017).

[320] S. A. Siddiqui, J. Han, J. T. Finley, C. A. Ross, and L. Liu, Phys. Rev. Lett. **121**, 57701 (2018).

[321] R. F. Evans, T. A. Ostler, R. W. Chantrell, I. Radu, and T. Rasing, Appl. Phys. Lett. **104**, 082410 (2014).

[322] T. A. Ostler, J. Barker, R. F. Evans, R. W. Chantrell, U. Atxitia, O. Chubykalo-Fesenko, S. El Moussaoui, L. Le Guyader, E. Mengotti, L. J. Heyderman, F. Nolting, A. Tsukamoto, A. Itoh, D. Afanasiev, B. A. Ivanov, A. M. Kalashnikova, K. Vahaplar, J. Mentink, A. Kirilyuk, T. Rasing, and A. V. Kimel, Nat. Commun. **3**, 666 (2012).

[323] Y. Hirata, D. H. Kim, S. K. Kim, D. K. Lee, S. H. Oh, D. Y. Kim, T. Nishimura, T. Okuno, Y. Futakawa, H. Yoshikawa, A. Tsukamoto, Y. Tserkovnyak, Y. Shiota, T. Moriyama, S. B. Choe, K. J. Lee, and T. Ono, Nat. Nanotechnol. **14**, 232 (2019).

[324] S. K. Kim, K. J. Lee, and Y. Tserkovnyak, Phys. Rev. B **95**, 140404(R) (2017).

[325] J. Finley and L. Liu, Phys. Rev. Appl. **6**, 054001 (2016).

[326] R. Mishra, J. Yu, X. Qiu, M. Motapothula, T. Venkatesan, and H. Yang, Phys. Rev. Lett. **118**, 167201 (2017).

[327] N. Roschewsky, T. Matsumura, S. Cheema, F. Hellman, T. Kato, S. Iwata, and S. Salahuddin, Appl. Phys. Lett. **109**, 112403 (2016).

[328] N. Roschewsky, C. H. Lambert, and S. Salahuddin, Phys. Rev. B **96**, 064406 (2017).

[329] J. Han, A. Richardella, S. A. Siddiqui, J. Finley, N. Samarth, and L. Liu, Phys. Rev. Lett. **119**, 077702 (2017).

[330] O. Inyang, A. Rafiq, C. Swindells, S. Ali, and D. Atkinson, Sci. Rep. **10**, 1 (2020).

[331] L. Frackowiak, P. Kuświk, G. D. Chaves-O'Flynn, M. Urbaniak, M. Matczak, P. P. Michalowski, A. Maziewski, M. Reginka, A. Ehresmann, and F. Stobiecki, Phys. Rev. Lett. **124**, 047203 (2020).

[332] F. Leuenberger, A. Parge, W. Felsch, F. Baudelet, C. Giorgetti, E. Dartyge, and F. Wilhelm, Phys. Rev. B **73**, 214430 (2006).

[333] J. Andrés, J. González, T. Hase, B. Tanner, and J. Riveiro, Phys. Rev. B **77**, 144407 (2008).

[334] A. Berger, A. Pang, and H. Hopster, Phys. Rev. B **52**, 1078 (1995).

[335] A. Talapatra, J. Arout Chelvane, and J. Mohanty, J. Magn. Magn. Mater **489**, 165469 (2019).

[336] G. Champion, N. Lalioti, V. Tangoulis, M. A. Arrio, P. Sainctavit, F. Villain, A. Caneschi, D. Gatteschi, C. Giorgetti, F. Baudelet, M. Verdaguer, and C. C. Dit Moulin, J. Am. Chem. Soc. **125**, 8371 (2003).

[337] Y. C. Tseng, D. Haskel, J. C. Lang, Y. Mudryk, V. K. Pecharsky, and K. A. Gschneidner, J. Appl. Phys. **103**, 07B301 (2008).

[338] R. Streubel, C. H. Lambert, N. Kent, P. Ercius, A. T. N'Diaye, C. Ophus, S. Salahuddin, and P. Fischer, Adv. Mater. **30**, 1800199 (2018).

[339] Y. C. Lau, Z. Chi, T. Taniguchi, M. Kawaguchi, G. Shibata, N. Kawamura, M. Suzuki, S. Fukami, A. Fujimori, H. Ohno, and M. Hayashi, Phys. Rev. Mater. **3**, 104419 (2019).

[340] T. Miyake and H. Akai, Journal of the Physical Society of Japan **87**, 041009 (2018).

[341] A. T. Hindmarch and B. J. Hickey, Phys. Rev. Lett. **91**, 116601 (2003).

[342] D.-O. Kim, K. M. Song, Y. Choi, B.-C. Min, J.-S. Kim, J. W. Choi, and D. R. Lee, Sci. Rep. **6**, 1 (2016).

[343] A. Sakuma, J. Phys. D. Appl. Phys **48**, 164011 (2015).

[344] P. Omelchenko, E. Girt, and B. Heinrich, Phys. Rev. B **100**, 144418 (2019).

[345] K. Wu, J. Mao, Y. Zuo, J. Yun, B. Cui, X. Zhang, Y. Wang, H. Shi, and X. Li, IEEE Trans. Magn **55**, 1 (2019).

[346] E. Villamor, M. Isasa, L. E. Hueso, and F. Casanova, Phys. Rev. B **87**, 094417 (2013).

[347] K.-H. Ko and G.-M. Choi, J. Magn. Magn. Mater , 166945 (2020).

[348] J. Okabayashi, T. Koyama, M. Suzuki, M. Tsujikawa, M. Shirai, and D. Chiba, Sci. Rep. **7**, 46132 (2017).

[349] C. Galinon, K. Tewolde, R. Loloee, W.-C. Chiang, S. Olson, H. Kurt, W. Pratt Jr, J. Bass, P. Xu, K. Xia, *et al.*, Appl. Phys. Lett. **86**, 182502 (2005).

[350] J. King, A. Ganguly, D. Burn, S. Pal, E. Sallabank, T. Hase, A. Hindmarch, A. Barman, and D. Atkinson, Appl. Phys. Lett. **104**, 242410 (2014).

[351] M. Bischoff, T. Yamada, A. Quinn, R. Van Der Kraan, and H. Van Kempen, Phys. Rev. Lett. **87**, 246102 (2001).

[352] Y.-R. Jang and B. Yu, J. Korean Phys. Soc. **60**, 445 (2012).

[353] S. Mathias, L.-O. Chan, P. Grychtol, P. Granitzka, E. Turgut, J. M. Shaw, R. Adam, H. T. Nembach, M. E. Siemens, S. Eich, *et al.*, Proc. Natl. Acad. Sci. U.S.A **109**, 4792 (2012).

[354] W. P. Davey, Physical Review **25**, 753 (1925).

[355] J. Cable and E. Wollan, Phys. Rev. B **7**, 2005 (1973).

[356] L. Uba, S. Uba, V. Antonov, A. Yaresko, T. Ślezak, and J. Korecki, Phys. Rev. B **62**, 13731 (2000).

[357] K. Kirk, J. Chapman, and C. Wilkinson, Appl. Phys. Lett. **71**, 539 (1997).

[358] C. Bayer, J. Park, H. Wang, M. Yan, C. Campbell, and P. Crowell, Phys. Rev. B **69**, 134401 (2004).

[359] R. D. McMichael and B. B. Maranville, Phys. Rev. B **74**, 024424 (2006).

[360] H.-J. Chia, F. Guo, L. M. Belova, and R. D. McMichael, Phys. Rev. B **86**, 184406 (2012).

[361] E. V. Skorohodov, R. V. Gorev, R. R. Yakubov, E. S. Demidov, Y. V. Khivintsev, Y. A. Filimonov, and V. L. Mironov, J. Magn. Magn. Mater. **424**, 118 (2017).

[362] O. N. Martyanov, V. F. Yudanov, R. N. Lee, S. A. Nepijko, H. J. Elmers, R. Hertel, C. M. Schneider, and G. Schönhense, Phys. Rev. B **75**, 174429 (2007).

[363] B. Kuanr, R. E. Camley, and Z. Celinski, Appl. Phys. Lett. **87**, 012502 (2005).

[364] I. Kim, J. Kim, K. H. Kim, and M. Yamaguchi, IEEE Trans. Magn **40**, 2706 (2004).

[365] G. Lebedev, B. Viala, T. Lafont, D. Zakharov, O. Cugat, and J. Delamare, J. Appl. Phys **111**, 07C725 (2012).

[366] Q. Xue, L. Zhang, J. Li, Y. Zhang, C. Wang, Q. Li, J. Xu, Y. Li, and S. Li, IEEE Trans. Magn **51**, 2801204 (2015).

[367] S. van Dijken, G. Di Santo, and B. Poelsema, Appl. Phys. Lett. **77**, 2030 (2000).

[368] M. Umlor, Appl. Phys. Lett. **87**, 082505 (2005).